Investigation of Multiwavelength Correlations for the VHE Gamma-ray Blazar Markarian 421 from 1995 to 2009

Victor Abelardo Acciari

Thesis presented for the award of Ph.D.

Department of Life & Physical Sciences

Galway-Mayo Institute of Technology

Supervisors: Dr. Patrick Moriarty
Dr. Trevor C. Weekes

Submitted to the Higher Education and Training Awards Council

February 2011

To my parents,
Vittorio and Clara

Abstract

The blazar Markarian 421 is an excellent laboratory for studying the physical processes within the jets of active galactic nuclei. In this thesis, a multiwavelength database has been compiled using data from the Whipple Observatory, the Milagro Observatory, the Fermi Gamma-ray Space Telescope, the *RXTE* satellite, the Very Long Baseline Array, the Metsähovi Radio Observatory and the University of Michigan Radio Astronomy Observatory. The Whipple data comprise 878.4 hours of high-quality γ-ray observations taken with the 10m atmospheric Cherenkov telescope over the 14-year period 1995 – 2009; these observations constitute an unprecedented database for examining the long-term very-high-energy (VHE) variability of this source.

The level of variability at VHE γ-ray energies was examined on timescales from days to years. Over the 14-year period the annual mean rate is highly variable with values ranging from 0.18 ± 0.02 Crab units to 2.25 ± 0.31 Crab units; a test for constant rate gives a χ^2 value of 2669 for 13 degrees of freedom. Within each season the rate is highly variable from month to month with mean monthly rate from less than 0.1 Crab to more than 4 Crab; on the basis of the χ^2 test, the most variable season was 2003–2004 while the least variable was 1996–1997. The mean nightly rate exceeds 2 Crab for ~6% of the nights on which the source was observed. On a run-by-run basis (28 minutes), the rate is over 1 Crab for 30% of the runs and over 3 Crab for 5% of the runs. For the other energy bands, the level of variability is found to be lower.

The various datasets were examined for correlations, both quasi-simultaneous and with time delays. In particular, an investigation was carried out to determine whether changes in the radio morphology of Markarian 421 can be associated with the γ-ray emission. Over the 14-year timescale, a clear correlation was found between the X-ray flux and the TeV flux for zero delay; such correlations have been reported before but only on shorter timescales. No significant evidence was found for correlation on any timescale either between the TeV emission and the flux in any other energy band or between the TeV emission and the radio morphology. Searches for periodicity in the X-ray and γ-ray signals showed no evidence for periodic behaviour on any timescale between 2 months and 7 years.

Acknowledgements

I would like to thank all the people that made this research possible, and all those who provided me with moral support, giving me lots of “very high energy” during this long period of hard work! It’s a difficult task to do in just few lines…so I used two pages!

This work wouldn’t have been possible without the limitless help of my supervisors, Dr. Pat Moriarty and Dr. Trevor Weekes, neither of whom likes to be called “Dr”! I hope they will forgive me again this time. For all their guidance and advice and revisions during my studies, I want to thank both of them. No matter how busy they were, they always had time to introduce this interesting field to me, to answer my naïve questions patiently and to give me the opportunity and support to spend time in two wonderful places: Galway and Arizona! *Go raibh maith agaibh*! Thank you also to the Smithsonian and to GMIT for providing “material” help to allow me to have this nice experience, and to IoTI, for providing funding at the start of this adventure. Thanks to Wystan for taking care of all the boring bureaucratic stuff after Trevor (theoretically!) retired; to Mark Lang for useful advice, for being one of my predoc references and for being a good hiking guide! Thanks to those at GMIT: Mark Q, Gary K and Andrew, for helping me at the beginning of my postgraduate studies. To the 10m team: Andy S and John T for helping with my first time in AZ, for giving me the “10 m intensive training” (showing me which cables not to touch!) and for helping me move into a new house, grazie! Also, John K and Ana P (“JJSShhon, queres un poco de mate?” :-)), it was a pleasure working with both of you. Deirdre and Steve, I hope you soon start to make lots of little γ-ray astronomers that want to work at the 10m! To the Basecamp people: Gene G, Jeremy P, Ken G, Karen, Grace, Cesar, Danny, Ryan, George and Jack; the Ridge dorm mates: the belly dancer (and good cook!) Mary K, the guy “from the other planet,” Larry Ciupik (long story! :-)), the DJ David Steele, the Latin dancer Roxanne G, and Perry, Gil, Mike C, thanks to all of you for making the long days (and nights!) at the Ridge nicer. Thanks also to Andrew McC and Stephanie W (with whom I shared a

wonderful time in Erice!); the pool players: Jamie H, John Q and Asif; the Italian team: Andrea C, Angelo V and Nicola (Forza Azzurri!); the Irish team: Josh R, Gary G, JohnE W, and Anna C, *sláinte*!. Thanks to David H (did you already read the book *Darwin's Angel*?), Sagar G, Daniel G, Martin S, Jeff G, John M, Mark T, Ben Z (Dr Zee!), Glen S … I am probably going to forget someone. Just to make sure, should I say thanks to *Acciari et al.*?! :-) By the way guys, I really did read and understand all those papers… I promise! I guess it's almost time for VERITAS publications to be called *Aliu et al.* Congratulations Ester! :-)

I would like to thank my family in Venezuela and Italy. Papá, mamá, a ustedes dedico esta tesis; gracias por sus consejos, paciencia y afecto. A special thanks to my sister Dalia, my brother Jean Pedro, and my aunt Elodia for being always present. Vi voglio molto bene! Vorrei anche ringraziare zio Tonino, e le mie tre cugine: Elvira, Marina e Simona (e i loro rispettivi mariti!); mio caro zio Luciano e famiglia, e i miei zii: Enzo, Rosetta e Oriana; tías Eladia, Pasquala y Milagro; tío Ricardo; y todos mis primos y primitos! Un saluto a mio cognato Pietro, mio nipotino Francesco, i cari Domenica e Fabio, e tutta la famiglia Di Mattia!

Special thanks to Dr.ssa Michelle (grazie, gracias, merci beaucoup, obrigado, شكرا …how many other lenguajes do you speak?!) for the great time we spend together and for all your important help (you are very beautiful and useful! :-)) …"May the river of red wine flow through your life (without damaging the carpets)."

Thanks to my good friends in Tucson: David Turner, Arturo Valenzuela, and Massimo Trovato (ma dove sei? Ti hanno trovato?!) Guys, we have still projects together! And thanks also to Matteo, Alissa, Tod, Jeff, Jacob, Veronica and Hanna for all the pasta parties together! The best Italian food in AZ is in Tubac: *Melios*! Elio e Melinda, grazie per la vostra amicizia e per il delizioso cibo!

I would like to say hello to my "old" and good friends in Ancona: Daniele Diotallevi (lontano ma vicino!), Roberta, Oriella, Gino fan club, and to the members of ex-Casa Farnelli. Also to Gregory, Aurelio, Donato e Fausto. I have nice memories of all of you!

Thanks to the Creator of the blazars for allowing me to study a "small" piece of "this" Universe, for introducing me to all these wonderful people over the past few years and for taking good care of my family and friends.


Markarian 421
“I cieli narrano la gloria di Dio,
e l’immesità del firmamento
mostra l’opera delle sue mani.
Ogni giorno essi parlano,
ed ogni notte ne diffondono
la conoscenza.”
(Salmi 19:1-2)

Contents

List of Figures

List of Tables

Preface

"In the 1st year of the period Chih-ho, the 5th moon, the day chi-ch'ou, a guest star appeared approximately several inches south-east of Tien-Kuan. After more than a year, it gradually became invisible …" …and after more than 935 years it became the standard candle for γ-ray astronomy! This relatively new discipline looks at the Universe through the last of the electromagnetic windows to open to us. I often think about how many other windows may exist and how many other Universes! I feel very lucky to have had the opportunity to have a look "out there" through this fascinating new window using the legendary Whipple 10m telescope, the first ground-based instrument capable of detecting γ-ray photons from astronomical sources.

Cosmic rays were discovered during a series of balloon flights in 1912 by the Austrian physicist, Victor Hess, marking the beginning of a new era of high-energy astrophysics. It was another half-century before γ-ray astronomy became possible. The number of photons available to γ-ray astronomy is very small, but nevertheless a considerable amount of progress has been made during the last few decades. With advances in technology, γ-ray astronomy is now at an exciting stage with the development of sophisticated instruments, including ground-based observatories such as VERITAS working at higher energies and the successful *Fermi* space mission at lower energies.

The original objective of this work was to analyse a few "well-known" γ-ray blazars in an unbiased way for an extended period. The decision to focus on a single source and study Markarian 421 (Mrk 421) in detail was motivated by the large amount of archival data available (recorded over many years of observations), the relatively strong γ-ray signals from this source and the vast coverage of observations by other instruments from radio to X-ray, making it possible to investigate correlations between different energy bands. This thesis deals primarily with the *long-term* behaviour of Mrk 421, but strong, short, historical flares are also

Chapter 1

Astrophysics of Active Galactic Nuclei

Active galactic nuclei (AGN) are galaxies in which a compact nucleus may outshine the rest of the galaxy by a factor of as much as a thousand. *Blazars* are one of the most extreme classes of AGN; they are the most luminous, and they exhibit the most variability and the highest degree of radio and optical polarisation (see Section 1.2.2). Many blazars have been detected at X-ray and γ-ray energies, where they also exhibit high amplitude variability. The subject of this thesis is the investigation both of the variability and of the correlations between different energy regimes for the blazar Markarian 421 (Mrk 421). In order to put these studies in context, a brief introduction to the astrophysics of AGN is given in the following sections, with particular emphasis on the blazar subclass.

The physical processes responsible for the high-energy emission from blazars are discussed in Section 1.3. Models for explaining the broadband emission from blazars will also be described in this chapter, focusing on the implications relevant to the results presented on this work.

1.1 Active Galactic Nuclei – An Overview

The first detection of radio waves from an astronomical object, the Milky Way, was made in the 1930s (see Section 3.2.1). Subsequent advances, especially post-World War II, have identified a number of new classes of objects, such as radio galaxies and pulsars. The discovery of the Cosmic Microwave Background Radiation (CMBR) in 1964 was a particularly significant event.

Radio galaxies and their relatives, quasars (quasi-stellar radio sources) and blazars, are types of AGN that are very luminous at radio wavelengths. Quasars are

enigmatic objects that, like stars, appear as points of light in the sky. AGN were first identified in 1962 when the optical spectrum of 3C 273, previously catalogued as a star, revealed that this object was not in our galaxy (Schmidt 1963) and the term “quasar” was then coined. The most important characteristic of quasars is their significantly high redshift, indicating that they are traveling away from Earth at tremendous speeds, making them the most distant objects observed.

Seyfert galaxies are another type of AGN: weak radio emitters, usually spiral-shaped, that reveal unusual emission lines from the nucleus (Seyfert 1943). Many other different types of objects also belong to the AGN class of galaxies. A way to classify these objects is described in the following section.

1.2 Taxonomy of Active Galactic Nuclei

From an observational point of view, AGN can be divided into objects that are radio-loud (where jets dominate the luminosity of the AGN) and those that are radio-quiet (where jet emission can be neglected). The radio-quiet objects can be further categorised as Seyfert galaxies or quasi-stellar objects (QSOs); the radio-loud objects encompass radio galaxies, quasars and blazars (see Figure 1.1).

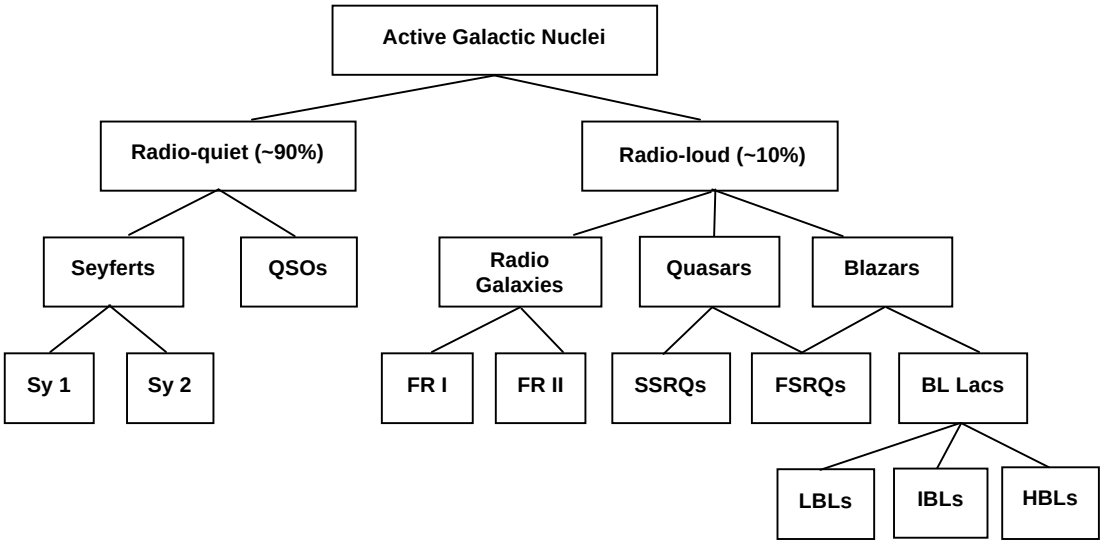

Figure 1.1 Classification scheme for AGN.

Classification of Seyfert galaxies into types Sy 1 and Sy 2 depends on the width of the optical emission lines, narrow or broad, respectively. The subclassification of the radio galaxies, according to their radio morphology (Section 1.2.1), is based on the measurement of the ratio R of the distance between the two brightest spots and the overall size of the radio image: Fanaroff-Riley (FR I) with $R < 0.5$ and Fanaroff-Riley (FR II) with $R > 0.5$ (Fanaroff & Riley 1974). FSRQs and SSRQs are flat-spectrum and steep-spectrum radio quasars, respectively (by convention a power law radio spectrum is said to be flat when the spectral index $\alpha \leq 0.5$ and steep otherwise). Blazars are subclassified into BL Lacertae (BL Lac) objects and FSRQs. Mrk 421 falls into the category of BL Lacs, which are highly variable and are usually seen to be devoid of optical emission lines. The different types of BL Lacs, based on whether they were discovered in X-ray or radio surveys, will be discussed in detail in Section 1.2.2.

It is difficult to estimate the numbers of AGN in the different subclasses shown in Figure 1.1 because of large selection biases in the surveys that identify them. However, it is likely that about 10% of the radio-loud AGN are blazars, and that BL Lacs account for something in the region of 10% of blazars (see, for example, the catalogue compiled by Véron-Cetty & Véron (2010)).

The energy produced by many AGN can vary on short time scales. The luminosity of the broad emission lines and continua of some Sy 1 galaxies and QSOs can change by a factor of two within a few days, weeks or months, while the TeV emission from blazars has been seen to vary by an order of magnitude, with doubling times on the scale of minutes.

The taxonomy of AGN, shown in Figure 1.1 is complex, with subdivisions often being more historical than physical. As in biology however, taxonomy derived from empirical observations can impose some order on the chaos.

1.2.1 Morphological Features in Radio-loud Objects

The primary features in a radio source are the *core*, *lobes*, *hotspots* and *jets*. Not all of these features occur in all sources, and quite often the morphology is too complex to provide an unambiguous separation into these parts. It is, however, convenient to

view a radio source as being built up from them and consider any complex or ill-defined features to be produced from disturbances in the source itself, or in interaction with the ambient intergalactic environment (Kembhavi & Narlikar 1999). A brief description of these features is shown below.

- **Cores**

These are compact components, unresolved when observed with angular resolution ≥ 0.1 arcsecond, and coincident with the nucleus of the associated optical object. They usually have flat power law or complex spectra, which points to synchrotron self-absorption, as explained in Section 1.4. The contribution of the core to the total radio luminosity of a source varies from under 1% in some sources to almost 100% in some quasars.

- **Lobes**

These are extended regions of radio emission. There are often two lobes approximately symmetrically placed on opposite sides of the source. The lobes sometimes contain regions of enhanced emission called hotspots (see below), which are colinear with the central source. The lines joining the extended structure to the central source are sometimes bent back, so that the opening angle is less than 180°.

The lobes often show rotational symmetry and have Z- or S-shaped structures. These shapes are most naturally interpreted as being due to the precession of the axes of the jets.

- **Jets**

These are narrow features that link the compact core to the outer regions. A jet can be interpreted as radio emission from beams that transport energy from the AGN to the extended regions (see Section 1.4). Radio jets occur on parsec as well as kiloparsec scales and can be smooth or knotty. Jets are said to be two-sided when they are seen on both sides of the central source (jet and counterjet). In the more luminous radio galaxies and in all quasars jets are only one sided, while those in the less luminous radio galaxies are two-sided. In blazars the counterjet is not usually visible, since its radiation is beamed away from us (Lister & Homan 2005).

- **Hotspots**

These are intensity maxima located towards the outer extremities of the lobes of highly luminous sources. Hotspot have a linear size of ~1 kpc and a power law spectrum which is steep (i.e., in the range 0.5–1) but generally flatter than the spectral index of the lobe as a whole. This is consistent with the interpretation of a hotspot as the place at which a jet from the nucleus hits the ambient medium, producing a shock in which bulk kinetic energy of the beam is converted to random motion. Jets too can be composed of a number of knots that appear as intensity enhancements and it is difficult to distinguish between these knots and genuine hotspots, yet the two have quite different physical significance. When a jet is detected, one condition is provided so that hotspots can be distinguished from jet knots; the hotspot must be further from the nucleus than the end of the jet.

1.2.2 Blazars and the BL Lac Subclass

It is now generally accepted that the same engine, fuelled by accretion onto a supermassive black hole, powers all AGN (Urry & Padovani 1995), as shown in Figure 1.2a. Accordingly, the observational differences between different types of AGN are attributed to the different orientations of the objects as viewed from Earth (Figure 1.2b) and to the different rates of accretion and masses of the central black hole. Small, dense, fast-moving clouds of matter orbiting above or below the accretion disk exhibit broad optical emission lines (Holt et al. 1980). Larger clouds of matter, moving at slower speeds, and farther from the black hole, exhibit narrow-line emission. A large torus of gas and dust resides outside both the accretion disk and the broad-line emission region. This torus tends to obscure the accretion disk and the broad-line region along most lines of sight.

Among AGN, blazars are the most powerful sources known. They show emission across the entire electromagnetic spectrum in a broad continuum extending from radio through γ-rays. The radio emission is core-dominated with a flat spectrum (see Section 4.2.1 for details), while the optical emission dominates any host galaxy.

In blazars, as in other radio-loud objects, jets emanate from the region near the black hole, initially at relativistic speeds. Powerful magnetic fields exist in these

jets, causing relativistic particles to emit synchrotron radiation (see Section 1.3.1) from radio through to X-ray wavelengths. The jets are roughly perpendicular to the accretion disk that surrounds the black hole, as shown in Figure 1.2. Blazars are believed to have their jets more closely aligned (<10°) with the line of sight than any other class of radio-loud AGN.

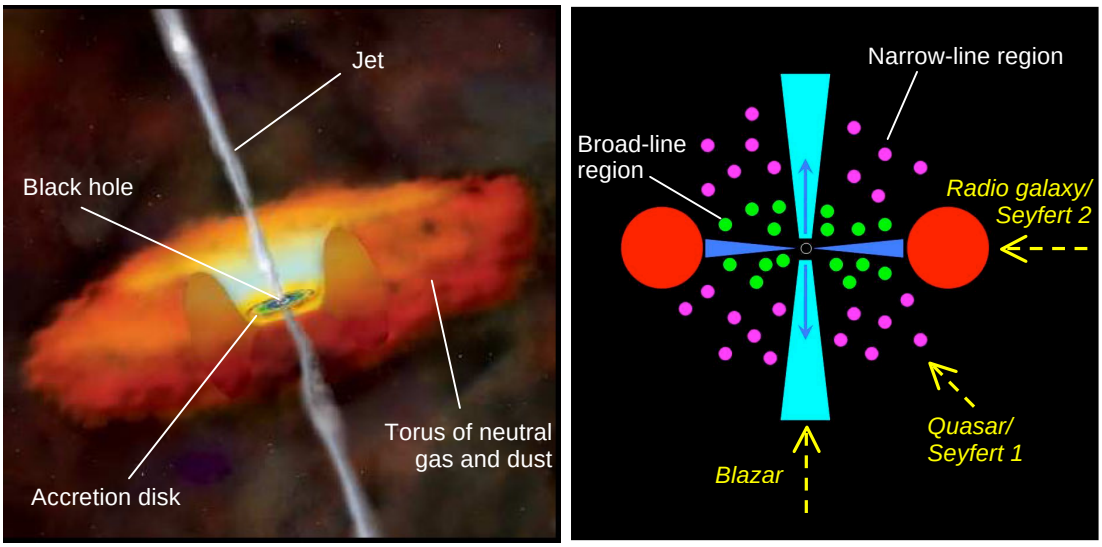

(*a*) (*b*)

Figure 1.2 (*a*) Artist's impression of an AGN, showing the generally accepted model for its physical structure (NASA/CXC/M. Weiss). Jets of high-energy charged particles accelerated away from the black hole give rise to the observed non-thermal radiation. (*b*) Broad- and narrow-line emission regions, and lines of sight for different classes of AGN.

With the exception of M87 (Aharonian et al. 2003; Acciari et al. 2008) and Centaurus A (Aharonian et al. 2009), which are both FR I galaxies, all of the AGN detected at γ-rays energies fall into the blazar class and all of those detected at TeV energies are members of the BL Lac subclass.

BL Lacs are characterized by extremely rapid time-variability: their optical luminosities may change by up to 30% in just 24 hours, and by a factor of 100 over a longer time period (Carroll & Ostlie 1996). BL Lacertae, the prototype of this AGN class, had been mistakenly classified as a variable star in 1928, but was later shown to be the optical counterpart of a peculiar radio source. The main property distinguishing BL Lacs from other AGN is an almost complete lack of emission

lines. Thus, in contrast to most other astronomical sources, BL Lacs have been almost exclusively discovered at either X-ray or radio frequencies.

The *spectral energy distribution* (SED) of BL Lacs, when plotted as the product of frequency and flux, νF_ν, versus frequency ν, is characterised by two broad peaks (see Figure 1.6). BL Lacs can be subdivided into two groups based on the waveband in which the first of these peaks falls (Section 1.4): *high-frequency-peaked BL Lacs* (HBLs) and *low-frequency-peaked BL Lacs* (LBLs) (Horan 2001). More recently, a new class of *intermediate-frequency-peaked BL Lacs* (IBL), lying between HBLs and LBLs, has been introduced.

1.3 Mechanisms of Gamma-ray Production

Electromagnetic energy can be emitted when charged particles are accelerated and also during particle decay processes. In the astrophysical situation, radiative processes related to the production of γ-rays have been studied and described in great detail. In this section, a summary of the most important mechanisms is presented.

1.3.1 Synchrotron Radiation

Synchrotron radiation is the main non-thermal emission process in astrophysics. To produce high-energy photons by this mechanism, ultra-relativistic charged particles moving in strong magnetic fields are required. When a charged particle travels at relativistic speed in a static magnetic field, synchrotron radiation is emitted as the particle spirals around the magnetic field lines. As shown in Figure 1.3a, the radiation is beamed in the direction of the particle's motion, and the observer sees a pulse of radiation each time the beam passes through his line of sight. The pulse is strongly polarized and the frequency spectrum is a continuum, with maximum frequency depending on the particle energy and the magnetic field. The energy loss for a given particle energy is proportional to γ^3, where $\gamma = 1/\sqrt{1-v^2/c^2}$ is equal to the ratio of the energy of the particle to its rest energy, mc^2. While this mechanism

does not contribute significantly to the direct production of TeV radiation, it is extremely important in astrophysical contexts as a source of seed photons for inverse-Compton scattering (Section 1.3.3).

1.3.2 Electron Bremsstrahlung

When an incident charged particle is deflected in the electric field of a nucleus, it emits electromagnetic radiation (Figure 1.3b) whose amplitude is proportional to the acceleration causing the deflection. In the classical case, the acceleration, produced by a nucleus of charge Ze on a particle of charge e and mass m, is proportional to Ze^2/m (Weekes 2003). This acceleration (actually a deceleration) is called *Bremsstrahlung*.

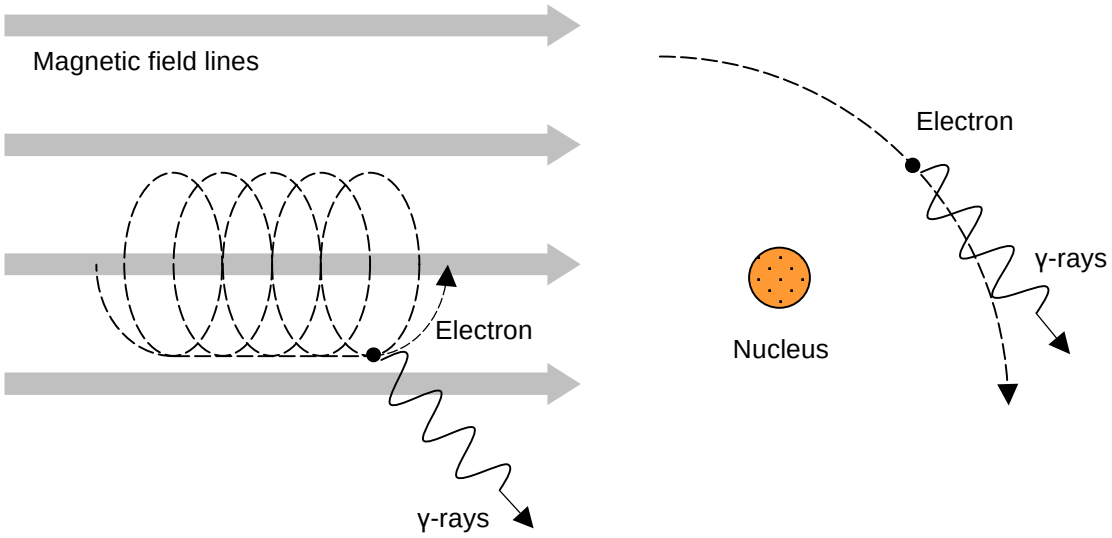

Figure 1.3 (*a*) Synchrotron radiation occurs when charged particles spiral around magnetic-field lines. In both mechanisms, the direction of the radiation is tangential to the electron's trajectory. (*b*) Bremsstrahlung occurs when charged particles are deflected by atomic nuclei.

In the astrophysical situation, this process is most important for relativistic electrons in the presence of atomic or molecular material, for example in supernova remnants (SNR) and in the interstellar medium (Harwit 1988). The overall γ-ray flux

produced by electrons moving in an ionized gas will be proportional to the product of the electron flux and the density of the ionized gas.

1.3.3 Inverse-Compton Scattering

When a photon of wavelength λ interacts with a stationary electron, the photon may transfer part of its energy to the electron, resulting in an increase Δλ in the photon wavelength, given by

$$\Delta\lambda = \frac{h}{m_e c}(1 - \cos\theta) \tag{1.1}$$

where θ is the angle through which the photon is scattered (Figure 1.4a) and m_e is the electron mass. This is *Compton scattering*.

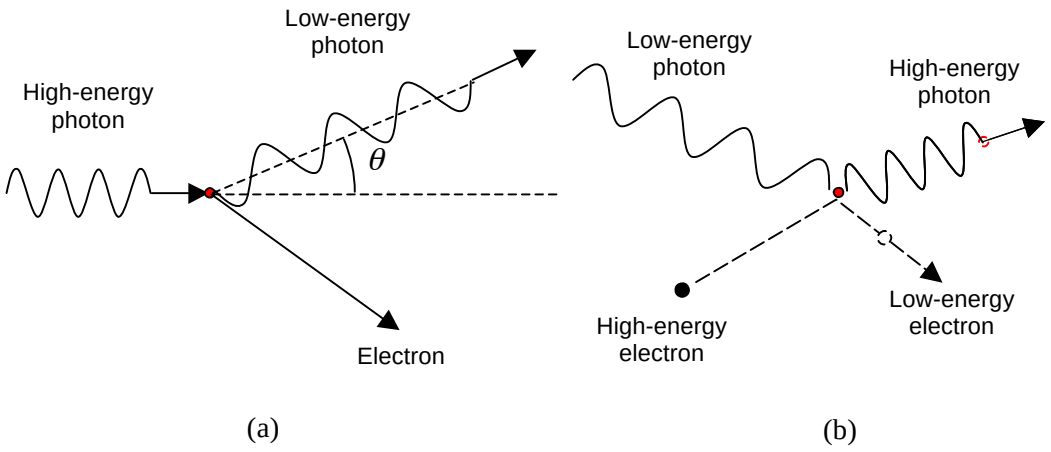

Figure 1.4 *(a)* Compton scattering: A photon scatters off a stationary electron, imparting part of its energy to the electron. *(b)* Inverse-Compton scattering: a low-energy photon is upscattered to higher energy by an electron, which loses energy in the process.

If the photon energy in the electron's rest frame is small compared to the electron rest energy, $h\nu << m_e c^2$, the effect reduces to Thomson scattering, which is well described by classical electrodynamics. The differential scattering cross section in that case is

$$\frac{d\sigma_T}{d\Omega} = \frac{e^4}{2m_e^2c^2}\left(1+\cos^2\theta\right) \tag{1.2}$$

so the photons are redirected over a wide range of angles (equally forwards and backwards), and the total cross section $\sigma_T = 8\pi r_0^2/3$ is independent of photon energy ($r_0 = 2.82\times10^{-15}$ m is the classical electron radius).

If $h\nu >> m_e c^2$, the scattering is concentrated in the forward direction and the outgoing energy in the electron's frame is angle-dependent. In this case, the total cross section is described by the more general Klein-Nishina formula:

$$\sigma_{\mathrm{KN}} = \pi r_0^2\left[\frac{\left(1/x^3\right)\ln\left(1+2x\right)+2\left(1+x\right)\left(2x^2-2x-1\right)}{x^2\left(1+2x\right)^2+8x^2/3\left(1+2x\right)^3}\right], \tag{1.3}$$

where $x = h\nu/m_e c^2$ is the ratio of photon energy to electron rest energy.

Conversely, low-energy photons may be scattered to higher energies by collision with relativistic electrons. This process, called *inverse-Compton scattering* (see Figure 1.4b) is widely believed to be responsible for the observed X-ray and γ-ray emission from AGN.

1.3.4 Pion Decay

The decay of some elementary particles may result in the production of γ-rays. Accelerated protons colliding with other protons or target nuclei produce charged and neutral *pions*, which are unstable (Figure 1.5). In particular, the neutral pion, π^0, has a half-life of 8.4 x 10^{-17}s, and decays into two γ-rays, each with energy $1/2m_{\pi^0}$ in the rest frame of the pion.

This process is important for the development of electromagnetic cascades in the atmosphere (Section 2.2.2), and is also the basis for so-called hadronic models of TeV γ-ray emission in extreme astrophysical environments. Such environments include shell-type SNR and the jets of AGN.

Neutral pions are rarely created at rest, and generally decay in flight. A π^0 that decays while travelling at relativistic velocities can produce γ-rays with energies

in the GeV – PeV range in the "laboratory" reference frame. Identification in astronomical observations of the γ-ray signature of pion production and decay provides critical evidence for astrophysical proton acceleration, as recently demonstrated in the case of the starburst galaxies M82 and NGC253 (Acciari et al. 2009a; Acero et al. 2009).

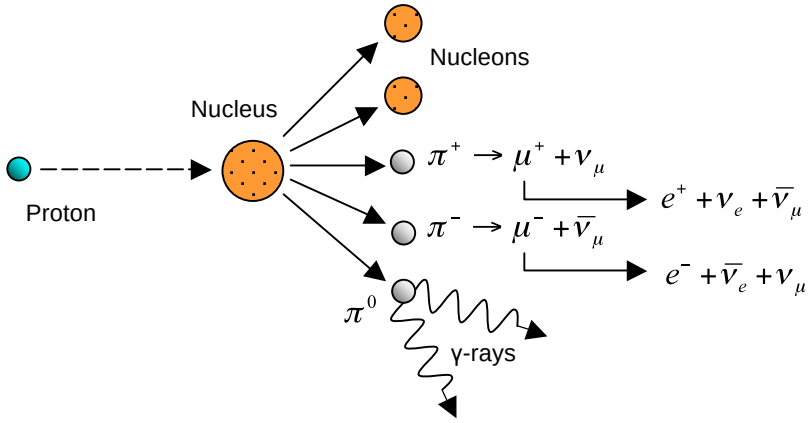

Figure 1.5 Neutral pions, produced by high-energy proton collisions, decay into γ-rays. Decay of charged pions gives rise to muons and neutrinos.

1.3.5 Particle-antiparticle Annihilation

Mutual annihilation of a particle and its antiparticle can produce a pair of γ-ray photons. For example, an electron and positron can annihilate:

$$e^+ + e^- \rightarrow \gamma + \gamma \tag{1.4}$$

If the particles are at rest prior to the annihilation, both γ-ray photons have energy equal to the rest energy of the particle: for the example shown, the photon energy is 511 keV.

Annihilation processes are extremely important in the search for dark matter in the Universe. The putative neutralino (χ_0), the lightest supersymmetric particle and the favoured candidate for weakly interacting dark matter, is its own antiparticle. The process

$$\chi_0 + \chi_0 \rightarrow \gamma + \gamma \tag{1.5}$$

with neutralino mass in the GeV-TeV range could then be expected to give rise to quasi-monochromatic gamma radiation which would be a characteristic signature indicating the presence of dark matter. Indirect searches for dark matter based on this process have targeted environments such as dwarf galaxies and globular clusters where a high density of dark matter is expected, although these searches have so far proved unsuccessful (see, e.g., Acciari et al. 2010a).

1.3.6 Curvature Radiation

For a relativistic charged particle in an very strong magnetic field, synchrotron radiation leads to rapid damping of the velocity component perpendicular to the magnetic field, so the particle is essentially forced to follow the field lines. If the field lines are curved, the particle then accelerates, resulting in emission of radiation called “curvature radiation”. This process is expected to occur, for example, for electrons in the intense magnetic fields close to the surface of pulsars (Gil, Lyubarsky & Melikidze 2004).

1.4 Blazar Spectral Energy Distribution and Emission Models

The characteristic SED for a blazar shows continuum emission extending from radio to γ-ray energies, with two broad components. For more powerful blazars, the energy output in the first (lower energy) SED component (attributed to synchrotron radiation) peaks in the infrared to optical band, whereas for low-power blazars the synchrotron peak is located at UV to X-ray energies (Fossati et al. 1998). The location of the second peak is closely correlated with the synchrotron peak energy, and for low-power blazars is expected to lie in the GeV-TeV region of the spectrum (Grube 2007). The SEDs shown in Figure 1.6 are all for low-power blazars, with the lower-energy component peaking above 10^{15} Hz (photon energy > 4eV, wavelength < 300nm), and the higher-energy peak well up into the GeV and TeV regions.

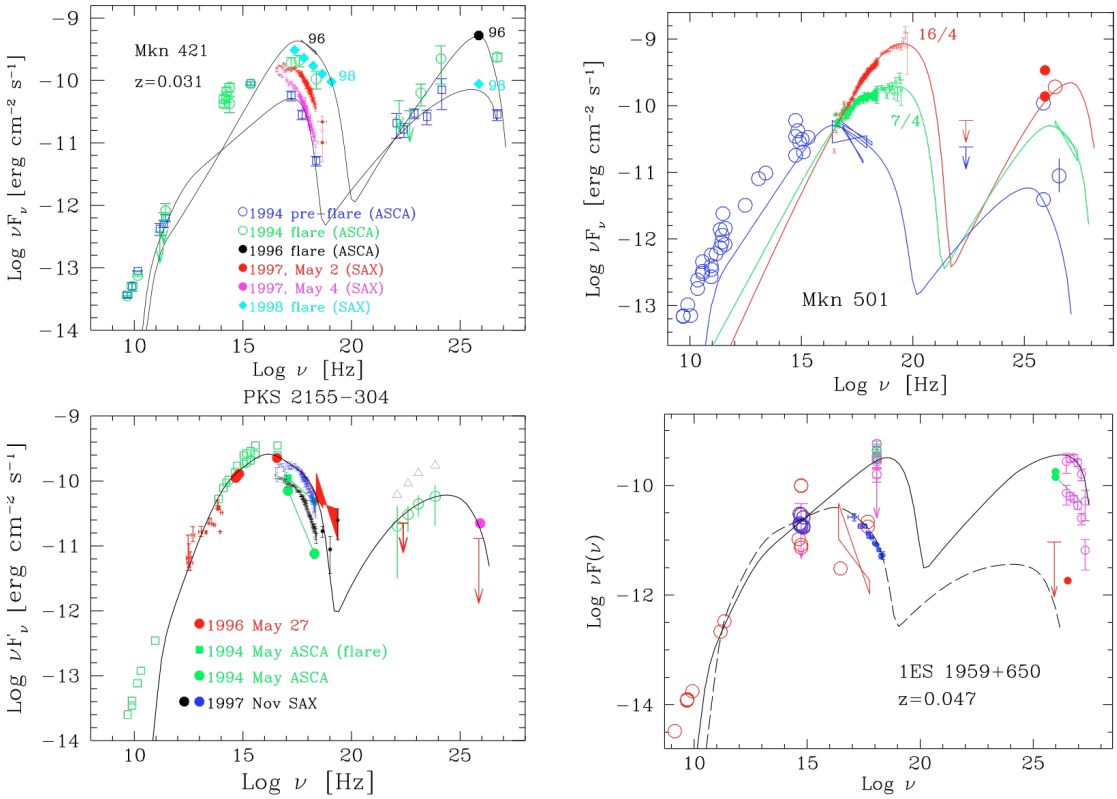

Figure 1.6 The SEDs of four blazars (Mrk 421, PKS 2155-304, Mrk 501 and 1ES1959+650) showing different spectral variability with different flux levels (Costamante 2004).

W Comae was the first intermediate-frequency peaked BL Lacertae object (IBL) to be detected at TeV energies. A detection was made by VERITAS (Section 2.4) in 2008 (Acciari et al 2008). The SED of this source is shown in Figure 1.7a.

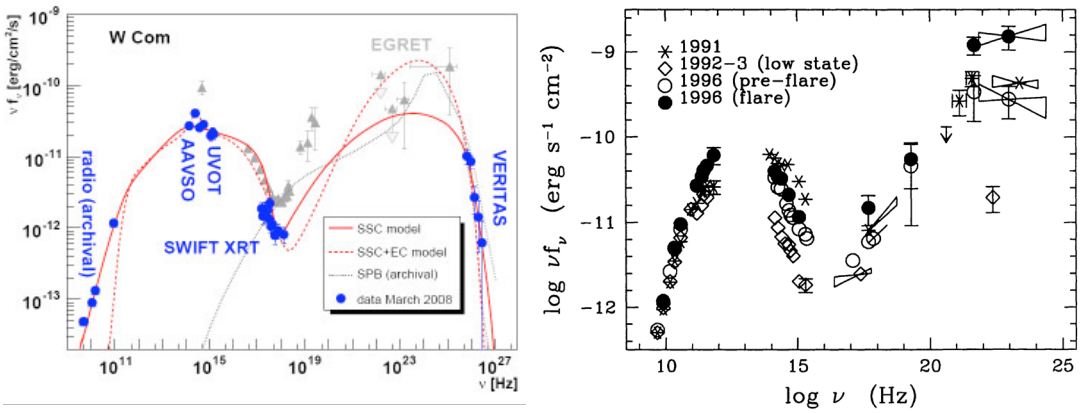

(*a*) (*b*)

Figure 1.7 (*a*) Quasi-simultaneous SED of WComae. (*b*) SED of 3C 279. Figure taken from Urry (1999).

The blazar 3C 279 has been detected by EGRET, high-energy instrument on board of the space-based telescope Compton Gamma Ray Observatory (CGRO), at GeV energies. This source is one of the best-monitored at lower frequencies. Its detection by EGRET during the very low state in December 1992 (Maraschi et al. 1994) is undoubtedly due to the fact that 3C 279 is one of the closest (redshift $z = 0.538$) of the EGRET-detected flat-spectrum radio-loud quasars (FSRQs). Figure 1.7b shows its SED.

Several models have been proposed to explain the overall SED of blazars. The starting point for these models is a population of either high-energy electrons/positrons (*leptonic models*) or high-energy protons (*hadronic models*). These particles may acquire their high energy through reflection in inhomogeneous magnetic fields at shock fronts, a process called Fermi acceleration. This is believed to be the primary mechanism by which particles gain energy in astrophysical shock waves within the jets of blazars.

- **Leptonic Models**

Synchrotron Self-Compton (SSC) and External Compton (EC) are leptonic models with the non-thermal emission coming from a population of electrons and positrons in the jet. The acceleration of the particles occurs in shock waves propagating along the jet. The resulting energy spectrum from this process typically follows a power law $N(E) \propto E^{-p}$, where N is the number of particles of energy E and p is the spectral index. The observed SED shape of blazars suggests an electron spectrum that steepens with increasing energy.

SSC is a mechanism in which a population of high-energy electrons emits synchrotron radiation (from the far IR or radio to the UV – soft X-rays) followed by inverse-Compton scattering of synchrotron photons (interacting with the *same electron population*) to TeV energies. The simplest SSC model is the *one-component* version, where the radiation observed at any given moment is produced by a shock moving along the jet of the blazar (Sikora & Madejski 2001). Here, the emission region is assumed to be a single zone, with a homogeneous magnetic field, moving at relativistic speed. The size of this region can be estimated from the variability time-scale, as explained in Chapter 6 (Equation 6.1). Bloom & Marscher (1996) found

that, for a SSC model, varying the magnetic field strength alters the flux in both the synchrotron and self-Compton regime; below the Klein-Nishina limit ($h\nu = m_e c^2$), the synchrotron and self-Compton cut-off energies are shifted, while above this limit the influence of the magnetic field is suppressed.

The EC process is similar to what occurs in the SSC model except that the dominant source of seed photons for upscattering in the inverse-Compton process is ambient radiation, rather than synchrotron radiation from the jet itself. In order for this process to dominate over the SSC mechanism, the energy density of the external radiation must exceed the energy density of synchrotron radiation produced in the jet. Several sources of external radiation have been considered, including: accretion-disk photons directly entering the jet (Dermer et al 1992); disk radiation reprocessed by emission-line clouds, dust and intercloud medium (Sikora et al 1994); and synchrotron radiation re-scattered back into the jet by broad-line clouds (Ghisellini & Madau 1996).

- **Hadronic Models**

In hadronic models for blazars, shock-accelerated protons and electrons give rise to two different populations of particles, protons and electron-positron pairs, which are responsible for the entire SED through synchrotron emission (Mannheim & Biermann 1992; Mastichiadis 1996).

In this scenario, electrons cool via synchrotron radiation, explaining the radio to optical continuum from low-density hot spots in the radio jets. Protons are shock-accelerated to extremely high energy, and are immersed in this soft photon field. These protons produce extremely energetic neutral pions, which decay into photons (Equation 1.6) with energies ranging from ~keV to ~TeV.

$$\begin{aligned} p + p &\rightarrow \pi^0 + \textit{other hadrons} \\ \pi^0 &\rightarrow \gamma + \gamma \end{aligned} \tag{1.6}$$

Two main families of hadronic models exist. The first involves beams of protons with energies in excess of 10^{16} eV. The second requires beams of ultra-high-energy protons, with energies greater than 10^{19} eV. Dar & Laor (1997) consider clouds of gas with high column density crossing the jet of accelerated protons. The

broad-line region is proposed here as the source of such clouds. The electrons and positrons generated by the decay of charged pions then cool by synchrotron radiation and inverse-Compton scattering to produce wideband emission (optical through to TeV). Within the family of ultra-high-energy proton beam models, Mannheim (1993) suggests that both electrons and protons might be accelerated by multiple crossings of shock-waves in the jet. The protons can be accelerated to energies in excess of 100 TeV by this process. They can then lose energy by adiabatic expansion (proton pressure decreases as the shock wave dissipates), synchrotron cooling, ionisation, or interaction with photons in the region via

$$p + \gamma \rightarrow \pi^0 + p \tag{1.7}$$

The neutral pion then decays into a γ-ray pair, as in (Equation 1.6), and the γ-ray photons interact in the optically-thick jet to produce an electromagnetic cascade, referred to as a proton-induced cascade. Both the lower and higher peaks in the blazar's SED can be explained by these cascades.

Although observations can challenge both leptonic and hadronic models, neither can be convincingly ruled out. However, leptonic models (SSC and EC) are usually favoured over hadronic models. One reason for this is the strong correlation between observed X-ray and TeV fluxes. This correlation indicates that the same population of electrons is responsible for both the synchrotron and inverse Compton components of blazar SEDs. Moreover, the rapidity of the flaring exhibited by TeV blazars (often on time scales as short as minutes) is difficult to explain using hadronic scenarios as protons have considerably longer cooling times than electrons (Toner 2008).

1.5 Markarian 421

At a redshift of z = 0.031 (distance = 127.2 Mpc; Crook et al. 2007), Markarian 421 (Mrk 421) is located in the constellation of Ursa Major (Figure 1.8) at RA: 11h 04m 27.3s, Dec: 38° 12' 32" (J2000), and was the first extragalactic source of very-high-energy (VHE; Energy > 100 GeV) γ-rays to be discovered. Mrk 421 was detected by

the Whipple Collaboration in 1992 at the 6σ level, with a flux above 500 GeV approximately 30% that of the Crab Nebula (Punch et al. 1992).

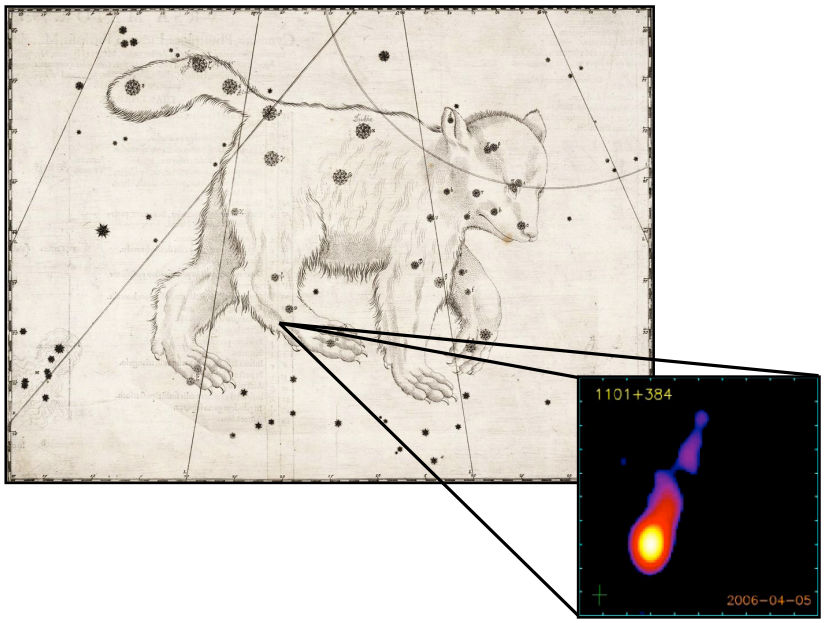

Figure 1.8 Location and VLBA intensity image of Mrk 421 (at 15 GHz, MOJAVE) in Ursa Major (J. Bayer, *Uranometria*, 1603).

Mrk 421 is categorized as a high-frequency-peaked BL Lac object (HBL), where the synchrotron peak lies in the X-ray regime (See Figure 1.6). Historically it has exhibited shifts in both the peak frequency and in the power of the first and second components of the SED (Fossati et al. 2008). During 2005 and 2006, a multiwavelength campaign of Mrk 421 was conducted, i.e., different instruments and systems were involved to cover observations of this source in the radio, optical, X-ray and γ-ray bands.

Figure 1.9 shows the SED of Mrk 421 during this campaign. Two representative dates were chosen, defined by the γ-ray data as “high state” and “medium state”; archival data were used where no contemporaneous observations were available (Buckley 2000). The dashed purple lines in Figure 1.9 show the synchrotron and self-Compton distributions for a model based on the parameters listed in Table 1.1. As in previous studies (Krawczynski et al. 2001; Rebillot et al. 2006), it was necessary to use a high Doppler factor ($\delta = 90$), a low magnetic field ($B \sim 0.12$ Gauss) and a very small emission region R (~70 gravitational radii) in

order to match the observations. A very hard electron spectrum (~$E^{-1.5}$) and low acceleration efficiency were also required, with the mean free path for scattering ~20 times the Bohm limit and a shock velocity of $0.02c$, resulting in relatively few shock crossings (Horan et al. 2009).

Parameter	Value
Doppler Factor, δ	90
Magnetic field in the bulk frame, B	0.12 Gauss
Electron energy density compared with equipartition value	0.3
Electron spectral index	1.5
Size of emission region, R	70 R_{Sch}
Electron mean-free-path compared with gyroradius	20
Cooling time at maximum electron energy	2.25 min
Acceleration time at maximum electron energy	2.25 min
Shock velocity in bulk frame	0.02 c
Soft photon peak wavelength	1.0 μm
Mass of black hole	$10^8 M_\odot$

Table 1.1 The model parameters used on the SED plots shown in Figure 1.9.

In Figure 1.9, the black dot-dashed curves show a hypothetical blackbody component peaked at 1 μm and the corresponding external Compton component, while the red solid line shows the sum of the SSC and EC models results, which, in both cases, is in good agreement with the simultaneous optical, X-ray and γ-data (Horan et al. 2009).

Markarian 421 has been observed quasi-continuously with the Whipple 10m telescope during the period from December 1995 to June 2009. Note that because of its RA/Dec, Mrk 421 can only be observed at reasonable elevations from Arizona between December and June, and only on dark, moonless nights. Following the application of quality selection criteria (elevation > 55°, good weather and absence of instrumental problems), the result is a total of 878.4 hours of high-quality data, representing an unprecedented database for examining the long-term VHE behaviour of this enigmatic object. In this thesis, the results of analysing these TeV γ-ray observations are presented in Chapter 5. These results are then used to study the long-term variability of the source, and to investigate correlations between the TeV measurements and observations at other wavelengths.

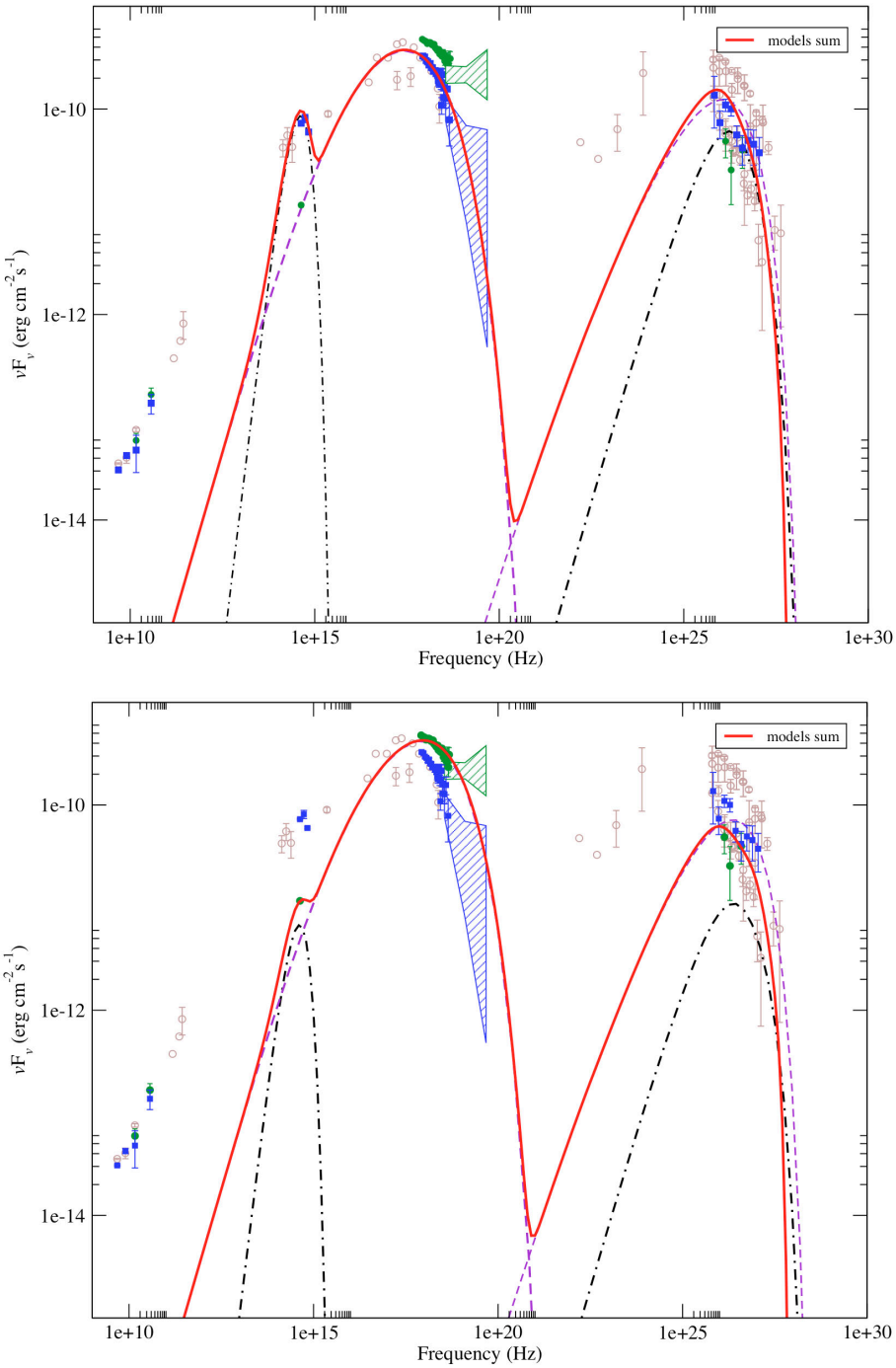

Figure 1.9 SEDs for Mrk 421. Data points in blue filled squares are from MJD 53763, when the VHE emission was at a high level, while the green filled circles are from MJD 53852, when it was at a medium emission level. Archival data are shown in brown open circles. The solid red curve in each plot represents a combined SSC and EC model, with parameters (Table 1.1) chosen to reproduce the high emission state (top) and the medium emission state (bottom). In both cases, the model provides a good description of the optical to TeV data.

Chapter 2

Ground-based Gamma-ray Astronomy

For photon energies above ~20 GeV, astronomical γ-ray observations are possible using ground-based telescopes. The γ-ray photons are not detected directly, but rather through their interactions in the Earth's atmosphere, which essentially acts as the calorimeter in the atmospheric Cherenkov technique. VHE γ-ray photons initiate extensive air showers (Section 2.2) in the upper atmosphere, and the charged particles in these showers induce Cherenkov radiation (Section 2.3), which is detectable from the ground with large optical reflectors (Section 2.4).

Unlike the distribution of cosmic rays incident on Earth's atmosphere, the flux of incident VHE γ-ray photons is not isotropic. Since γ-ray photons are uncharged, they are not deflected in the magnetic fields that exist throughout space and so their trajectories point directly back toward their origin.

2.1 Historical Note

The seeds of ground-based γ-ray astronomy were sown in 1953, when Galbraith and Jelley, using a simple mirror-PMT arrangement, first succeeded in detecting Cherenkov radiation from extensive air showers produced by cosmic radiation in the upper atmosphere (Galbraith & Jelley 1953). Five years later, Morrison (1958) suggested that γ-rays in the cosmic radiation should be detectable at ground level in this way, and the following year Cocconi produced optimistic predictions for the detection of VHE γ-ray photons using arrays of particle detectors (Cocconi 1960). Subsequently, many ground-based γ-ray telescopes were built in the 1960s with the aim of detecting atmospheric Cherenkov radiation arising from γ-ray photons. These systems included the 12 light detectors operated by the Lebedev Institute at the

Crimean Astrophysical Observatory (1960–1964), and the first large optical reflector purpose-built for γ-ray astronomy – the Whipple 10m telescope, installed on Mount Hopkins (Arizona) in 1968 (see Figure 2.1). Unfortunately these systems did not succeed in detecting any sources.

The development of the imaging technique (see Section 4.1.1) with the Whipple 10m telescope over the next 20 years finally led to the detection of the Crab Nebula in 1988-89 (Weekes et al 1989), ending the prolonged period of uncertainty in the development of VHE γ-ray astronomy.

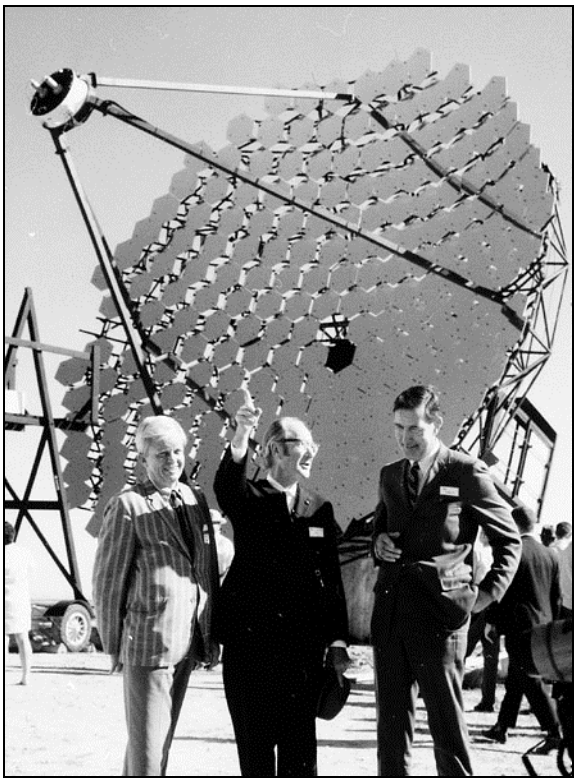

Figure 2.1 The Whipple 10m telescope in 1968.

2.2 Extensive Air Showers

Among the high-energy particles reaching the Earth, mostly electrically charged cosmic rays (protons and ionized atomic nuclei), there is a small flux of γ-ray photons. Such energetic particles initiate extensive air showers when they interact with the atoms of the Earth's atmosphere at altitudes of 10–20 km above sea level. These air showers are cascades of particles (electrons, muons and hadrons) and γ-ray

photons that propagate through the atmosphere until the energy of the cosmic initiator has been dissipated. Of the particles in the shower, only muons and neutrinos survive to sea level.

The development of the air shower is strongly dependent on whether it was initiated by a hadron or by a γ-ray photon. In particular, γ-rays interact higher in the atmosphere and the longitudinal spread of the shower is somewhat different in the two cases (see Figure 2.2). This allows for the separation of showers induced by hadrons from those induced by γ-ray photons, and is the basis of the imaging Cherenkov technique (Hillas 1985; Hillas 1996), described in detail in Section 4.1.1.

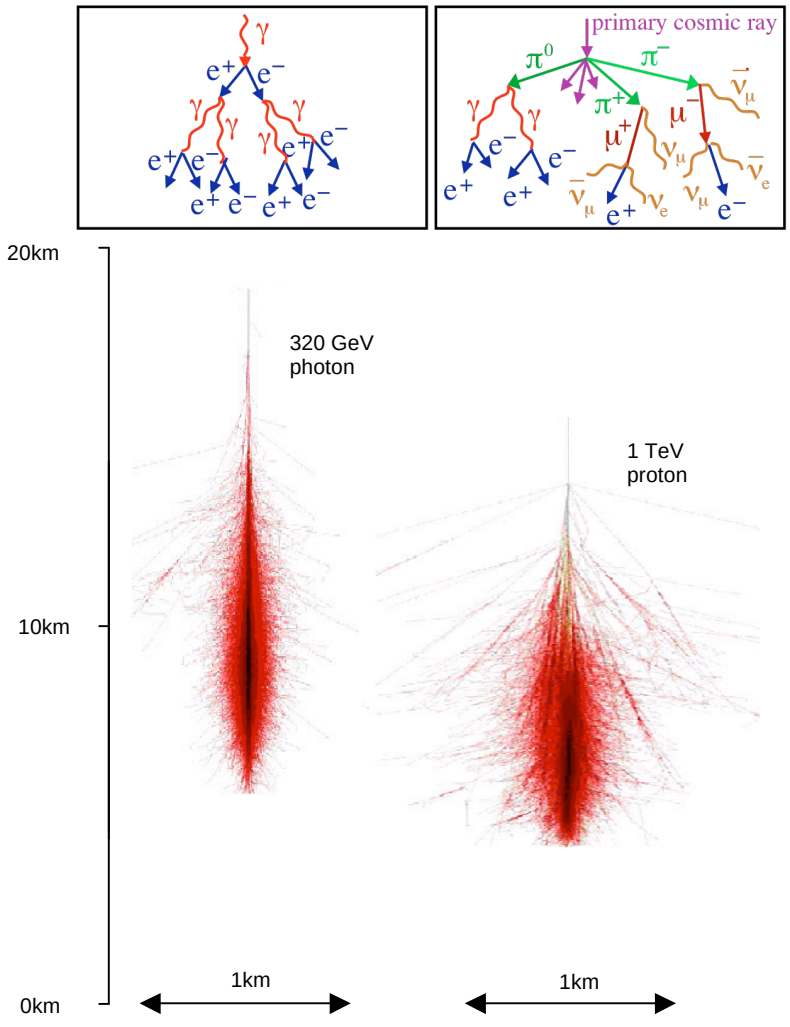

Figure 2.2 The development of γ-ray- (left) and hadron- (right) induced showers. The top panels show examples of the individual particles and radiation that are generated in the showers. Images from Horan (2001) and Grube (2007).

2.2.1 Gamma-ray-induced Showers

A *γ-ray-induced shower* is produced when a high-energy γ-ray photon enters the Earth's atmosphere and undergoes *pair production*: $h\nu \rightarrow e^- + e^+$. The relativistic electron/positron pair subsequently loses energy through Bremsstrahlung, emitting high-energy γ-ray photons that can, in turn, undergo pair production. This cycle continues, resulting in an exponentially growing cascade of particles and radiation, until the mean energy of the electrons falls below ~100 MeV. At this point, energy loss by ionization exceeds that due to Bremsstrahlung; cascade multiplication then ceases and the particles are subsequently absorbed (Cranshaw 1963). As the relativistic electrons and positrons pass through the atmosphere, they induce Cherenkov radiation (see Section 2.3). This radiation is strongly beamed to within about 1° of the arrival direction of the primary γ-ray. The total amount of Cherenkov light radiated is proportional to the total number of particles in the shower, which depends on the energy of the initiating photon. Thus, the Cherenkov light behaves like a penetrating component and provides a good estimate of the energy of the primary γ-ray.

2.2.2 Hadron-induced Showers

Hadron-induced showers are caused by the isotropic flux of cosmic rays incident on the Earth. Cosmic ray particles are mainly protons, but also include nuclei of heavier elements. When these particles collide with oxygen and nitrogen nuclei in the atmosphere, cascades containing large numbers of elementary particles and radiation are induced. The initial products include nucleons and kaons, but the cascade consists primarily of charged pions, which subsequently decay into muons and neutrinos, and neutral pions, which decay to γ-ray pairs:

$$\begin{aligned} &\pi^+ \rightarrow \mu^+ + \nu_\mu, && \tau = 2.6\times10^{-8}\,\mathrm{s} \\ &\pi^- \rightarrow \mu^- + \bar{\nu}_\mu, && \tau = 2.6\times10^{-8}\,\mathrm{s} \\ &\pi^0 \rightarrow \gamma + \gamma, && \tau = 8.4\times10^{-17}\,\mathrm{s} \end{aligned} \qquad (2.1)$$

where τ is the decay lifetime. Muons do not interact strongly, they have lifetimes ~2.2×10^{-6} s and they travel close enough to the speed of light for relativistic effects to be significant, so many of them penetrate to the Earth's surface. The neutral pions π^0 rapidly decay into pairs of γ-ray photons, which subsequently undergo e^+e^- pair production. The secondary nucleons and charged pions continue to multiply until the energy per particle falls below the threshold for multiple pion production (~1 GeV). Since the pions are produced via the strong nuclear interaction, they can acquire a large transverse momentum, and the lateral spread of hadronic showers is therefore typically much greater and less symmetrical than that of γ-ray showers.

2.3 Cherenkov Radiation

When a charged particle travelling through a medium moves faster than the local speed of light, a wake of light is emitted. That is, $v > c/n$, where v is the velocity of the particle, c is the velocity of the light, and n is the refractive index of the medium. The geometry involved is shown in Figure 2.3 (Rolnick 1994).

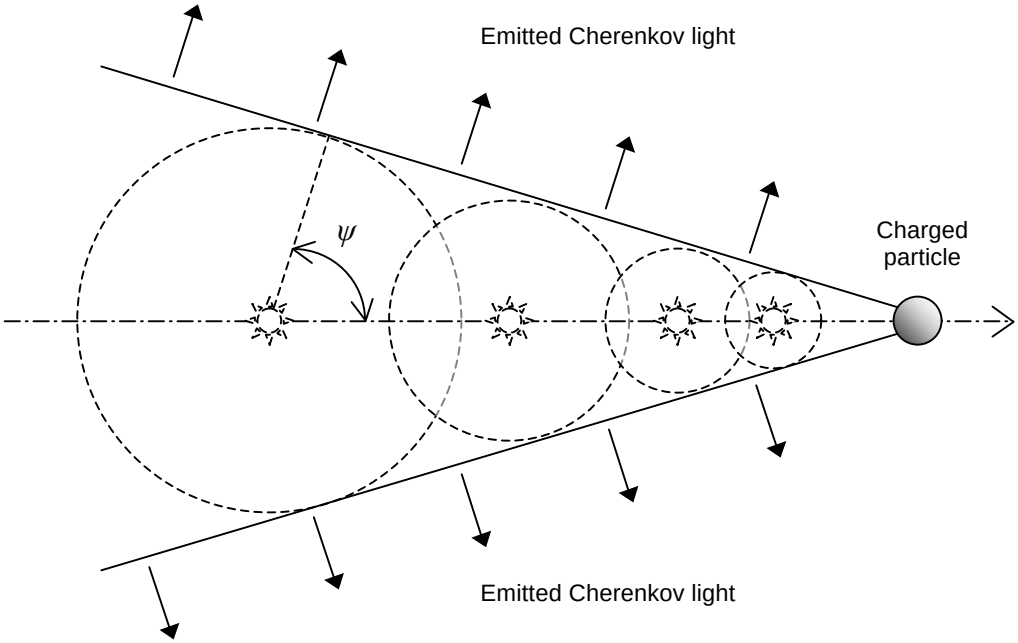

Figure 2.3 Cherenkov radiation from a moving charged particle.

The charged particle interacts electrically with the molecules in its immediate vicinity, inducing polarization that varies as the particle passes, thereby causing the molecules to radiate. Each finite element radiates a brief electromagnetic pulse (Weekes 2003). In the forward direction, the wavefronts from each element along the track will interfere constructively at an angle ψ (see Figure 2.3), determined from the values of v and n according to

$$\cos(\psi) = \frac{c}{nv} \tag{2.2}$$

This is the fundamental Cherenkov radiation equation. Clearly, there is a threshold velocity, $v = c/n$, and a maximum Cherenkov angle, $\psi = \cos^{-1}(1/n)$, so the radiation can only occur for $n > 1$, which covers the optical region of the spectrum for most materials. It is these properties of well-defined emission angle and threshold velocity that make Cherenkov radiation detectors so useful in particle physics.

Figure 2.4 shows schematically the emission of Cherenkov light in the atmosphere. The refractive index of air depends on the local pressure and temperature, but a good estimate at the altitude where most air showers are initiated is $n \sim 1.0001$. This corresponds to a local speed of light, $v \sim 0.9999c$, and maximum Cherenkov angle, $\psi \sim 0.8°$. The resulting light pool then has a radius of ~140 m at sea level and ~100 m at the Whipple 10m telescope, situated at an altitude $H_T = 2320$ m above sea level.

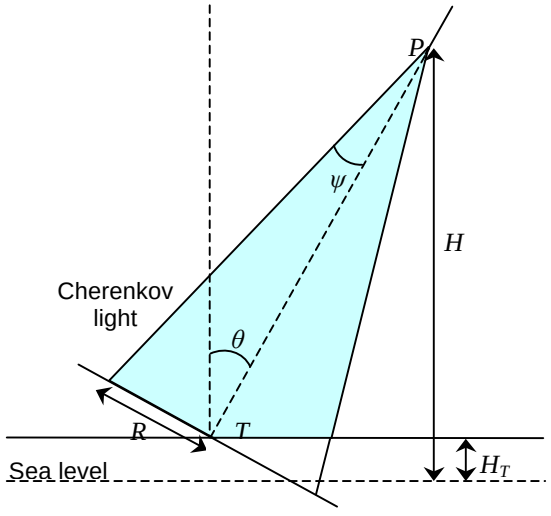

Figure 2.4 Emission of Cherenkov light in the atmosphere. The Cherenkov angle, ψ, is given by Equation 2.2.

2.4 Atmospheric Cherenkov Telescopes

The Earth's atmosphere is opaque to γ-ray photons. However, at energies above ~20 GeV, they produce extensive air showers of electrons and positrons along with more lower-energy photons. Electrons and positrons whose speeds exceed that of light in the atmosphere give rise to Cherenkov radiation that can be detected by ground-based instruments, allowing the arrival direction and energy of the incident γ-ray photon to be determined.

The basic atmospheric Cherenkov telescope can be very simple. First-generation systems consisted of just a single light detector, photomultiplier tube (PMT), in the focal plane of a searchlight mirror coupled to fast pulse-counting electronics. The basic elements are illustrated in Figure 2.5.

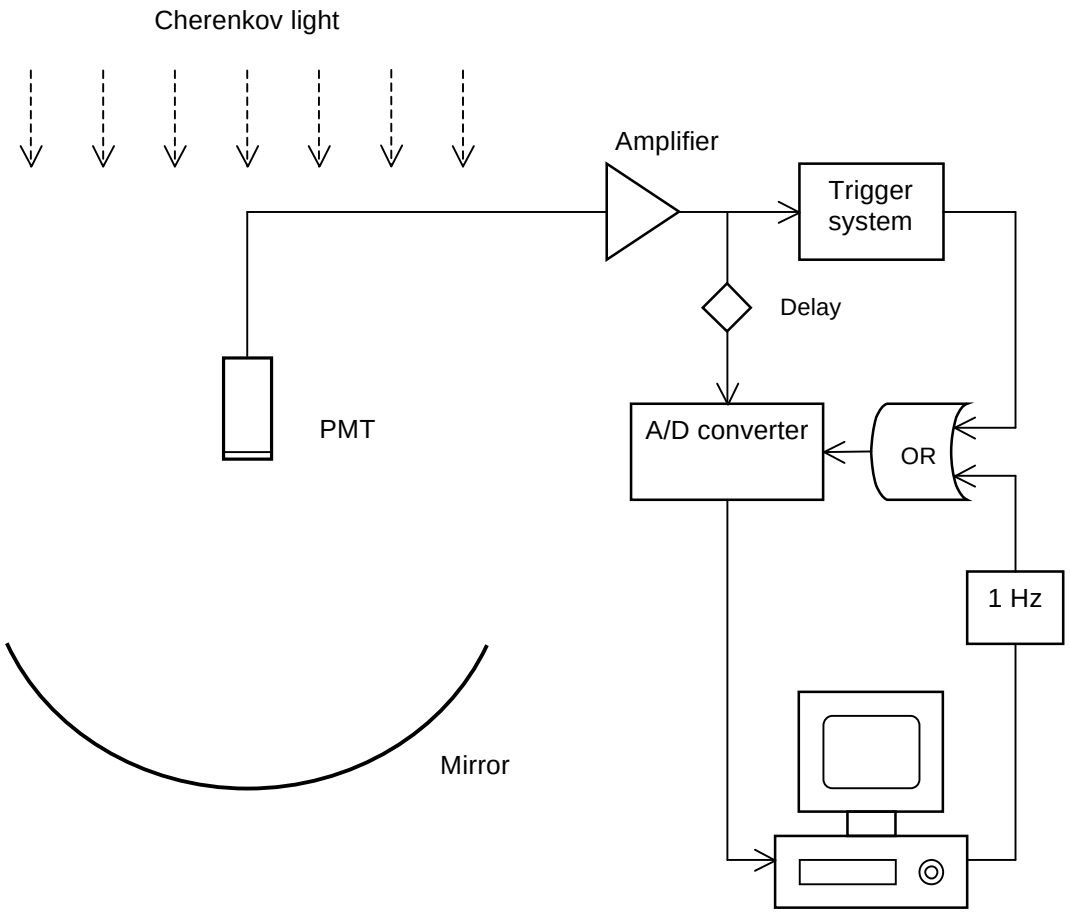

Figure 2.5 Schematic diagram of a simple atmospheric Cherenkov telescope.

If the integration time *t* of the photomultiplier pulse-counting system (shown in Figure 2.5) is greater than the duration of the Cherenkov light pulse (3-5ns), the ratio of the Cherenkov signal *S*, from an air shower, to the noise *N*, due to night-sky fluctuations *B*, is given by (Weekes 2003)

$$\frac{S}{N} = \frac{S}{\sqrt{B}} = \frac{\int_{\lambda_1}^{\lambda_2} C(\lambda)\,\varepsilon(\lambda)\,A\;\,d\lambda}{\sqrt{\int_{\lambda_1}^{\lambda_2} F(\lambda)\,\varepsilon(\lambda)\,\Omega\;t\;A\;\,d\lambda}} = \int_{\lambda_1}^{\lambda_2} C(\lambda)\sqrt{\frac{\varepsilon(\lambda)\;A}{F(\lambda)\,\Omega\,t}}\;d\lambda \qquad (2.3)$$

where

- $F(\lambda)$ is the night-sky background flux,
- $C(\lambda)$ is the Cherenkov photon flux,
- $\varepsilon(\lambda)$ is the quantum efficiency of the PMT,
- Ω is the solid angle of observation,
- *t* is the integration time (longer than the duration of the Cherenkov light pulse),
- *A* is the mirror area, and
- λ_1 and λ_2 are the minimum and maximum wavelengths between which the PMT responds.

The minimum detectable Cherenkov light pulse, and hence the threshold energy of the minimum shower detectable, E_T, is inversely proportional to *S/N*:

$$E_T \propto \frac{1}{C(\lambda)}\sqrt{\frac{F(\lambda)\,\Omega\,t}{\varepsilon(\lambda)\,A}} \qquad (2.4)$$

Thus, the energy threshold is minimized by integrating for a time as close as possible to the duration of the Cherenkov light pulse, and by maximizing the detector area and the quantum efficiency of the PMTs.

For the signal to be identified as real, and not due to an extreme fluctuation in the ambient light background, it is usual to require that $S/N > 5$ within the time interval *t*. The identification of the light signal as coming from a γ-ray induced

shower rather than from a cosmic ray air induced shower is quite a different matter. The development of the Cherenkov imaging technique (described in Section 4.1.1) gave the first effective shower discriminator. An *array* of PMTs (rather than a single PMT) in the focal plane of a large optical reflector constitutes a camera, which can be used effectively to record a Cherenkov-light image of each shower. The Whipple 10m telescope presently operates with a 379-pixel, 2.6° field-of-view camera that has been in place since 1999 (Kildea at al 2007). The camera is triggered when a preset number (usually ≥3) of the PMTs detect a light level above a set threshold within a short integration time (typically 15 ns). The light level in all pixels is then recorded digitally and the image is analysed to determine whether it has the expected characteristics of a γ-ray shower with a point of origin at the centre of the field of view (Weekes 2003). Discrimination against the background is based on the geometry and physics of the shower. This method is explained in Section 4.1.1.

The atmospheric Cherenkov imaging technique can be significantly improved by the use of multiple telescopes with separations of the same order as the lateral spread of the Cherenkov light from the air shower. Stereoscopic detection of the shower improves the angular resolution, flux sensitivity and energy resolution, reduces the energy threshold, and provides better rejection of background cosmic ray air showers. Such a system is implemented, for example, in the Very Energetic Radiation Imaging Telescope Array System (VERITAS), a group of four 12-metre aperture telescopes located at the base camp of the Fred Lawrence Whipple Observatory (FLWO) in southern Arizona at an altitude of 1268 m (Figure 2.6). The telescopes are separated by ~100 m, corresponding to the radius of the air shower (~120 m) at that altitude. VERITAS was officially inaugurated in April 2007 (Horan 2007) and is dedicated to observations in the energy band 100 GeV–30 TeV. It is at least ten times as sensitive as the pioneering Whipple 10m telescope.

Three other arrays are operating at present. MAGIC, comprising two 17-metre aperture reflectors, is located on La Palma in the Canary Islands; this system is capable of operating at energies as low as ~25 GeV (Aliu et al. 2008). The H.E.S.S. array of four 12-metre diameter telescopes is situated in the Khomas Highlands in Namibia (Hofmann et al. 2005). The Japan-Australia collaboration CANGAROO

operates a system of essentially three 10-metre diameter telescopes at Woomera in the Australian outback (Kiuchi et al. 2009).

Figure 2.6 The Very Energetic Radiation Imaging Telescope Array System (VERITAS). Figure courtesy of Criswell, FLWO.

Chapter 3

Detectors

Gamma-ray photons are photons with energy above about 100 keV. Such photons do not penetrate the Earth's atmosphere. However, photons with energy above about 20 GeV interact with air molecules at an altitude of around 10 km and give rise to showers of particles that move downward towards the ground (Section 2.2). Cherenkov light is emitted by the charged particles that comprise air showers, and the detection of this light forms the basis for the imaging technique (Section 4.1.1) employed by all ground-based atmospheric-Cherenkov telescopes. Therefore, one can observe γ-ray radiation above about 20 GeV from the ground by using the atmosphere as part of a detector, i.e., as a calorimeter. Below ~20 GeV, observations must rely on satellite-borne detectors (*Swift*, *INTEGRAL*, *AGILE*, and now *Fermi*).

The location of optical and radio astronomy in the electromagnetic spectrum coincides with the two principal transparent bands of the Earth's atmosphere and ionosphere. These transparent bands are commonly referred to as the optical and radio windows. The radio window extends from a wavelength of about 0.5 mm to 20 m. The range of energy between VHE γ-ray radiation and radio waves is about 20 orders of magnitude. This range is so large that widely different instrumentation and techniques are required. This chapter describes the instruments whose data has been used in this thesis.

The Whipple 10m telescope was the first large ground-based instrument purpose-built for γ-ray astronomy. The design of the structure, optics and electronic system of this telescope are discussed in Section 3.1. Some basic definitions of radio astronomy and the main tools used in this field are presented in Section 3.2, along with the description of the instruments that contributed to the results presented in this thesis. Two space-based observatories are presented in Section 3.3: the X-ray satellite, *RXTE*, and the high-energy γ-ray satellite, *Fermi*; the instrumentation and techniques applied to both satellites are described in that section. The Milagro

Gamma-ray Observatory is a ground-based TeV detector that makes use of the water-Cherenkov technique to detect Cherenkov radiation from secondary shower particles in extensive air showers. An overview of the Milagro detector configuration and trigger conditions is presented in Section 3.4.

3.1 The Whipple 10m Telescope

The Whipple 10m telescope (see Figure 3.1), built in Arizona in 1968, is currently the fourth most sensitive ground-based γ-ray system in the world, after VERITAS, HESS and MAGIC. VERITAS can detect a source at 1% of the Crab flux in 25 hours, and has been estimated to be a factor of ten more sensitive than the Whipple 10m (Weekes 2008).

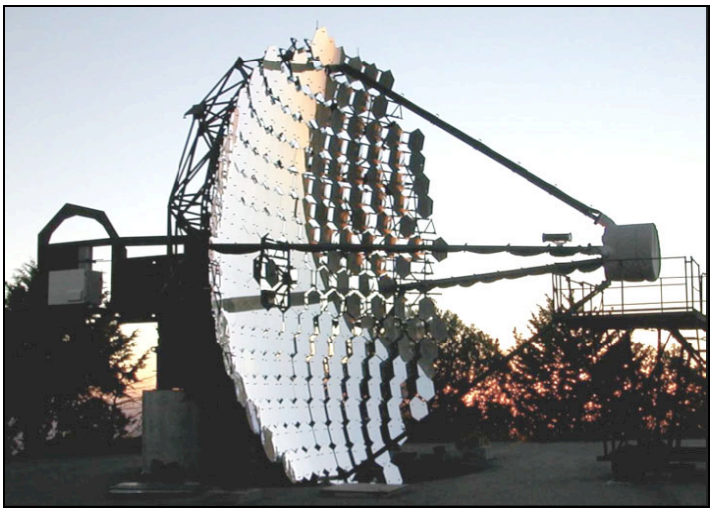

Figure 3.1 The Whipple 10-metre γ-ray Telescope, circa 2009.

The Whipple 10m telescope consists of two main parts: the *reflector* and the *detector*. The reflector comprises the physical and optical structure of the instrument. The detector, which includes the camera and associated electronic components, detects and records astronomical data. The characteristics of both the reflector and the detector are discussed in detail in the following subsections.

The Whipple 10m telescope has undergone a number of changes during its history (see Figure 3.4), including a major upgrade to the camera in 1999 (Finley et

al. 2001). Since then, the sensitivity of the telescope has changed very little, although there was some additional improvement during the 2007–2008 season. This was achieved by applying offline pointing corrections (Section 4.1.2), re-focusing the camera for the height of γ-ray shower maximum (Section 3.1.1) and carrying out a bias alignment of the mirror facets (Section 3.1.2). This section gives an overview of the entire Whipple 10m γ-ray system. A more detailed description will be given for the most recent hardware updates (current monitor, laser pulser, CCD camera) and for the work directly involved with this thesis.

3.1.1 Reflector and Camera

The reflector of the Whipple 10m telescope follows the solar-collector design proposed by Davies & Cotton (1957), comprising a spherical tubular steel optical support structure (OSS) with opening diameter 10 m and radius of curvature f = 7.3 m. The primary dish is composed of 248 spherical front-aluminised glass mirrors, each 61 cm across, 1 cm thick and hexagonal in shape. Each individual mirror facet has radius of curvature 14.6 m, twice that of the OSS (see Figure 3.2).

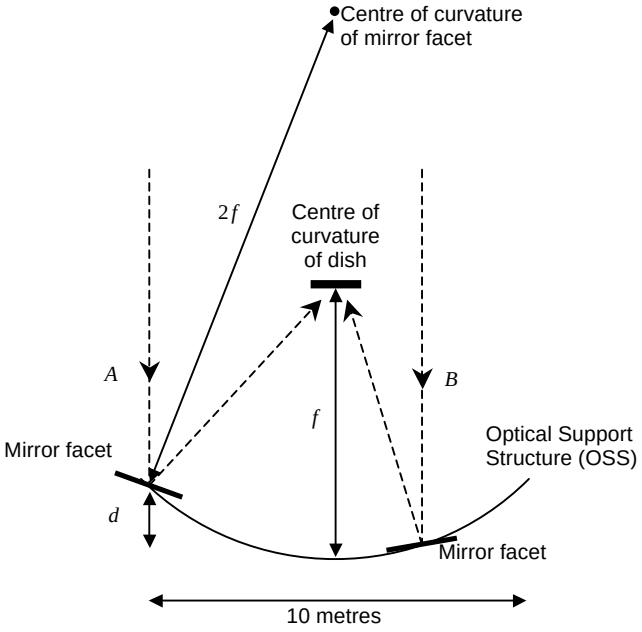

Figure 3.2 Davies-Cotton reflector design. The spherical dish has a radius of curvature half that of the individual mirror facets. The instrument is anisochronous: parallel rays *A* and *B* do not strike the focal plane simultaneously, due to the mirror separation *d*.

The Davies-Cotton configuration gives smaller off-axis optical aberrations than a parabolic design. One disadvantage for γ-ray air shower detection, however, is that, unlike a parabolic reflector, the structure is not isochronous. Rays striking mirrors at different distances from the optic axis have different transit times to the focal plane. For the Whipple telescope the spread of transit times is 6.5 ns (Kildea et al. 2007).

Front aluminization is used for the mirror surface because of its superior reflectivity in the blue and UV range – peak mirror reflectivity is typically around 90% at 310 nm and 85% from 280 nm to 450 nm (Roache et al. 2007), corresponding to the peak in the Cherenkov light spectrum from a γ-ray shower at about 325 nm. All the mirrors together provide an effective reflecting surface of 75 m^2. Mirror reflectivity is affected by washing, degradation (presumably due to wind-borne dust/sand) and re-coating. Mirror re-coating would ideally be carried out every two years, but the intervals have tended to be somewhat longer and not all mirrors are re-coated at the same time, particularly since the inception of VERITAS. The effect of re-coating on sensitivity can be seen in the plot of yearly Crab rate between 2002 and 2003 (Figure 4.17). Variation in the reflectivity from season to season is one of the factors the Crab normalisation (Section 4.1.4) is intended to account for.

The telescope has an altitude-over-azimuth mount supported by a concrete pedestal, with counterweights providing balance. A cylindrical focus box, containing the camera, is held at the focal plane of the reflector by four steel arms (see Figure 3.3).

The camera consists of an array of fast-response, high-quantum-efficiency photomultiplier tubes (PMTs). The basic camera (Cawley et al 1990) was upgraded during the course of the observations presented in this work. The different camera configurations are illustrated in Figure 3.4. Initially the camera consisted of a single PMT. The data used in this thesis start from 1995, at which time the camera consisted of a closely packed hexagonal array of 109 PMTs (one-inch diameter), each of which viewed a circular field of view (FOV) of 0.26° diameter, giving a total FOV of 3°. The current Whipple camera has 379 half-inch PMTs with 0.12° FOV each, giving a total FOV of 2.8°. Only the inner 331 PMTs contribute to the trigger (see Section 3.1.3), so the effective FOV of the camera can be considered to be 2.6°.

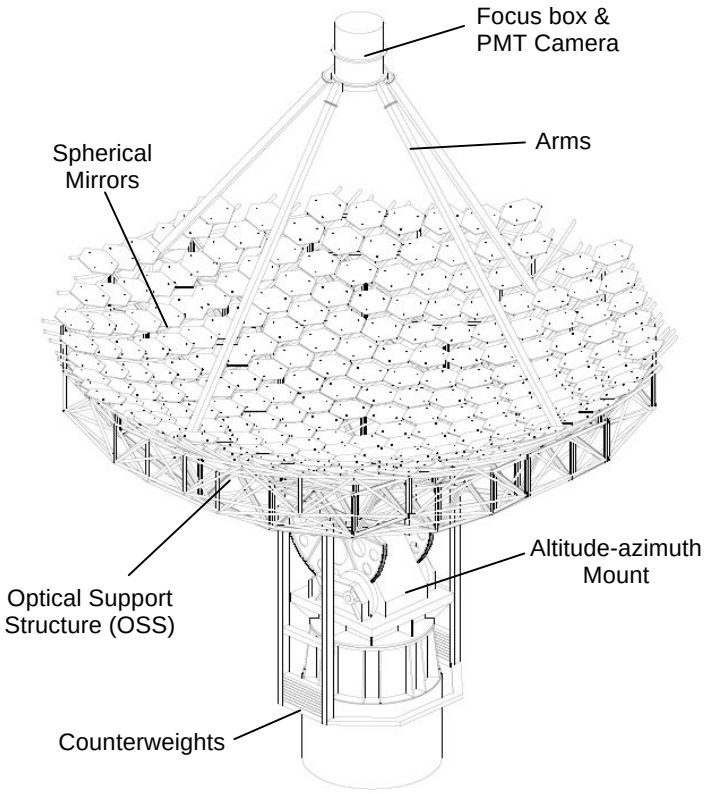

Figure 3.3 The physical structure of the Whipple 10m telescope. The 248 spherical mirrors are mounted on a spherical OSS with a focus box held in position by a tetrapod arrangement.

The PMT spectral responses are chosen so as to match the Cherenkov light spectrum, which peaks in the blue to near UV. Light-concentrating cones are employed at the focal plane, in front of the PMTs, to improve the light-collection efficiency of the camera (Figure 3.5). These “lightcones” help reflect photons, which would otherwise be lost in the inter-pixel spacing, onto the photosensitive area of the PMTs, and they also provide albedo protection against light from the night-sky background (NSB) and from the telescope’s surroundings. Typical efficiency improvements provided by light concentrators are between 30% and 40% (Kildea et al. 2007).

For the last three camera configurations shown in Figure 3.4, the high voltage (HV) to each PMT is supplied by an individual channel of a LeCroy 1458 HV module, located on the telescope’s counterweights. Voltages are typically in the neighbourhood of -900 V (cathode relative to grounded anode). Communication with the HV modules is through custom control software, which sends commands via Ethernet.

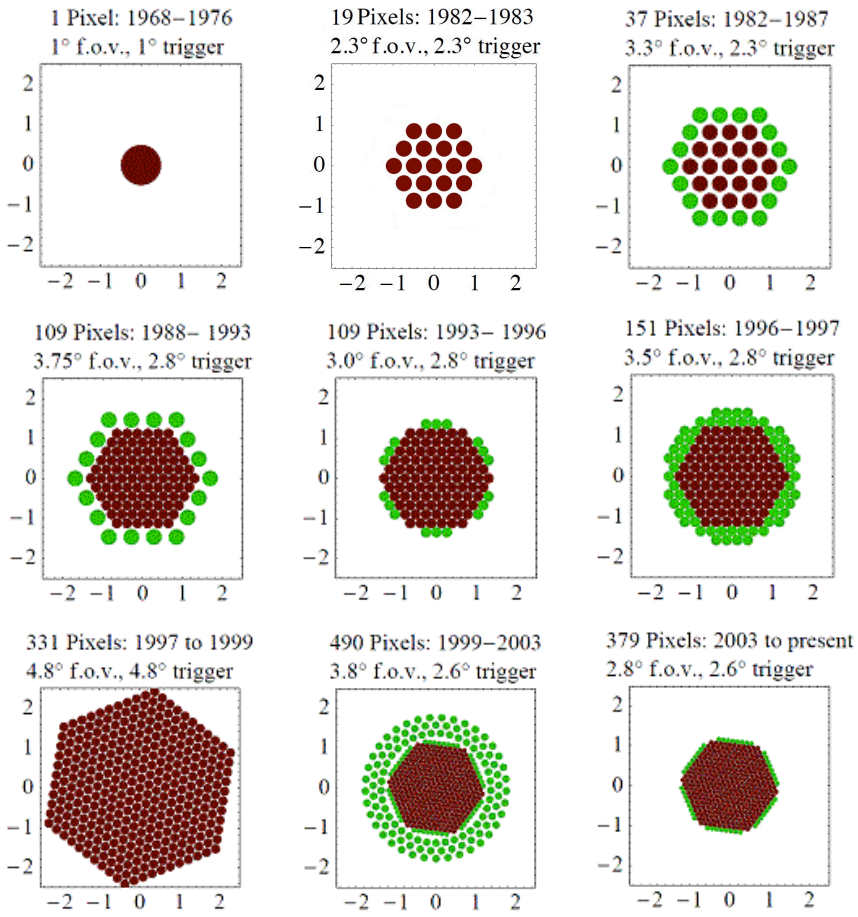

Figure 3.4 Configurations of various PMT cameras deployed on the Whipple 10m telescope from 1968 to present. The brown pixels were/are included in the telescope's triggering electronics (Schroedter 2004).

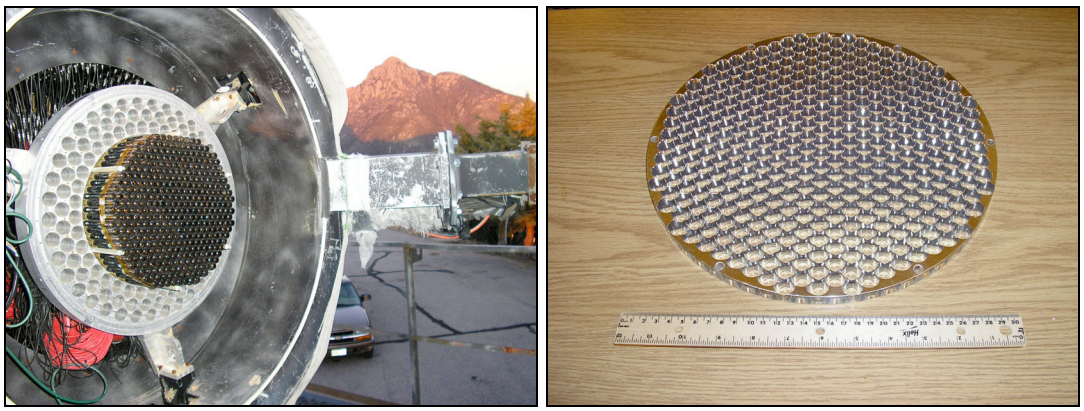

Figure 3.5 *Left*: The 379-PMT camera (without lightcones) in the focus box of the telescope. On the picture is partially visible one of the four arms, and Mount Wrightson in the background. *Right*: The lightcone plate, which fits onto the front of the camera.

The current camera of the Whipple 10m telescope was moved in February 2008, to bring it into focus for showers at a distance of 8 km from the camera, corresponding to the height at which the maximum shower development occurs for TeV γ-rays. To do so, the camera was moved forward by about 0.9 cm. This resulted in tightening of image parameters and some evidence for improvement in detected Crab Nebula rate (Kildea 2008).

3.1.2 Point-spread Function Measurements and Bias Alignment

The procedure for the mirror alignment of the telescope is based on the fact that, for a Davis-Cotton reflector, a light source at the 2*f* point, shining on the centre of any mirror facet, should retro-reflect. If the light is transmitted to the facet via a beam splitter, the return beam should then coincide with the beam reflected in the beam splitter. The alignment is carried out by adjusting each mirror facet so that the light from it *does* retro-reflect. This is done with the telescope stowed at its home position, at elevation 0° and azimuth 0° (north).

The point-spread function (PSF) of the telescope is measured by directly imaging stars onto the focal plane using a CCD camera mounted at the centre of the OSS viewing the PMT camera. The size of the PSF depends on the quality of the mirror alignment. Ideally, it should have a full width at half-maximum (FWHM) less than the angular size of the individual pixels in the camera (i.e., 0.12° or less). During observations, the PSF degrades due to a combination of two factors: gross deformation of the OSS and individual mirror motion. These effects can be reduced by the technique of *bias alignment*, whereby it is arranged that the mirrors will fall into correct alignment at typical observing elevations. In a bias alignment, the mirror facets are deliberately misaligned with the telescope in its home position so that they come into proper alignment at elevation 65°, which is a typical observing elevation (see, for example, Table 4.3). Bias measurements carried out by the author on VERITAS Telescope 3 (T3) are described here; a similar procedure applies to the Whipple 10m telescope.

In order to perform a bias alignment, the movement experienced by each mirror must be characterised. To do this, a small, lightweight laser unit is attached to a mirror facet (see Figure 3.6).

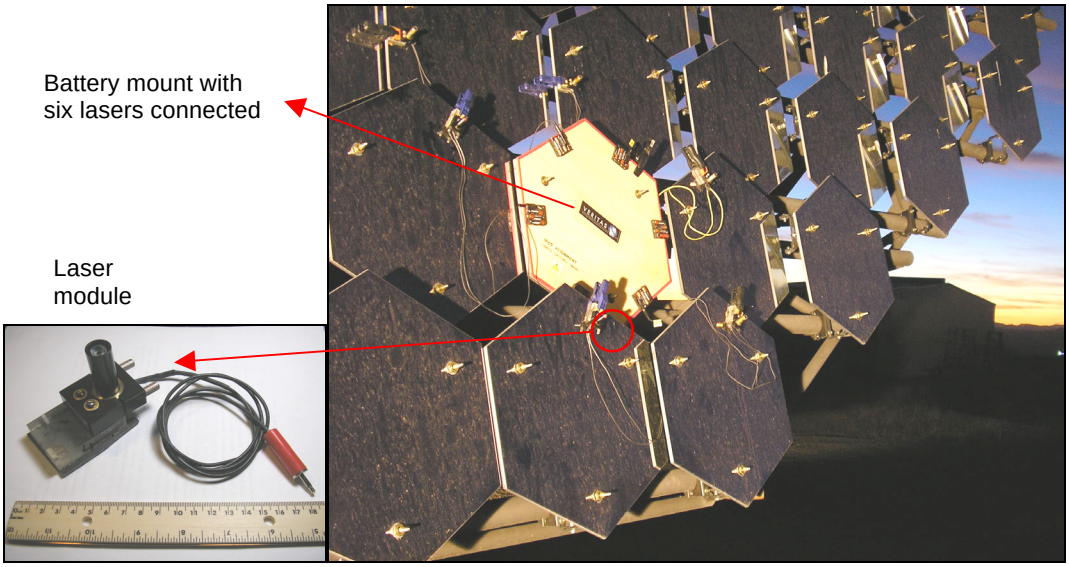

Figure 3.6 Single laser module (left panel). The author built a special mount in order to clamp the lasers independently of the battery packs (right panel). This helps to solve the problem of modules slippage when the telescope is moved, which can lead to erroneous results.

The laser beam is directed onto the focal plane of the telescope, where a white screen has been attached, and a CCD image of the focal plane is obtained. The telescope is then raised to the elevation of the desired best focus at 65°, and another CCD image is obtained. This is repeated for all mirror facets on the reflector. Typically six mirror facets were monitored at once (a *frame*), and then the lasers were moved onto a different set of mirrors. A *SBIG* CCD camera model ST-402 XME, positioned at the centre of the reflector, was used to take the images. The amount by which the laser spot moves on the focal plane is measured by comparing the images taken at the two different telescope positions. During all the bias measurement procedure, a reference laser was permanently clamped to the positioner plate in the centre of the OSS. The movement of each laser spot on the focal plane was calculated relative to this reference one (see Figure 3.7).

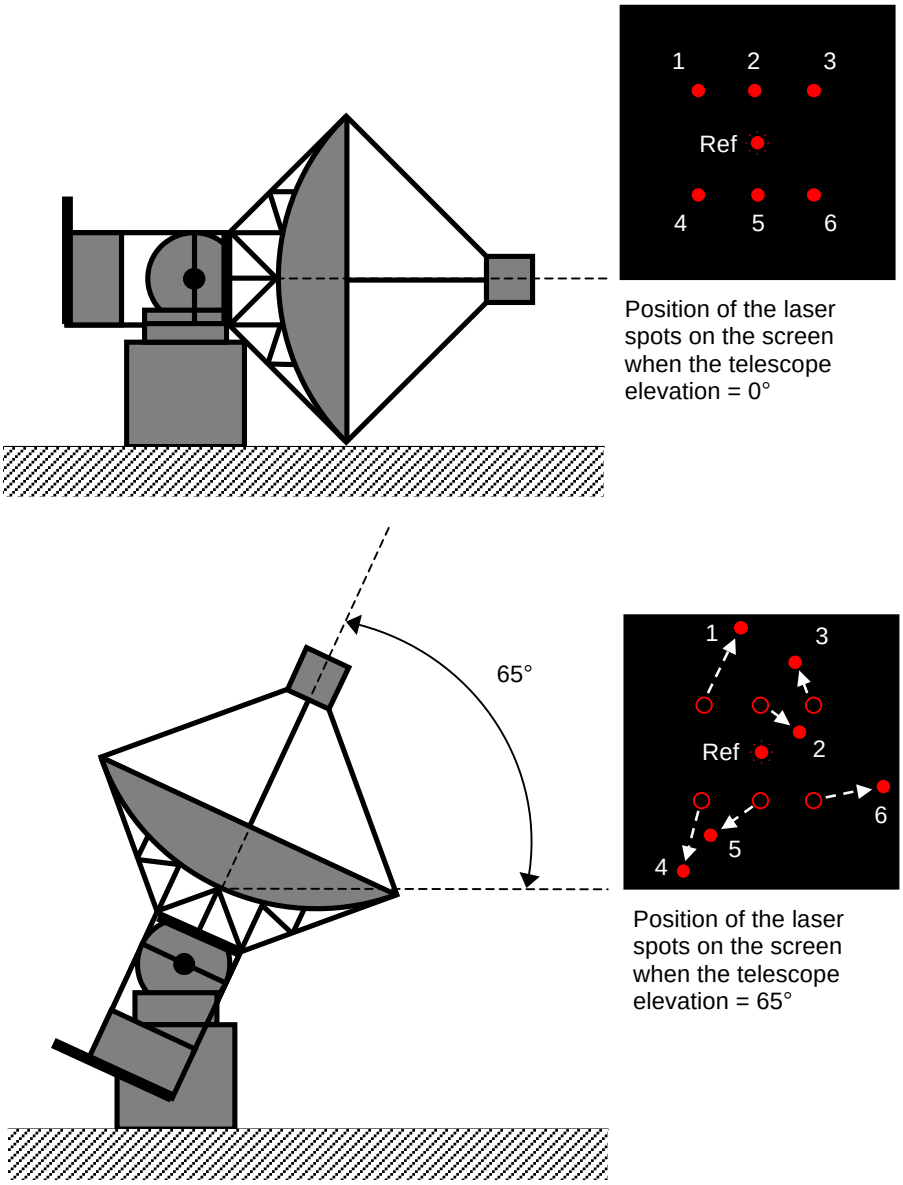

Figure 3.7 Bias measurements procedure.

Each frame, which consists of a set of three images at 0° → 65° → 0°, took an average of 30 minutes to complete. Imaging at 0° a second time provides a consistency check. The positions of each laser spot in the images were measured using the *SkyCat* software developed at the *European Southern Observatory* (Brighton et al. 2001). Table 3.1 shows typical results for one frame of T3.

Mirror #	Frame	x0	y0	x65	y65	x0_B	y0_B
356	4	495.6	33.4	490.4	120.4	495.1	34.1
340	4	528.5	232.4	532.5	320.4	528.5	232.4
339	4	396.5	367.5	396.8	448.5	395.8	368.2
357	4	266.4	261.8	267	347.6	266.2	262.3
350	4	342.1	169.5	342.8	253.2	343.3	168.7
358	4	285.4	69	286.8	157	284.7	69.8
Ref Laser	4	389.3	209.3	389.2	303.2	389	209.6

Table 3.1 Pixel coordinates of the spots corresponding to mirrors in frame 4 and the reference laser are shown in the table. (The coordinates are x0, y0: x and y at elevation 0°; x65, y65: at elevation 65°; x0_B, y0_B: on return to elevation 0°.) The CCD camera has a coordinate system of 765 pixels along the x-axis and 510 pixels along the y-axis.

Once the movement of the mirrors with elevation is known, each mirror is then deliberately misaligned while the telescope is at 0° elevation by an amount equal in magnitude to the movement due to gravitational slumping, but in the opposite direction (Schroedter 2004). Figure 3.8 shows the angular tilt of the mirrors of the Whipple 10m telescope, due to OSS deformation. A file containing information about the movement of each mirror is generated, called the *bias file*, for use by the alignment program so that the slumping effect can be negated. When all the mirror facets are adjusted following this procedure, the telescope's optics fall into optimum and correct alignment at an elevation of 65° (Toner et al. 2007).

Bias alignment was performed on all four VERITAS telescopes. To test the alignment of the reflectors, PSFs at various elevations were measured by finding the FWHM for a two-dimensional Gaussian function fitted to each star image, using the *SkyCat* program. Figure 3.9 shows a set of images and PSF values obtained before and after bias alignment of Telescope 1 (T1).

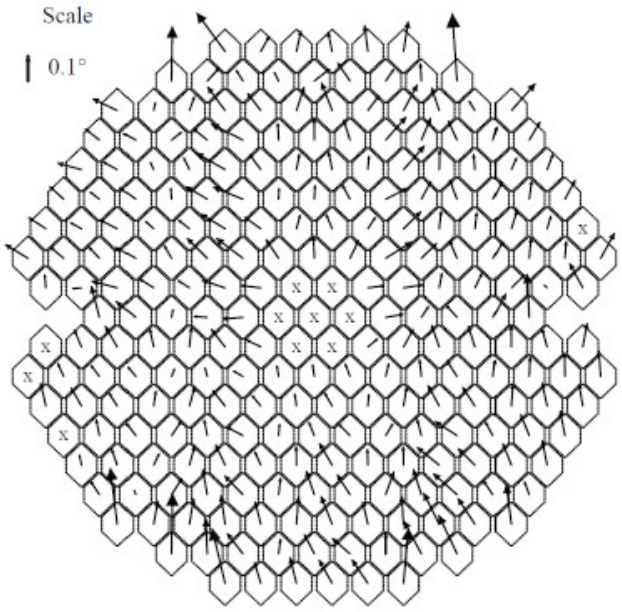

Figure 3.8 Gravitational slumping effects as the telescope moves from horizontal to zenith pointing. The arrows indicate the magnitude and direction of the resulting tilt for each mirror. The results are derived from measurements such as those in Table 3.1.

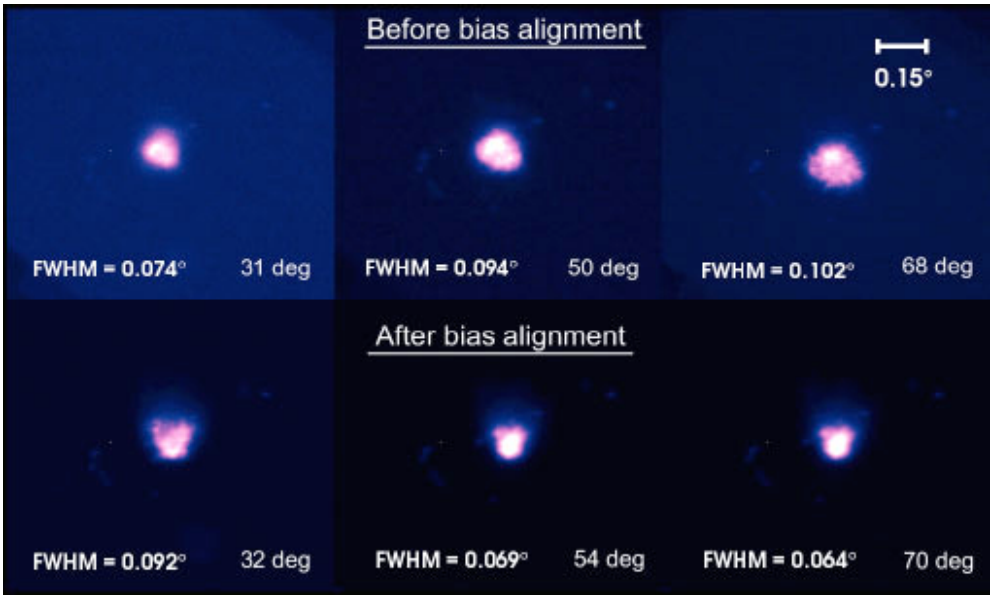

Figure 3.9 PSF before and after bias alignment for T1. The values 31deg, 50 deg, 68 deg, etc refer to *elevation* angles. The line labelled 0.15° shows the angular size of the PMTs which comprise the camera on the VERITAS telescopes (Toner et al. 2007).

After bias alignment, the PSF is found to improve at higher elevations. In the case of the Whipple 10m telescope, a comparison of the PSF values is shown in Figure 3.10. After bias alignment of the telescope, the value for the PSF is optimized for elevations in the region of 60°–70°, at a value of ~0.11°, comparable with the PMT diameter. Either side of this, the value varies only slightly in the region where most observations are taken.

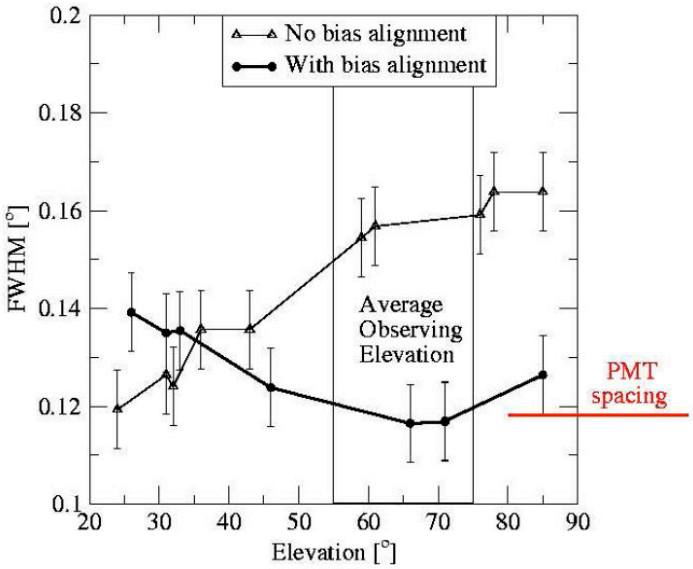

Figure 3.10 PSF measurements for the Whipple 10m reflector. The spacing of the PMTs in the imaging camera of the telescope is also indicated. Figure from Kildea et al (2007).

An alternative alignment system has recently been developed by the McGill University group (McCann et al. 2009). Paraxial rays (for the telescope) striking any mirror facet should be focused on the centre point of the focal plane. A planar secondary mirror just in front of the primary focal plane deflects the light by 90° onto a CCD camera positioned so that its distance from the primary is equal to the focal length of the primary. This CCD camera views the entire reflector. The reflected light intensity from each facet is monitored as the telescope is moved in a raster scan about a bright star. For each facet the brightest reflection in the scan reveals its orientation, and shows what adjustments are required to bring it in to optimal alignment. This procedure has been successfully tested on the VERITAS reflectors but has not yet been applied to the Whipple 10m telescope. This alignment

procedure is easier to implement than the previous alignment method. Moreover, mirror adjustments can be made during daylight hours, avoiding competition with observing time (McCann et al. 2010).

A typical set of measurements on one of the VERITAS telescopes (PMT angular diameter of 0.15°) gave a PSF result of ~0.055° FWHM at elevation ~60° following bias alignment with the McGill system, compared with ~0.070° FWHM using the older alignment system. This reduction in the PSFs of the telescopes has improved the overall sensitivity of VERITAS, but it is not possible to quantify this effect because other substantial hardware changes were implemented concurrently with the new alignment technique.

3.1.3 Data Acquisition System

The major components of the data acquisition system (DAQ) at the Whipple 10m telescope are shown in Figure 3.11.

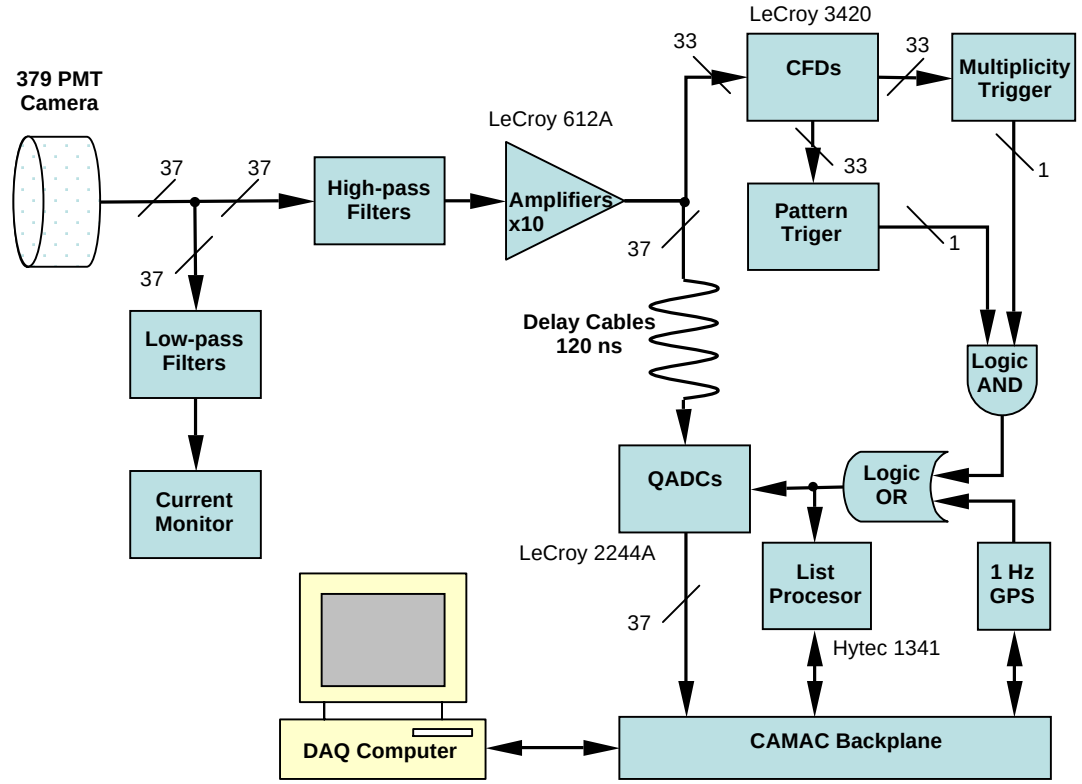

Figure 3.11 Data Acquisition System.

A photon incident on the PMT may produce a photoelectron (pe). The probability for this to occur depends on the wavelength of the light and on the specific PMT photocathode. Electron multiplication in the dynode chain of the PMT results in an anode current linearly proportional to the number of photoelectrons. The anode currents are monitored and in case of over-current, the HV supply to that PMT can be shut down by the observer. The signal from the PMT is AC-coupled to an amplifier with a gain of 10 and the output is sent in parallel to both the trigger system and a charge-to-digital converter (QADC). While the trigger system processes the signal, the other part of the split signal passes through a 120 ns delay cable to the QADC. The trigger system is composed of two parts, one providing a decision on whether or not to record an event, the other deciding when to start the recording. Below is an overview of the main components of the DAQ.

- **Amplifiers and Current Monitor**

The 379 PMT signals coming from the camera are first amplified using customized LeCroy 612A modules (see Figure 3.12).

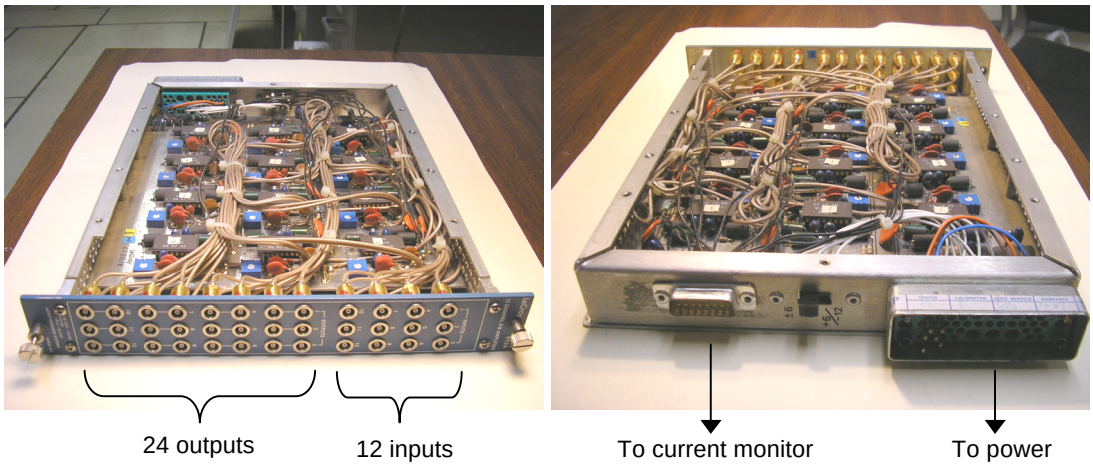

Figure 3.12 The 12-channel LeCroy amplifier module. (*a*) Front view: each input is AC-coupled to a signal coming from a PMT. There are two amplified outputs: one goes to the QADC through delay cables and the other one goes to the trigger electronics. (*b*) Back view: the signals from the 12 input channels are DC-coupled to the current monitor system, through a ribbon cable plugged into the back of the module.

There are 32 modules of this type, each containing 12 amplifiers. Each amplifier has one input, for the AC-component of the signal, and two outputs, each with a gain of 10. One of the outputs is connected via a delay cable to a QADC, and the other is sent to the trigger electronics. At the back of each amplifier module, a ribbon cable connects the DC-component of the signals from 12 PMTs to a current-monitor system.

The original current monitor at the Whipple 10m telescope consisted of two ADC cards (Computer Boards 1401-2), each connected to twelve 16-channel analog multiplexers. A digital value between 0 and 15 sent to each ADC card selects which channel of each multiplexer is enabled. The 24 DC-coupled signals thus selected are digitised, and the system moves on to the next set of 24 by incrementing the digital value sent (Fegan 2006). A new current-monitor system was installed in September 2008, consisting of five National Instruments devices (NI USB-6225), one 7-port USB 2.0 hub (D-Link DUB-H7) and a dedicated PC (see Figure 3.13).

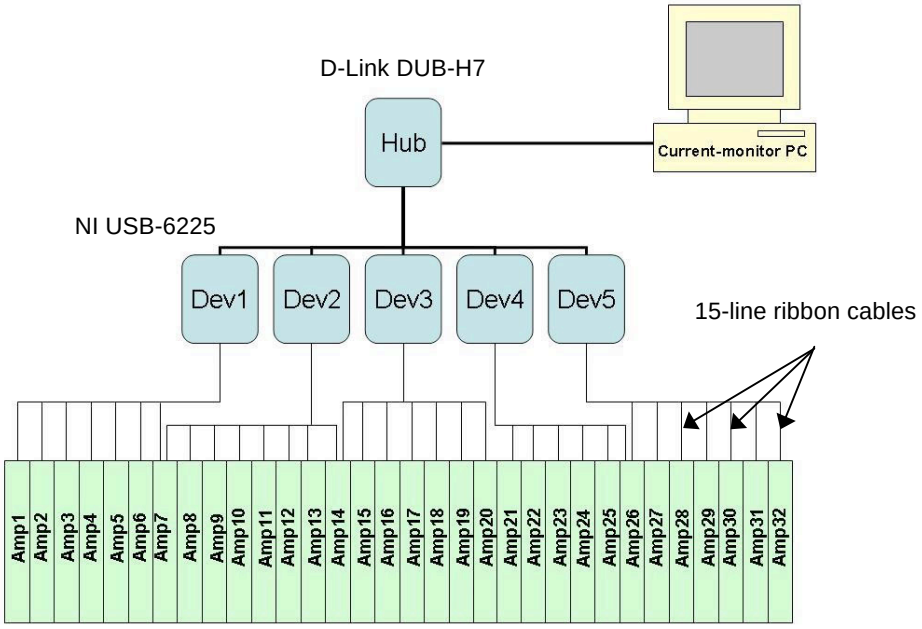

Figure 3.13 Schematic diagram of the current-monitor system. Modules Dev1 – Dev5 are National Instruments USB-6225 devices.

Each of the five NI devices (see Figure 3.14) is DC-coupled to ~80 signals coming from the camera, through 15-line ribbon cables that come from the back of 6-8 amplifier modules. The NI modules are then connected to the PC via the USB hub.

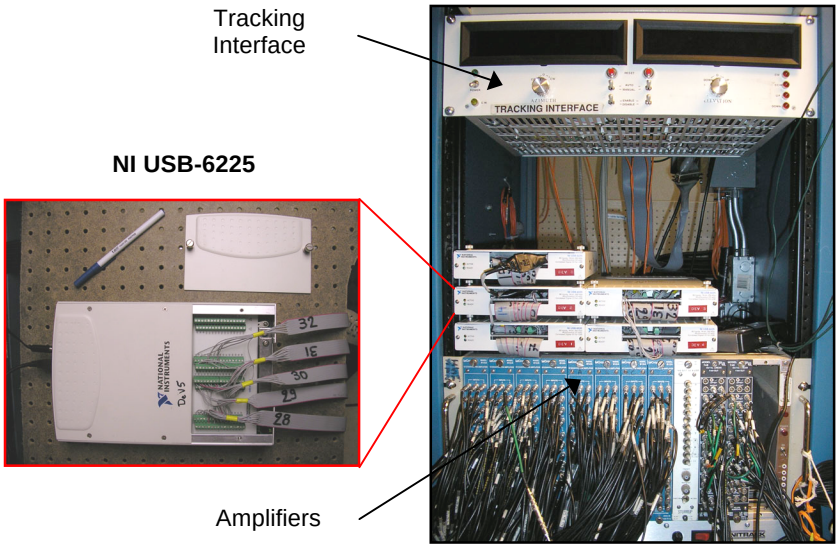

Figure 3.14 Portion of the Whipple 10m electronics system, showing the tracking interface, amplifiers and current-monitor system.

The anode current of each PMT is monitored using software installed on the PC so that in the case of high current (due to bright stars in the field of view, background light, etc), the HV supply to the PMT can be turned off by the observer via the tracking computer (which controls the HV crates as well as the tracking system of the telescope).

- **Trigger Electronics**

Sources of optical photons that produce a current in the PMTs include Cherenkov light from γ-rays and cosmic rays, and noise from the night-sky background (NSB). In order to select Cherenkov events caused by γ-rays or cosmic rays, and reduce the number of false random events due to the NSB, a trigger system is used to determine when data should be recorded.

The trigger system at the Whipple 10m telescope consists of constant-fraction discriminators (CFDs), one for each of the inner 331 PMTs, followed by a pattern-

selection trigger (PST) which is composed of two subsystems that operate in parallel: a *multiplicity* trigger and a *pattern* trigger.

The CFD for a PMT triggers when a certain preset fraction of the total pulse height is reached. In order to set the trigger at a fixed fraction f of the pulse height V, each pulse is split along two paths. On one path, the signal is attenuated to fV, while on the other path the unattenuated signal is delayed so that it can be compared with fV. The trigger is generated when the unattenuated pulse reaches the level fV. In this way, the trigger occurs independently of the signal amplitude V, so that small pulses and large pulses trigger at the same time relative to the commencement of the pulse (Figure 3.15b). This is in contrast to the case of fixed threshold, which results in time jitter because larger pulses trigger earlier than small ones (Figure 3.15a).

Gamma-ray-induced showers are more compact than hadronic showers and produce images with light concentrated in fewer PMTs. The pattern trigger uses pixel geometry information to discriminate against random background patterns in favour of compact candidate shower images. It requires signals in a minimum number, N, of adjacent PMTs to exceed a set threshold (typically 32 mV) within a ~5ns coincidence window. N can be set to 2, 3, or 4-fold coincidence but the normal operating mode is $N = 3$. One drawback of the pattern trigger is that the timing information becomes blurred through the complex hardware in the trigger module. Therefore, a simple $N-1$ multiplicity trigger is used in parallel with the pattern trigger to provide the precise timing information for enabling the QADCs.

- **Signal-recording System**

When a trigger occurs, the signal from each PMT is integrated for 15 ns and converted to a digital count (d.c.) value by the QADC. This information, along with the time and a trigger map, is transmitted along the CAMAC backplane and recorded by the DAQ computer, as shown in Figure 3.11. The integration time is longer than the ~4 ns duration of the Cherenkov pulse from an air shower (Hillas 1982), because of the ~6.5 ns time spread introduced by the optical geometry of the telescope (Section 3.1.1), pulse degradation of ~3 ns in the cables, and the rise and fall times of the PMT response.

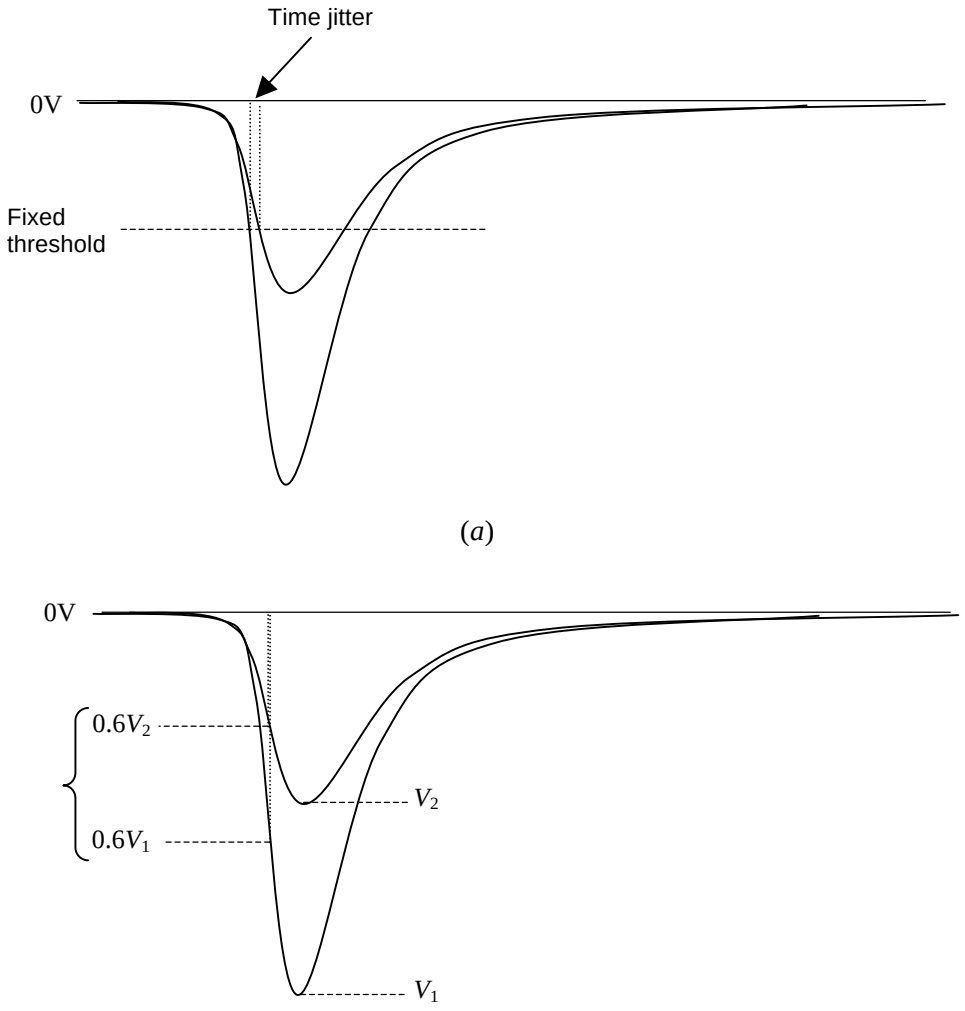

Figure 3.15 Discriminator operation. (a) Fixed threshold: for two simultaneous input pulses, the larger pulse reaches the threshold level and triggers the discriminator earlier, introducing time jitter. (b) Constant fraction discriminator: with the trigger threshold at a preset fraction of the pulse height (60% in the example shown), both pulses trigger the discriminator at virtually the same time, largely eliminating jitter.

A separate, independent trigger signal at a fixed rate of 1 Hz is supplied by a global position system (GPS) clock. Events triggered in this way are called “pedestal” events and are tagged as such in the data stream. Pedestal events contain no Cherenkov light, only NSB. They are used to measure the small steady offset introduced into each QADC channel to take account of the fact that the AC-coupled signal has both positive and negative fluctuations whereas the QADC can only digitize positive values. See Section 4.1.1 for further details.

For events that pass the hardware trigger, the QADC values are read out and buffered by Hytec 1341 List Processors until they can be handled by the DAQ software. The DAQ software, called GRANITE (Gamma-RAy New Imaging TElescope), runs on the DAQ computer, a Digital Alpha machine (Figure 3.11).

3.1.4 Flatfielding System and Pointing Monitor

In practice, the hardware gains in different PMT channels will differ slightly so that the same amount of light will produce different d.c. values for different pixels. In order to achieve a uniform response across the camera, the response of each pixel must be corrected to take account of these gain differences, a process referred to as *flatfielding*. To implement this process, the camera is illuminated using a nitrogen discharge tube (mounted at the centre of the reflector), which produces fast (~35 ns) pulses with a nearly uniform light intensity at a rate of ~750 Hz (Grube 2007). Flatfielding ("relative-gain") coefficients are determined for each pixel by comparing the d.c. value for the pixel with the mean d.c. value for all pixels, and these coefficients are used to correct the spread in pixel gains.

A new flatfielding system was implemented on the Whipple 10m telescope in May 2007. The nitrogen tube arrangement was replaced with a laser located inside the telescope control building, from which light pulses are transmitted by fibre-optic cable to illuminate a diffuser fixed at the centre of the reflector facing the PMT camera (see Figure 3.16).

The laser calibration runs (or nitrogen runs) are generally taken with the telescope in its stow position, but can be taken at any elevation provided there are no bright stars in the field of view.

The *pointing monitor* is another important calibration instrument installed on the Whipple 10m telescope. It consists of a Prosilica EC1380 CCD camera mounted at the centre of the OSS and viewing the PMT camera. This CCD camera, based on the Sony ICX285AL sensor, was installed on the telescope in 2008. It has gain settings from 1× to 32×, exposure times from 10 μs to 10 s and an IEEE 1394 Firewire port through which it connects to a computer. Four LEDs fixed in the focal plane allow the centre of the PMT camera to be precisely located in the CCD images.

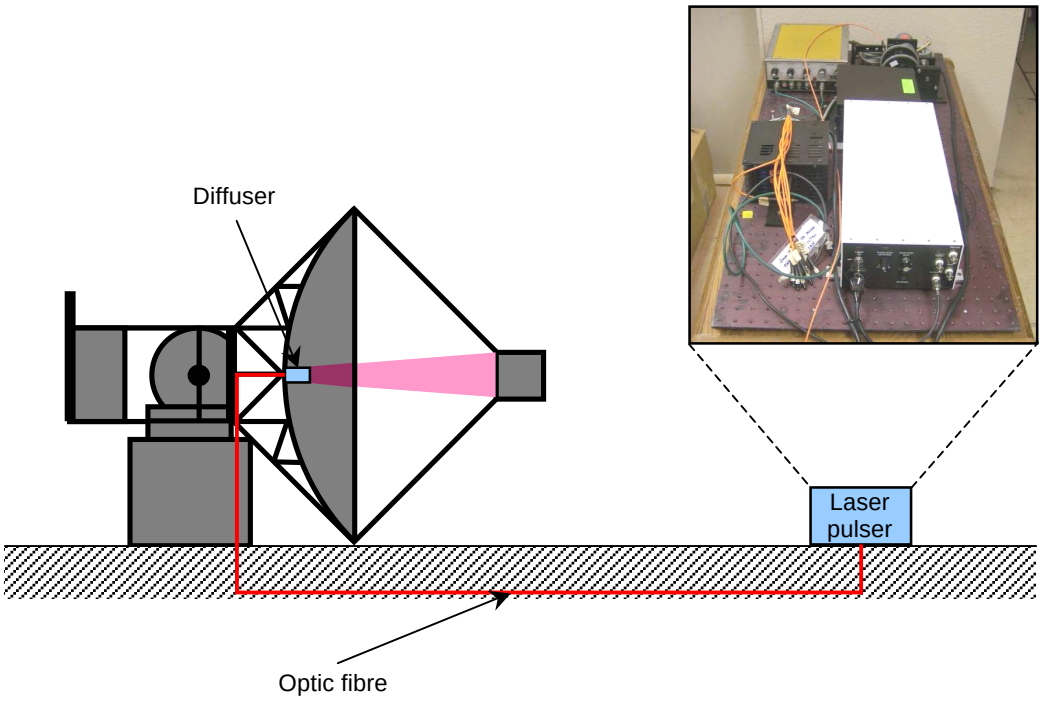

Figure 3.16 Flatfielding system. The diffuser illuminates the front of the camera uniformly and is used to determine the relative gains of the PMTs. The mean d.c. values for the PMTs are recorded and used to calculate the relative gains.

The pointing monitor has been used to find the pointing offset of the telescope in order to apply corrections to the data (see Section 4.1.2 for further details), and is also used for performing PSF and bias-alignment measurements.

3.2 Radio Telescopes

The purpose of this section is to provide a brief introduction to important quantities and techniques used in radio astronomy, and to present the basic principles behind radio telescopes and interferometers. In Section 3.2.4, a brief description is given of the instruments that provided the radio data used in this thesis.

3.2.1 The Radio Window

In 1931 Karl Jansky was conducting experiments for Bell Laboratories related to the production of radio-wavelength static from thunderstorms. During the course of his

investigation Jansky discovered that some of the static in his receiver was of "extraterrestrial origin", an observation confirmed by Grote Reber in 1938 (Kraus 1966). By 1935 Jansky had correctly concluded that much of the signal he was measuring originated in the plane of the Milky Way, with the strongest emission coming from the constellation Sagittarius, the direction in which the centre of our Galaxy lies. Jansky's pioneering work represented the birth of a whole new field of observational study, *radio astronomy* (Carroll & Ostlie 1996).

The Earth's atmosphere is transparent to radio waves, in a frequency window extending from ~15 MHz ($\lambda \sim 20$m) to ~600 GHz ($\lambda \sim 0.5$ mm), but these limits are not sharp and can vary both with geographical position and with time.

The high-frequency cut-off occurs because the resonant absorption of the lowest rotation bands of molecules in the troposphere fall into this frequency range. There are mainly two molecules responsible for this: water vapour, H_2O, with strong absorption bands at 22.2 GHz and 183 GHz; and molecular oxygen, O_2, with an exceedingly strong band at 60 GHz (note that these absorption bands are well below 600 GHz). At the lowest frequencies, the atmosphere ceases to be transparent because free electrons in the ionosphere absorb electromagnetic radiation if the frequency is below the *plasma frequency* ν_p, which is given by

$$\frac{\nu_p}{\text{kHz}} = 8.79\sqrt{\frac{N_e}{\text{cm}^{-3}}} \tag{3.1}$$

where N_e is the electron density of the plasma. Electron densities in the ionosphere depend on time of day and on solar activity, and therefore this low-frequency limit is variable (Rohlfs & Wilson 2000).

3.2.2 Basic Definitions and Tools

Consider electromagnetic radiation falling on a flat area A at the surface of the Earth, as shown in Figure 3.17. The infinitesimal power dW from a solid angle $d\Omega$ incident on a surface of area dA is

$$dW = I_\nu \cos\theta \; d\Omega \; dA \; d\nu \tag{3.2}$$

where

dW = infinitesimal power, in W

I_ν = brightness of sky or specific intensity, in W m^{-2} Hz^{-1} sr^{-1}

$d\Omega$ = infinitesimal solid angle of sky, in sr

θ = angle between the normal to dA and the direction to $d\Omega$, in rad

dA = infinitesimal area of surface, cm^2

$d\nu$ = infinitesimal element of bandwidth, in Hz.

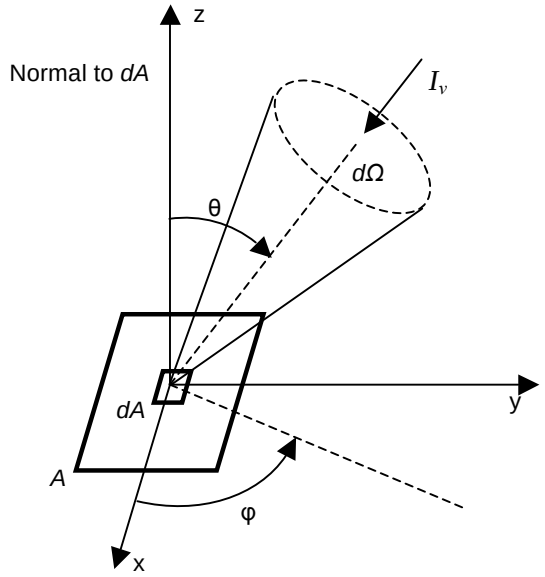

Figure 3.17 Basic geometry for radiation of intensity I_ν incident on a flat area.

In general the *specific intensity* (or *brightness*) I_ν is a function of both the position (in the sky) and of the frequency. It is a fundamental quantity of radio and optical astronomy and is a measure of the power received per unit area per unit solid angle per unit bandwidth (Kraus 1966).

The total flux of a source is obtained by integrating Equation (3.2) over the total solid angle Ω_s subtended by the source

$$S(\nu) = \int_{\Omega_s} I_\nu(\theta,\varphi) \cos\theta \; d\Omega \tag{3.3}$$

$S(\nu)$, called *spectral flux density*, is measured in units of W m^{-2} Hz^{-1}. Since the flux density of radio sources is usually very small, a special radio astronomical flux density unit, the jansky (abbreviated Jy), is commonly used.

$$1 \text{ Jy} = 10^{-26} \text{ W m}^{-2} \text{ Hz}^{-1} = 10^{-23} \text{ erg s}^{-1} \text{ cm}^{-2} \text{ Hz}^{-1} \tag{3.4}$$

To determine the total power W collected by the receiver, Equation (3.2) must be integrated also over the effective area of the telescope, A, and over the frequency interval $\Delta\nu$ (the bandwidth) for which the detector is sensitive, giving

$$W = \int_A \int_{\Delta\nu} S(\nu)\, d\nu\, dA \tag{3.5}$$

If $S(\nu)$ can be considered to be constant over the frequency interval $\Delta\nu$, the integral simplifies to give

$$W = A\, S\, \Delta\nu \tag{3.6}$$

Very few astronomical sources are as bright as 1 Jy, but even such a source would produce a signal of only 10^{-15} W with a 100m-diameter radio telescope, assuming that it is 100% efficient over a bandwidth of 10 MHz.

Astronomical radio sources can be classified into two categories: those which radiate by thermal mechanisms and those which radiate by nonthermal processes. In principle many different radiation mechanisms could be responsible for nonthermal emission, but in practice one single mechanism seems to dominate, i.e., *synchrotron emission* (Section 1.3.1).

The parabolic dish of a typical radio telescope reflects the radio energy of the source to an antenna. The signal from the antenna is amplified and processed to produce a *radio map* of the sky at a particular wavelength. Radio telescopes come in many different configurations. Figure 3.18 shows a common type called the *total power radio telescope*.

Details of the electronics have been omitted from Figure 3.18 in the interest of providing a general understanding of the entire system.

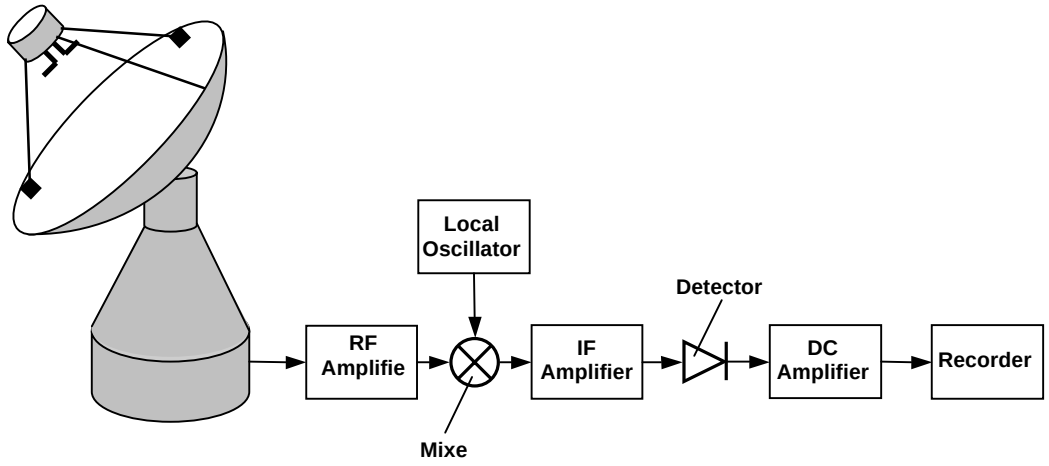

Figure 3.18 Simple superheterodyne total power radio telescope. The observing frequency range is adjusted by tuning the local oscillator.

The total power radio telescope employs a receiver called a *superheterodyne*, in which the radio-frequency (RF) amplifier is followed by a mixer that multiplies the RF signal by a sine wave of frequency ν_{LO} generated by a local oscillator (LO). The product of two sine waves contains the sum and difference frequency components.

$$2\sin\left(2\pi\nu_{LO}\,t\right)\times\sin\left(2\pi\nu_{RF}\,t\right)=\cos\left[2\pi\left(\nu_{LO}-\nu_{RF}\right)t\right]-\cos\left[2\pi\left(\nu_{LO}+\nu_{RF}\right)t\right] \quad (3.7)$$

The difference frequency is called the intermediate frequency (IF), ν_{IF}. The advantages of superheterodyne receivers are that most of the amplification can be done at lower frequencies ($\nu_{\mathrm{IF}} < \nu_{\mathrm{RF}}$), which is usually easier, and that the $\underline{\nu_{RF}}$ range can be controlled precisely by tuning *only* the local oscillator. Thus, back-end devices following the untuned IF amplifier (e.g., multichannel filter banks or digital spectrometers) can operate over fixed frequency ranges.

Single-dish radio telescopes have large collecting areas but relatively poor angular resolution at long wavelengths. Nearly all discrete continuum sources are extragalactic and extremely distant, so they are distributed randomly and isotropically on the sky. Sky-brightness fluctuations caused by numerous faint sources in the telescope beam (referred to as “confusion”) usually limit the sensitivity of single-dish continuum observations at frequencies below ~10 GHz

(Murphy 2009). Below that frequency, most continuum observations are made with interferometers (see Section 3.2.3) rather than single dishes because interferometers can synthesize much smaller beamwidths and hence have significantly lower confusion limits.

3.2.3 Radio Interferometry

The angular resolution of a radio telescope is given by $\delta \sim \lambda / D$, where δ is the smallest angular separation which two point sources must have in order to be recognized as separate objects, λ is the wavelength of the radiation received and D is the diameter of the telescope (Rohlfs & Wilson 2000).

The resolution of a radio telescope can be improved by increasing the diameter D. However, this may not be technically possible and/or financially feasible. Therefore radio astronomers have increased the effective resolving power of their instruments by combining the outputs of two or more separated telescopes. The effect of this is similar to that obtained using the interference technique in the Young double-slit experiment.

Figure 3.19 shows two radio telescopes separated by a baseline of distance d. Since the distance from telescope B to the source is greater than the distance from telescope A to the source by an amount L, a plane wavefront incident at angle θ will arrive at B after it has reached A. If L is equal to an integral number ($L = n\,\lambda$, where $n = 0, 1, 2, \ldots$) of wavelengths, the two signals will be in phase and their superposition will result in an intensity maximum.

The pointing angle θ is related to d and L by

$$\sin\theta = \frac{L}{d} \tag{3.8}$$

It is then possible to determine the source position precisely using the interference pattern produced by combining the signal of two or more antennas (Carroll & Ostlie 1996). Angular resolution values as small as 0.1 milliarcsecond (mas) have been accomplished using this technique.

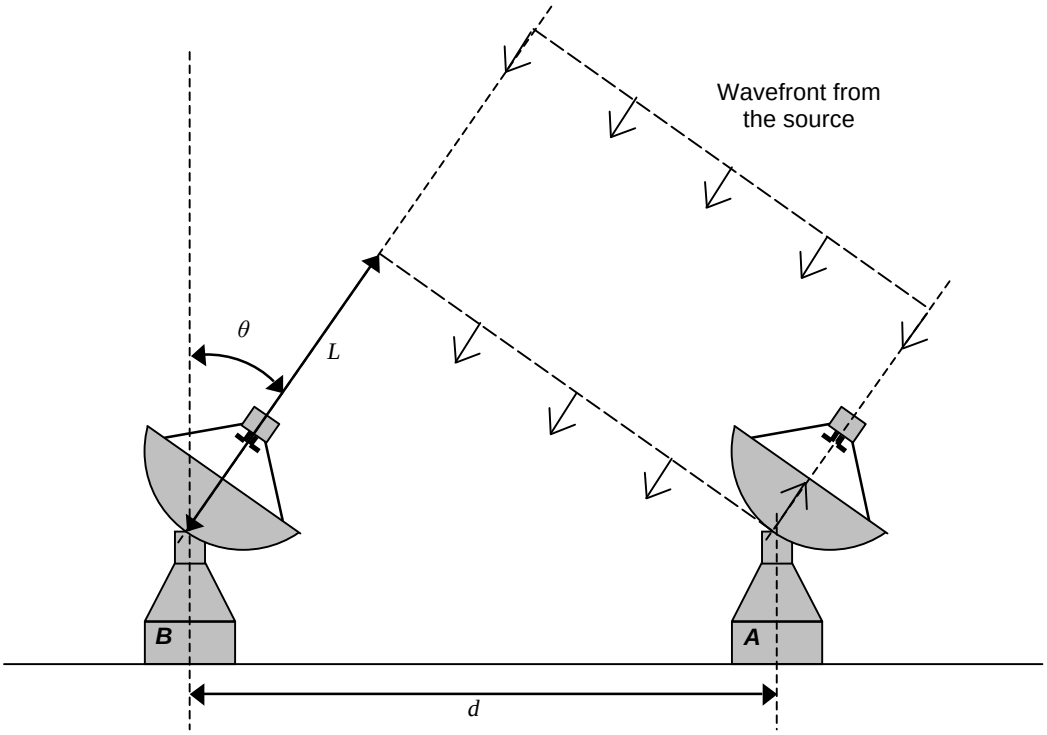

Figure 3.19 Radio interferometry.

3.2.4 Instruments

In this thesis, Mrk 421 radio data from the Metsähovi Radio Observatory and from the University of Michigan Radio Astronomy Observatory (UMRAO) have been used, and the results of the analysis are shown in Section 5.2. The Metsähovi radio telescope is a radome-enclosed paraboloid antenna with a diameter of 13.7 m (see Figure 3.20, left) situated at 60 m above sea level in Kirkkonummi, Finland (longitude 24° 23′ 38″ E, latitude +60° 13′ 0.5″). Its 37 GHz receiver is a dual-horn Dicke-switch receiver with a HEMPT (high-electron-mobility pseudomorphic transistor) front end operated at room temperature (Teräsranta et al 1998).

The data from UMRAO were taken using the 26m-diameter parabolic reflector (Figure 3.20, right) with receivers operating in frequency bands centred at 4.8 GHz, 8.0 GHz and 14.5 GHz.

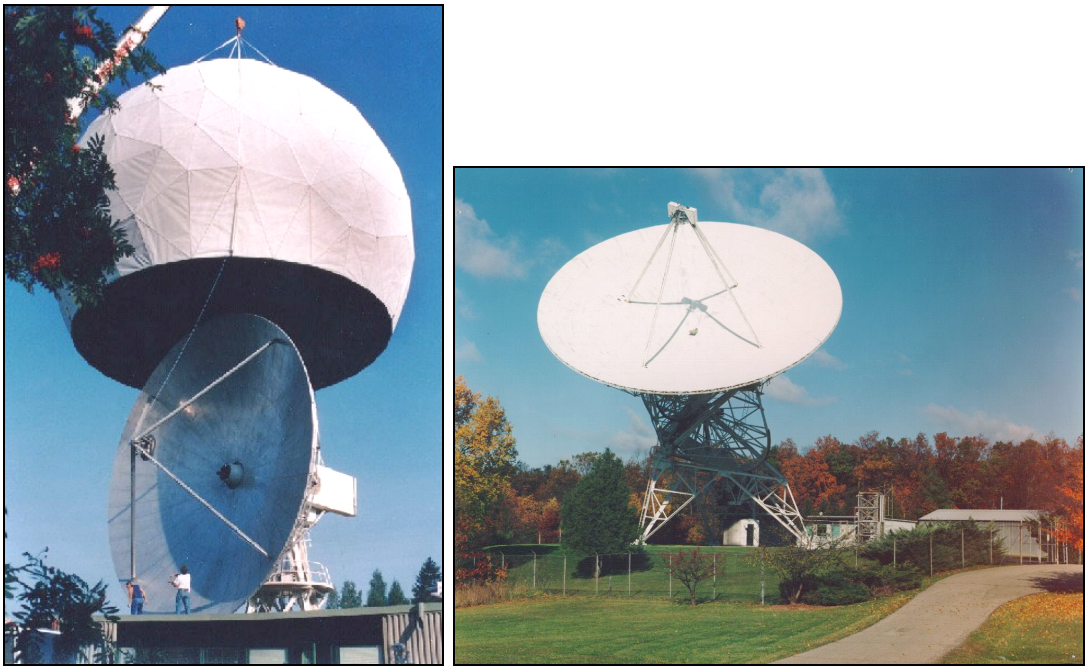

Figure 3.20 The Metsähovi radio telescope (left) and the antenna of the UMRAO (right).

Milliarcsecond-scale images of Mrk 421 from the MOJAVE (Monitoring of Jets in Active Galactic Nuclei with VLBA Experiments) survey, from the period 1995–2000, have also been used in this thesis and the results are presented in Chapter 5. MOJAVE is a long-term observational program to study the structure and evolution of relativistic outflows in AGN (Lister & Homan 2005). The observations are made at a frequency of 15GHz using the Very Long Baseline Array (VLBA), which applies the interferometry technique using ten 25-metre radio telescopes at various locations, eight of them in the continental USA and one each in Hawaii and the Virgin Islands (see Figure 3.21).

The VLBA observations have radically changed the view of AGN jets, making it possible to obtain high dynamic range, full-polarization images at regular intervals, routinely obtaining a resolution better than 0.1 mas.

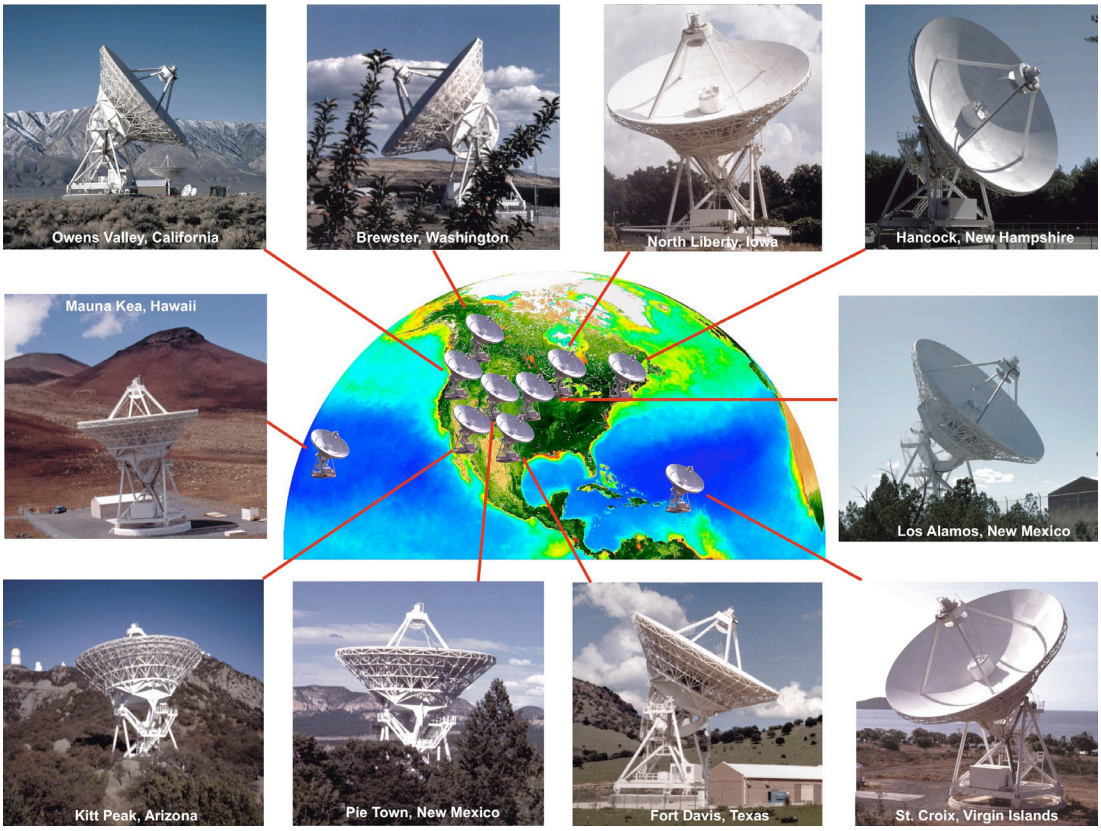

Figure 3.21 The Very Long Baseline Array (VLBA).

3.3 Space-based Detectors

Space-based detectors carried by satellites or high-altitude balloons detect X-ray and γ-ray photons directly when they pass through the detector and interact with the detector material. The resulting electron-positron pairs are used to determine the energy and direction of the original photon. Satellite detectors typically include three main components: a tracking chamber, a calorimeter, and an anti-coincidence shield. The tracking chamber records the path of charged particles within the detector. The tracks are used to identify electron-positron pairs and reconstruct the initial photon direction. The calorimeter measures the energy deposited in the detector to determine the initial photon energy. The anti-coincidence shielding is typically a scintillator detector used to veto events caused by *charged* particles passing through the detector.

Space-based detectors have an advantage over ground-based detectors in terms of exposure. They can be placed in orbits that allow year-long observation of sources. The high-duty-cycle monitoring available to satellite instruments not only avoids missing activity in transient sources but also eases coordination with simultaneous observations in other wavebands. The biggest limitation of satellite detectors has been the angular resolution. Although capable of monitoring a large portion of the sky simultaneously, location errors have been on the order of a degree. Most ground-based γ-ray detectors and telescopes in other wavebands resolve sources on smaller scales, which make it difficult to correlate observations.

In this work, data from two satellite detectors, *RXTE* and *Fermi*, have been analyzed to carry out variability studies and to look for correlations with the Whipple observations (see Sections 5.3.1 & 5.3.3). Technical details of these two instruments are presented in the following subsections.

3.3.1 The Rossi X-ray Timing Explorer

Photons with X-ray energies (0.1–100 keV) are absorbed high in the Earth's atmosphere, so to detect them it is necessary to get above the atmosphere. X-ray astronomy began in the 1960s with rocket experiments, and since then all major X-ray observatories have been satellite-based.

The NASA-built Rossi X-ray Timing Explorer (*RXTE*) observatory was launched in December 1995 and is still operational. Figure 3.22 shows a diagram of the *RXTE* spacecraft. *RXTE* is in a circular low-Earth orbit with period ~90 minutes, apogee 580 km and perigee 560 km.

RXTE has three non-imaging X-ray instruments on board: the Proportional Counter Array (PCA), the High Energy X-ray Timing Experiment (HEXTE), and the All-Sky Monitor (ASM) (Bradt et al. 1993). The PCA comprises of five proportional counter units (PCU) detectors covering the energy range 2–60 keV with energy resolution ~18% ($E/\Delta E \sim 5.5$) and total effective area 5200 cm^2 at 6 keV (Jahoda et al. 1996; Jahoda et al. 2006). Higher energy (20–200 keV) X-rays are detected by the HEXTE at a comparable energy resolution of 15%, but with much lower sensitivity than the PCA (Rothschild et al. 1998). The PCA and HEXTE each have a 1° field of

view. The ASM instrument consists of three proportional counter scanning shadow cameras (SSCs) mounted on a motorized rotation drive. The ASM scans nearly 80% of the sky during every orbit, providing long-term X-ray rate monitoring of ~350 sources in the energy band 1.2–10 keV (Levine et al. 1996). X-ray point sources are identified in the wide 6° × 90° ASM field of view by shadow patterns in the slit masked detector. The systematic uncertainties in the ASM rate are large (5%), and only relative flux estimates are available for long-term (month timescale) monitoring (Grube 2007).

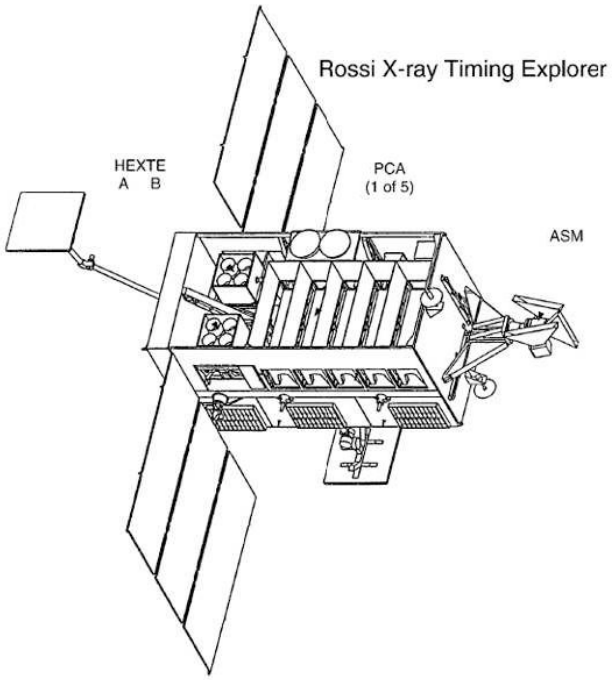

Figure 3.22 Diagram of the *RXTE* Observatory, from Rothschild et al. (1998), showing the five PCA Proportional Counter Units (PCUs), the two HEXTE cluster detectors to the left and the ASM instrument on the right.

In this work, 13.5 years of *RXTE* ASM data from January 1996 to June 2009 have been used for variability and correlation studies. A series of 90-second integrated data was derived from ASM archives and binned in ~21-day intervals to reduce statistical errors. *RXTE* observations and results are described in Chapter 5.

3.3.2 The Fermi Gamma-ray Space Telescope

The Fermi Gamma-ray Space Telescope (*Fermi*) is a new-generation high-energy γ-ray observatory designed for making observations of celestial objects in the energy band extending from 8 keV to ~300 GeV. It was launched from Cape Canaveral (Florida), on June 11, 2008. *Fermi* travels in a circular low-Earth orbit, at altitude 565 km with inclination ~24.7°. The observatory circles Earth every 90 minutes and is able to view the entire sky in every three hours. The mission is designed for a lifetime of five years with a goal of ten years of operations.

Fermi (see Figure 3.23) carries two instruments: the Large Area Telescope (LAT) and the Gamma-ray Burst Monitor (GBM). The main instrument, the LAT (Figure 3.24), has a field of view of ~2 sr (~20% of the entire sky). Within its 1.8 m^3 housing, it uses 880,000 silicon strips to detect γ-ray photons in the energy range from 30 MeV to ~300 GeV. The LAT has high sensitivity above 10 GeV, and is at least 30 times more sensitive than any previous γ-ray instrument flown in space. The complementary GBM instrument is designed to detect gamma-ray bursts (GRBs) over a wide range of timescales.

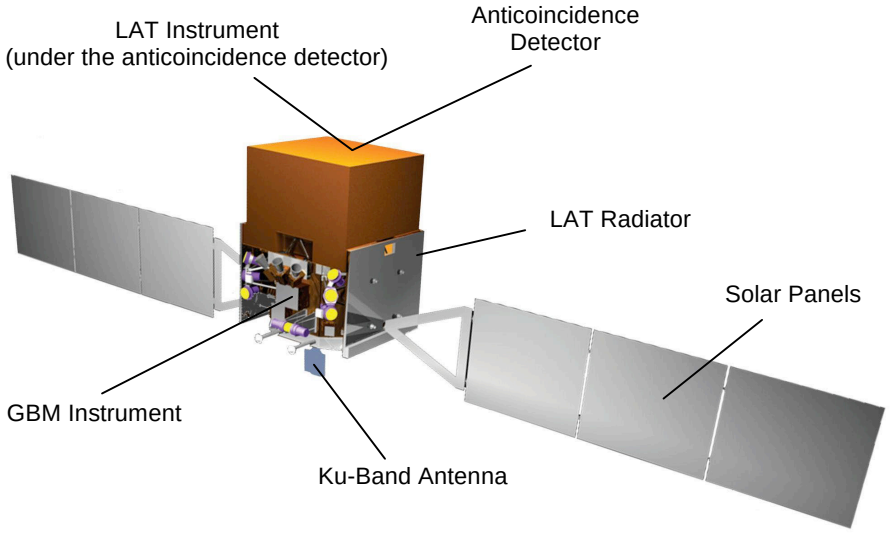

Figure 3.23 The Fermi Gamma-ray Space Telescope. Drawing courtesy of NASA.

The LAT data used in this thesis are the product of an intensive period of observations of Mrk421 (January–June, 2009), as part of a multiwavelength

campaign carried out with the Whipple 10m telescope in collaboration with a range of other instruments (Chapter 5).

The four main subsystems of the LAT are: a tracker, a calorimeter, an anticoincidence detector (ACD) and the data acquisition system (DAQ).

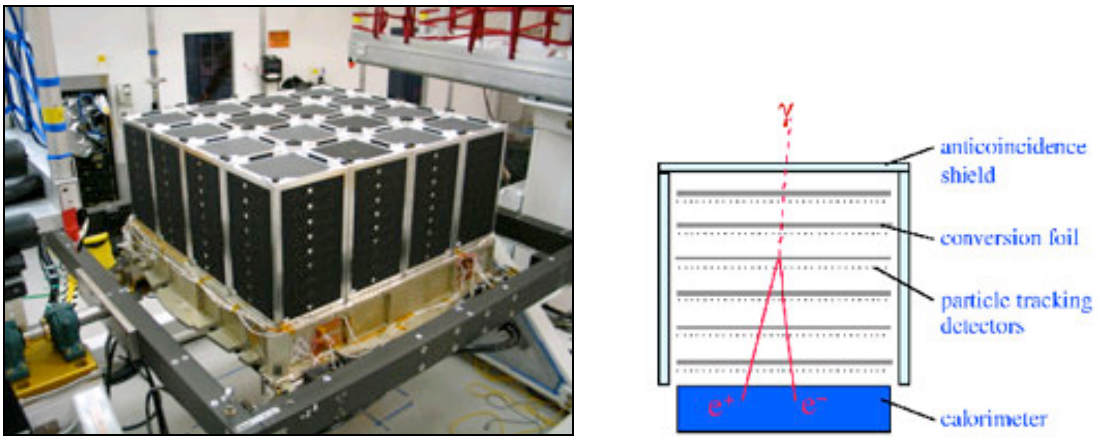

Figure 3.24 The LAT has 16 towers of particle detectors, seen here (left) before the installation of the anticoincidence detector. Each tower contains a tracker module and a calorimeter module (right). The data acquisition system is located underneath the towers. (Images from *Fermi*-LAT Collaboration.)

When a γ-ray photon enters the LAT (see right diagram in Figure 3.24), it first passes through the ACD without producing a signal. The γ-ray photon interacts in one of 16 thin tungsten sheets, converting into an electron and a positron. The tracker uses silicon strips to measure the paths of the electron and positron, allowing the arrival direction of the photon to be determined. The electron and positron enter the caesium iodide calorimeter, which measures the energies of the particles, so that the energy of the photon can be determined. The ACD makes it possible to reject 99.97% of unwanted events due to cosmic rays (Jenner 2008).

3.4 The Milagro Observatory

The Milagro Gamma-ray Observatory operated from June 1999 to April 2008, continuously observing the sky overhead (FOV ~ 2 sr) twenty-four hours a day. The

Milagro detector identified high-velocity charged particles coming from extensive air showers (EASs), by using an array of PMTs to detect the Cherenkov radiation produced by these particles in a large tank of water.

The Milagro Observatory was located in the Jemez Mountains near Los Alamos, New Mexico, at an altitude of 2650 m. This altitude allows the detection of EAS particles that do not survive to greater depths in the atmosphere. The Milagro detector consisted of a large made-man pond of water, protected and shielded from light by a polypropylene cover (See Figure 3.25). The pond measures 80 m × 60 m and 8 m deep, and was instrumented with two layers of PMTs (Smith et al. 2001). The top layer, 1.5m below the surface of the water, contained 450 PMTs distributed in a rectangular grid and was used primarily to determine the arrival times and directions of air shower particles. The bottom layer of 273 PMTs on a smaller grid was placed 6 m below the surface and acted as an imaging calorimeter to detect penetrating particles such as muons and hadrons (which deposit dense clumps of energy in the detector) and distinguish them from electrons and γ-ray photons.

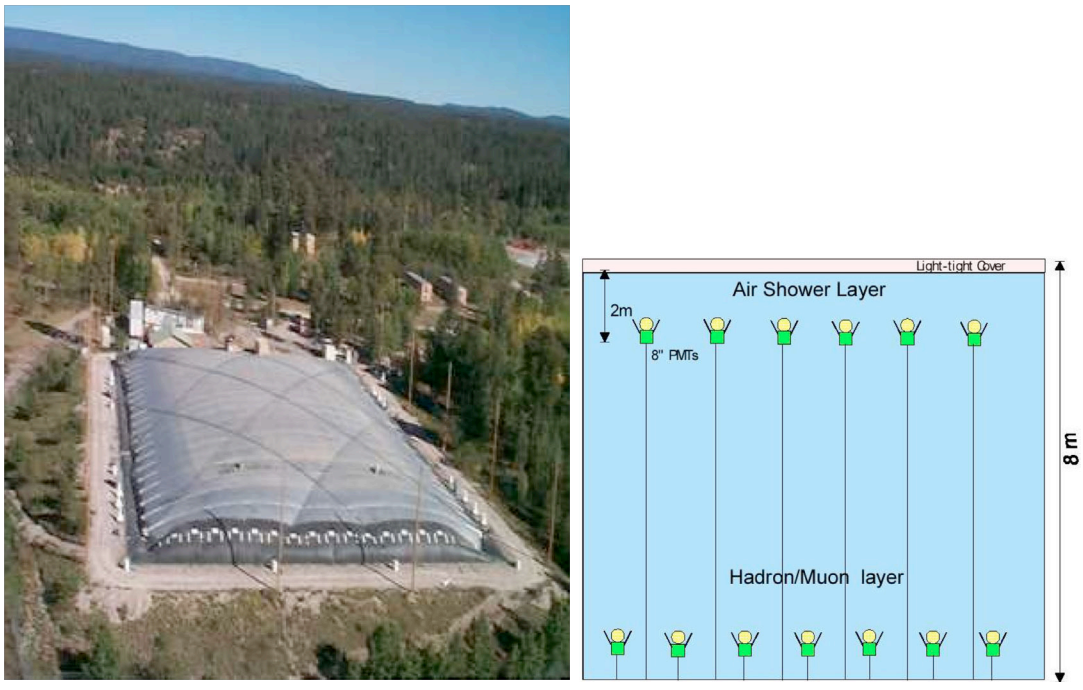

Figure 3.25 *Left*: Aerial view of the Milagro installation (from Smith et al. 2007). *Right*: Illustration of PMT placement in the pond (from Hays 2004).

Simple cuts on the measured quantities allow for removal of over 90% of the hadronic background while preserving more than 60% of γ-ray-induced showers. The technique was verified through observations of Mrk 421 (Benbow 2001) and the Crab Nebula (Sinnis et al. 2001).

The Milagro system operated with a trigger that required roughly 50 PMTs to be hit within a 200 ns time window. Under normal operating conditions, this criterion provided about 1500 triggers per second (Smith et al. 2001). EAS detectors such as Milagro can operate continuously day and night and are typically not affected by the weather. The Milagro detector achieved a sensitivity of $12\sigma / \sqrt{\text{yr}}$ on the Crab Nebula with a median energy of roughly 12 TeV (Abdo et al 2007a). While this sensitivity is considerably less than that of atmospheric-Cherenkov telescopes (ACTs) such as VERITAS, H.E.S.S. or Whipple, instruments like Milagro are well suited to the study of long-duration variability.

Its wide field of view (~2 sr) and high duty cycle (>90%) made the Milagro detector an important survey instrument for a broad range of γ-ray and cosmic ray phenomena (Hays 2004). The effective area and energy threshold of Milagro were dependent on zenith angle, due to the increased atmospheric overburden at larger zenith angles which tends to attenuate the particles in the air shower before they reach the ground. The sensitivity of Milagro varied slowly with zenith angle from 0° to ~30° and then decreased more rapidly (Atkins et al. 2005).

Chapter 4

Reduction and Calibration of Observational Data

This chapter focuses on the methods used to treat the γ-ray and radio data to extract useful information from them. Similar principles are applied to the data taken in the other energy bands covered in this work.

It is a fortunate coincidence in nature that while a γ-ray photon itself may not survive to ground level, the secondary products of its interaction with the atmosphere do survive and can be detected with simple detectors (Section 2.4). There is then a "γ-ray window" in the atmosphere, extending from below 50 GeV to ~50 TeV (Weekes 2003). The Whipple 10m telescope was the first large instrument capable of recording signals within this window, and the techniques that are used to analyze the raw data recorded by this telescope are described in Section 4.1.

The second part of this chapter is devoted to the radio data. An introduction is given to the instruments used to obtain the data discussed in this thesis. An overview of the morphological features of radio sources was given in Section 1.2.1; here we focus on how to extract useful information from these features in the case of Mrk 421.

4.1 Gamma-ray Data

The Mrk 421 γ-ray data presented in this thesis were analyzed using the imaging technique and analysis procedures described in Section 4.1.1. Since γ-ray images are known to be compact and elliptical in shape while those due to cosmic-ray showers tend to be broader with more fluctuations, selection criteria ("cuts") can be derived from the imaging technique parameters such that approximately 99% of the background images can be rejected.

Two quantities which are important for analysis and calibration of the γ-ray data and which must be determined for each observing season are the tracking ratio and the Crab Nebula rate.

The *tracking ratio* is defined as the ratio of the number of events passing cuts in a "source region" to the number passing the same cuts in a "control region" for a sample of data containing no source of γ-rays ("darkfield data"). This quantity is required in order to analyze the Mrk 421 data using the TRACKING method. The values of the tracking ratio for all seasons within the period 1995 – 2009 were calculated by analysing a large sample of darkfield data. The results are shown in Table 4.2.

Crab Nebula data (a total of 242.4 hours of observations) from the same period were analyzed in order to calibrate the overall telescope response for each season. The results are discussed in Section 4.1.4. These results were used to convert the Mrk 421 γ-ray rates into equivalent "Crab units".

4.1.1 Imaging Atmospheric Cherenkov Technique

The overall goal of an imaging Cherenkov telescope is the unambiguous detection of γ-ray radiation from celestial sources. However, the vast majority of the images recorded by such a telescope (over 99% of them) originate from events which are due not to γ-ray photons, but to hadronic showers, radiation from single local muons or sky-noise fluctuations. The key to the imaging atmospheric Cherenkov technique is to record as much information as possible about each image and to exploit the differences between γ-ray images and background images so as to achieve maximal rejection of the background events (Quinn 2005).

There are five principal steps in the analysis of data recorded with the Whipple 10m telescope:

1) Data selection

When selecting a database of observations to use for detailed analysis, a number of factors must be taken into account, such as sky conditions, the elevation angle of the source and the condition of the telescope system during the course of the

observations. Only observations taken under very good atmospheric conditions, free from hardware malfunctions and at elevation angles greater than 55º were used in the Mrk 421 analysis presented in this thesis. For data taken at zenith angle θ_z, the observed event rate can be shown to be approximately proportional to $\cos(\theta_z)$ (Le Bohec & Holder 2003). If the observations are restricted to a narrow range of zenith angles, as in this work ($7° \leq \theta_z < 34°$), the effect of zenith angle on the rates is relatively small (Toner 2008).

2) Image preparation

The light incident on each PMT in the camera produces at the anode a current pulse which is converted to voltage. As explained in Section 3.1.3, when the data acquisition system is triggered to "record an image", this voltage is input to a charge-to-digital converter (QADC), whose output is a number (digital count, d.c.) representing the amount of light incident on the PMT. There is a separate QADC channel for each PMT. The "raw data" of an image then consists of the set of these d.c. values for all PMTs in the camera.

Due to the 15 ns QADC integration time (Section 3.1.3), the signal will include some contamination from night-sky background. A small offset value, or "pedestal", is imposed on each QADC channel so that negative fluctuations in the PMT signal still result in a positive QADC value when integrated over the gate time. The pedestal of a channel is a measure of its mean integrated charge in the absence of a Cherenkov signal. The d.c. value corresponding to the pedestal is determined using randomly-triggered snapshots of the sky (i.e., not triggered by an air shower) recorded at a rate of 1 Hz. The variance of the pedestal value for each channel gives an indication of the night-sky background fluctuations for that channel. For a Cherenkov event, the average pedestal value in each channel is subtracted from the d.c. value recorded for that channel to derive the signal due the Cherenkov light.

Each PMT in the camera can be considered as a "pixel". For an event recorded by the telescope, some of these pixels will contain only background light while others will contain a mixture of background and Cherenkov light. Each event is "cleaned" on a pixel-by-pixel basis to suppress pixels containing only background light. To be considered part of the *picture* (essentially the core of the Cherenkov

image), the signal recorded from a pixel must be at least 4.25 times the standard deviation of the pedestal distribution for that pixel. To be part of the *boundary* for an image, a pixel must have a signal that is at least 2.25 times the standard deviation of the pedestal distribution and must also be adjacent to a pixel that is part of the picture. These picture/boundary values (4.25/2.25) are derived from optimization of the signal-to-noise ratio for Crab Nebula observations. Pixels which pass these picture/boundary cleaning conditions together make up the image of the Cherenkov event. All other pixels are treated as not belonging to the image, and their d.c. values are set to zero for all subsequent analysis.

Following pedestal subtraction and image cleaning, each surviving channel must undergo *flatfielding*, or gain normalization (Section 3.1.4), which compensates for the differing gain of each PMT. The relative gain factors are calculated from laser calibration data taken each night (Section 4.1.2).

3) Image parameterisation

Following pedestal subtraction, cleaning and flatfielding, the image of each event is parameterised: assuming the image is elliptical in shape, a set of parameters is calculated based on the shape (*length and width*), location (*distance*) and orientation (*alpha*) of the ellipse (Hillas 1985). These parameters are collectively known as Hillas parameters and are illustrated in Figure 4.1. In addition, image *size* is defined as the total number of d.c. in the cleaned image, corresponding to the total light content in all tubes that are part of the image, and is related to the energy of the primary particle that produced the shower. Image *asymmetry* is a parameter determined by the distribution of light along the major axis of the ellipse; γ-ray images tend to have more light in the direction in which the shower is pointing and less in the direction from which it came.

4) Gamma-ray selection

One of the most powerful methods for distinguishing γ-ray images from those caused by hadronic showers, muons or noise is selection based on image parameterisation. The images produced by γ-ray showers are compact whereas hadronic showers

produce images that tend to be broader and individual muons give rise to ring-like images or arcs in the focal plane.

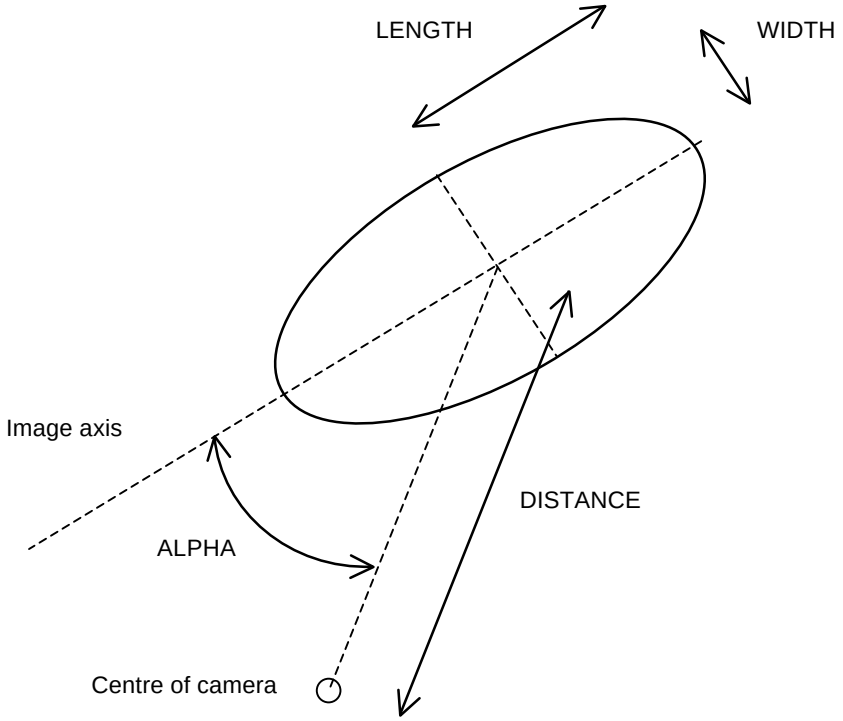

Figure 4.1 Illustration of the main Hillas image parameters.

Consequently, *length* and *width* for γ-ray events tend to be smaller than those for background events (see Figure 4.2). The γ-ray images from a source at the centre of FOV will tend to point to the centre of the camera and so will have small values of *alpha*, whereas background images will have their axes oriented randomly. Appropriate selection cuts can therefore be applied to the data so as to reject approximately 99% of the background images while retaining about 50% of those generated by γ-ray showers.

The data are subjected to a *size* cut which essentially acts as an energy filter. This cut criterion will only pass events in which the two or three PMTs with the highest signals have d.c. values above certain defined thresholds. This is similar to the hardware trigger, rejecting small background events. Cherenkov light from individual muons (from hadronic showers not detected by the telescope) that pass close to the telescope can trigger the system. Images of such muon events tend to

have less light per pixel than γ-ray images and to be very elongated by comparison. A *length/size* cut applied to the data reduces the number of such events (Moriarty et al. 1997).

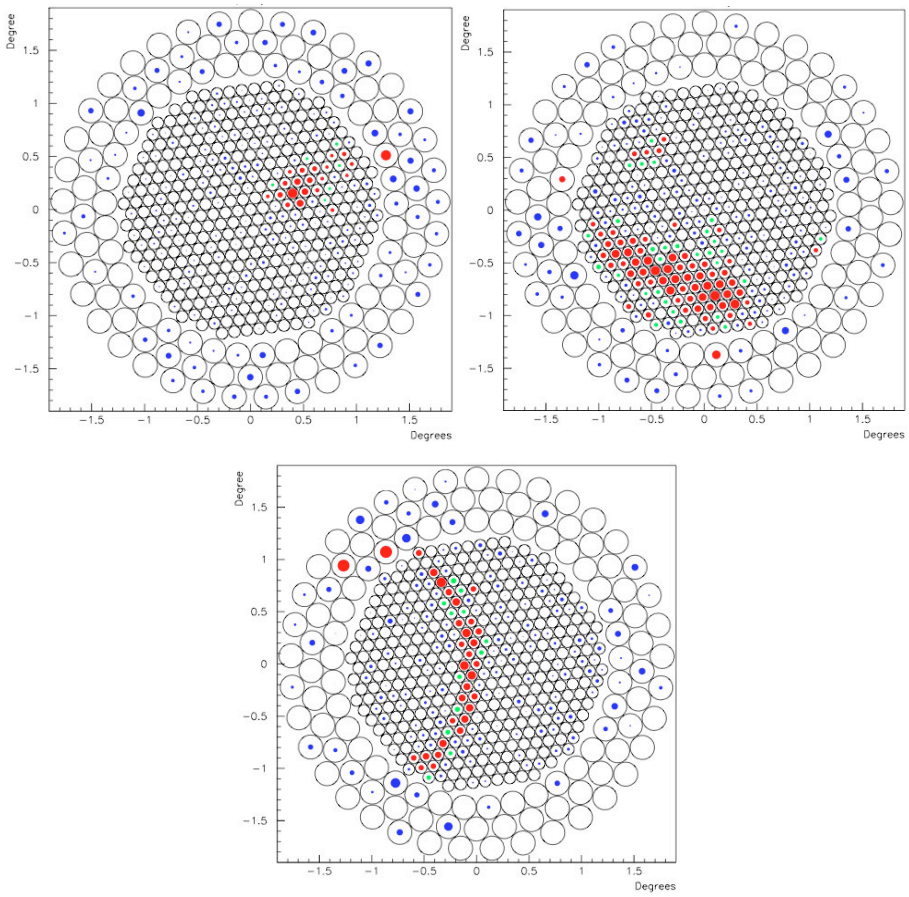

Figure 4.2 Typical images recorded by the Whipple 10m telescope: candidate γ-ray event (top left), cosmic-ray (top right) and segment of the ring generated by a local muon (bottom). Images from Dunlea (2001). Open circles represent the PMTs and the size of the filled circles is a measure of the amount of light recorded in each PMT; "image" pixels are shown in red and "boundary" pixels are shown in green. Blue circles correspond to pixels that fail the picture/boundary criteria and are excluded in the subsequent analysis.

The optimum values of the parameter cuts are determined as those that give the highest γ-ray signal-to-noise ratio (significance) for Crab Nebula observations. The optimised cuts developed using data from the 2000 observing season (following the major camera upgrade in 1999) are referred as "Supercuts 2000" and have proven

to be close to optimal for observations from all subsequent seasons. The list of Supercuts 2000 parameter cuts used in this work is shown in Figure 4.4.

5) Signal calculation

Even in the absence of a γ-ray source, some proportion of the events recorded will pass all of the selection cuts, implying that they are classified as γ-ray events. The rate of these background events, which depends on a number of factors including sky brightness, elevation and weather, must be established in order to calculate the statistical significance of any apparent excess of γ-ray photons detected. Different methods are employed to estimate this background depending on the observation mode used (Horan 2001).

For data taken in "ON/OFF mode", as described in Section 4.1.2, the *γ-ray rate* (r) and its statistical uncertainty (σ_r) are defined as:

$$r \pm \sigma_r = \frac{N_{ON} - N_{OFF}}{t} \pm \frac{\sqrt{N_{ON} + N_{OFF}}}{t} \tag{4.1}$$

where N_{ON} and N_{OFF} are the numbers of events passing all cuts for the ON run and the OFF run, respectively, and t is the duration of the observing run. The *significance* (Sig) of any excess is then given by:

$$Sig = \frac{r}{\sigma_r} = \frac{N_{ON} - N_{OFF}}{\sqrt{N_{ON} + N_{OFF}}} \tag{4.2}$$

This significance represents the ratio of signal to noise, and is related to the probability that the signal is real rather than a random fluctuation in the background level.

Most γ-rays from an object at the centre of the field of view will have small values of the *alpha* parameter. Hence, the alpha distribution beyond ~20° should consist of background events which mimic γ-ray events. For "TRACKING mode" observations (i.e., in the absence of an OFF run), events in the 20°–65° region of an ON-source *alpha* plot can be used to estimate the background from the source direction. This method is explained in detail on Section 4.1.3.

4.1.2 Analysis Software and Pointing Corrections

The raw data from the Whipple 10m telescope were analyzed using a software package that was originally developed at University College Dublin (UCD), and subsequently modified and installed on site at the Fred Lawrence Whipple Observatory (FLWO). This analysis software will be referred to hereafter as the "Dublin Analysis".

Each *run* (producing a raw data file) is taken in one of four modes: ON, OFF, TRACKING or Nitrogen. An ON/OFF pair consists of two consecutive exposures: the telescope is aligned with its optical axis pointed at the position of the source in the sky (RA and dec) and moved to track this position for 28 minutes ("ON run"); the telescope is then moved back to the same elevation and azimuth as at the start of the ON run, and this position (RA and dec) is observed for 28 minutes without any source, as a control region of the sky ("OFF run"). The OFF run provides a background comparison for the ON run. In the TRACKING mode, no OFF runs are taken, allowing the source to be followed continuously; in this case, the background is estimated from the *alpha* distribution, as indicated above. In order to flatfield the camera, the PMTs are illuminated with a nitrogen flash tube. Nitrogen runs are taken each night so as to determine the response of the camera to a uniform stimulus (see Section 3.1.4 for further details). In May 2007, the nitrogen tube was replaced with a laser pulser (Figure 3.16).

The raw data are stored in each file in ZEBRA format (developed at CERN), and consist of a set of data structures which hold all the information associated with each camera event (γ-ray or otherwise). The raw data files are given a `.fz` (ZEBRA format) extension, and are named by consecutive numbers, prefixed with "gt" (e.g., `gt035464.fz`).

The Dublin Analysis Code

This code is designed to extract, parameterise and analyze the information stored in the raw data files (UCD Data Analysis Manual). Figure 4.3 provides a functional overview of the Dublin analysis procedure, beginning with the `.fz` files and producing final output in HTML and/or eps format. The purpose of the each of the

intermediate routines shown in Figure 4.3 is as follows. The *xfastlook* routine outputs a postscript file which contains information about the run, such as number of events, duration, raw data rates and tracking information, as well as a data file (`gtxxxxxx.hdf`) in which the raw data have been converted to HDF (Hierarchical Data Format).

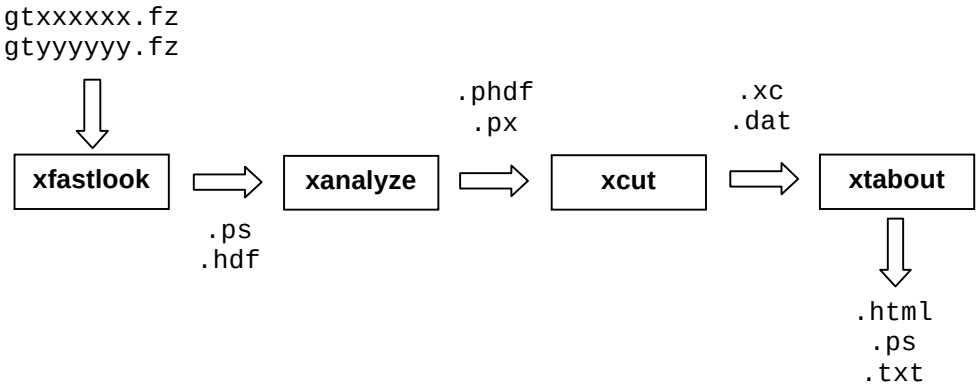

Figure 4.3 The Dublin analysis procedure in practice, where `gtxxxxxx.fz` is the raw data file and `gtyyyyyy.fz` is the appropriate nitrogen file. If an OFF run is taken, the input to *xfastlook* also includes an OFF data file.

The *xanalyze* program performs Hillas parameterisation for each of the events in this `.hdf` file; the output is either a file in HDF format (with a `.phdf` extension) or an ascii file (with a `.px` extension) containing parameter values for each event in the data run. The *xcut* program selects events that pass a set of predetermined cut values. The *xtabout* program generates a summary of the results (see Figure 4.4) in postscript, HTML or ascii format, along with an alpha distribution plot (Figure 4.5).

Pointing corrections

The accuracy with which the telescope tracks the position to which it is pointing is of vital importance in the imaging atmospheric Cherenkov technique. The *alpha* parameter depends completely on the position of the source in the field-of-view (Kildea 2002). At the beginning of the season 2007–2008, the *alpha* plots generated by the analysis appeared to be less peaked and the Crab Nebula rates lower than expected, suggesting that there was a small offset in the telescope pointing. In early 2008, the author carried out pointing measurements on the Whipple 10m telescope in

order to determine this offset so that corrections could be implemented in the Dublin analysis code. A white screen was placed in front of the PMT camera and CCD images of stars were taken at different elevations and azimuths (see Figure 4.6) using the pointing monitor (Section 3.1.4).

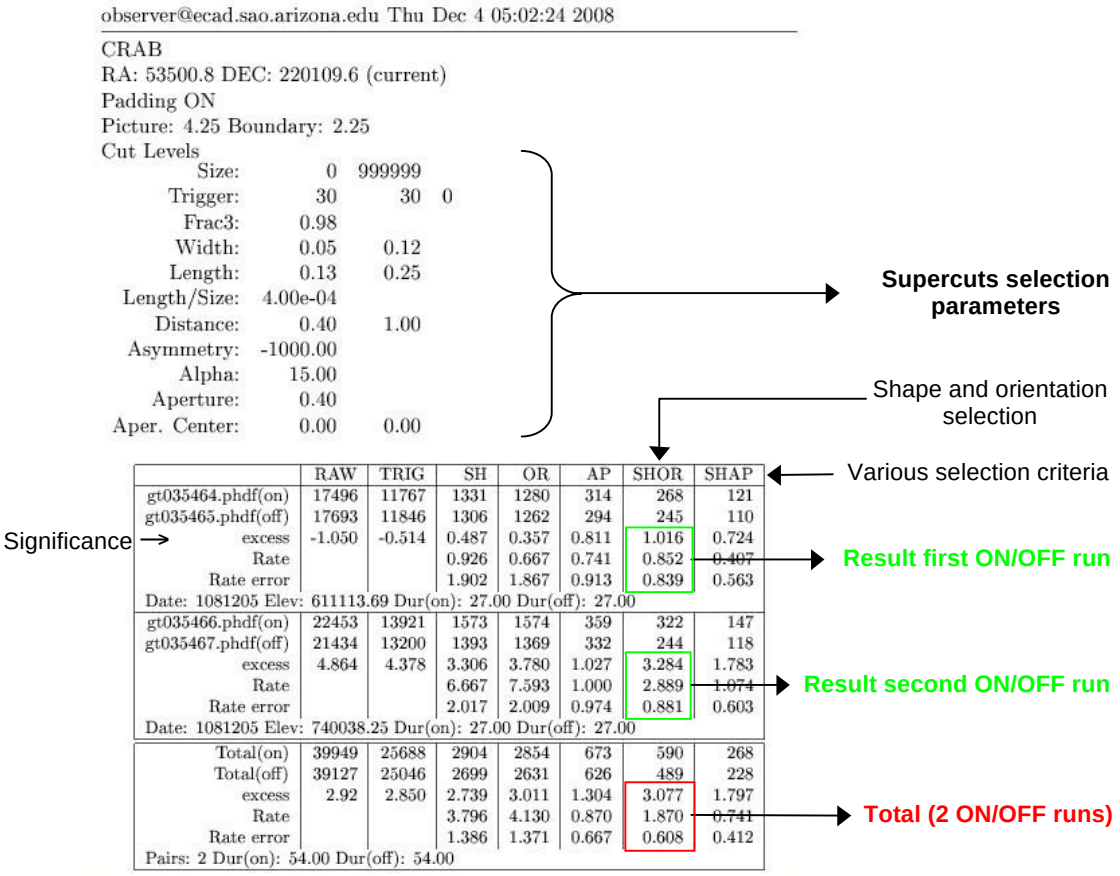

	RAW	TRIG	SH	OR	AP	SHOR	SHAP
gt035464.phdf(on)	17496	11767	1331	1280	314	268	121
gt035465.phdf(off)	17693	11846	1306	1262	294	245	110
excess	-1.050	-0.514	0.487	0.357	0.811	1.016	0.724
Rate			0.926	0.667	0.741	0.852	0.407
Rate error			1.902	1.867	0.913	0.839	0.563
Date: 1081205 Elev: 611113.69 Dur(on): 27.00 Dur(off): 27.00							
gt035466.phdf(on)	22453	13921	1573	1574	359	322	147
gt035467.phdf(off)	21434	13200	1393	1369	332	244	118
excess	4.864	4.378	3.306	3.780	1.027	3.284	1.783
Rate			6.667	7.593	1.000	2.889	1.074
Rate error			2.017	2.009	0.974	0.881	0.603
Date: 1081205 Elev: 740038.25 Dur(on): 27.00 Dur(off): 27.00							
Total(on)	39949	25688	2904	2854	673	590	268
Total(off)	39127	25046	2699	2631	626	489	228
excess	2.92	2.850	2.739	3.011	1.304	3.077	1.797
Rate			3.796	4.130	0.870	1.870	0.741
Rate error			1.386	1.371	0.667	0.608	0.412
Pairs: 2 Dur(on): 54.00 Dur(off): 54.00							

Figure 4.4 The Dublin analysis output file `xtabout.ps`, for two ON/OFF runs taken on the Crab Nebula. The numbers shown in the rows labelled "excess" are the significance values (Equation 4.2) for the different selection criteria. Subsequent analysis is based on the results from the combined shape and orientation selection criteria (SHOR). All rates and associated errors are given in γ/min.

The telescope should have pointed directly at the star in each case, so that the image should have been in the centre of the camera, at coordinates (0,0). The author used the program *xyExtract Graph Digitizer* (Silva 2008) to determine the actual position of the star on the screen in degrees relative to the centre of the PMT camera. This software extracts data from a two-dimensional bitmap plot derived from a graphics

file (scanned, PDF document, gif, jpg, etc) and allows positions on the plot to be determined relative to any orthogonal and non-orthogonal reference system.

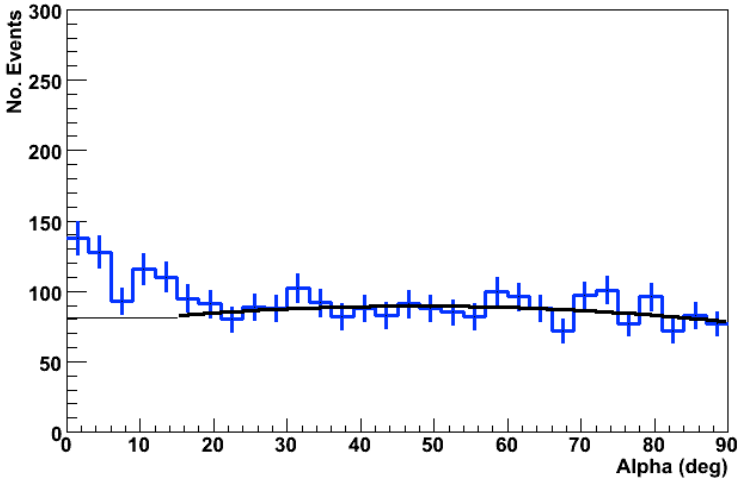

Figure 4.5 The output *alpha* distribution plot for the analysis shown in Figure 4.4.

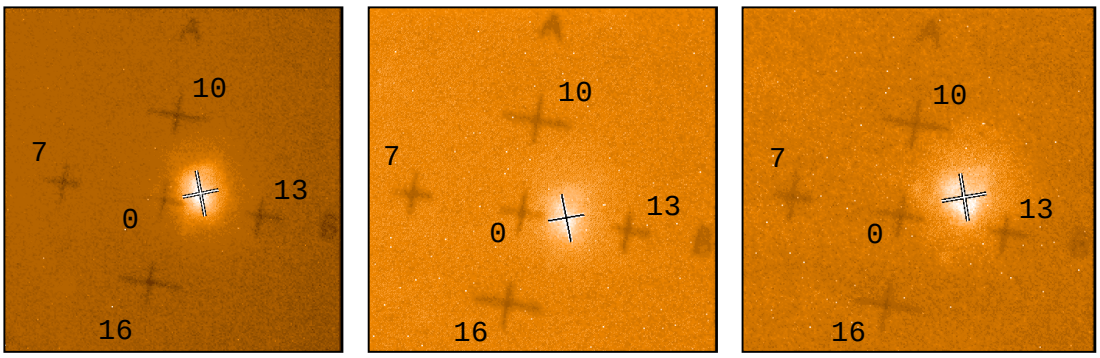

Figure 4.6 Star images at the focal plane of the Whipple 10m telescope. Pixel 0 corresponds to the coordinates (0, 0), Pixel 7 (-0.234, 0.030), Pixel 10 (0.026, 0.202), Pixel 13 (0.234, -0.030), Pixel 16 (-0.026, -0.202). The coordinate system is centred on the central pixel of the PMT camera. The *x* axis is the horizontal direction of the camera and the *y* axis is the vertical direction. Axes units are degrees.

The centre of each star image was obtained using the program *ESO SkyCat* (Brighton et al. 2001). The *x* and *y* coordinates of the images were found to be clearly correlated with the elevation angle of the telescope (Figure 4.7). However, there

appears to be no correlation with the azimuthal pointing of the telescope (Figure 4.8), so corrections were applied only for elevation.

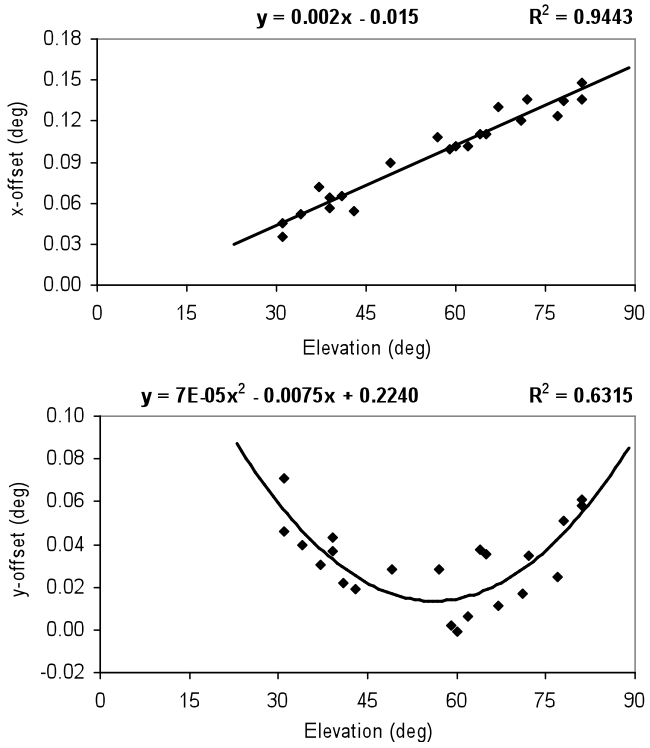

Figure 4.7 Star offsets versus elevation. Observing season 2007–2008.

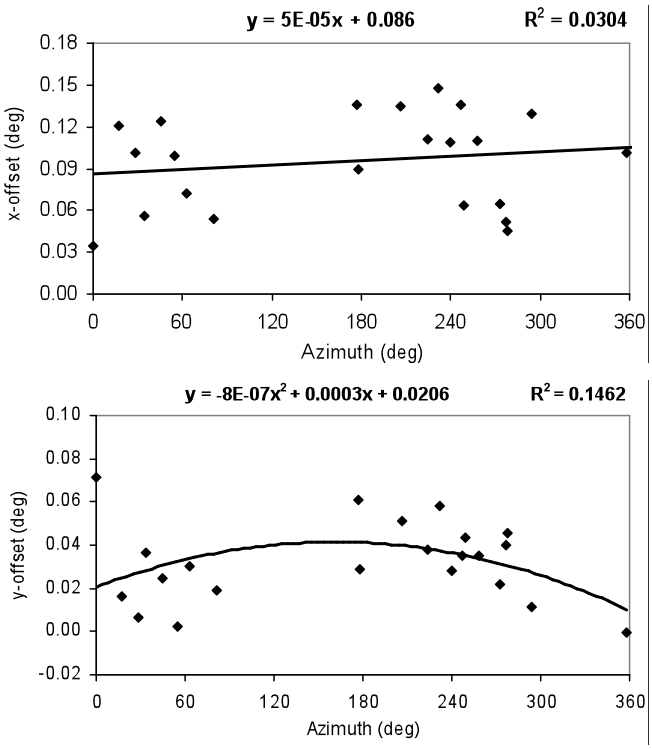

Figure 4.8 Star offsets versus azimuth. Observing season 2007–2008.

The corrections were incorporated into the *xanalyze* program so that the code effectively re-centred the camera as appropriate during the analysis (by adding an offset to the *x* and *y* coordinates of the PMTs) to correct for the mis-pointing. The corrections clearly improve the *alpha* plots for a detected source (Figure 4.9): the maximum number of events is obtained within the first bin, and the γ-ray rate has higher values and smaller error bars.

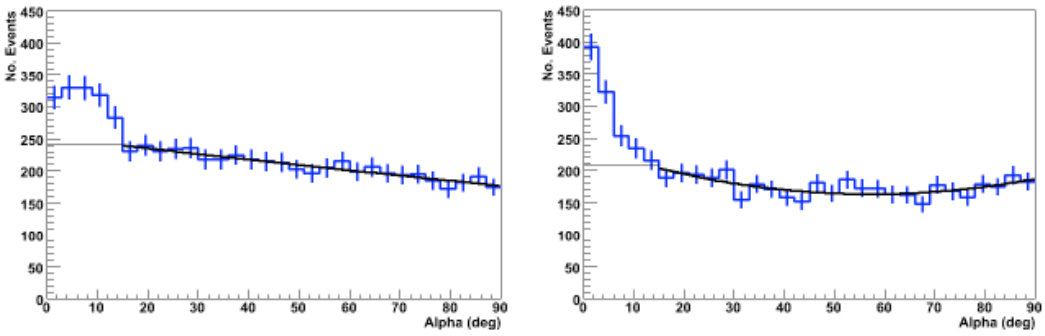

Figure 4.9 *Alpha* plots for Mrk 421 without and with corrections applied, left and right respectively (exposure time = 1.4 hours).

To check the stability of the telescope pointing, a number of relatively simple *pointing checks* are performed during each observing night. The procedure necessitates moving the reflector to point at a reasonably bright star near the source under observation. Anode current readings from the inner seven PMTs are then recorded. If the telescope is pointing correctly at the star, the current readings are reasonably symmetrical around the centre of the camera with maximum reading in the central tube (Pixel 1). With poor pointing, the distribution of anode currents is not symmetrical around the central tube, and the highest current may not even be in the central PMT. Table 4.1 shows the current readings for some pointing checks performed during the 2004–2005 observing season.

PSF measurements (see Section 3.1.2 for details) are used to provide a more accurate measure of the instrument's pointing, but these measurements are more complex and so are not carried out on a nightly basis. The author proposed an alternative method using the "barycentre" of the anode currents (as in Table 4.1, for example), which provides a crude method of determining the offset for archival data

so that corrections can be applied if necessary. Figure 4.10 shows the configuration of the inner seven PMTs.

Elevation (°)	C_1	C_2	C_3	C_4	C_5	C_6	C_7
30	111	26	19	24	125	164	58
40	105	19	22	28	102	118	41
42	139	21	24	36	159	143	28
45	60	11	15	27	87	50	21
54	122	22	12	31	111	96	26
61	172	21	20	35	85	103	34
63	80	26	22	20	26	50	36
71	52	17	15	14	22	35	30
75	48	20	15	16	18	35	31
80	133	37	14	16	35	108	114
82	147	29	16	17	35	115	128

Table 4.1 Pointing checks for the observing season 2004–2005. C_i is the anode current (in μA) in PMT number *i* (see Fig. 4.10 for numbering of PMTs).

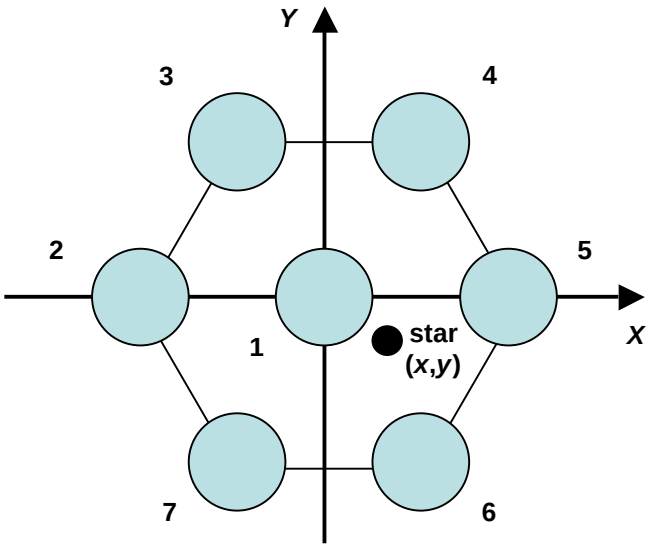

Figure 4.10 The inner seven PMTs of the camera and the star position.

The position of the star (the *x* and *y* coordinates), for a particular elevation, can be calculated from the values in table 4.1 using the following equations

$$x = \frac{\sum_{i=1}^{7} C_i \cdot x_i}{\sum_{i=1}^{7} C_i} \tag{4.3}$$

$$y = \frac{\sum_{i=1}^{7} C_i \cdot y_i}{\sum_{i=1}^{7} C_i} \tag{4.4}$$

where x_i and y_i are the coordinates of PMT number i, and C_i is anode current reading for this PMT. Figure 4.11 shows some images simulated using this method, for comparison with those shown on Figure 4.6.

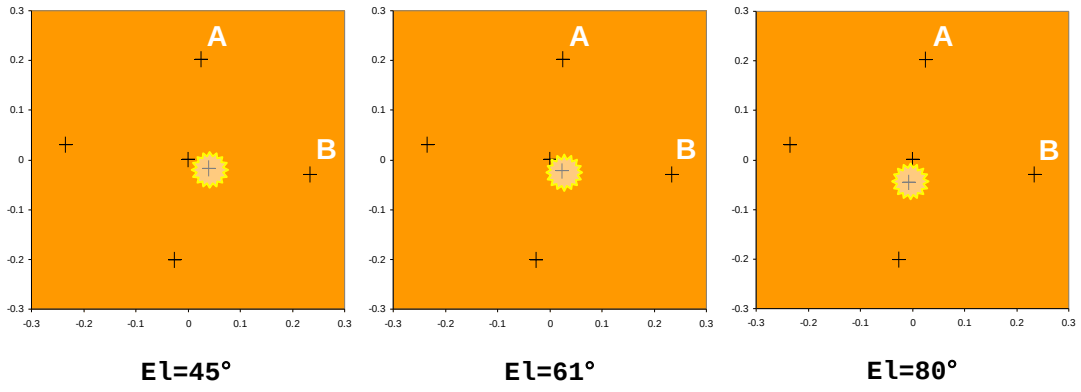

Figure 4.11 Simulated star images at the focal plane.

The resulting x and y offsets are plotted as a function of the elevation in Figure 4.12. In can be seen that in this case (for the observing season 2004–2005), the x-offset decreases at higher elevations, opposite to the behaviour seen in 2007–2008. It is worth noting that the precision of these measurements (~ 0.01°) is comparable with that achieved using the CCD recording of star images.

The star images shown in Figure 4.6 indicate that during the 2007–2008 observing season, the telescope pointing was incorrect to the extent of about one pixel diameter, and it was necessary to apply the appropriate correction in the analysis. However, for the 2004–2005 season, the star images were much closer to

the centre of the camera, and the offsets were small enough that corrections were deemed unnecessary for that season.

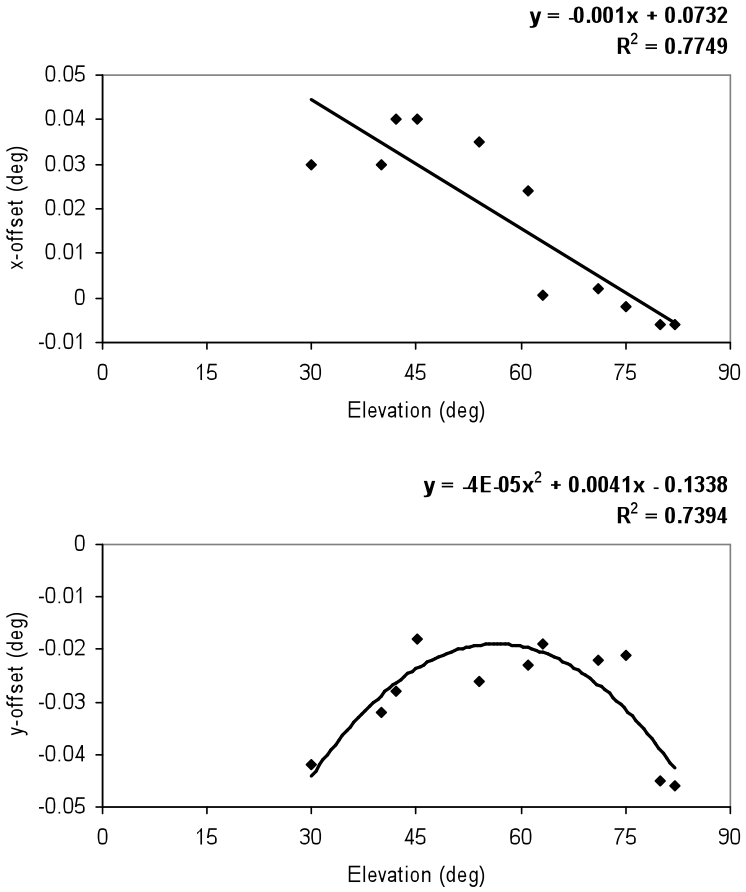

Figure 4.12 Star offsets versus elevation. Observing season 2004–2005.

4.1.3 Determination of the Tracking Ratio

As previously mentioned (Section 4.1.2), two different modes of observation are employed at the Whipple telescope, ON/OFF and TRACKING (Catanese et al. 1998). In both modes, the data are usually taken in 28-minute runs. Unlike data taken in the ON/OFF mode, a run taken in TRACKING mode does not have an independent associated OFF control run which can be used to establish the background level of γ-ray-like events during the TRACKING run. These control data are essential in order to estimate the number of events passing all cuts that would have been recorded during the run in the absence of the candidate γ-ray source. In order to obtain a background estimate for TRACKING mode data, a *tracking ratio* is

calculated by analysing darkfield data (Horan et al. 2002), consisting of OFF-source data taken in ON/OFF mode along with observations of objects found not to be sources of γ-rays. A large database of these runs is analyzed and, in this way, the level of background events passing all γ-ray selection criteria can be characterised as a function of zenith angle.

Under ideal conditions the *alpha* distribution is flat in the absence of a source; with a source present, an excess is seen for *alpha* < 15°. Geometric effects due to truncated events at the edge of the camera and effects due to pixels turned off (for example, due to the presence of bright stars) introduce some structure into the *alpha* distribution, but the shape of this distribution is reasonably constant in the absence of a source (McEnery 1997). The tracking ratio (ρ) is defined, for darkfield data after shape cuts, as the ratio of the number of events with $0° \leq alpha < 15°$ to those with $20° \leq alpha < 65°$. These two intervals are treated as "source" and "control" regions respectively (see Figure 4.13). For the example shown, the number of events in the source region is $N_{source} = 2719$ and the number in the control region is $N_{control} = 8132$, giving $\rho = 0.334 \pm 0.007$.

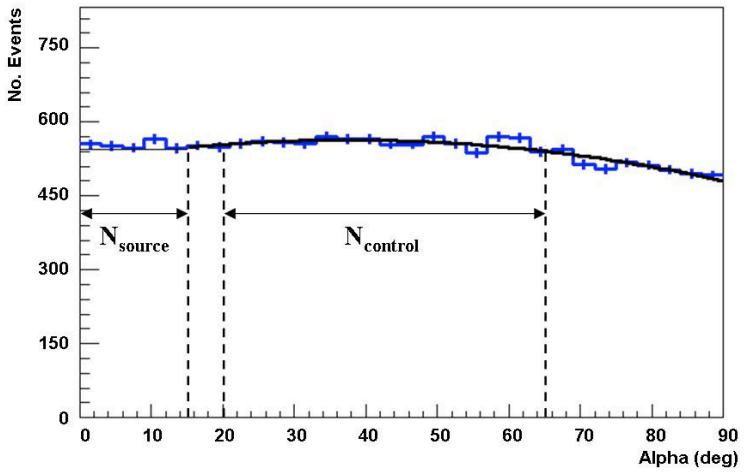

Figure 4.13 *Alpha* plot for the darkfield data from the 2004–2005 season. The total exposure for this database was 11.2 hours. The regions of the *alpha* plot used for the calculation of the tracking ratio are shown.

The values of the tracking ratios obtained for darkfield data for the observing seasons 1995–1996 to 2008–2009 are presented in Table 4.2. The error on the tracking ratio is calculated as

$$\sigma = \frac{N_{source}}{N_{control}}\sqrt{\frac{1}{N_{source}} + \frac{1}{N_{control}}} = \rho\sqrt{\frac{1}{N_{source}} + \frac{1}{N_{control}}} \tag{4.5}$$

The darkfield data presented here are mostly OFF-source data from ON/OFF observations of Mrk 421. In some cases, darkfield data from other targets have been included in order to improve the statistics for seasons where not many OFF runs were taken for Mrk 421. In such cases, the tracking ratio was determined using a database composed of mixed runs taken in OFF mode for different targets such as Mrk 501, W Comae and H 1426.

Season	No. of darkfields	N_{source}	$N_{control}$	Tracking Ratio (ρ)	Error (σ_ρ)
1995-1996	22	1213	4003	0.303	0.010
1996-1997	37	3815	12800	0.298	0.005
1997-1998	30	1258	3710	0.339	0.011
1998-1999	25	1133	4780	0.237	0.008
1999-2000	32	2586	8479	0.305	0.007
2000-2001	42	6645	20815	0.319	0.004
2001-2002	38	4044	12924	0.313	0.006
2002-2003	47	3089	10322	0.299	0.006
2003-2004	29	3956	11826	0.335	0.006
2004-2005	24	2719	8132	0.334	0.007
2005-2006	20	2266	6845	0.331	0.008
2006-2007	15	2030	6041	0.336	0.009
2007-2008	25	2719	8141	0.334	0.007
2008-2009	40	4350	12584	0.346	0.006

Table 4.2 Tracking ratios for Mrk 421 for observing seasons from 1995–1996 to 2008–2009.

The tracking ratios with their respective errors are displayed for all seasons in Figure 4.14. The average tracking ratio is 0.316 ± 0.002. A test for a constant value (Equations 4.7 and 4.8) was applied to this dataset and gives χ^2/dof = 183.7/13, $P_{\chi 2} = 2.95\times10^{-32}$. Such a probability is small enough to confirm that the tracking ratios are not consistent with a constant value, so it is important to use the value for each season rather than an overall average. There is much less variation after the 1999 upgrade, most likely due to the larger number of smaller pixels, while the

elimination of the outer pixels from 2003 onwards appears to lead to a more stable (though slightly higher) value. Changes in the tracking ratio can also arise from changing levels of sky noise across the camera (for example, as a result of changing telescope elevation), degradation and recoating of mirrors, variation in PMT gains, problem pixels etc.

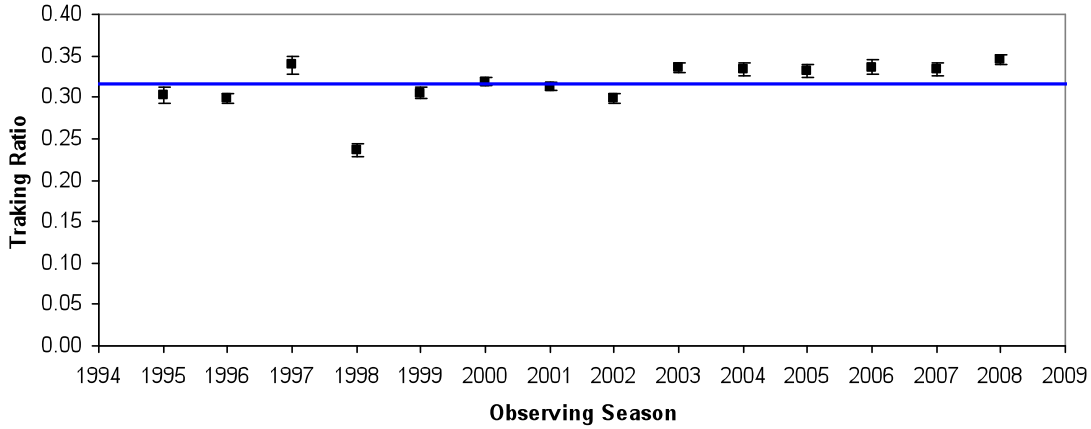

Figure 4.14 The tracking ratios for the 14-year period 1995 – 2009. The blue line represents the average for the entire dataset.

Non-statistical variation of the tracking ratio has serious implications when searching for variability in TRACKING mode data (Section 5.1). However, there is no evidence for any major systematic error affecting the tracking ratio within a given season, and the tracking ratio shows little or no elevation dependence (Horan 2001). Therefore, one can safely use the average value of the tracking ratio for each year.

For data recorded in TRACKING mode, the γ-ray rate (r) and its statistical uncertainty (σ_r) are then given by:

$$r \pm \sigma_r = \frac{N_{ON} - \rho N_{OFF}}{t} \pm \frac{\sqrt{N_{ON} + \rho^2 N_{OFF} + \sigma_\rho^2 N_{OFF}^2}}{t} \qquad (4.6)$$

where N_{ON} is the number of events that pass the *alpha* cut, N_{OFF} is the number of events in the control region of the *alpha* plot, and t is the duration of the TRACKING run. The significance is once again given by Equation 4.2.

4.1.4 Observations of the Crab Nebula

The Crab Nebula is a steady, strong source of TeV γ-rays (Weekes 2003), and is considered as the "standard candle" for VHE γ-ray astronomy using the atmospheric Cherenkov technique. The birth of the nebula was recorded by early Chinese and Native American astronomers in 1054 A.D., during which time it was visible in daylight for several weeks (Clark & Stephenson 1977). Sometime around 1850 it was observed by William Parsons, third Earl of Rosse, who subsequently named it the "Crab Nebula" (it is referred to as M1 in the Messier catalogue). In modern times the Crab Nebula has formed the basis for many exciting astrophysical discoveries over a broad range of wavelengths. It was the first object identified as a supernova remnant (SNR), and the first SNR connected with a central pulsar (PSR 0531+21). The Crab Nebula was detected at TeV energies in 1989, at the 9σ level, after 60 hours of observation at the Whipple Observatory (Weekes et al. 1989). Multiwavelength images of the Crab Nebula are shown in Figure 4.15.

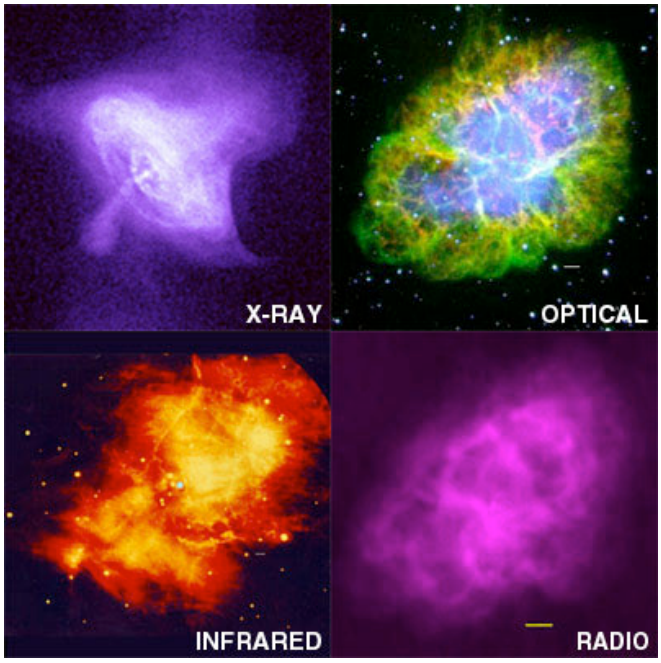

Figure 4.15 Multiwavelength images of the Crab Nebula (Physics News Graphics, AIP).

From 1995 to 2009, the Crab Nebula was observed with the Whipple 10m telescope almost every night during moonless periods from October to April. For the

seasons from 2003 to 2009, when a single camera configuration (379 pixels) was used and a consistent set of selection cuts applied (for elevation angles greater than about 55°), the source was routinely detected by the Whipple 10m telescope at a significance level of ~5σ in one hour of observation with an average rate of 2.91 ± 0.06 γ/min over the range 0.4-10 TeV. For comparison, the corresponding rate for the full VERITAS array is ~10 γ/min (~40σ in one hour), due to the larger collection area and lower energy threshold of VERITAS. The Crab Nebula data were used to characterize the performance of the telescope, and the Mrk 421 data are expressed as a fraction of the Crab Nebula flux, so that data from different observing seasons, with slightly different energy thresholds, can be compared. There is substantial overlap in the times of year when Mrk 421 and the Crab Nebula are observable, so effects due to variation in telescope performance *within* an observing season can be ignored. It should be noted that this simplistic scaling is strictly only valid for a TeV energy spectrum close to that of the Crab Nebula (spectral index of -2.49; Hillas et al. 1998). In so far as the Mrk 421 spectrum can be described by a simple power-law function, the spectral index is also in the region of -2.5 (e.g., Krennrich et al. (1999) give -2.54 ± 0.03). Although Mrk 421 has been known to display spectral variability (Krennrich et al. 2002), the measurement uncertainties on the flux points are such that the effect of spectral variability should not be significant (Horan et al. 2009).

The TeV γ-ray light curve for the Crab Nebula for the 2007–2008 observing season is shown in Figure 4.16. Each data point on the graph is an average of the flux for a single night. Since the Whipple 10m telescope can only operate during moonless conditions, there is a period centred on full Moon each month when γ-ray observations are not possible, and for this reason there are gaps on the light curve shown in Figure 4.16. The mean rate for that season was 2.79 ± 0.17 γ/min, based on a total exposure time of 17.6 hours at an average elevation of 73°. This rate value is used in Chapter 5 to express the γ-ray rates from Mrk 421 during the 2007–2008 season in Crab units.

Table 4.3 shows a summary of the Whipple 10m observations of the Crab Nebula between 1995 and 2009. In total, 524 pairs (524 ON runs and 524 OFF runs) were selected, and a weighted mean rate (Equation 5.2) was calculated for each

season. Only ON/OFF runs taken in good weather conditions at elevation higher than 55° were considered. Runs interrupted by hardware problems or with duration less than 25 minutes were excluded from this database.

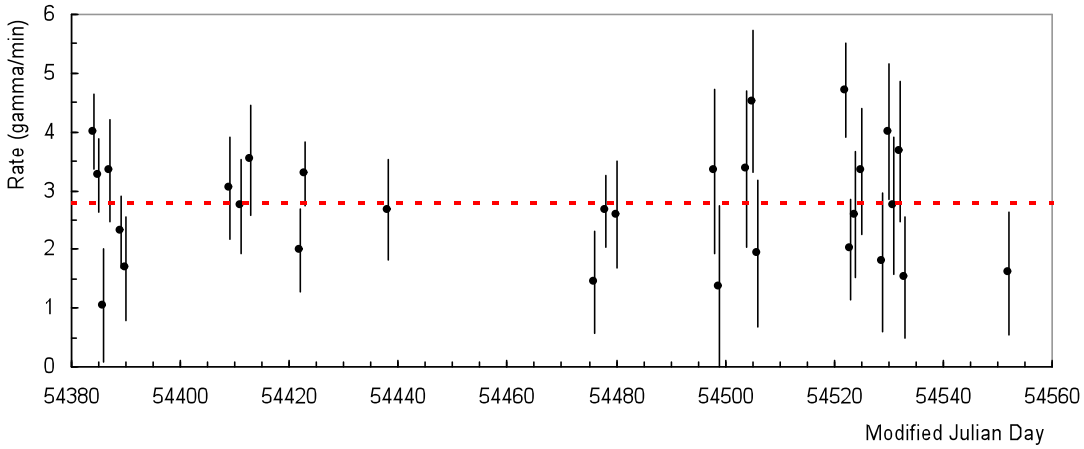

Figure 4.16 Nightly γ-ray rate from the Crab Nebula from October 2007 to March 2008. The mean rate for the season is represented by the red dashed line. The chi-square (χ^2) test for a constant rate, described later in this Section (Equations 4.7 and 4.8), has been applied to this dataset. The resulting χ^2 value is 31.6 for 29 degrees of freedom, giving a probability of 34% ($P_{\chi 2}$ = 0.34) that the rate is constant about the mean.

Season	No. of Pairs	Exposure Time (h)	Average Elevation (°)	Rate (γ/min)	χ^2 / dof	$P_{\chi 2}$	Analysis Package
1995-1996	21	9.6	67	1.46 ± 0.08	21.6 / 17	0.20	Quicklook
1996-1997	14	6.4	69	1.73 ± 0.15	16.3 / 12	0.18	Quicklook
1997-1998	28	13.1	63	1.11 ± 0.08	17.5 / 14	0.23	Quicklook
1998-1999	49	22.9	69	1.33 ± 0.06	32.8 / 31	0.38	Quicklook
1999-2000	99	46.2	71	2.26 ± 0.08	50.0 / 43	0.22	Quicklook
2000-2001	7	3.2	62	2.25 ± 0.31	11.3 / 6	0.08	Dublin
2001-2002	67	30.8	72	2.73 ± 0.09	83.5 / 66	0.07	Dublin
2002-2003	38	17.5	69	2.42 ± 0.10	50.5 / 37	0.07	Dublin
2003-2004	26	12.1	71	2.74 ± 0.16	23.2 / 16	0.11	Dublin
2004-2005	32	14.9	73	2.93 ± 0.13	23.6 / 24	0.48	Dublin
2005-2006	48	22.4	71	3.01 ± 0.12	33.5 / 31	0.35	Dublin
2006-2007	28	13.1	72	3.09 ± 0.18	25.8 / 20	0.17	Dublin
2007-2008	39	17.6	73	2.79 ± 0.17	31.6 / 29	0.34	Dublin
2008-2009	28	12.6	71	2.64 ± 0.13	25.0 / 21	0.25	Dublin

Table 4.3 Whipple 10m observations of the Crab Nebula during 1995–2009.

Observations from 2000 onwards were analyzed using the Dublin analysis code. However, this code was not set up to analyze data taken with older camera configurations (Figure 3.4), prior to the 2000–2001 observing season. An earlier analysis program ("Quicklook"), designed to analyze data runs as soon as they are completed, was therefore used to deal with these camera configurations. The γ-ray rates obtained (shown in Table 4.3) have been plotted in Figure 4.17.

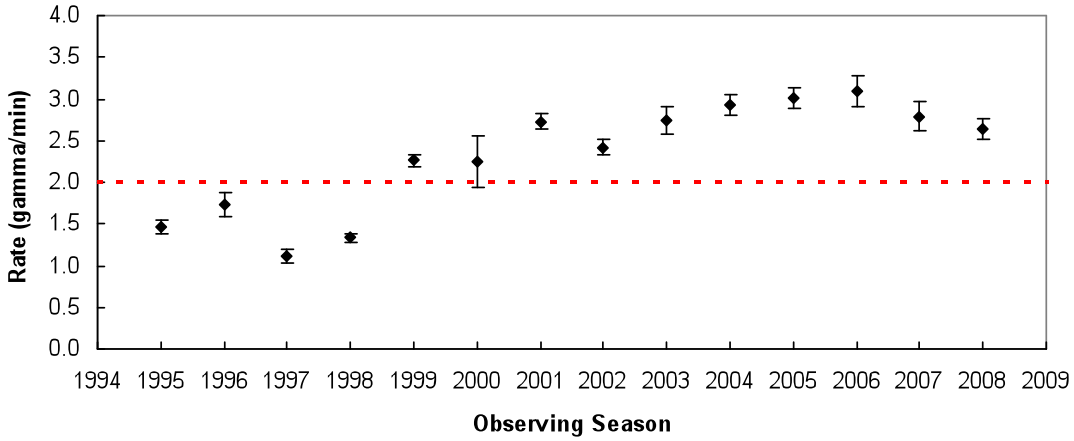

Figure 4.17 Annual mean rates for the Crab Nebula data. The red dashed line represents the average of the entire database.

The total exposure time of the entire database, taken over 14 years of observations of the Crab Nebula, is 242.4 hours of good-quality data with average elevation 70°, and the average γ-ray rate is 2.00 ± 0.03 γ/min. For seasons prior to 1999–2000 the rates look rather low (Figure 4.17), but this can be attributed to differences in camera configurations, numbers of PMTs employed and other hardware differences, given the major camera upgrade that was carried out between the 1998–1999 and 1999–2000 seasons (Finley et al. 2001). The change in analysis software can be excluded as the cause of the change in rates, as the largest change is seen between the 1998–1999 and 1999–2000 seasons (both of which were analysed with Quicklook), whereas the change between 1999–2000 and 2000–2001 (when the software was switched from Quicklook to the Dublin analysis) is negligible.

A consistency check (described below) for a constant rate was applied to this database, using Equations 4.7 and 4.8, giving $\chi^2 = 623.8$ for 13 degrees of freedom. The resulting probability ($P_{\chi 2} = 6.62\times10^{-125}$) is extremely small, implying that the

measured γ-ray rates are not consistent with a constant rate. Based on the premise that the TeV flux from Crab Nebula is constant, the variation in observed γ-ray rate can be used to compensate for the hardware changes. This is the rationale for using the Crab Nebula data to normalize the Mrk 421 observations.

Very recently, both AGILE and *Fermi*-LAT have observed flaring activity in the MeV-GeV emission range from the Crab system (Abdo et al. 2011, Tavani et al. 2011), and there has been some controversy as to whether flaring occurs at TeV energies as well (ARGO-YBJ *ATel#2921*, MAGIC *ATel#2967*, VERITAS *ATel#2968*). In view of this, the stability of the Crab Nebula rates measured with the Whipple 10m telescope within individual observing seasons has been critically examined. For most of the observing seasons between 1995–1996 and 2008–2009, the χ^2 test indicates that the night-to-night rates are consistent with a constant rate for each season ($P_{\chi 2} > 0.05$). However, for the season 2003–2004, a large χ^2 value was found (χ^2/dof = 55.4/20). This can be traced to four nights with exceptionally high rate (~5 γ/min) during the period November–December 2003; to avoid any possibility of contamination by flaring activity (which is outside the scope of this thesis), these "anomalous" points were excluded from determination of the seasonal Crab rate in Table 4.3.

All the data used in these analyses were taken at elevation angles greater than 55°, where significant elevation effects are generally not seen. However, to ensure that there was no elevation dependence in the Crab rates obtained, the Crab data for each observing season were plotted as a function of elevation. The resulting plots for three different seasons are shown in Figure 4.18. Each data point on the plots represents the mean rate in a 1° elevation bin. The mean rate for each dataset is shown as a horizontal line on each panel.

For each season, a *chi-square* (χ^2) *test* for constant rate was applied. The χ^2 value is calculated using the following equation:

$$\chi^2 = \sum_{i=1}^{N} \frac{\left(r_i - \langle r \rangle\right)^2}{\sigma^2} \tag{4.7}$$

where r_i, σ_i is the γ-ray rate and error from an individual data point, N is the number

of data points and $\langle r \rangle$ is the average rate over the entire dataset.

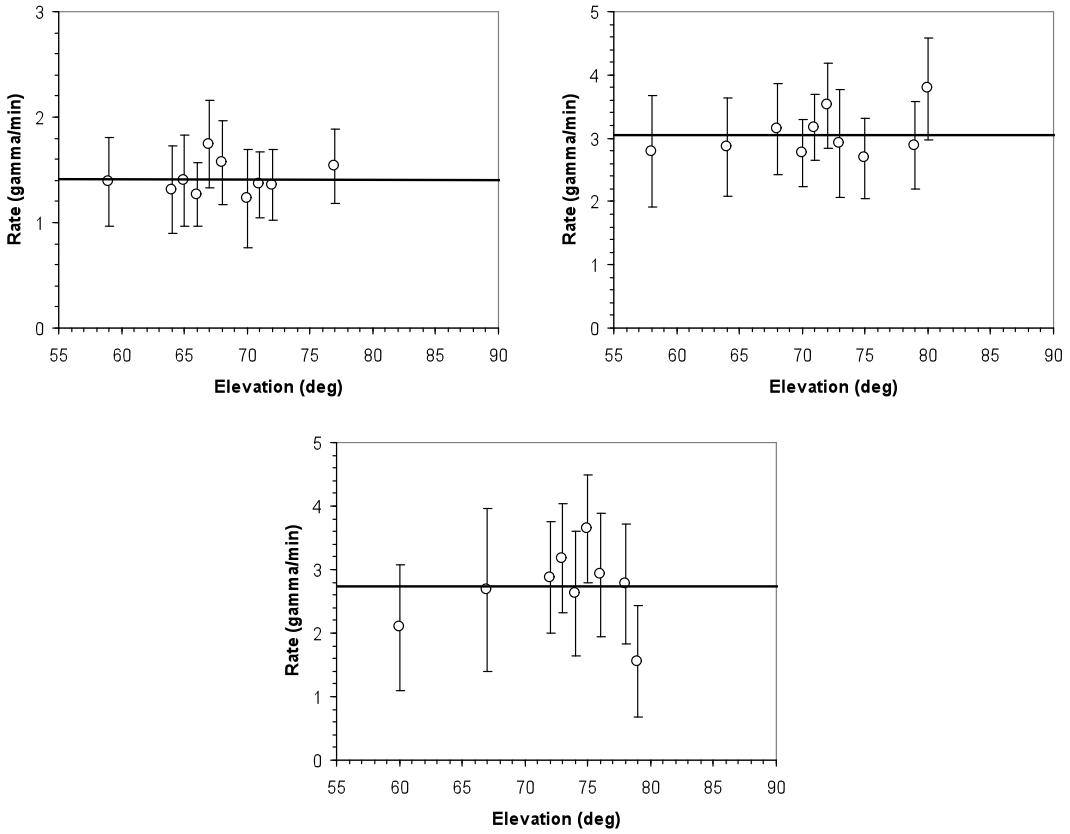

Figure 4.18 The Crab rate as a function of elevation for the seasons 1998-1999 (top left), 2005-2006 (top-right), and the 2007-2008 (bottom). The horizontal lines represent the mean rate for each season.

Given a χ^2 value and the degrees of freedom (dof), the one-tailed probability value, $P_{\chi 2}$, of the χ^2 test is the area under the χ^2 distribution from the χ^2 value to infinity. The formulas involved for the computation of $P_{\chi 2}$ are detailed below

$$P_{\chi^2} = \int_{\chi^2}^{\infty} f(x,k)\, dx \tag{4.8}$$

$$f(x,k) = \frac{1}{2^{\frac{k}{2}}\,\Gamma\left(\frac{k}{2}\right)} x^{\frac{k}{2}-1} e^{-\frac{x}{2}} \tag{4.9}$$

where $f(x,k)$ is the χ^2 distribution and k is the degrees of freedom (equal to N-1). Equation (4.8) is the upper incomplete gamma function $gammaq(x,a)$, with $x = \chi^2/2$ and $a = k/2$, which can be used to calculate $P_{\chi 2}$ (Press et al. 2007). Therefore, it represents the probability that the rate is constant about the mean. The results for the data shown in Figure 4.18 are summarized in Table 4.4.

Season	Mean Rate (γ/min)	χ^2	dof	P_{χ^2}
1998-1999	1.41 ± 0.12	1.438	9	0.998
2005-2006	3.04 ± 0.22	2.238	9	0.987
2007-2008	2.73 ± 0.32	3.246	8	0.882

Table 4.4 The χ^2 values, degrees of freedom and probability for three observing seasons.

The results of the χ^2 test shown in Table 4.4 confirm that the Crab Nebula rates obtained for each observing season are consistent with having no significant elevation dependence above 55°, i.e., they can be fit with a straight line of slope zero. The Crab Nebula rates shown in Table 4.3 are used to calibrate the Mrk 421 data for each observing season between December 1995 and May 2009.

4.2 Radio Data

The strength of a radio source, as discussed on Section 3.2, is measured in terms of *spectral flux density*, S(ν). This is the amount of energy per second, per unit frequency interval striking a unit area of the telescope. The flux density of most of the radio sources is of the order of one jansky (Jy), where $1\ Jy = 10^{-23}\ erg\ s^{-1}\ cm^{-2}\ Hz^{-1}$. The second strongest radio source in the sky, after the Sun, is the galaxy Cygnus A. At 400 MHz, its spectral flux density is 4500 Jy (Carroll & Ostlie 1996). Weak radio emissions, with S(ν) equal to few mJy, come from supernova remnants, short-lived ($\tau < 10^7$ yr) stars and low-luminosity AGN (Condon et al. 1998).

As shown in Section 5.2, Mrk 421 data from the University of Michigan Radio Astronomy Observatory (UMRAO) and from the Metsähovi Radio

Observatory have been analyzed for this Thesis. Table 4.5 shows typical flux densities from Mrk 421 obtained at those observatories over the last four years. In spite of updates to instruments and electronics, the quoted flux values can be considered robust because the measurements are always calibrated against standard sources (see Section 5.2).

Frequency (GHz)	Average Flux (Jy)	Minimum Flux (Jy)	Maximum Flux (Jy)
4.8	0.64	0.57	0.75
8.0	0.51	0.15	0.99
14.5	0.48	0.33	0.90
36.8	0.40	0.05	0.80

Table 4.5 Flux densities from Mrk 421 at 4.8 GHz, 8 GHz and 14.5 GHz from UMRAO, and at 36.8 GHz from Metsähovi Radio Observatory.

The parabolic antennas of the UMRAO and Metsähovi radio telescopes have diameters of 26 and 13.7 metres respectively. To obtain a greater resolution, in order to study in detail the radio morphology of Mrk 421, much larger antenna-diameters are needed. As explained in Section 3.2, remarkable resolutions can also be accomplished using the technique of radio interferometry. In this work, analysis of radio maps (two-dimensional intensity graphs) of Mrk 421 from the Very Long Baseline Array (VLBA) has been also performed. The resolution of the measurements is ~0.1 mas.

4.2.1 Measurement of Morphological Features

Several observational and theoretical clues suggest that jets in extragalactic sources may be structured, with a fast core (*spine*) surrounded by a slower *layer*. The existence of such a velocity structure has a strong impact on the observed emission properties of jets. The spine-layer scenario can be used to interpret the observed TeV emission from M87 (see Figure 4.19) and the rapid variability (down to a few minutes) observed in some TeV Blazars (Tavecchio & Ghisellini 2008). M87 was the

first non-BL Lac galaxy to be detected at TeV energies (Aharonian et al. 2003; Beilicke et al. 2007; Acciari et al. 2008).

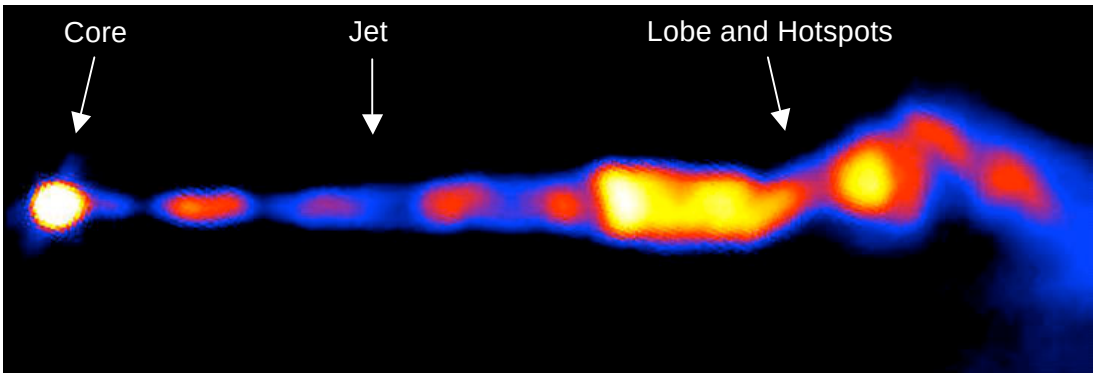

Figure 4.19 Radio map of M87 produced by the Very Large Array (Biretta et al. 1999).

Figure 4.20 shows a sequence of Very Long Baseline Array (VLBA) images and polarization measurements of the blazar BL Lacertae. The data reveal a bright feature in the jet (knot) that causes a double flare radiation from optical frequencies to TeV γ-ray energies, as well as a delayed outburst at radio wavelengths (Marscher et al. 2008). For other sources (including Mrk 421), no clear connection between radio jet components and γ-ray flares has been found (Piner & Edwards 2004).

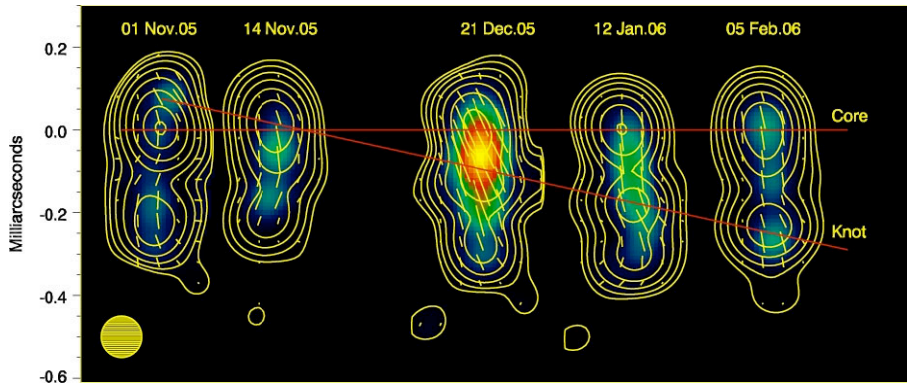

Figure 4.20 High-resolution radio images of BL Lac at 43 GHz (Marscher et al. 2008).

Radio maps of Mrk 421 show a morphological structure a few parsecs in extent, with a compact nucleus and jet-like feature. Figure 4.21 shows an image of Mrk 421 from the VLBA. The source is a core-dominated (the contribution of the

core to the total flux density is ~85%) and the extended structure occurs on only one side of the nucleus (one-sided jet); one of the reasons for this could be that the double structure is oriented very close to the line of sight, so that the structures on either side of the nucleus appear to be merged together.

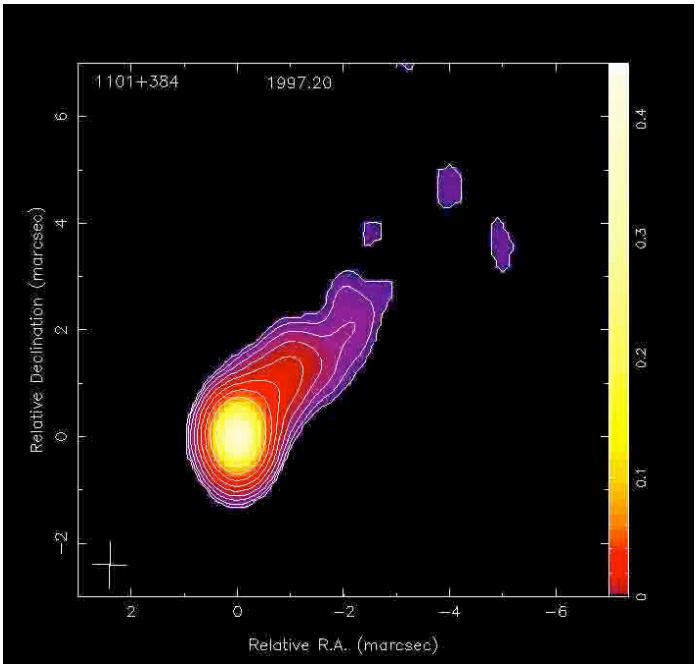

Figure 4.21 The VLBA radio map of Mrk 421 at 15 GHz. The contours show lines of constant radio power. The distance to the source is 127.2 Mpc (Crook et al. 2007) and the angular scaling conversion of this image is ~0.61 pc mas^{-1}.

The four high-dynamic-range observations of Mrk 421 at 22 GHz shown in Figure 4.22 were taken throughout the year following the source's unprecedented high γ-ray state in early 2001. No new components associated with the 2001 flare were seen in the total intensity images.

A measure of "jet length" can be obtained on the basis of the distance from the bright core to an outer contour. In this work, core-contour distance measurements have been performed along a fixed direction for a set of radio images of Mrk 421, taken at 1-month intervals between 1995 and 2001. The results of these measurements will be shown in Section 5.2.

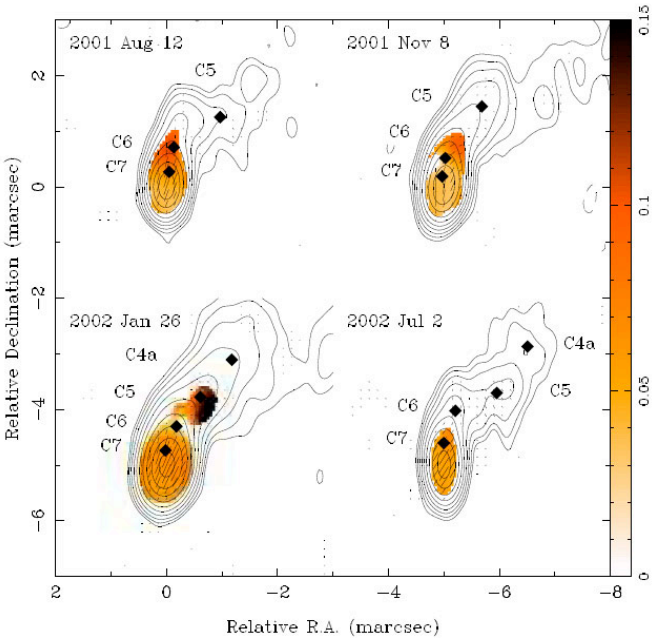

Figure 4.22 VLBA images of Mrk 421 at 22 GHz (Piner & Edwards 2005). Contours show the total intensity; the lowest contours are set to three times the rms noise, and each successive contour is a factor of two higher. Colours show the fractional polarization (scale at right). Locations of circular Gaussian components from model fitting are marked by diamonds. The linear scale is 0.59 pc mas^{-1}.

Chapter 5

Long-term Multiwavelength Observations of Markarian 421

This chapter provides a detailed study of the multiwavelength properties of Markarian 421 (Mrk 421) over an extended period of time. The behaviour of the γ-ray light curves between 1995 and 2009 will be presented in Section 5.1.1. Three episodes of dramatic flaring activity observed during this period will be described in Section 5.1.2.

Good-quality X-ray and Whipple 10m γ-ray data exist for those 14 years, while the data from the Milagro Observatory overlap for approximately half the time and radio data are available for various intervals within the 14-year period. After the launch of the *Fermi* satellite in 2008, an intensive monitoring campaign on Mrk 421 was carried out in 2009 using the Large Area Telescope (LAT); the *Fermi*-LAT observations will be discussed in Section 5.3.3 in relation to the TeV γ-ray behaviour. Table 5.1 summarizes the observations carried out during the 14-year period covered in this thesis.

Instrument	Energy Range (eV)	Period
UMRAO	(1.8-2.2 / 3.0-3.6 / 5.2-6.8) x 10^{-5}	2005 – 2008
VLBA	~6 x 10^{-5}	1995 – 2001
Metsähovi	(1.5 – 1.6) x 10^{-4}	2002 – 2008
RXTE ASM	(2 – 10) x 10^{3}	1995 – 2009
Fermi-LAT	(0.01 – 100) x 10^{9}	2009
Milagro	~12 x 10^{12}	2000 – 2007
Whipple 10m	(0.4 – 10) x 10^{12}	1995 – 2009

Table 5.1 Details of the observations presented in this thesis.

Variability studies of these multiwavelength data are covered in this chapter and in Chapter 6, where different methods will be applied to investigate the level of flux variation at different time scales.

5.1 TeV γ-ray Observations, 1995 – 2009

In this section the γ-ray data for Mrk 421, taken at the Whipple 10m telescope between December 1995 and May 2009, will be presented. These data comprise a total exposure time of 878.4 hours.

The Dublin analysis package described in Section 4.1.2 was used to reduce and analyze the raw data from observations taken between 2000 and 2009. Observations taken with earlier configurations of the Whipple 10m camera were analyzed using the Quicklook package.

The Pattern Selection Trigger (PST) was installed at the Whipple 10m telescope in 1998 (see Section 3.1.3) but was disconnected from the data acquisition system in 2008 due to problems with the stability of event rates. Therefore, data from the 1995–1996, 1996–1997 and 2008–2009 observing seasons were taken without this "second-level" trigger. The consequence of operating without this trigger is that more noise events will probably be recorded. Although these additional noise events are readily excluded by the selection cuts applied during data analysis, they do have the effect of increasing both the deadtime of the system and the amount of raw data recorded. The increase in deadtime was partly offset by increasing the multiplicity trigger requirement from three PMTs to four PMTs, while the increase in the amount of data recorded was not important because additional storage capacity had already been installed.

In order to analyze all the Mrk 421 data in a uniform manner, the Crab Nebula flux for each observing season has been used for calibration (Section 4.1.4). Observations of Mrk 421 taken in the ON or TRACKING mode were selected and tracking ratios were used to analyze the data. If a sufficient number of Mrk 421 darkfield runs (OFF-source observations) were available, these were used to calculate the tracking ratio for each season (Section 4.1.3), otherwise they have been combined with darkfield runs from different sources.

Since γ-ray observations can only be taken with the Whipple 10m telescope on moonless nights, there are about six nights around the time of full moon each month when no observations can be made. The periods (~21 days each) during which the γ-ray data are taken are referred to as *darkruns*. Typically, each observing season

for Mrk 421 (from November/December to May/June, when Mrk 421 is observable) spans from 6 to 8 darkruns.

5.1.1 Mean Nightly, Monthly and Annual Rates

The γ-ray rate, *r*, for any given exposure time, *t*, is determined as

$$r = \frac{N_\gamma}{t} \tag{5.1}$$

where N_γ is the number of γ-ray events recorded in time *t*. The exposure time is typically given in minutes and the rate in events per minute. For normalisation purposes, the rate in events per minute is converted to "Crab units" by dividing by the Crab Nebula γ-ray rate (in events per minute) for the relevant observing season (see Section 4.1.4).

If we have *n* independent measurements of the rate, r_i, each with associated error σ_i, the best combined measurement is the *weighted mean* ($\bar{r}$), given by

$$\bar{r} = \frac{\sum_{i=1}^{n} w_i r_i}{\sum_{i=1}^{n} w_i} \tag{5.2}$$

where the weights w_i are the reciprocals of the sample variances, $w_i = 1/\sigma_i^2$. The best estimate of the error on $\bar{r}$ is

$$\sigma_{\bar{r}} = \frac{1}{\sqrt{\sum_{i=1}^{n} 1/\sigma_i^2}} \tag{5.3}$$

The *statistical significance* of a single measurement is given by $S_i = r_i/\sigma_i$. If the variances are the same for all measurements, the significance of the mean rate is given by

$$S_{\bar{r}} = \frac{\sum_{i=1}^{n} S_i}{\sqrt{n}} \tag{5.4}$$

In this case, the error of the mean rate, $\sigma_{\bar{r}}$, can be calculated from $S_{\bar{r}} = \bar{r}/\sigma_{\bar{r}}$.

As an example, consider the γ-ray light curve for Mrk 421 during the season 2005–2006, shown in Figure 5.1 (top). Each point represents the mean γ-ray rate calculated for one night, corresponding in some cases to a single 28-minute run and in others to multiple runs, up to a total duration of 4 hours. Only data taken in good weather conditions and at high elevation angles (≥55°) were used.

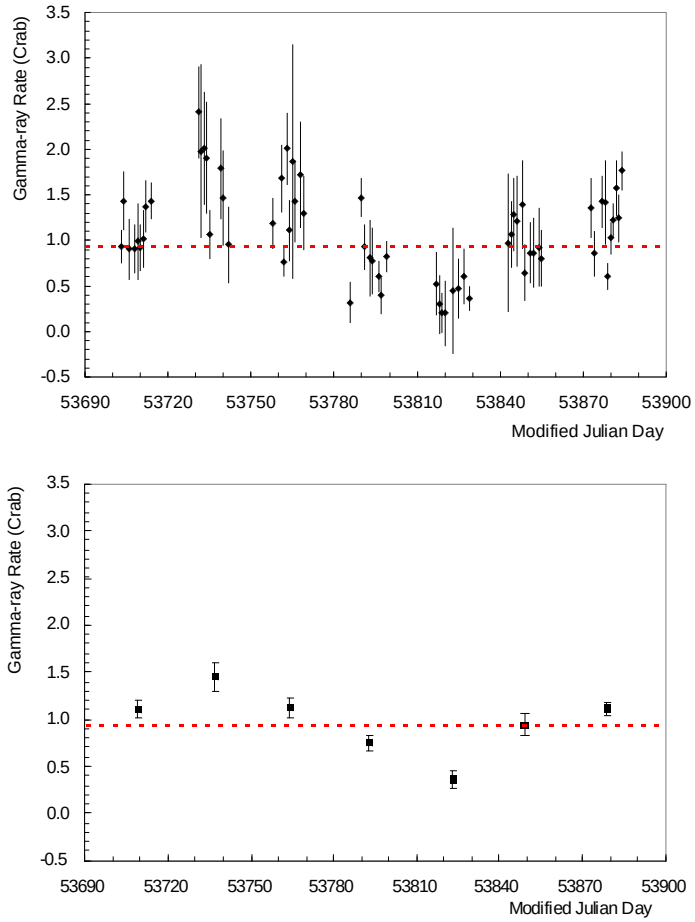

Figure 5.1 Markarian 421 γ-ray light curves for the 2005–2006 observing season. *Top*: daily γ-ray rate; *Bottom*: monthly γ-ray rate. The dashed horizontal red lines represent the mean γ-ray rate for that season.

Runs with duration less than 25 minutes (because of hardware faults or other technical problems) were excluded from the dataset to minimise systematic errors by ensuring that the mean rate for the night was always calculated using runs with similar duration (~28 minutes). The γ-ray rates plotted in Figure 5.1 have been normalised by dividing the Mrk 421 rate in γ-ray events per minute by the Crab Nebula rate for the 2005–2006 season, namely, (3.01 ± 0.12) min^{-1}. The entire set of 75.1 hours of on-source data (i.e., TRACKING runs or ON runs analysed as TRACKING data) for the 2005–2006 season gave a detection at a significance level of 26.3σ with an average rate of 2.83 ± 0.11 γ/min (~94% of the Crab Nebula rate for that observing season). For each month (darkrun) of the 2005–2006 observing season, the mean γ-ray rate and its associated error were calculated using Equations 5.2 and 5.3, respectively; the results are shown in Figure 5.1 (bottom).

Variability is evident at significant levels in the light curves shown in Figure 5.1. A χ^2 test (as described in Section 4.1.4) was performed to compute the chance probability, $P_{\chi 2}$, that the variation in γ-ray rate is due to random fluctuations about the average rate for the season. For the daily binned data plotted in the top panel of Figure 5.1, the χ^2 value is 154.5 for 61 degrees of freedom (dof), corresponding to a chance probability of 4.6×10^{-13}, confirming that the γ-ray rate is highly variable on a timescale of one day.

As a further example, Figure 5.2 shows the daily and monthly γ-ray rates during the 2007–2008 season, to illustrate how the behaviour changes between observing seasons. The Crab Nebula rate for this season was 2.79 ± 0.17 γ/min. Once again, the light curve shows extreme variability: a χ^2 test applied to the daily γ-ray rates shown in the top panel of Figure 5.2 yields $\chi^2/\text{dof} = 2228/85$, giving a probability $P_{\chi 2} < 10^{-300}$ that the daily rate is constant. Note that a pronounced TeV γ-ray flare was observed in May 2008. A description of that event and the finer structure of the light curve will be given in the next section.

In addition to the day-scale and month-scale variability evident in Figures 5.1 and 5.2, the γ-ray rate is highly variable from year to year. For example, the mean γ-ray rate for Mrk 421 for the entire 2005–2006 season is 0.94 ± 0.05 Crab, while for the 2007–2008 season the mean rate is 1.43 ± 0.09 Crab (the errors here include the effect of the errors on the Crab Nebula rate for each season) The difference between

these rates is 0.49 ± 0.10 Crab, representing almost five standard deviations: the probability that the rates are actually the same is ~5×10^{-7}. A more complete quantitative analysis of the variability exhibited by Mrk 421 during the entire 1995 – 2009 period will be presented in Section 6.1

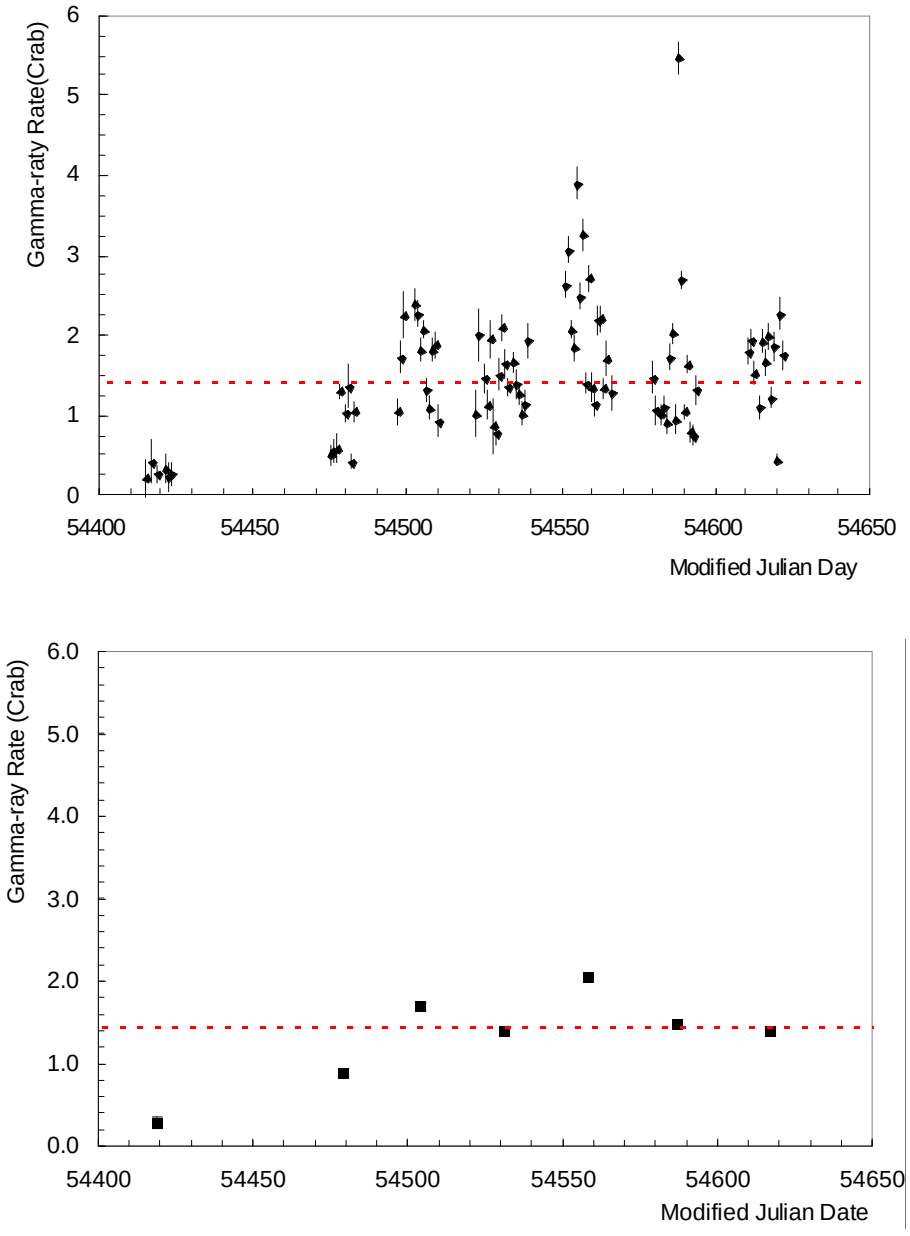

Figure 5.2 The light curve of Mrk 421 for the 2007–2008 observing season. *Top*: daily γ-ray rate; *Bottom*: monthly γ-ray rate (the error bars are smaller than the size of the data points). The dashed red lines represent the mean annual rate.

Figure 5.3 shows the γ-ray rate averaged over each darkrun (monthly) for five years of data, from December 1995 to May 2000 (Quicklook analysis), while the corresponding rates for the nine years of data from December 2000 to May 2009 (Dublin analysis) are shown in Figure 5.4.

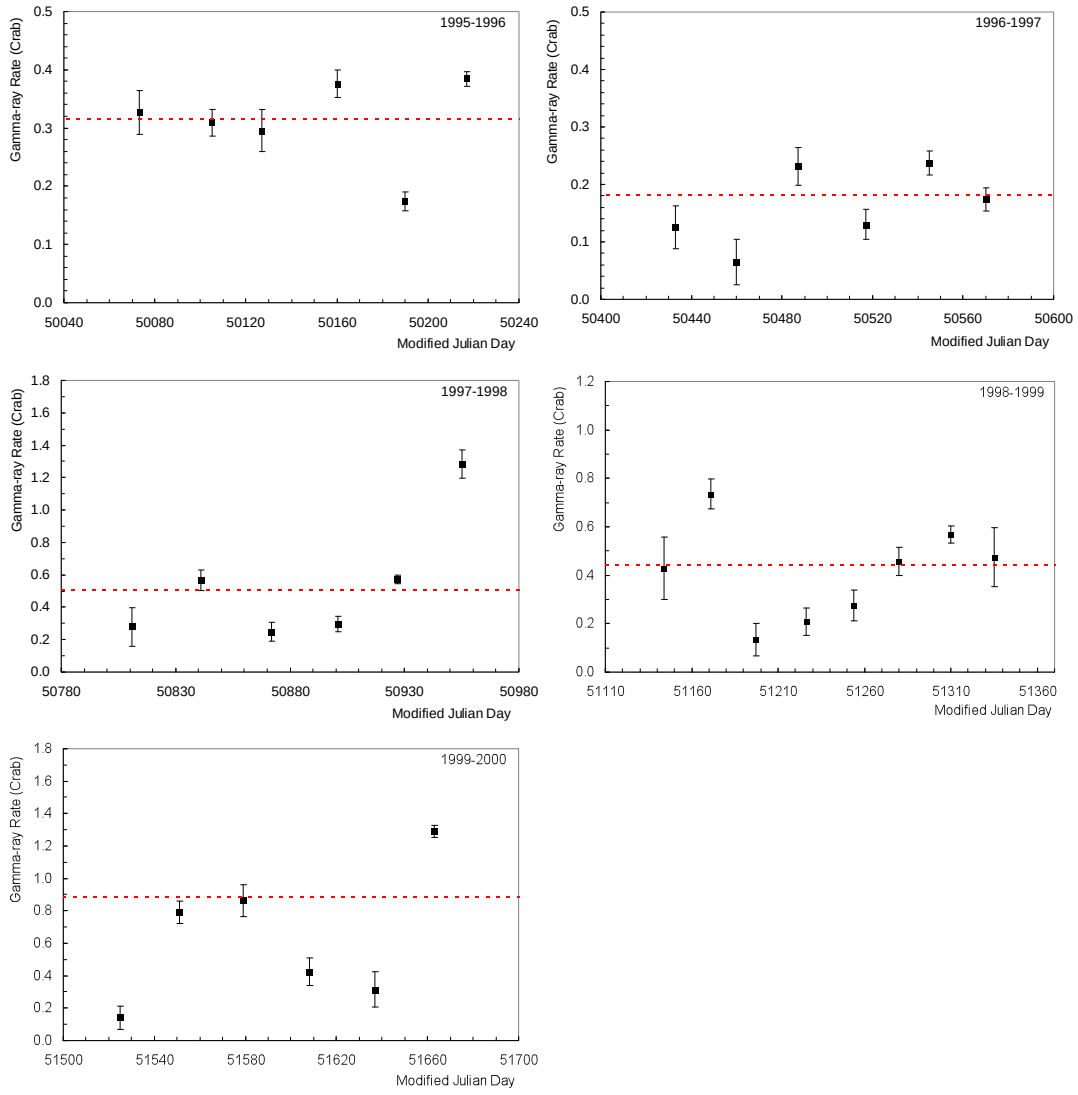

Figure 5.3 Mean monthly γ-ray rate for Mrk 421 between 1995 and 2000 (Quicklook analysis). Each dashed line represents the weighted mean (Equation 5.2) for the season.

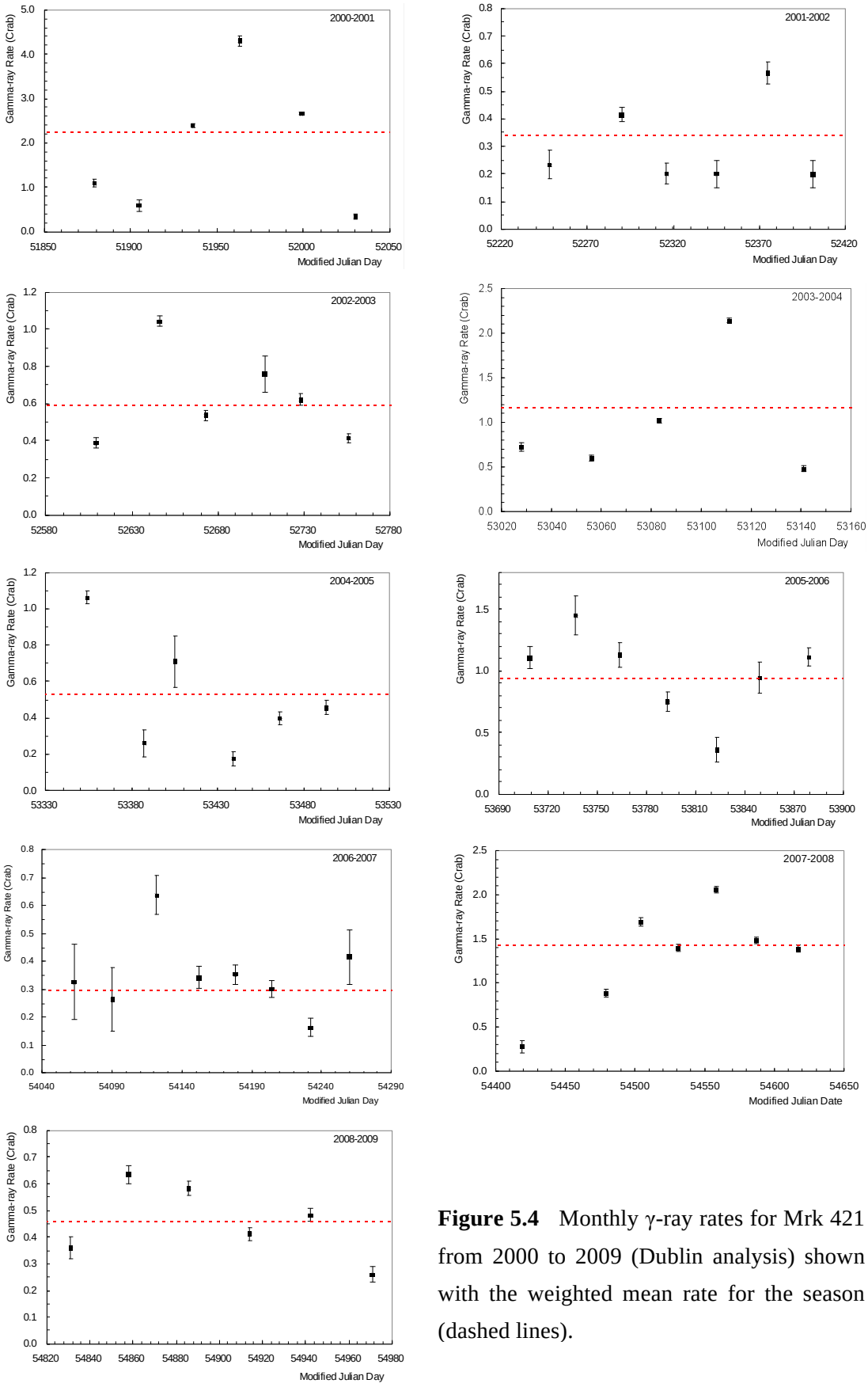

Figure 5.4 Monthly γ-ray rates for Mrk 421 from 2000 to 2009 (Dublin analysis) shown with the weighted mean rate for the season (dashed lines).

The mean γ-ray rate was calculated for each observing season and the results are given in Table 5.2. The table includes the on-source exposure time and statistical significance for each season, as well as the χ^2 values and corresponding chance probability P_{χ^2} that the monthly averaged rate is constant within each season. The annual mean rates for Mrk 421 are plotted in Figure 5.5. For the hypothesis that the annual rate is a constant, equal to the overall mean rate for the complete 14-year dataset, the χ^2 value is 2669 for 13 dof, corresponding to a chance probability $P_{\chi^2} < 10^{-300}$.

Season	Exposure (h)	Significance	Mean γ-ray rate (Crab units)	χ^2 / dof	P_{χ^2}
1995-1996	51.8	36 σ	0.32 ± 0.02	110 / 5	3.2×10^{-22}
1996-1997	53.2	15 σ	0.18 ± 0.02	25 / 5	1.7×10^{-4}
1997-1998	52.1	24 σ	0.51 ± 0.04	133 / 5	4.3×10^{-27}
1998-1999	45.2	19 σ	0.44 ± 0.03	80 / 7	1.7×10^{-15}
1999-2000	38.7	26 σ	0.89 ± 0.05	284 / 5	2.3×10^{-59}
2000-2001	78.1	88 σ	2.25 ± 0.31	1880 / 5	$<10^{-300}$
2001-2002	32.9	20 σ	0.34 ± 0.02	74 / 5	1.8×10^{-14}
2002-2003	45.0	46 σ	0.59 ± 0.03	365 / 5	8.3×10^{-77}
2003-2004	51.8	78 σ	1.16 ± 0.06	2418 / 4	$<10^{-300}$
2004-2005	23.0	27 σ	0.53 ± 0.03	351 / 5	1.3×10^{-73}
2005-2006	75.1	26 σ	0.94 ± 0.05	66 / 6	2.8×10^{-12}
2006-2007	52.0	18 σ	0.30 ± 0.02	47 / 7	6.0×10^{-8}
2007-2008	148.9	84 σ	1.43 ± 0.09	698 / 6	1.9×10^{-147}
2008-2009	130.6	39 σ	0.46 ± 0.02	99 / 5	6.9×10^{-20}

Table 5.2 Summary of Whipple 10m telescope observations of Mrk 421 between December 1995 and May 2009. Note that the error quoted for the rate includes the effect of the error on the Crab Nebula rate for each season. P_{χ^2} represents the probability that the monthly γ-ray rate is constant and equal to the mean annual rate.

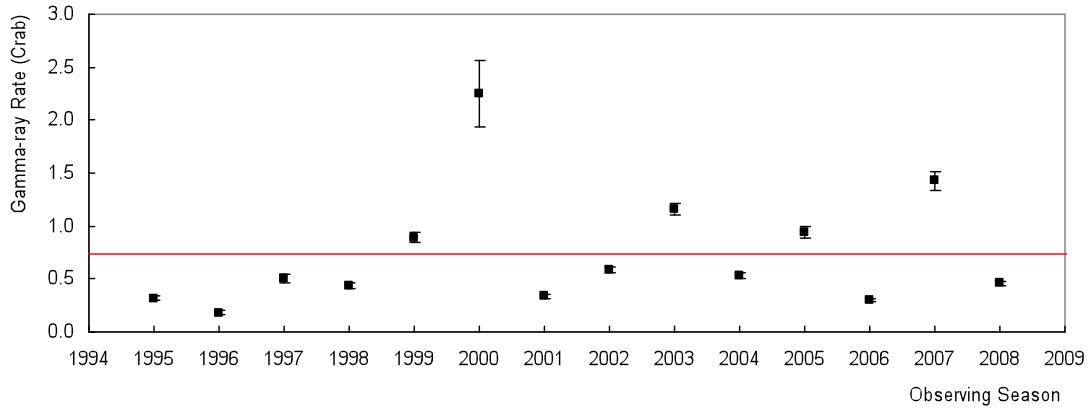

Figure 5.5 The γ-ray light curve for Mrk 421 from 1995 to 2009, showing the mean rate for each observing season. The horizontal red line represents the mean γ-ray rate (0.74 ± 0.01 Crab) for the entire 14-year dataset.

For observing seasons from 1995–1996 to 2004–2005, there exists a potential for bias in the γ-ray rates, because the observers were more likely to continue observing the source if the first run of the night appeared to show a high rate and significance. As a result, there may be a bias in favour of higher rates. From 2005–2006 onwards, this bias is certainly not present, because the source was observed for as long as possible each night, irrespective of the measured rate and significance. To investigate the effect of such a bias, the γ-ray data have also been analysed using only the first run of each night. Three representative seasons (2000–2001, 2003–2004 and 2006–2007) were chosen in order to represent different annual γ-ray rate levels (high, medium and low). Figure 5.6 shows the light curves obtained using the two datasets per each season. For the 2006–2007 season, the two light curves are in good agreement, confirming the absence of bias in the observations for this season. For the 2000–2001 season, the light curve based on all the data appears to be higher and more variable than that based on only the first run for each night; however, for the 2003–2004 season, the trend is opposite. This suggests that there is no significant bias in the earlier datasets, and therefore the subsequent variability analyses have been carried out using all the available data for every observing season.

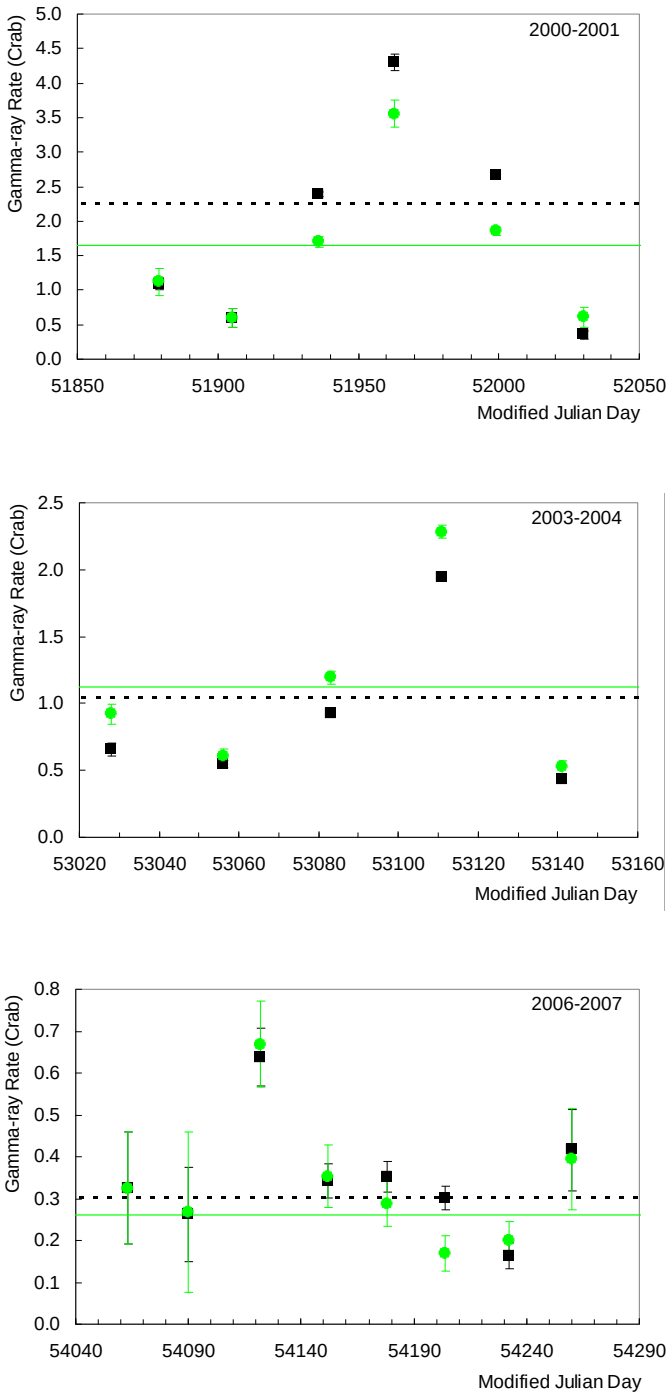

Figure 5.6 The γ-ray light curves for Mrk 421 (monthly binned data). The black squares are based on all the available data, while the green circles use only the first run of each night. The corresponding mean rate for each season is indicated by the dashed black lines and the solid green lines, respectively.

5.1.2 Flaring Activity

Blazar flares are thought to be related to internal shocks in the blazar jet (Spada et al. 2001), or to the ejection of relativistic plasma into the jet (Mastichiadis & Kirk 1997). More recently, it has been suggested that the flares could also be associated with magnetic reconnection events in a magnetically dominated jet (Lyutikov 2003) and thus they could be similar to solar flares in this regard. The flares have been observed over a wide range of timescales, from months down to less than an hour. Mrk 421 has been known to demonstrate rapid, sub-hour flaring behaviour at keV and TeV energies during the course of an outburst (Cui 2004; Gaidos et al. 1996) indicating very compact emission regions (see Equation 6.1).

Observations of blazars have revealed that, at least during flares, they emit most of their power in the γ-ray band. For HBLs, it has been found that the peak of the synchrotron emissions shifts to higher energies when the source gets brighter. This was illustrated in Figure 1.6 (in Section 1.4) where the spectral energy distribution (SED) of four blazars, derived during flaring and non-flaring periods, was shown.

Many periods of intense variability in the VHE band have been observed for Mrk 421. Historically, it has exhibited three major flaring episodes: in 1996 and 2008, bright TeV γ-ray flares were detected with fluxes reaching a level of 10 Crab, with doubling and decay times of a few minutes; in 2001, Mrk 421 went through a prolonged high-state period during which the flux reached its highest level known so far (~13 Crab), becoming the most intense source of TeV γ-rays observed up to that point.

Figure 5.7 shows the light curve of Mrk 421 during the 1995–1996 season, when the source was relatively quiet apart from two remarkable outbursts of TeV γ-rays detected in May 1996 (Gaidos et al. 1996). The first of these occurred on May 7, when over the course of two and a half hours of observations the flux increased by a factor of five and reached a maximum rate of ~10 Crab (30 times the average flux for that season). A second flare of lower intensity, unusual for its very short duration, occurred on May 15, when a rise and fall within ~30 minutes was observed, with peak TeV flux ~14 times the average for the season (McEnery et al. 1997).

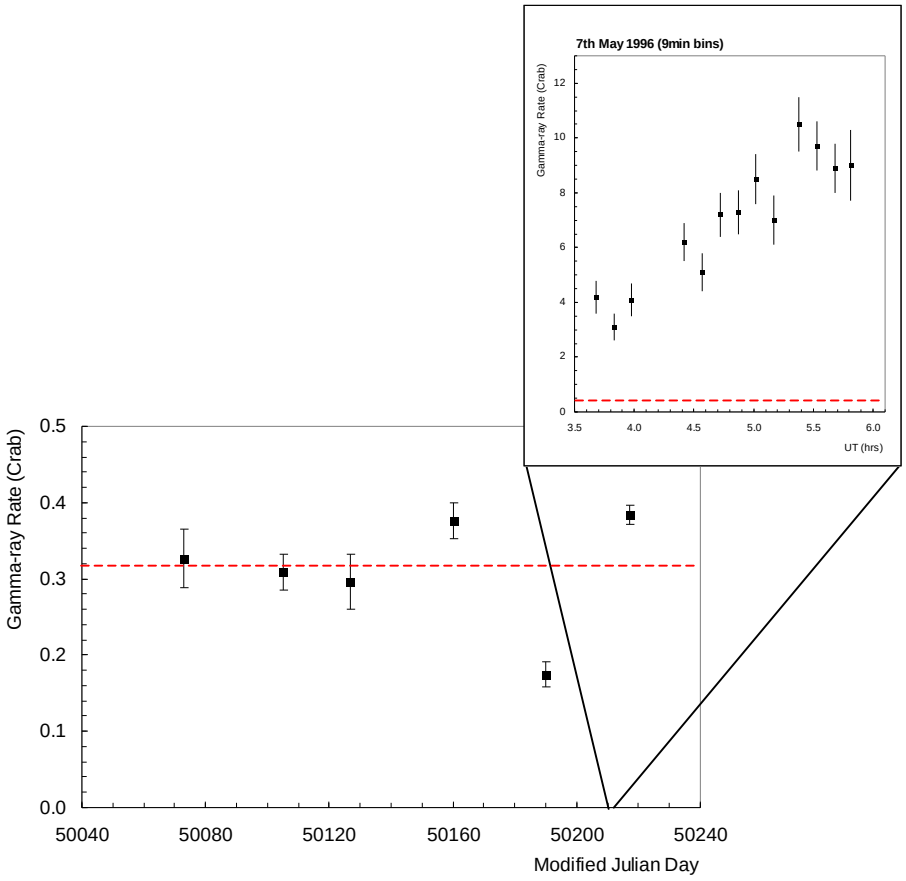

Figure 5.7 Mrk 421 in 1995–1996. The mean γ-ray rate for the season was 0.32 ± 0.01 Crab, with a significance of 36σ for a total exposure of 33 hours. The top panel shows the temporal history of the flare event of 1996 May 7 (plotted in 9-minute intervals). The red dashed line shows the annual mean rate.

Mrk 421 became much more active in 2001, with an exceptional bright long-term γ-ray flaring state lasting from January to May 2001 (see Figure 5.8 left panel). In particular, a high TeV flux state in February/March 2001 gave a detection significance of 37.4σ for a 3.2 hour exposure. The source reached a maximum peak flux of ~13 Crab on February 27.

In previous work, the energy spectrum of Mrk 421 in the 0.5−6 TeV was measured with the Whipple 10m telescope on timescales of a month over a large range of flux states. Since curvature is expected in the Mrk 421 spectrum above 1 TeV based on previous measurements, a power law with exponential-cutoff model

(PLC) was fitted to the energy spectrum (Krennrich et al. 2002; Aharonian et al. 2005b). The PLC model follows the form:

$$\frac{dN}{dE} = F_0 \cdot \left(\frac{E}{1\,TeV}\right)^{-\alpha} \cdot \exp\left(-\frac{E}{E_c}\right) \tag{5.5}$$

The position of the cut-off energy E_c is highly correlated with the photon index α. For the monthly energy spectra, the PLC model with fixed cut-off energy $E_c = 3.5$ TeV was chosen to test for spectral variability. The right panel in Figure 5.8 shows the TeV γ-ray energy spectrum of Mrk 421 on monthly timescales from November 2000 to April 2001. The spectrum hardened from a PLC photon index $\alpha = 2.54 \pm 0.19$ at the onset of the large flare to $\alpha = 2.00 \pm 0.06$ at the peak flux state in late February 2001. The spectrum then softened during the decay of the flare event, as shown in the left panel of the monthly-binned light curve of Figure 5.8. This month-scale flare provides evidence for a shift in the spectral energy distribution to higher energies in the GeV–TeV band during the peak of the flaring episode. For shorter flaring events, however, there is no clear correlation between the TeV γ-ray rate and the spectral shape (Grube 2007).

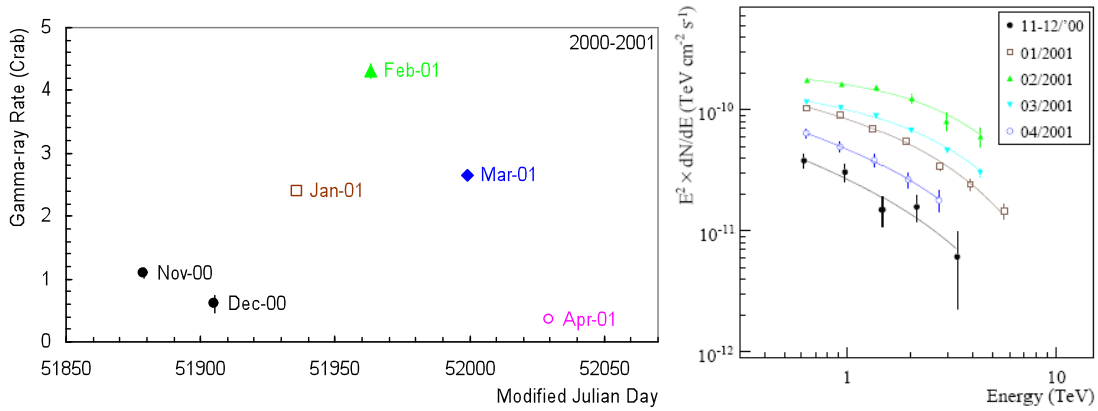

Figure 5.8 The left panel shows the monthly-binned γ-ray light curve of Mrk 421 and the right panel shows the TeV energy spectrum (taken from Grube 2007) from Whipple 10m observations during the 2000–2001 season.

The Mrk 421 monitoring program at the Whipple 10m telescope found the source in a strong flaring state on 2008 May 2 (see Figure 5.2, top panel); VERITAS observations were triggered and confirmed the high γ-ray activity, which was

announced via *The Astronomer's Telegram* (VERITAS *ATel#1506*). Analysis of the measurements shows a peak TeV luminosity approaching 10 times that of the Crab Nebula (see Figure 5.9). The Crab Nebula flux for that year was 2.79 ± 0.17 γ/min.

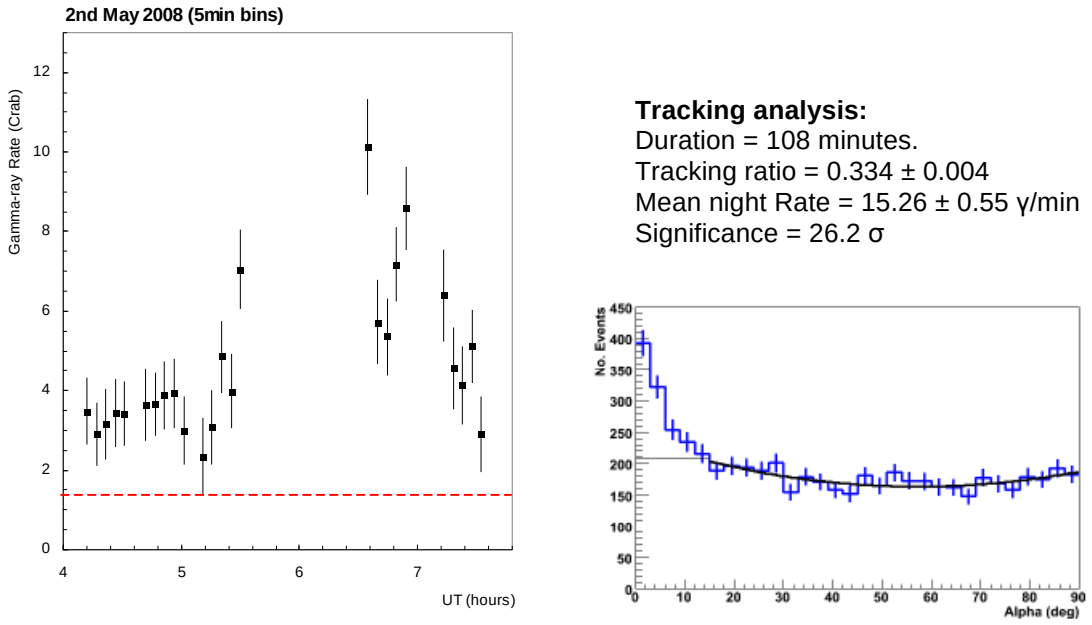

Figure 5.9 Whipple 10m γ-ray light curve and alpha plot for Mrk 421 on 2008 May 2. The dashed red line shows the mean rate for the 2007–2008 season. The gap in the plot arises from two factors: firstly, the data run immediately before the gap was taken in ON/OFF mode, and secondly, the telescope had already been slewed to observe another target before the analysis of the Mrk 421 run showed that a major flare was taking place.

On the following night, May 3, Whipple and VERITAS again observed Mrk 421. Figure 5.10 shows the light curves obtained on that night with the two systems, binned in two-minute intervals. Figure 5.11 shows a plot of the Whipple γ-ray rate against the VERITAS γ-ray rate (both expressed in Crab units), where the data have been re-binned to various intervals between four minutes and twelve minutes. This re-binning was carried out in order to reduce the statistical errors on the rates (particularly for the Whipple measurements) without smoothing out the rate variations to an unacceptable extent, and the placement of the bins was chosen to align the average times of the bins as closely as possible between the two systems.

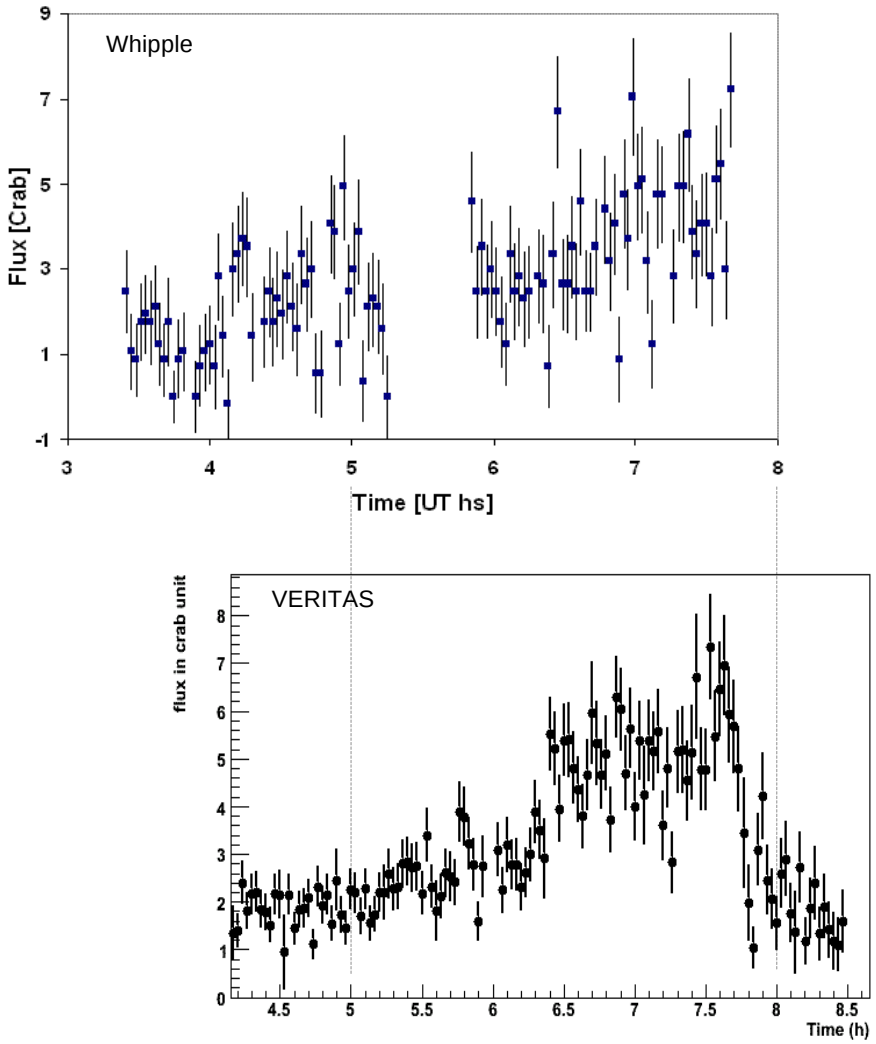

Figure 5.10 Mrk 421 γ-ray rate on 2008 May 3 from Whipple and VERITAS observations (top and bottom panels, respectively). Both light curves are binned in 2-minute intervals. The gap in the Whipple data is due to an OFF run inserted in the observing schedule to help with spectral reconstruction.

The solid red line (slope = 1) in Figure 5.11 is what would be expected if the rates recorded by both systems were identical, while the dashed red line is the weighted least-squares regression line. The rates recorded by the two systems are seen to be fairly well correlated, as indicated by the R^2 value of 0.60. However, there is a tendency for the Whipple rate to fall below the VERITAS rate at the higher fluxes. This can be attributed to a number of factors, chief among them the fact that the last hour and a half of Whipple observations (when the rates were highest) were taken at elevations angles less than 55°. For these low elevations, the Whipple γ-ray selection

cuts are not optimised and the Whipple Crab Nebula γ-ray rate for the 2007–2008 observing season is not well characterised at low elevation (only ~70 minutes of Crab observations were carried out at elevations below 55° during that season). In addition, the broader energy range of VERITAS, taken together with the known hardening of the Mrk 421 spectrum at higher fluxes (Krennrich et al. 2002), will affect the comparison of the γ-ray rates between the Whipple 10m telescope and VERITAS.

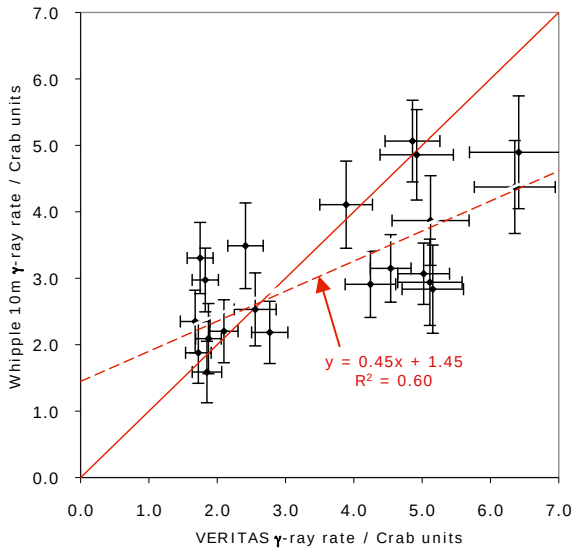

Figure 5.11 Whipple 10m γ-ray rate plotted against VERITAS γ-ray rate during the Mrk 421 flare on 2008 May 3. The data have been binned in various intervals between 4 minutes and 12 minutes to align the observation times and to reduce the statistical uncertainties as much as possible without unacceptable smoothing of the variations in rate. The solid red line with slope = 1 is what would be expected if the rates recorded by both instruments were identical. The dashed red line is the weighted least-squares regression line.

Multiwavelength campaigns on Mrk 421 show that during short flares the X-ray and TeV γ-ray fluxes tend to track one another. However, X-ray flares that are not accompanied by TeV γ-ray flares and vice versa have also been observed (Rebillot et al. 2006; Fossati et al. 2008). X-ray/TeV γ-ray correlations are of great interest, because they can help to constrain the emission models. Attempts to establish convincing evidence for correlation between the γ-ray flux and flux variability at radio to optical wavelengths have so far been unsuccessful

(Błażejowski et al. 2005; Horan et al. 2009). Variability and correlation studies will be dealt with in detail in Chapter 6.

5.2 Radio fluxes and radio maps for Mrk 421

Typically, the variations in AGN are slower at radio frequencies than at the higher frequency bands and hence the data are not taken as frequently. The data for the radio light curves presented here were taken at four different frequencies at two different radio observatories. The fluxes and their associated standard errors are given in jansky (Jy), so they have already been normalized for the bandwidth of their receivers. Generally, Mrk 421 is found to vary on monthly timescales. In addition to the light curves, morphological data from the 2cm VLBA/MOJAVE monitoring program (Kellerman et al. 2004; Lister & Homan 2005) for the period 1995–2001 were used. The radio data and analysis from the participating observatories are described in the following subsections.

Metsähovi Radio Observatory

The 37 GHz observations were made with the 13.7m-diameter Metsähovi radio telescope (shown in Figure 3.2.1) using a 1 GHz-band dual-beam receiver centred at 36.8 GHz. The observations were taken in ON-ON mode, alternating the source and the sky in each feed horn. A typical integration time to obtain one flux density data point is 1200-1400 seconds. The detection limit of the telescope at 37 GHz is ~0.2 Jy under optimal conditions (Nieppola et al. 2007). Data points with a signal-to-noise ratio < 4 are treated as non-detections.

The choice of 37 GHz was based on the availability of suitable detection components for this frequency. Furthermore, the attenuation at 37 GHz (mainly due to the oxygen) remains essentially constant throughout the year. The observations are calibrated against reference source DR21 (a star-forming region in Cygnus), whose flux density at 37 GHz is 17.9 Jy. The flux is calculated using the following equation:

$$S = K_1 K_2 K_3 \frac{U}{U_{cal}} e^{d/\cos(z)} \tag{5.6}$$

where K_1, K_2, K_3 are parameters related to the receiver, antenna and source size; U and U_{cal} are the A/D converter voltage and the calibration voltage respectively; d is the optical depth of the atmosphere (at 37GHz); and z is the zenith angle.

The 37 GHz radio light curve for Mrk 421 in 2005–2006, is shown in Figure 5.12. The mean flux was found to be 0.35 ± 0.02 Jy.

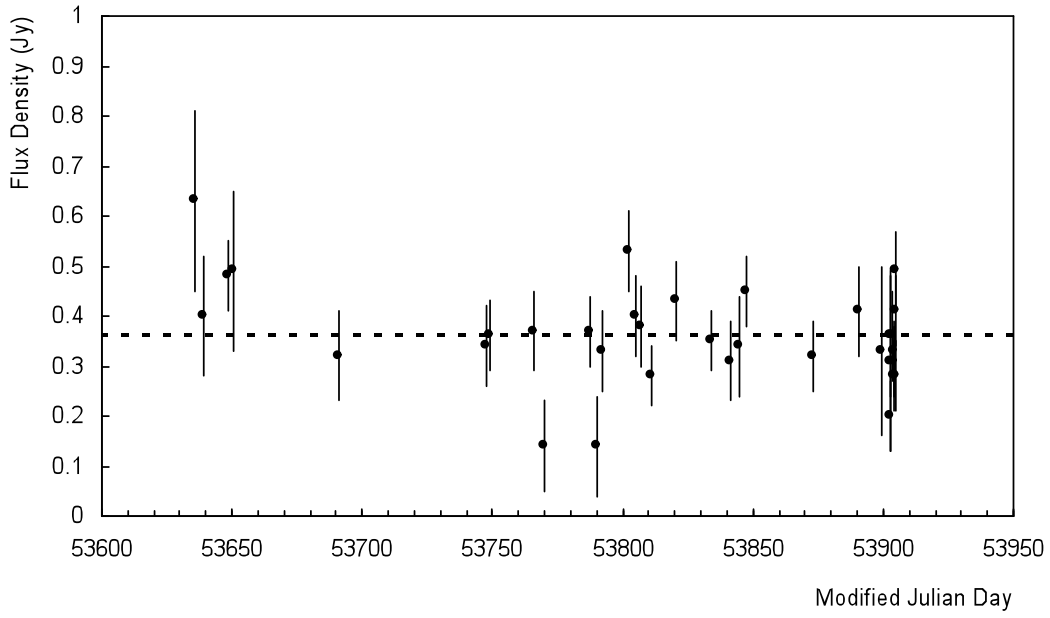

Figure 5.12 Metsähovi radio observations of Mrk 421 (run by run) at 37 GHz, during the season 2005–2006. The dashed line is the mean annual flux and the resulting χ^2 value is 39.2 for 33 degrees of freedom, giving a probability of 21% ($P_{\chi 2} = 0.21$) that the flux is constant.

The mean annual flux was calculated for each season from 2002 to 2008 and the results are plotted in Figure 5.13.

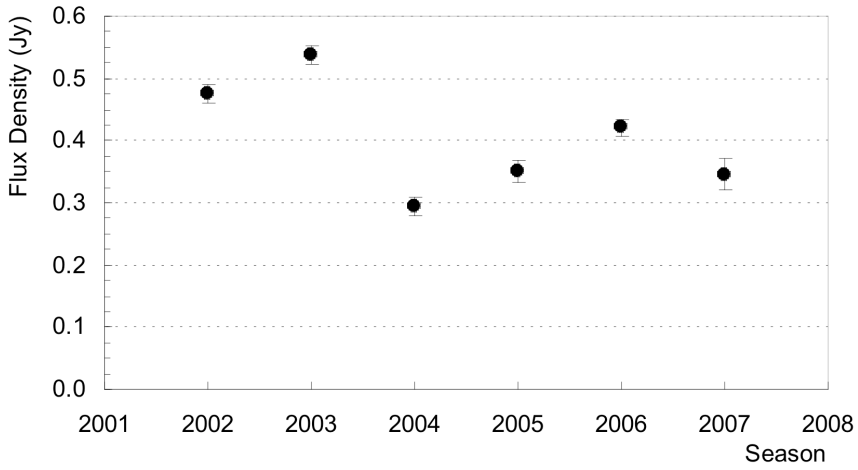

Figure 5.13 Mean annual flux of Mrk 421 at 37 GHz.

University of Michigan Radio Astronomy Observatory

The data at 4.8 GHz, 8.0 GHz and 14.5 GHz came from the University of Michigan Radio Astronomy Observatory (UMRAO) using the 26m-diameter parabolic reflector shown on Figure 3.19 (right picture). Both on-source and background flux measurements were performed. To provide improved sensitivity, the receivers have bandwidths of 500 MHz, 780 MHz and 2000 MHz at the three frequencies, respectively. The flux density scale adopted is based on Cassiopeia A using its measured decay rate at centimetre wavelengths. In order to correct for environmental variations, the calibration source was observed typically once every 1-2 hours. The integration times at UMRAO are typically 30 minutes and measurements are usually taken within ±2.5 hours of meridian passage (Horan et al. 2009). Gain corrections must be applied to the raw data because the aperture efficiency varies with telescope position. The major terms in the position-dependent gain variation have been modelled as

$$G = G_0\left(1 - A\left[1 - \cos(z)\right]\right) \tag{5.7}$$

where G_0 is the gain of the antenna at zenith, z is the zenith distance of the telescope, and A is a parameter that depends on the frequency (Aller et al. 1985). The radio data taken at UMRAO in 2005–2006 are plotted in Figure 5.14 as daily averages of total flux density.

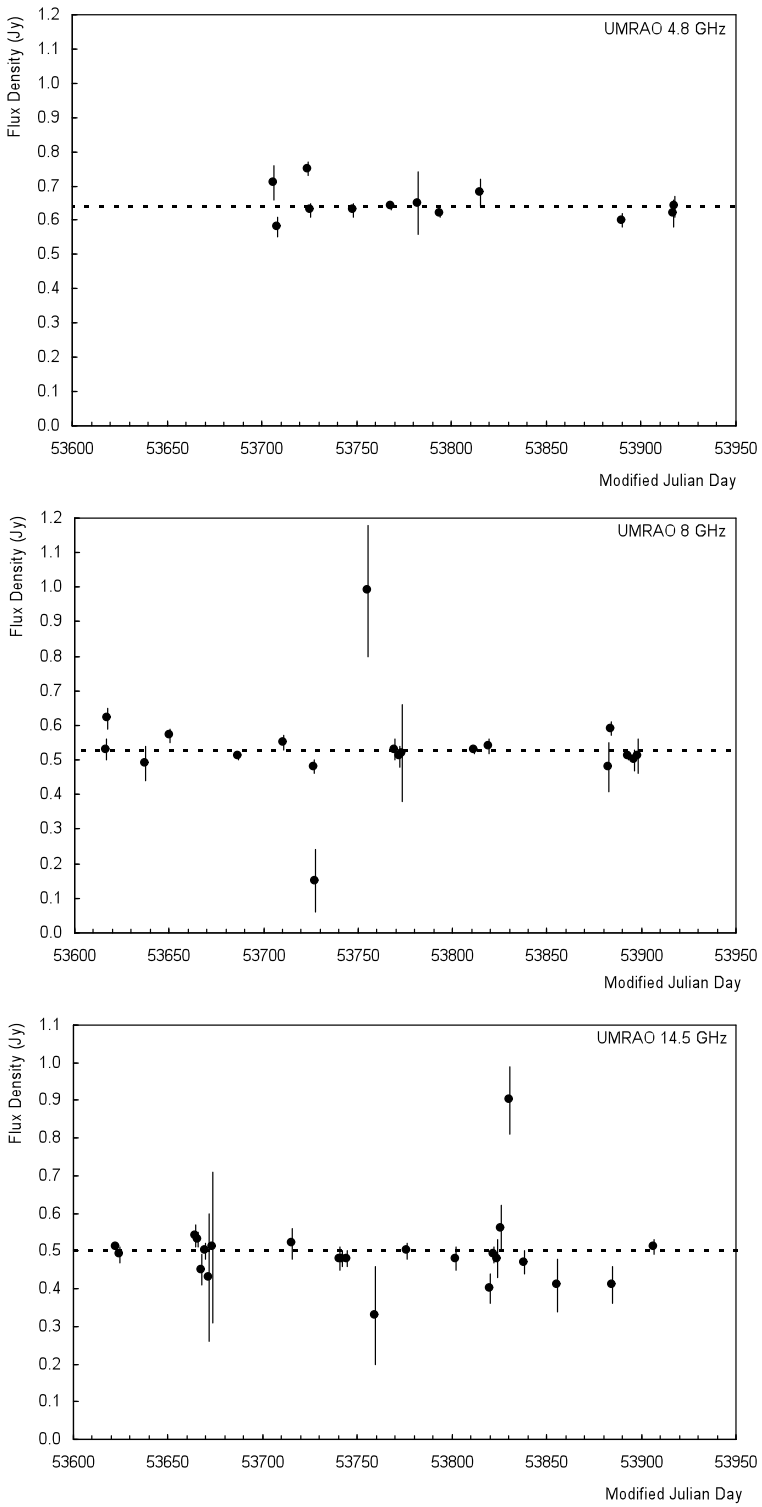

Figure 5.14 UMRAO data for Mrk 421 at 4.8 GHz, 8.0 GHz and 14.5 GHz, 2005–2006 season. Each data point represents all of the data obtained in one night. The horizontal dashed line shows the mean flux during the 2005–2006 season. The χ^2 test was performed for these datasets and the probabilities, $P_{\chi 2}$, for constant rates are shown in Table 6.6.

Three years (2005 – 2008) of UMRAO radio data were available. The annual flux density is shown in Figure 5.15. The average flux is seen to decrease as the frequency increases. A detailed study of the radio variability is described in Section 6.1.

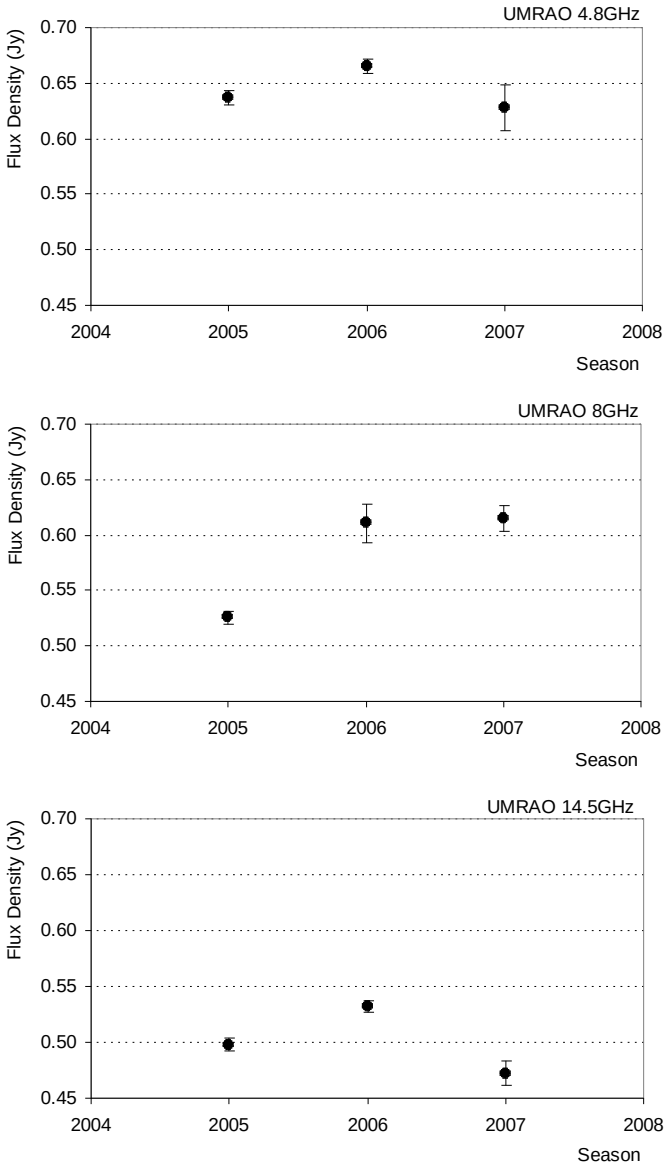

Figure 5.15 The annual flux density of Mrk 421 at 4.8 GHz, 8.0 GHz and 14.5 GHz (top, middle and bottom panels, respectively). The difference in behaviour at 8GHz compared to the other bands during 2007–2008 may be due to the somewhat higher variability of the source at that frequency during that season (see Table 6.6).

VLBA: MOJAVE program

The 15 GHz VLBA image of Mrk 421 for the epoch 05 April 2006 is shown in Figure 5.16. The total flux density (Stokes I) at 15 GHz integrated over this image is 336 mJy. The flux density from the core region modelled using a circular Gaussian is 288 mJy, so Mrk 421 was very core-dominated at this time, implying that the bulk of the radio-band variability is associated with the VLBI-imaged core. The angular size of the core at the half-power level is 0.46 milliarcseconds (mas). The core-size resolution limit was estimated for this dataset (Kovalev et al. 2005) and appeared to be less than the measured core size. The linearly polarized flux density is 6 mJy. This polarized flux is detected from the core region only. VLBI core brightness temperature in the source frame is estimated to be 8×10^{11} K (Horan et al. 2009).

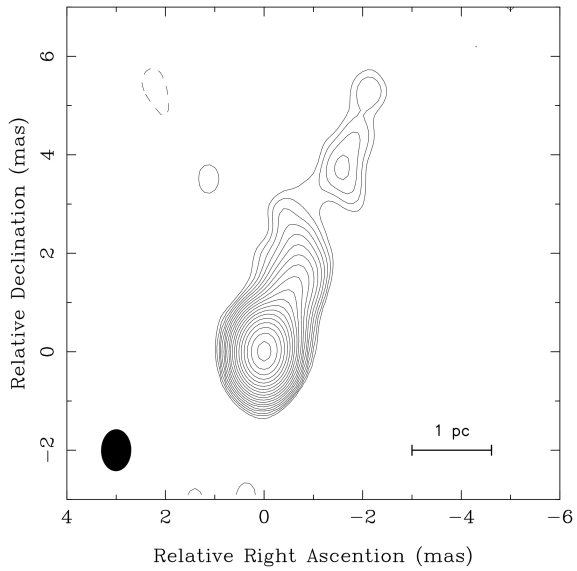

Figure 5.16 VLBA Stokes I 15.3GHz image of Mrk 421 on MJD 53830. Contours are plotted in successive powers of $\sqrt{2}$ times the lowest contour of 0.5 mJy. The peak intensity is 296 mJy beam^{-1}. The synthesized beam is shown as the black ellipse in the lower left corner.

A correlation between the radio and γ-ray fluxes of AGN cannot be claimed. However, since there is evidence that both the radio emission and the γ-ray emission from blazars are strongly beamed and anisotropic, it is interesting to compare the structural evolution of the jet with the γ-ray light curves. Figure 5.17 shows radio images of Mrk 421 during different months in 1995–1996 and the γ-ray light curve during the same season (McEnery et al. 1997). Figure 5.18 shows the corresponding results for Mrk 421 in 1996–1997. The radio images were obtained by extracting

single frames from the MPEG movie files provided by MOJAVE. These images can be used to determine the angular distance from the position of peak flux to a specific contour in a particular direction at a given time.

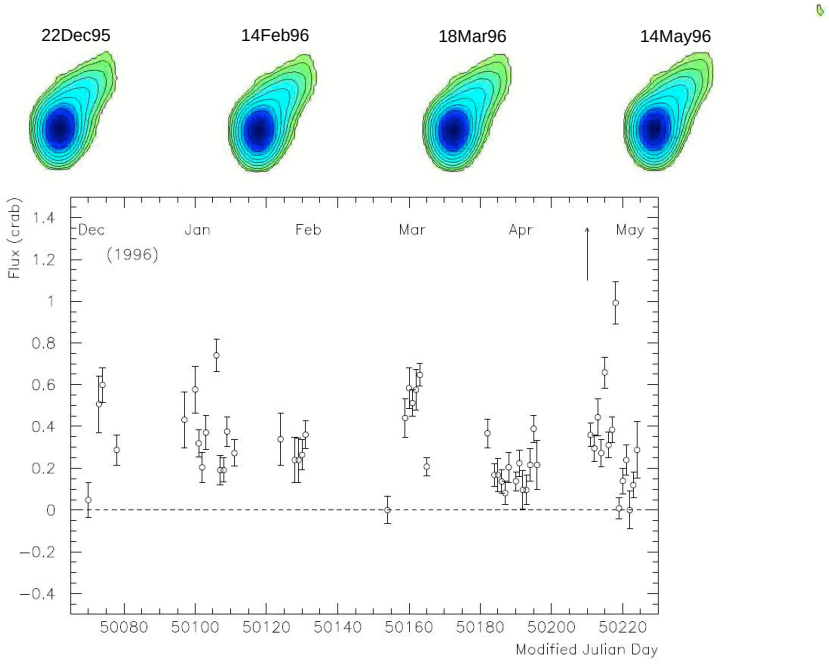

Figure 5.17 15GHz radio maps and γ-ray light curve for Mrk 421 in 1995–1996.

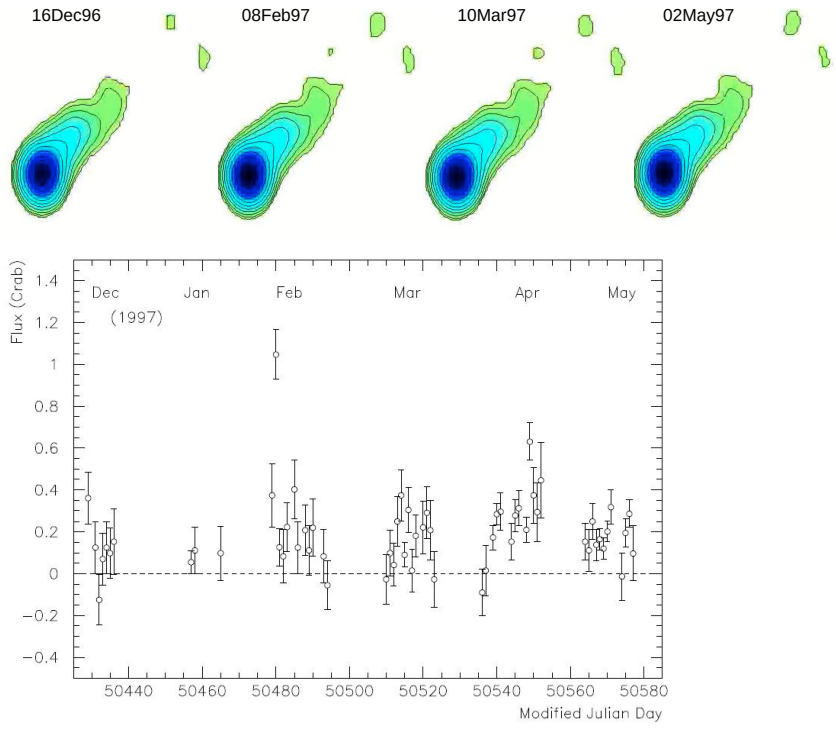

Figure 5.18 15GHz radio maps and γ-ray light curve for Mrk 421 in 1996–1997.

In Figure 5.19, the parameter called *c4* can be defined as the angular size (or core-contour distance) of the fourth contour (the outermost contour on these images is considered the first one, corresponding to a flux level of 0.6 mJy), i.e., *c4* represents the extent of the source at a flux level of 4.8 mJy. The temporal variation of this contour must be studied in conjunction with orientation effects because of the asymmetry of the Mrk 421 radio image.

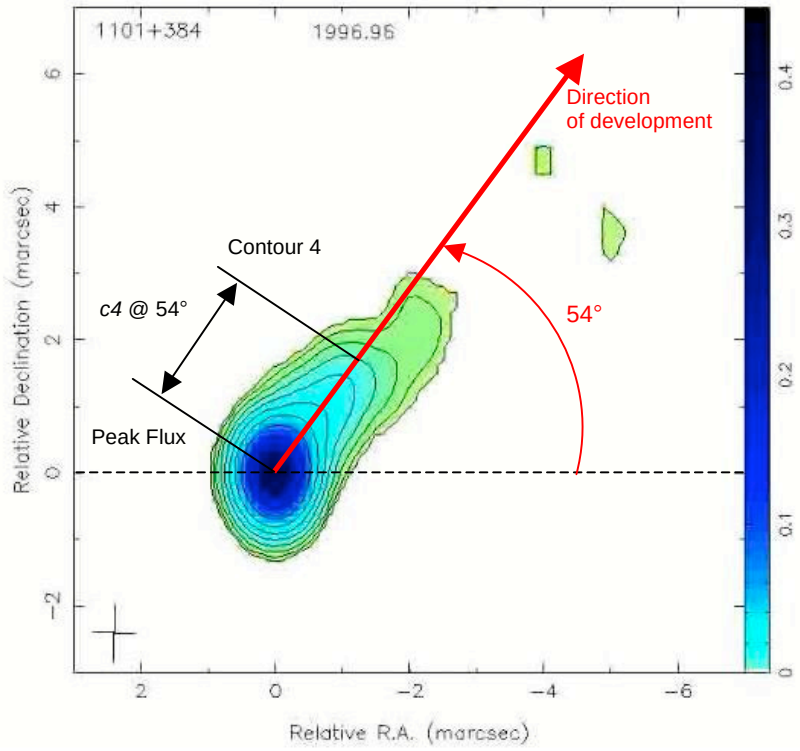

Figure 5.19 15GHz radio map of Mrk 421 in December 1996, showing the angular distance, *c4*, of contour 4 from the peak flux position. The contours are plotted in successive powers of 2 times the lowest contour at 0.6 mJy

The parameter *c4* was measured for different times between 1995 and 2001, using both the radio images that overlap with the darkruns of the Whipple 10m telescope and those taken when the 10m telescope was not observing. The program *xyExtract Graph Digitizer* (described in Section 4.1.2) was used to measure the core-contour distances from VLBA images of Mrk 421 contained in bitmap files. Essentially, the method measures the position corresponding to an absolute flux level of 4.8 mJy in a direction at an angle of 54° to the right-ascension axis; this angle was

chosen because this seems to be the direction of the blob development. The results for the period 1995 – 1997 (based on analysis of the data shown in Figures 5.17 and 5.18) are plotted in Figure 5.20 (top) along with the mean monthly γ-ray rates (bottom).

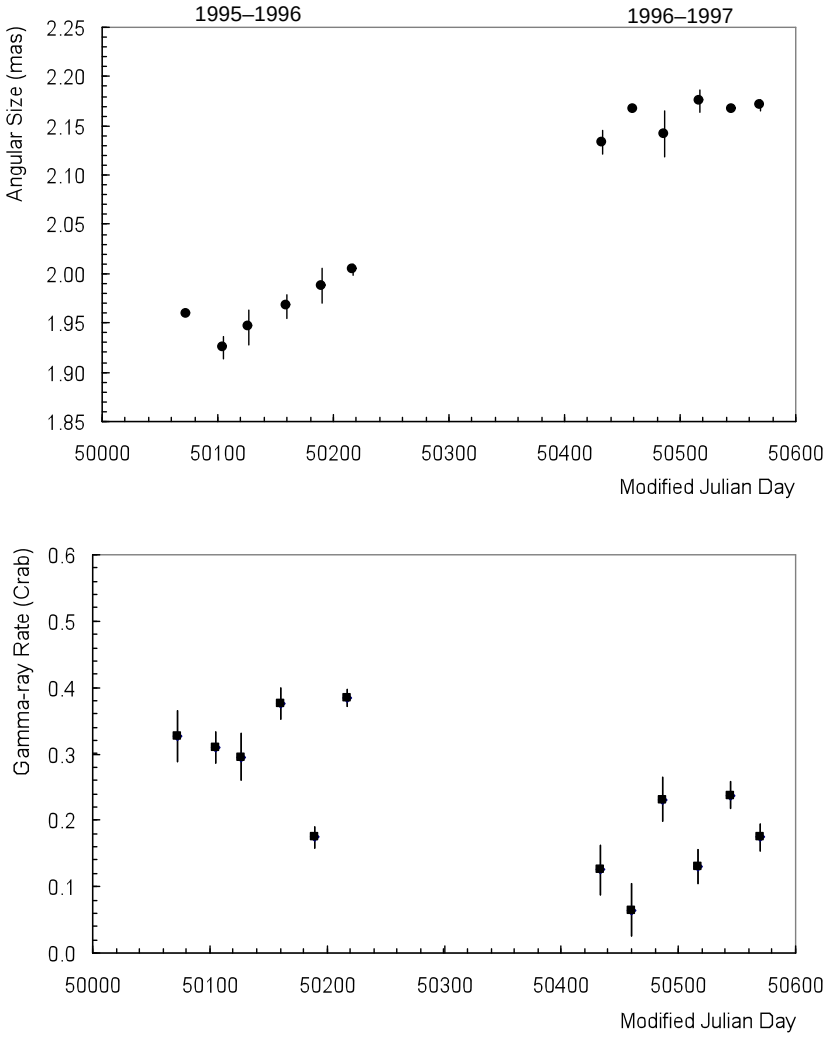

Figure 5.20 Angular size of contour 4 (top) and γ-ray rates (bottom) for Mrk 421 in 1995–1996 and 1996–1997, binned in monthly intervals.

The entire radio dataset (1995 – 2001), binned in monthly intervals, is shown in Figure 5.21 for three different contours, corresponding to absolute flux levels of 4.8 mJy, 19.2 mJy and 76.8 mJy. Figure 5.22 shows the annual binned data for *c4*.

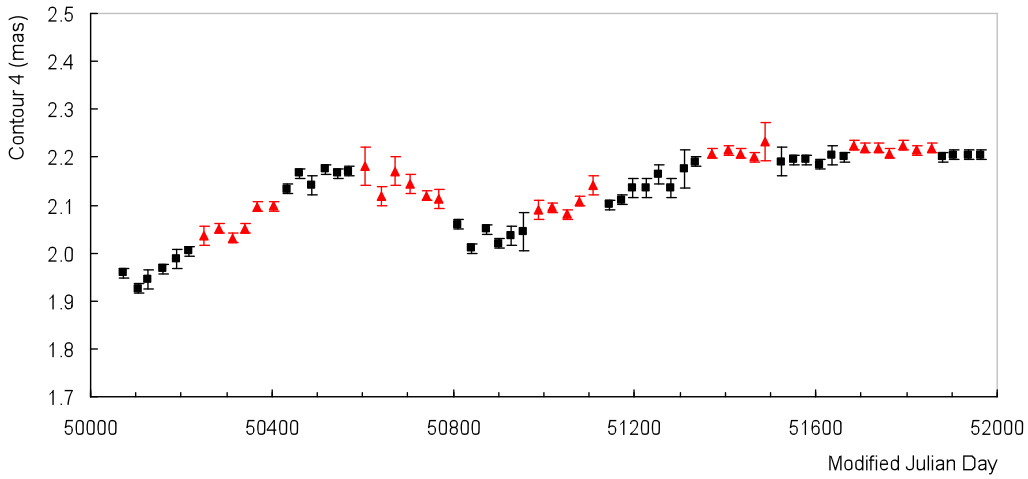
Contour 4 (mas)
2.5
2.4
2.3
2.2
2.1
2.0
1.9
1.8
1.7
50000
50400
50800
51200
51600
52000
Modified Julian Day

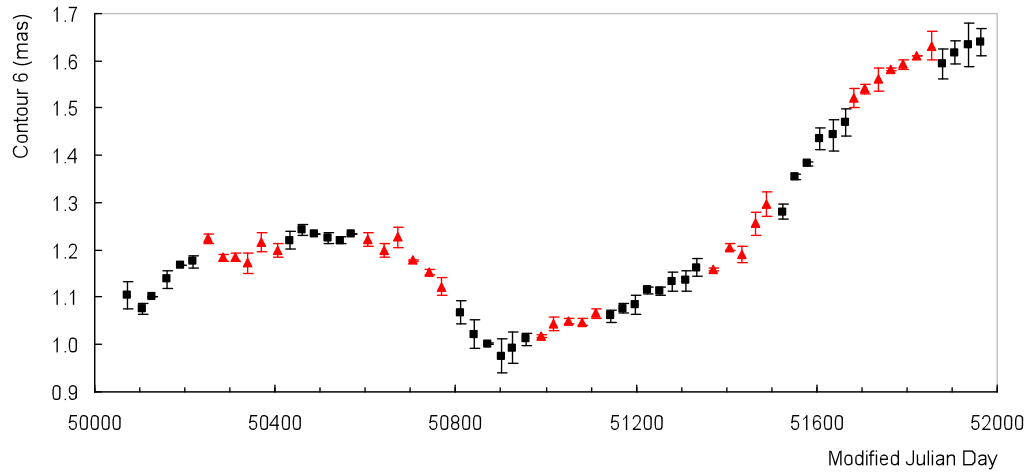
Contour 6 (mas)
1.7
1.6
1.5
1.4
1.3
1.2
1.1
1.0
0.9
50000
50400
50800
51200
51600
52000
Modified Julian Day

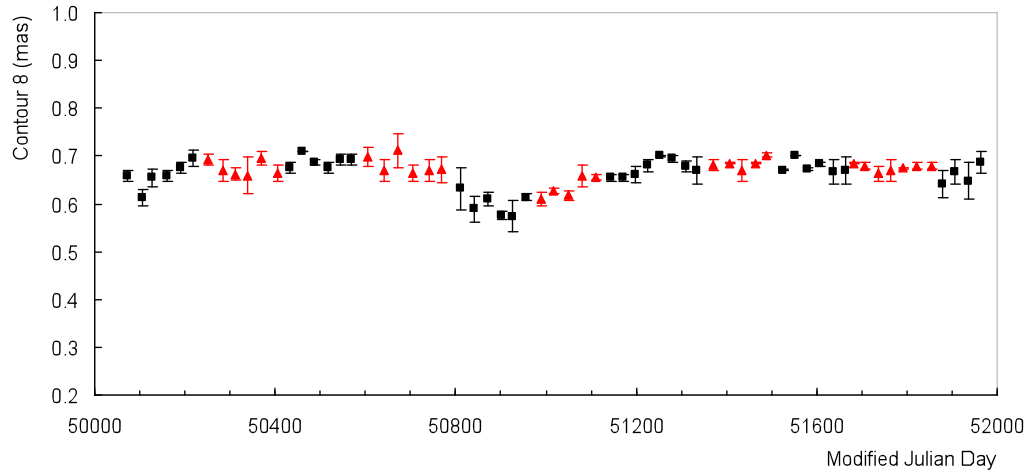
Contour 8 (mas)
1.0
0.9
0.8
0.7
0.6
0.5
0.4
0.3
0.2
50000
50400
50800
51200
51600
52000
Modified Julian Day

Figure 5.21 Core-contour distances for Mrk 421: *c4* (top), *c6* (middle) and *c8* (bottom), corresponding to flux levels of 4.8 mJy, 19.2 mJy and 76.8 mJy, respectively. The data are shown for one-month intervals, both when the Whipple 10m telescope was observing (black squares) and when it was not observing (red triangles).

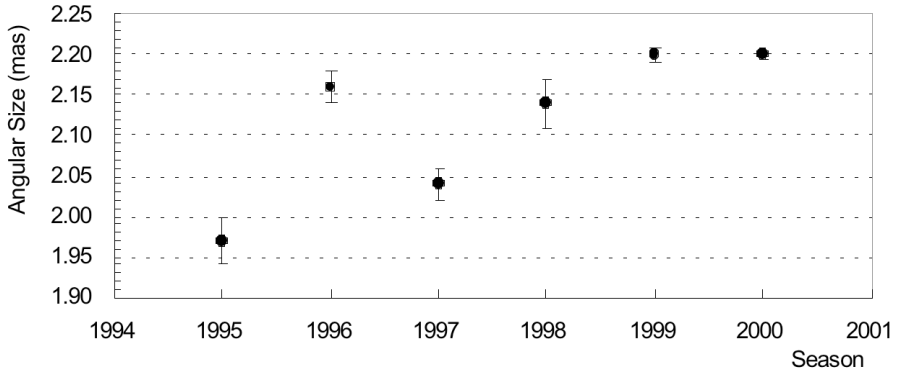

Figure 5.22 Mrk 421 core-contour distance *c4*, averaged over one-year intervals.

In Section 6.6.1, the relationship between the γ-ray light curves and the core-contour distance is investigated in detail.

5.3 Comparison of Gamma-ray and X-ray Observations

In this section, 14 years of X-ray data from the Rossi X-ray Timing Explorer (*RXTE*) satellite, 7 years of TeV data from the Milagro experiment and results from the 2009 *Fermi*-LAT campaign are compared with the γ-ray light curves of Mrk 421 from the Whipple 10m telescope. Variability and correlation studies will be covered in Chapter 6.

5.3.1 *RXTE* observations, 1995 – 2009

The γ-ray rates for the 1995 – 2009 Mrk 421 observations were compared with the X-ray flux from the All-Sky Monitor (ASM) instrument (Section 3.3) on board the *RXTE*.

The light curves for the X-ray and γ-ray data from December 1995 to May 2009 are plotted in Figure 5.23. The data are plotted for the Whipple 10m darkrun periods (usually there are 6 periods for each season) in which both X-ray and γ-ray data were taken, i.e., the X-ray data were averaged for each period in which γ-ray data from the Whipple 10m telescope were available (usually 21-day periods).

In the original X-ray data (from which the monthly mean rates were calculated), each data point represents the one-day average of the fitted source fluxes from a number (typically 5 – 10) of individual ASM dwells (90 seconds each). These data are quoted as nominal 2 – 10 keV rates in ASM counts per second, where the Crab Nebula flux is about 75 counts per second.

The annual-binned light curves for the X-ray and γ-ray data from 1995 to 2009 are plotted in Figure 5.24. Evidence for correlation was found for both monthly and annual-averaged data sets: the results of testing for correlations are summarized in Sections 6.3 and 6.5.

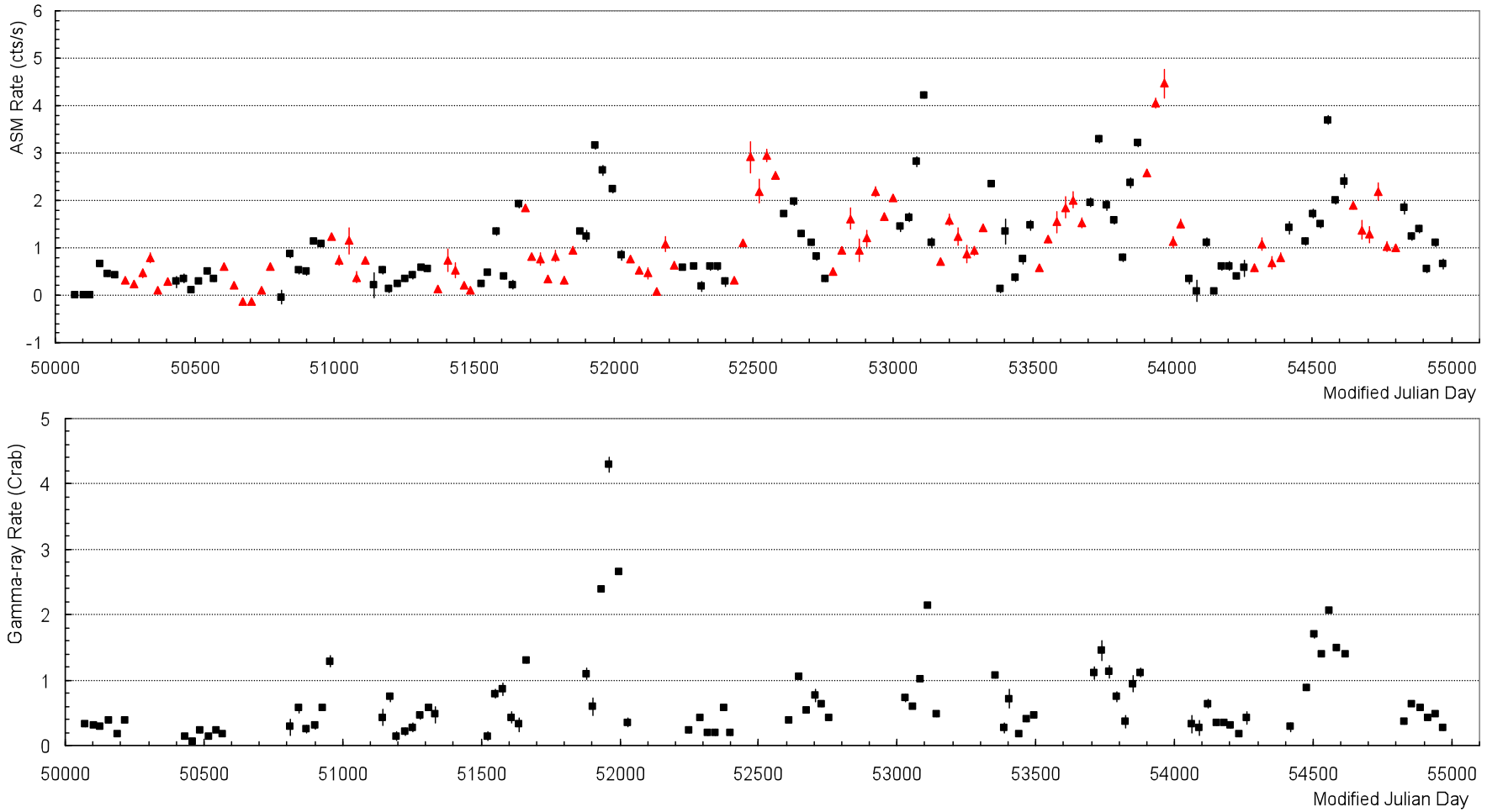

Figure 5.23 The X-ray and γ-ray light curves for Mrk 421 (1995 – 2009): *RXTE* ASM (top) and Whipple 10m telescope (bottom). Each data point represents the monthly mean rate (black squares when Whipple 10m was observing, red triangles when it was not observing).

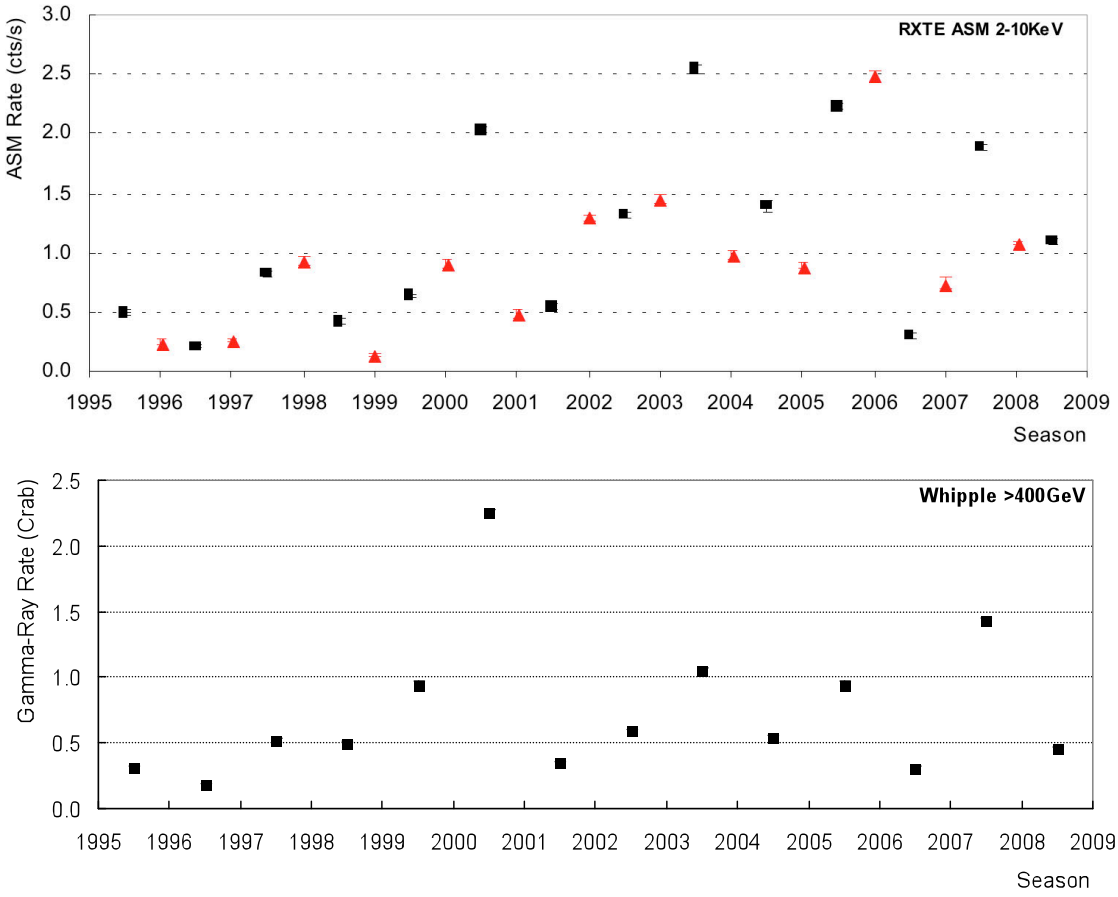

Figure 5.24 Annual mean rates for Mrk 421: *RXTE* (top) and Whipple (bottom). Data points are black squares for data taken when the Whipple 10m was observing and red triangles for data taken when it was not observing.

5.3.2 Milagro observations, 2000 – 2007

The Milagro Gamma-ray Observatory (Section 3.4) operated continuously from June 1999 to April 2008 with 90% on-time. With the most recent reconstruction and analysis, Milagro obtains $12\sigma/\sqrt{yr}$ on the Crab Nebula with a median energy of roughly 12 TeV (Abdo et al. 2007b). Results from almost seven years of Milagro Mrk 421 data taken between 2000 and 2007 are shown in Figure 5.25. For this dataset, an excess of 9.9σ is obtained at the known position of Mrk 421. The measured excess rate is (18 ± 3) events/day compared with (25 ± 4) events/day for a Crab-like source transiting at the declination of Mrk 421 (Smith et al. 2007).

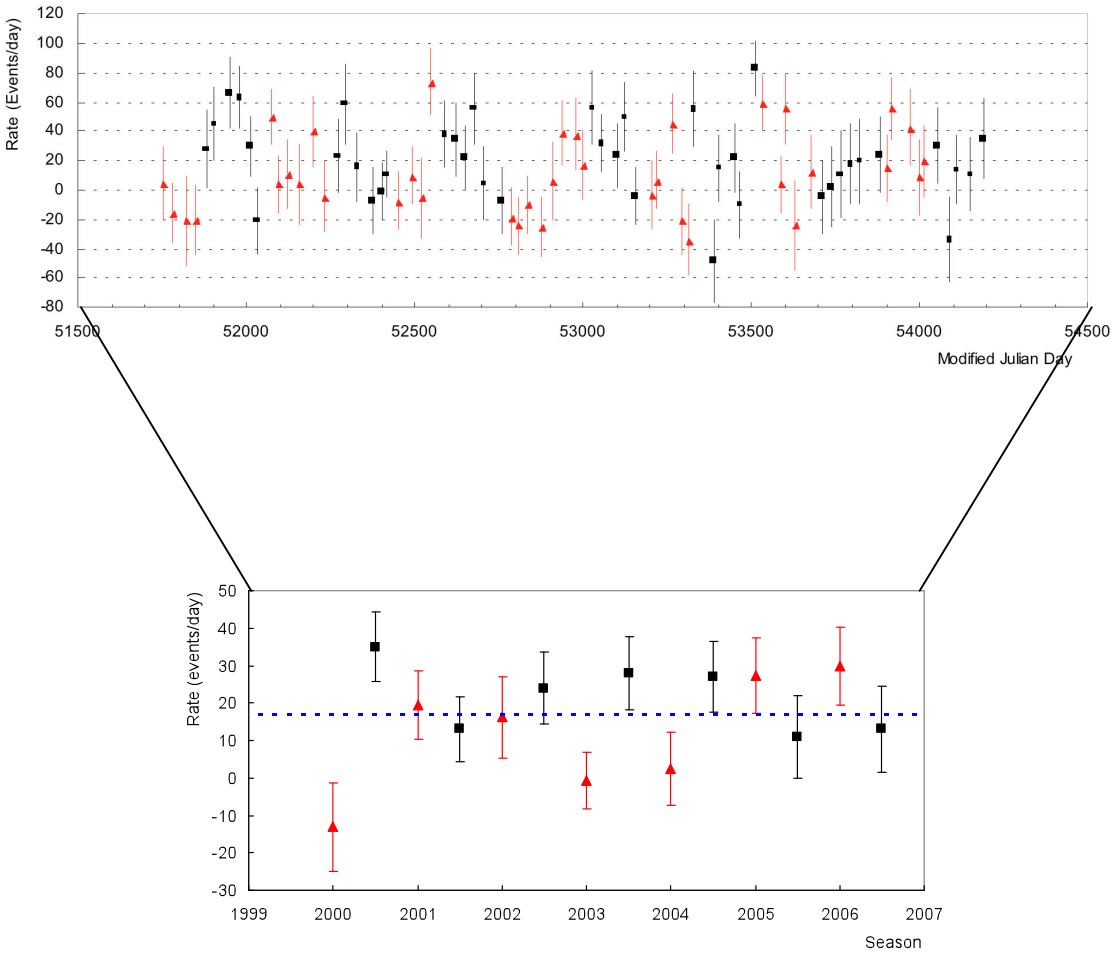

Figure 5.25 Milagro data for Mrk 421 from 2000 to 2007. The top panel shows the data binned in 32-day bins; data taken when the Whipple 10m telescope was observing are shown by black squares. The bottom panel shows the mean rate obtained for intervals of ~6 months, both during (black squares) and outside (red triangles) the observing periods of the 10m telescope. The blue horizontal dashed line gives the average rate and a χ^2 test gives χ^2/dof = 24.1/13 and a probability $P_{\chi 2} = 0.03$.

The annual binned data for Milagro and the Whipple 10m is shown in Figure 5.26. Long-duration variability is difficult to monitor with the Whipple 10m telescope due to its intermittent exposure. The Milagro Observatory, in contrast, was able to monitor Mrk 421 with daily observations throughout the entire year. A summary of the results of the correlation analysis performed on the Milagro and Whipple data for the period 2000 – 2007 will be given in Sections 6.3 and 6.5.

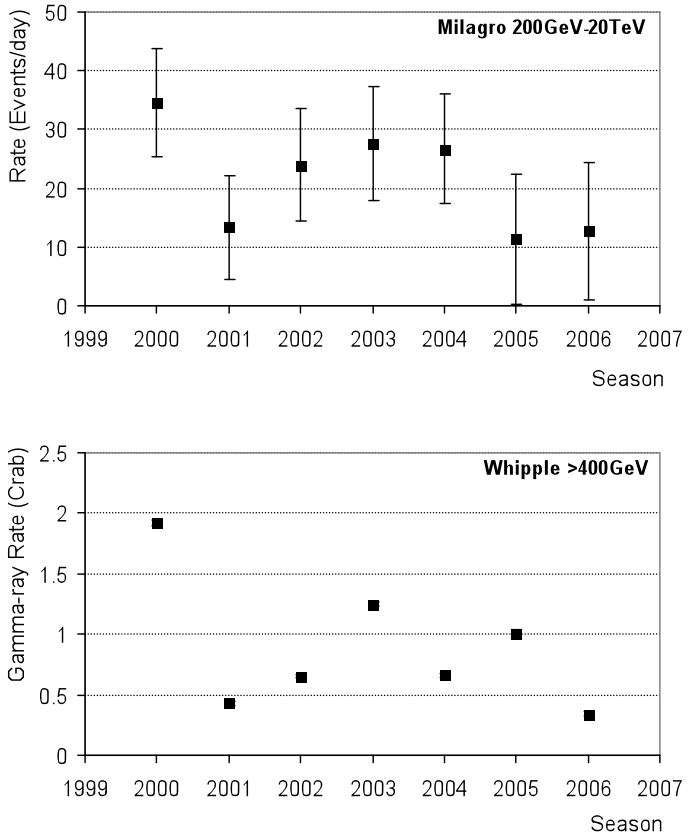

Figure 5.26 Annual mean rate of Mrk 421 from Milagro (top) and Whipple (bottom). The Milagro data points shown here are those shown as the black squares in the bottom panel of Figure 5.25.

5.3.3 *Fermi*-LAT and Whipple observations, 2009 campaign

In this section, γ-ray observations of Mrk 421 over the period December 2008 – May 2009 as measured by the *Fermi*-LAT and by the Whipple 10m telescope are presented. Figure 5.27 shows the daily-binned light curves. The significance level of the *Fermi*-LAT detection was less than 3σ on most nights (60%) during this campaign.

The large error bars on the *Fermi*-LAT flux points make it difficult to follow the flux behaviour. The horizontal dashed line in the top panel of Figure 5.27 represents the annual weighted mean ($0.074 \pm 0.003 \times 10^{-6}$ photons cm^{-2} s^{-1}), and a χ^2 test applied to this dataset yields χ^2/dof = 83.7/59, giving a probability $P_{\chi 2} = 0.02$ that the daily flux is constant. For the Whipple data (bottom panel of Figure 5.27), the χ^2 test yields χ^2/dof = 253.6/70 and a probability $P_{\chi 2} = 1.3 \times 10^{-22}$.

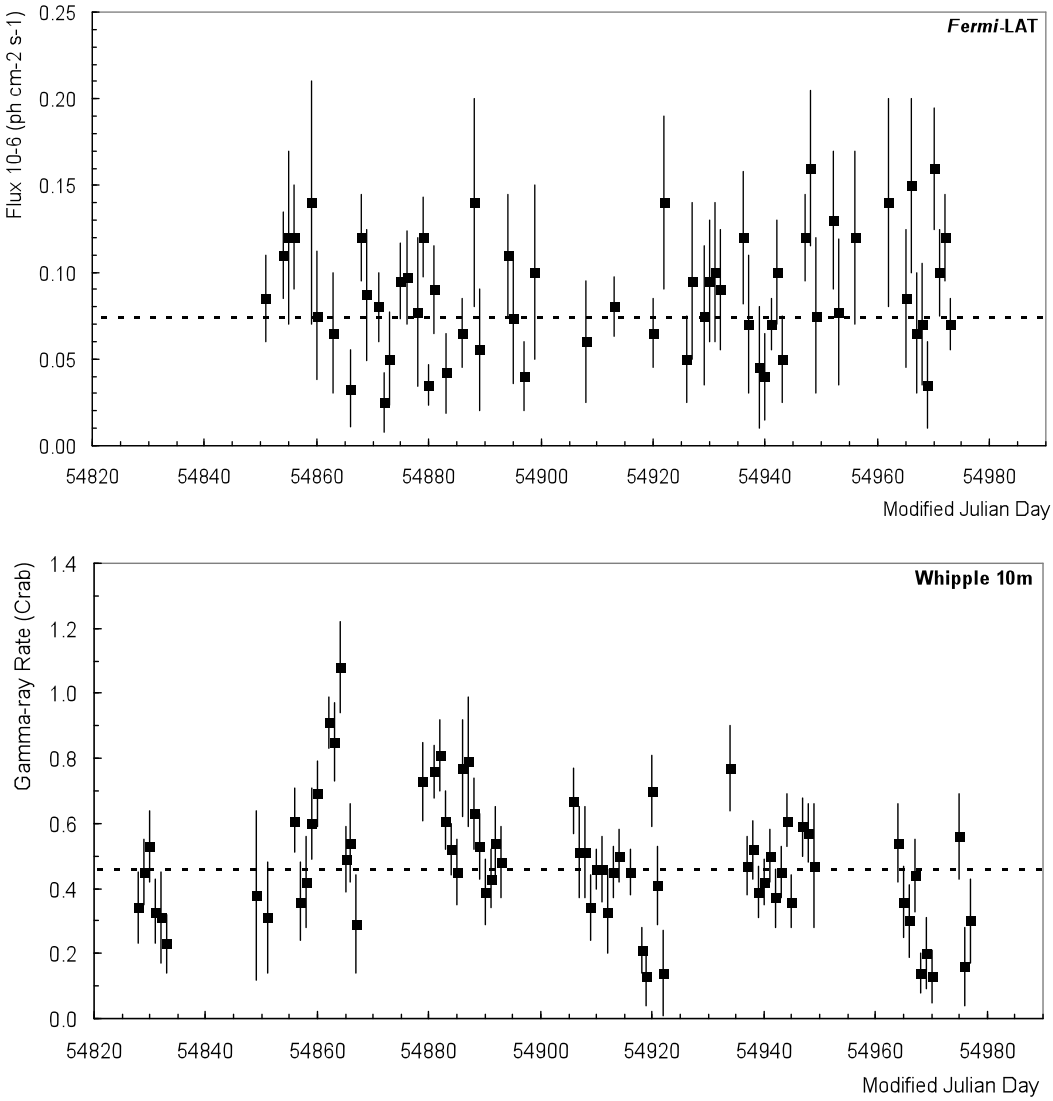

Figure 5.27 Daily mean rate for Mrk 421 (December 2008 – May 2009) from the *Fermi*-LAT (top) and the Whipple 10m telescope (bottom). The energy band of the *Fermi* observations extends from 10 MeV to more than 100 GeV. The peak response energy of the Whipple 10m is approximately 400 GeV.

The trend is clearer in the monthly-binned light curves shown in Figure 5.28. As will be shown later (Figure 6.9), there is no evidence of correlation between the two data sets. The variability amplitudes computed for the *Fermi*-LAT and Whipple data will be given in Chapter 6.

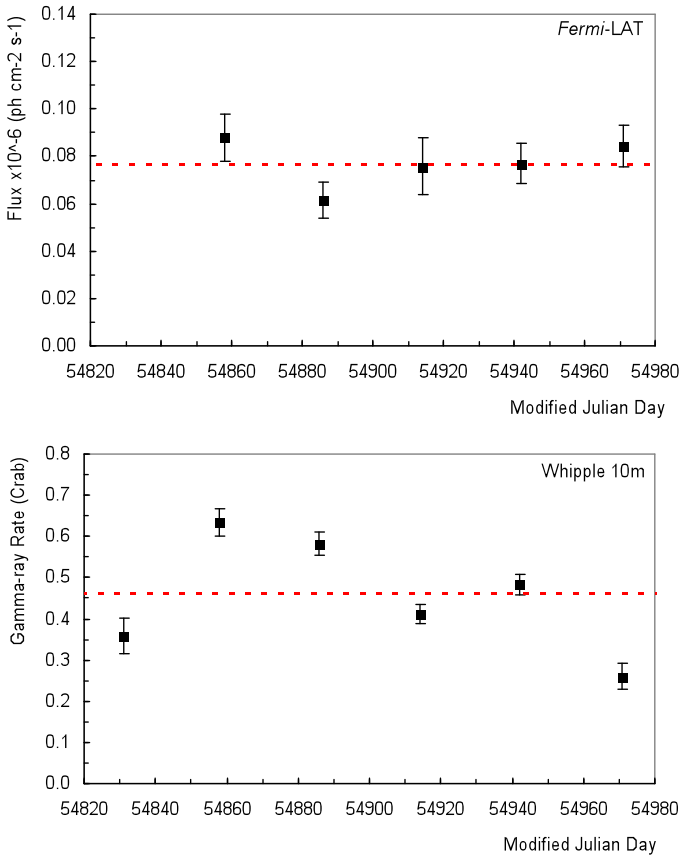

Figure 5.28 Monthly-binned light curves for Mrk 421 for the season 2008–2009. *Fermi* (top) and Whipple (bottom). The horizontal dashed lines give the annual mean rate. The χ^2 test applied to the *Fermi* data (top) gives χ^2/dof = 5.9/4 and a probability of $P_{\chi 2}$=0.21. Whipple (bottom) results for this season are given in Table 5.2.

Chapter 6

Variability and Correlation Studies

Variability studies are very important in identifying the physical processes and the size of the region in which the radiation in a given wavelength range is produced. If variability is observed on a time scale Δt_{var} in the source frame, then the radiation must be produced in a region with size constrained by

$$R \leq c\Delta t_{\mathrm{var}} \tag{6.1}$$

If the source is bigger than this limit, then different parts of the source would not be causally connected, so that they could not vary in phase with each other. This would lead to greatly reduced amplitude for the variation. When different variability time scales are found in a source at the same energy range, the most rapid variability is taken to be indicative of the source size, after allowing for redshift and relativistic beaming effects. The slower variations are likely to be due to slow changes in the source structure and other effects such as heating or cooling (Kembhavi & Narlikar, 1999).

Blazars as a class are found to have rapid, large-amplitude variability, which distinguishes them from other quasars and AGN. This is particularly evident in the case of the blazars PKS 2155-304 and Markarian 421 (Mrk 421). PKS 2155-304, which was initially detected by the Durham group during 1996 (Chadwick et al. 1999), is a relatively distant HBL, with redshift z = 0.116. Detection of the source was confirmed by the H.E.S.S Collaboration (Aharonian et al. 2005a), and variability on short timescales was noted. H.E.S.S. later detected PKS 2155-304 in an extremely high state of activity in July 2006 (Aharonian et al. 2007). Fluxes measured with one-minute resolution exhibited peak values in excess of 14 times the Crab Nebula flux, and variability on timescales <4 minutes was observed.

The blazar Mrk 421 has been found to be variable at all wavelengths from the radio to γ-ray waveband, and on all time scales from minutes to years (Acciari et al. 2009c). This chapter focuses on variability studies of this source at different wavelengths, particularly on the long time scales made possible by the Whipple 10m data set. Although the data available for Mrk 421 is often too sparse and unevenly sampled for analysis in the frequency domain, analysis can be carried out in the time domain using the *cross-correlation function* (CCF). There are two approaches for dealing with the gaps in the data: interpolation and discrete binning. Interpolation becomes unreliable when there is significant power on time scales smaller than the typical gap size. The *discrete correlation function* (DCF) method (Edelson & Krolik, 1988) avoids interpolation by binning the time-difference pairs and calculating the mean and variance of each bin. The latter approach is the one used in this thesis and the results are shown in Section 6.5.

6.1 Fractional Variability Amplitude

In Section 5.1.1, χ^2 tests to determine whether the γ-ray emission was constant or not were described. To determine the degree of variability, a variety of measures are in use for estimating the variability amplitude in AGN light curves, including the *excess variance*, σ^2_{XS}, and the *fractional rms variability amplitude*, F_{var}. The variance estimate provides a simple and straightforward means of quantifying the variability of the source at different wavelengths. However, there is a rather large scatter in the variance associated with the stochastic nature of red-noise variability. It has been found that, when significant variability is observed, the fractional variability amplitude of some blazars increases logarithmically with the photon energy, indicating significant spectral variability. The short-timescale variability amplitude may also track this trend, suggesting that the slopes of the power spectral density of the source are independent of energy (Zhang et al. 2005).

In this section, the variability of Mrk 421 across the spectrum is investigated by computing the fractional rms variability amplitude, F_{var}, for each of the eight wavebands (four radio bands, one X-ray band and three γ-ray bands). In addition, for

each data set, the probability $P_{\chi 2}$ (Equation 4.8) is quoted to show how constant the rate is about the annual mean.

The observed variance can be simply obtained from the light curves:

$$s^2 = \frac{1}{N-1}\sum_{i=1}^{N}(x_i - \bar{x})^2 \tag{6.2}$$

where $\bar{x}$ is the arithmetic mean of the fluxes x_i, and N is the number of data points. F_{var}, which also corrects for the effects of the measurement errors, is defined as (Zhang et al. 2005)

$$F_{\mathrm{var}} = \frac{\sqrt{s^2 - \overline{\sigma^2}}}{\bar{x}} \tag{6.3}$$

where $\overline{\sigma^2}$ is the mean error squared. If each flux measurement x_i has uncertainty σ_i, then

$$\overline{\sigma^2} = \frac{1}{N}\sum_{i=1}^{N}\sigma_i^2 \tag{6.4}$$

The value of F_{var} was calculated for each season; the results for the Mrk 421 observations from the Whipple 10m, Milagro, *Fermi*-LAT, *RXTE* ASM, Metsähovi and UMRAO datasets are shown in Tables 6.1 – 6.6.

For the Milagro data from the 2001–2002, 2005–2006, and 2006–2007 seasons, the difference between the terms to be subtracted in Equation 6.3 is *negative*; this can happen when the amount of variation in the data points is smaller than the measurement errors (perhaps indicating that the errors are overestimated). In such cases, the true level of variability cannot be determined.

Whipple 10m					
Season	**No. of nights**	**Minimum rate (Crab units)**	**Maximum rate (Crab units)**	F_{var}	P_{χ^2}
1995-1996	53	0.17	0.38	0.228	3.2×10^{-22}
1996-1997	60	0.06	0.24	0.373	1.7×10^{-4}
1997-1998	38	0.25	1.28	0.711	4.3×10^{-27}
1998-1999	56	0.15	0.81	0.439	1.7×10^{-15}
1999-2000	41	0.15	1.36	0.650	2.3×10^{-59}
2000-2001	64	0.35	4.30	0.792	$<10^{-300}$
2001-2002	27	0.20	0.57	0.490	1.8×10^{-14}
2002-2003	37	0.39	1.04	0.385	8.3×10^{-77}
2003-2004	43	0.44	1.94	0.677	$<10^{-300}$
2004-2005	19	0.18	1.06	0.625	1.3×10^{-73}
2005-2006	62	0.36	1.45	0.335	2.8×10^{-12}
2006-2007	43	0.16	0.64	0.322	6.0×10^{-8}
2007-2008	86	0.28	2.06	0.438	1.9×10^{-147}
2008-2009	71	0.26	0.63	0.299	6.9×10^{-20}

Table 6.1 The fractional rms variability amplitude, F_{var}, for the Whipple 10m Mrk 421 γ-ray data. The minimum and maximum monthly-averaged rates for each season are also shown.

Milagro					
Season	**No. of points**	**Minimum flux (events/day)**	**Maximum flux (events/day)**	F_{var}	P_{χ^2}
2000-2001	10	-21	66	1.621	0.01
2001-2002	12	-7	59	N/A	0.53
2002-2003	10	-7	56	0.735	0.13
2003-2004	13	-4	56	1.280	0.05
2004-2005	11	-48	83	3.183	4.5×10^{-4}
2005-2006	11	-4	24	N/A	0.35
2006-2007	10	-34	35	N/A	0.53

Table 6.2 The fractional rms variability amplitude, F_{var}, for the Milagro Mrk 421 γ-ray data. Also shown are the minimum and maximum monthly-averaged fluxes (events/day) for each season. Each flux value is the mean flux in a 32-day period.

The *Fermi*-LAT results for the 2008–2009 campaign are shown in Table 6.3. The value for F_{var} could be calculated only for the data binned in 1-month intervals. The value obtained is very low, probably due to the relatively low sensitivity of the instrument on such a short timescale.

Fermi-LAT					
Data bins	**No. of points**	**Minimum flux ($\times10^{-6}$ph cm^{-2} s^{-1})**	**Maximum flux ($\times10^{-6}$ph cm^{-2} s^{-1})**	F_{var}	P_{χ^2}
1-day	60	0.025	0.160	N/A	0.02
1-month	5	0.062	0.088	0.047	0.21

Table 6.3 The fractional rms variability amplitude, F_{var}, for the *Fermi*-LAT Mrk 421 data.

Tables 6.4, 6.5 and 6.6 show the results for the X-ray and radio data. Table 6.6 shows the variability amplitude at three different radio frequencies from the University of Michigan Radio Astronomy Observatory (UMRAO). In Table 6.6, the variability amplitude for the 4.8 GHz data could not be calculated for 2007 because a negative sign was obtained under the square root in Equation 6.3.

RXTE ASM					
Season	**Total exposure time (ks)**	**Minimum rate (counts/s)**	**Maximum rate (counts/s)**	F_{var}	P_{χ^2}
1995-1996	71	0.42	0.67	0.251	2.1×10^{-3}
1996-1997	129	0.10	0.50	0.351	1.4×10^{-24}
1997-1998	126	-0.04	1.13	0.645	8.0×10^{-36}
1998-1999	136	0.14	0.57	0.339	1.1×10^{-6}
1999-2000	109	0.22	1.92	0.915	4.4×10^{-106}
2000-2001	138	0.85	3.15	0.469	1.9×10^{-159}
2001-2002	150	0.19	0.61	0.361	5.6×10^{-5}
2002-2003	143	0.35	1.97	0.486	9.7×10^{-154}
2003-2004	109	1.10	4.22	0.569	6.4×10^{-229}
2004-2005	92	0.12	2.33	0.751	6.2×10^{-289}
2005-2006	148	0.79	3.29	0.411	1.5×10^{-140}
2006-2007	119	0.09	1.11	0.652	3.9×10^{-46}
2007-2008	153	1.13	3.69	0.433	1.9×10^{-121}
2008-2009	144	0.55	1.85	0.418	1.4×10^{-24}

Table 6.4 The fractional rms variability, F_{var}, for Mrk 421 in the X-ray band. The minimum and maximum rates are monthly averaged values.

Metsähovi					
Season	**No. of points**	**Minimum flux (Jy)**	**Maximum flux (Jy)**	F_{var}	P_{χ^2}
2002-2003	34	0.10	0.78	0.217	2.5×10^{-8}
2003-2004	24	0.17	0.69	0.165	3.0×10^{-4}
2004-2005	24	0.04	0.69	0.320	3.2×10^{-5}
2005-2006	19	0.14	0.53	0.132	0.27
2006-2007	35	0.18	0.72	0.169	1.7×10^{-3}
2007-2008	25	-0.02	0.80	0.338	8.9×10^{-3}

Table 6.5 The fractional rms variability, F_{var}, for the radio band centred at 37 GHz. The integration time for one flux density data point is ~1400 seconds. The minimum and maximum fluxes are taken from the scan-by-scan data set.

UMRAO									
Season	**4.8 GHz**			**8.0 GHz**			**14.5 GHz**		
	No. of days	F_{var}	P_{χ^2}	**No. of days**	F_{var}	P_{χ^2}	**No. of days**	F_{var}	P_{χ^2}
2005-2006	12	0.043	3.5×10^{-7}	19	0.244	4.6×10^{-7}	24	0.145	1.8×10^{-3}
2006-2007	16	0.130	3.5×10^{-33}	10	0.300	1.1×10^{-8}	17	0.153	1.8×10^{-39}
2007-2008	3	N/A	0.66	6	0.374	3.8×10^{-68}	13	0.114	0.08

Table 6.6 The fractional rms variability, F_{var}, for Mrk 421 at three radio frequencies from UMRAO (centred at 4.8 GHz, 8.0 GHz and 14.5 GHz), calculated with 1-day binning for each data set.

The results for four different wavebands from 1995 to 2009 are plotted together in Figure 6.1, showing the trend of the variability amplitude through the years for each waveband. The *Fermi*-LAT data (10 MeV – 100 GeV) are not included in Figure 6.1; these data had the lowest value of F_{var} (0.047), but cover only a single season, and a statistically significant detection (>3σ) was obtained in only 42% of the observations.

The variability amplitude for the four radio bands from data taken between 2002 and 2008 is shown in Figure 6.2. The data at 4.8 GHz, 8.0 GHz and 14.5 GHz are from UMRAO, and the data at 37.0 GHz are from Metsähovi.

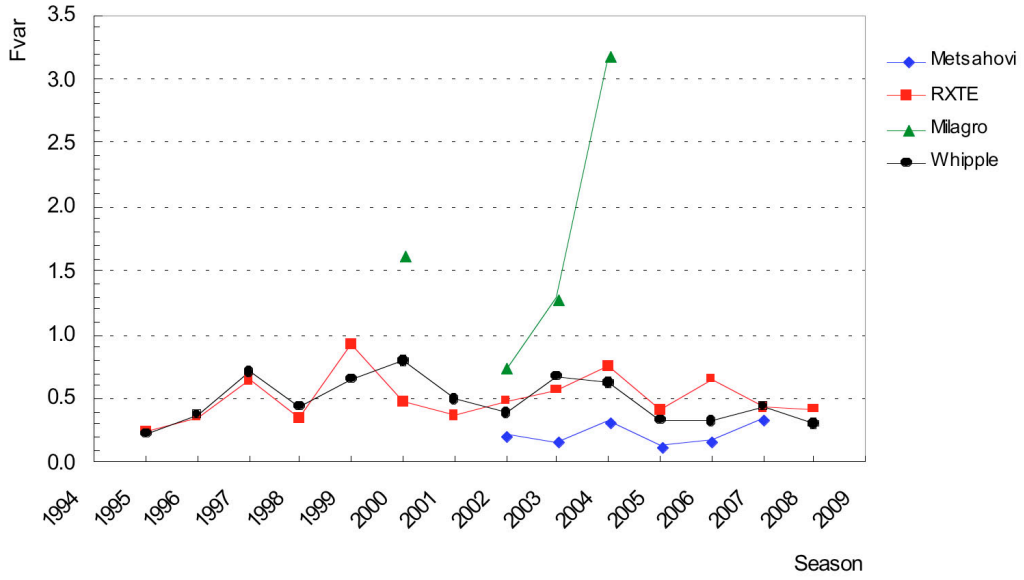

Figure 6.1 Fractional rms variability amplitudes for Mrk 421 from all the multiwavelength data taken during the period 1995 – 2009 (data points have been joined with lines to guide the reader).

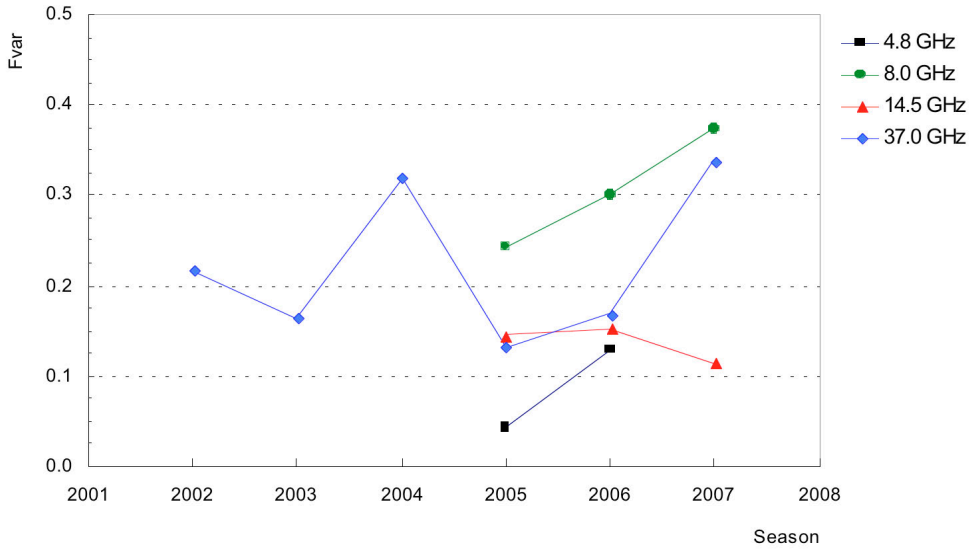

Figure 6.2 Fractional variability amplitudes for Mrk 421 at radio wavelengths.

In order to examine dependence of the variability on energy, the average value of F_{var} over the period 2000 – 2009 was calculated (data from all wavebands, except from the *Fermi*-LAT, were available for that period) and plotted against energy (Figure 6.3). Because the value of F_{var} for the Milagro observations cannot be

computed for all of the seasons, the Milagro data have been omitted from this plot. The F_{var} parameter appears to be higher for the X-ray and γ-ray data than for the radio data. The average value of F_{var} over all the wavebands plotted is 0.161 ± 0.018; a χ^2 test for the hypothesis that F_{var} is a constant equal to the mean value yields χ^2/dof = 18.8/5 corresponding to a chance probability of only 0.2%. Combining the results for the radio data gives F_{var} = 0.15 ± 0.02, while combining the X-ray and γ-ray results gives F_{var} = 0.50 ± 0.10. There is therefore a statistically significant difference in variability between the high-energy regime (X-ray/γ-ray) and the low-energy regime (radio), but only at a rather marginal level (~3.5σ).

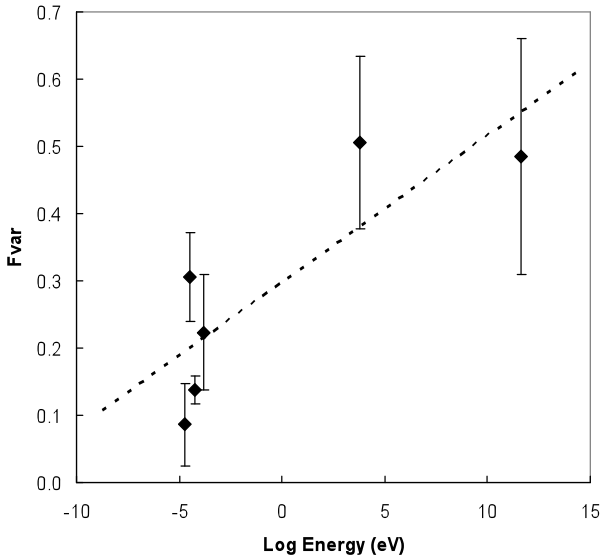

Figure 6.3 The fractional rms variability amplitude, F_{var}, as a function of energy.

6.1.1 Statistical Distribution of the Variability of Mrk 421

Mrk 421 is the brightest AGN at TeV energies (on average) and the first such AGN to be discovered. As such, it is not unreasonable to regard Mrk 421 as the prototype TeV AGN although it has been suggested that it may have a greater degree of variability than the norm on all timescales. It is certainly the most studied of the known TeV blazars; the variations seen on short time scales are often duplicated in other AGN. It is the closest such AGN and hence has the lowest spectral distortion due to absorption by pair production with the extragalactic background light (EBL).

It is difficult to compile a large data sample from a variety of observations, because observing modes may be quite different and the sensitivity is often not well-defined. The Whipple 10m database is comparatively uniform and covers a long time interval; during the period 1995 – 2009, the system was operated in a relatively stable configuration of telescope and camera. It is thus useful to use this database to investigate the statistical distribution of the time variability of Mrk 421 and by inference that of other AGN. If Mrk 421 is typical of all (or a subclass of) TeV AGN, then we can use these distributions to predict how often a more distant AGN might flare or be above a certain level of brightness. We consider four different timescales: yearly, monthly, daily and run-by-run (hourly). Nightly and run-by-run results are shown only for the years in which the Dublin analysis package was used.

Yearly variations: As shown in the Figure 6.4, there are significant variations on a yearly timescale, with mean annual rates ranging from 0.2 Crab units to 2.3 Crab units.

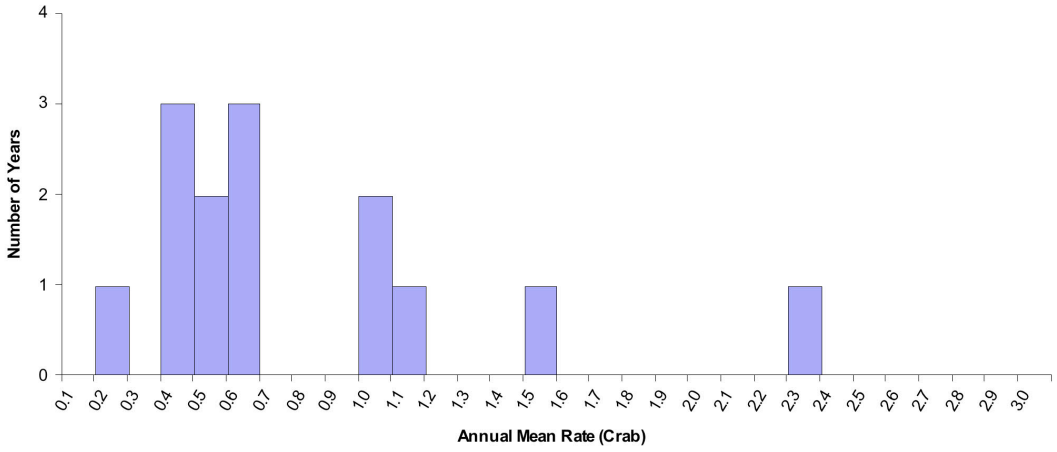

Figure 6.4 Histogram of the annual-binned Mrk 421 TeV γ-ray rate for a total of 14 years.

Monthly variations (Figure 6.5): There are clearly large variations over the full 14 years of data. There were 21 months (out of a total of 89 months) in which the average rate was at least 1 Crab unit.

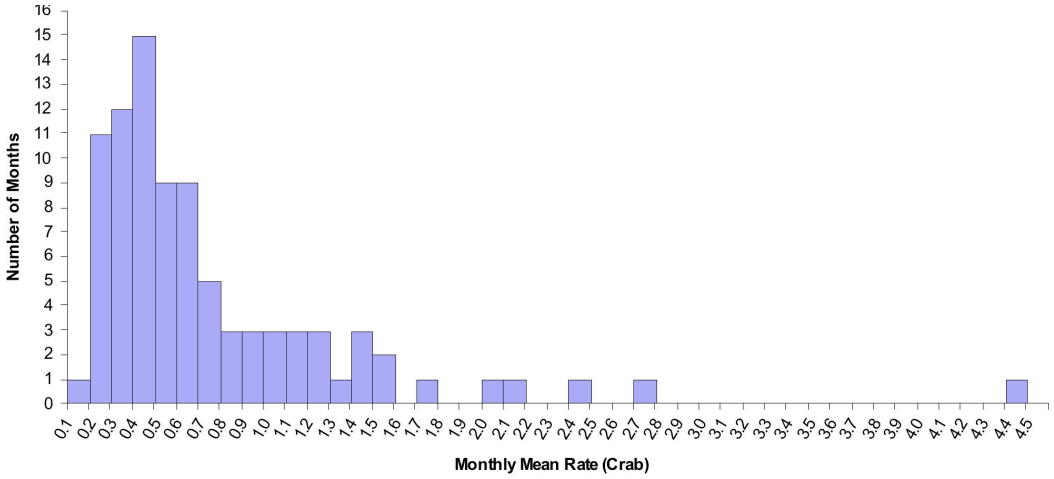

Figure 6.5 The monthly-binned Mrk 421 TeV γ-ray rate for 14 years of data (December 1995 – May 2009), covering 89 darkruns.

Nightly variations: The distribution of the average rate for each night of observation is shown in Figure 6.6 for nine years of data (2000 – 2009). The duration of the observations on which the average is based varied from night to night as observing priorities, weather, etc. changed. There were ~30 nights (out of a total of 510 nights) for which the average rate was at least 2 Crab units.

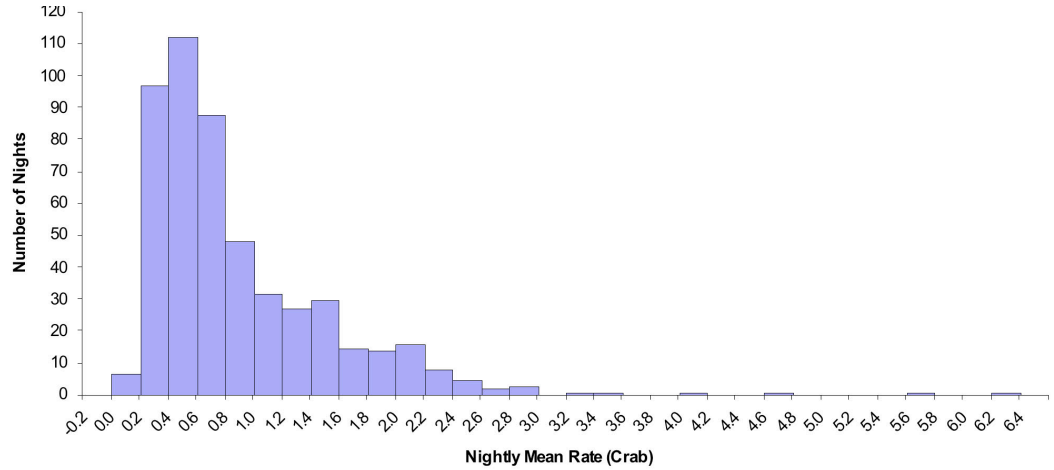

Figure 6.6 The nightly-binned Mrk 421 TeV γ-ray rate for nine years of data (November 2000 – May 2009), covering 510 nights.

Run variations: Observing runs were generally of 28-minute duration. The distribution of the run-by-run rates is shown in Figure 6.7. This distribution is not a completely unbiased sample as there is a tendency for the observers to continue observations when the observed signal is high. There is therefore some bias towards stronger levels of emission. However, it is fair to say that ~30% of the observing time, taken at random, shows the source to be at an emission level of 1 Crab unit and 5% of the runs have levels above 3 Crab units.

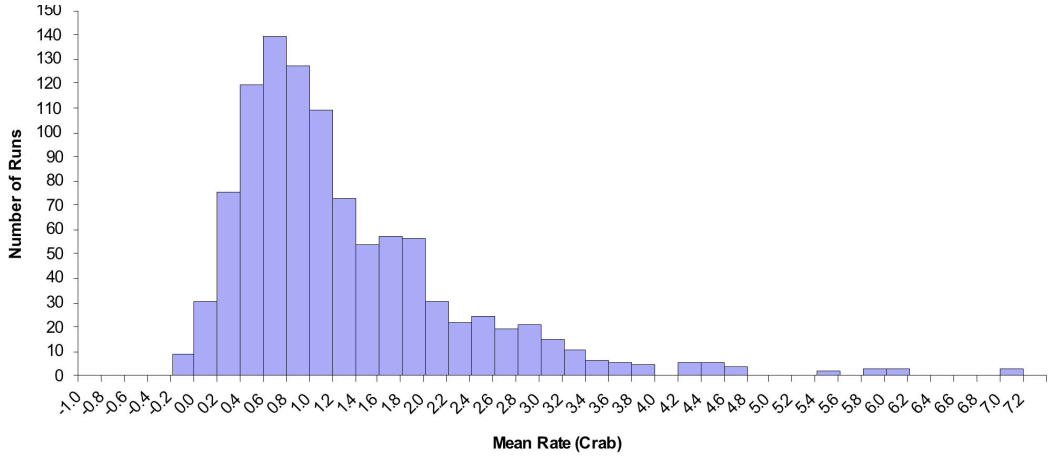

Figure 6.7 Run-by-run variation of the Mrk 421 TeV γ-ray rate for 1055 runs taken over nine years (2000 – 2009).

If we make the assumption that Mrk 421 is typical, these distributions can be used to predict the expected level of variation in other AGN, scaling by the ratio of their average intensity to that of Mrk421: e.g., for an AGN one-third as bright as Mrk 421 on average, ~5% of the runs taken on it can be expected to exhibit flaring at the 1 Crab level. In the case of the Whipple 10m telescope, only a small number of blazars have been detected (Mrk 421, Mrk 501, 1ES2344+514, H1426+428 and 1ES1959+650). Apart from Mrk 421 and Mrk 501, the average TeV level measured for these blazars is extremely low. For example, the average rate observed for H1426 during 2000 and 2001 was only 10 ± 2% of the Crab Nebula rate (Horan 2001), and 1ES2344 and 1ES1959 were only detected by the 10m telescope because of strong flaring activity (Catanese et al. 1998; Holder et al. 2003). It is therefore difficult to confirm the predictions of flaring frequency using 10m data alone. However, as more TeV blazars are identified using VERITAS, H.E.S.S. and MAGIC, and their average

flux levels determined over reasonable timescales, these predictions can be more readily tested.

6.2 Correlation Coefficient

The *correlation coefficient* is a measure of linear association between two variables. For sample data comprising N data points (x_i, y_i), the level of correlation between x and y is given by the *Pearson's product moment-correlation coefficient*, R, defined as

$$R = \frac{S_{xy}}{\sqrt{S_{xx}\, S_{yy}}} \tag{6.5}$$

where $S_{xx} = \sum_{i=1}^{N}\left(x_i - \bar{x}\right)^2$, $S_{yy} = \sum_{i=1}^{N}\left(y_i - \bar{y}\right)^2$, and $S_{xy} = \sum_{i=1}^{N}\left(x_i - \bar{x}\right)\left(y_i - \bar{y}\right)$.

R is a number between -1 and 1; R = 1 implies perfect positive correlation, R = -1 indicates perfect negative correlation, while R = 0 means that the variables are completely uncorrelated.

In Section 6.3, γ-ray flux is plotted against the flux in each of the other wavebands, to look for correlation between the flux levels. Using the *method of least-squares* (Porkess 2004), a straight line is fitted to each of the flux-flux plots. The *R-squared value* (R^2) shown on these plots is simply the square of the correlation coefficient (R), so it is a number between 0 and +1 indicating how closely the trendline (the straight line shown on the flux-flux plots) corresponds to the actual data. R^2 is also referred to as the *coefficient of determination* and can be interpreted as the proportion of the variance in y, which can be attributed to the variance in x.

6.3 Flux-flux Correlations in the Multiwavelength Data

Figure 6.8 shows the flux-flux correlation plot for the Whipple 10m and Milagro data (2000 – 2007). The values of the correlation coefficient are R = 0.40 for the monthly data and R = 0.69 for the annual-binned data.

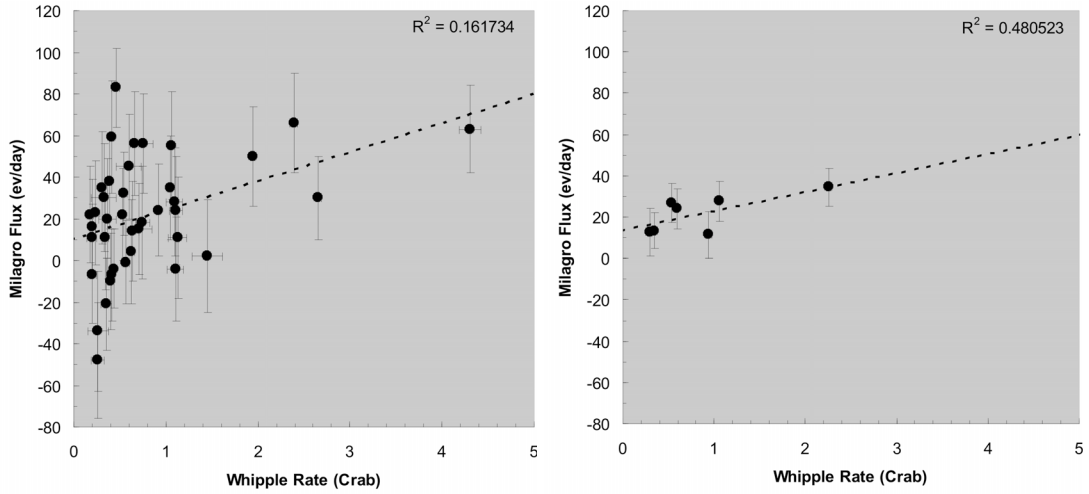

Figure 6.8 Flux-flux correlation for the Whipple 10m and Milagro Mrk 421 data on different timescales. *Left*: monthly-binned Whipple 10m and Milagro data; *Right*: annual-binned Whipple 10m and Milagro data.

The flux-flux plots for the *Fermi*-LAT and Whipple 10m data on daily and monthly timescales are shown in Figure 6.9. No evidence of correlation is found: R = -0.10 for the daily-binned data; R = -0.24 for the monthly-binned data. The absence of any correlation is hardly surprising since there is very little variation in the *Fermi*-LAT flux.

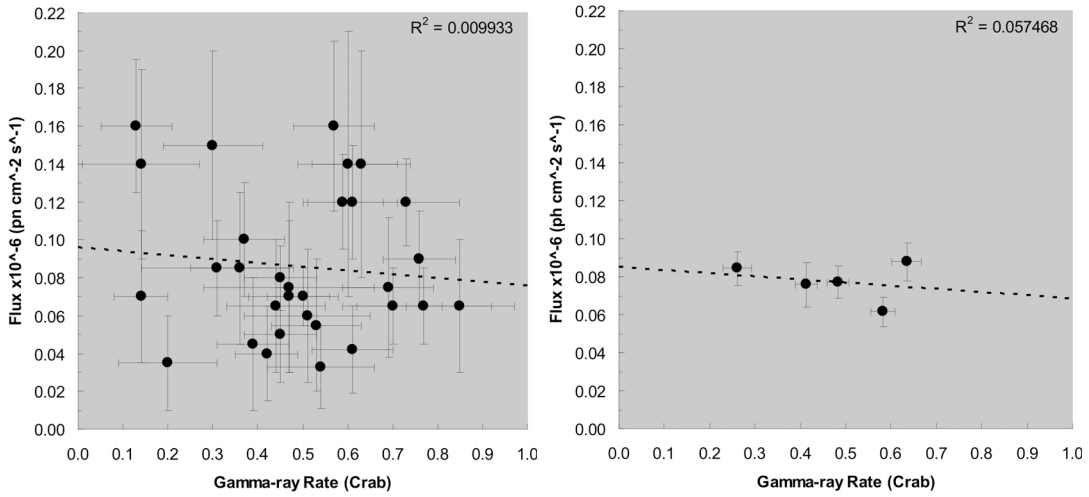

Figure 6.9 Flux-flux diagrams for the Whipple 10m and *Fermi*-LAT Mrk 421 data on different timescales. *Left*: daily-binned Whipple 10m and *Fermi*-LAT data (slope -0.020); *Right*: monthly-binned Whipple 10m and *Fermi*-LAT data (slope -0.017).

The *RXTE* ASM data (1995 – 2009) show evidence for emission correlated with the γ-ray data on monthly and annual timescales as shown in Figure 6.10. The correlation coefficients are $R = 0.74$ and $R = 0.71$ for the monthly and annual-binned data respectively.

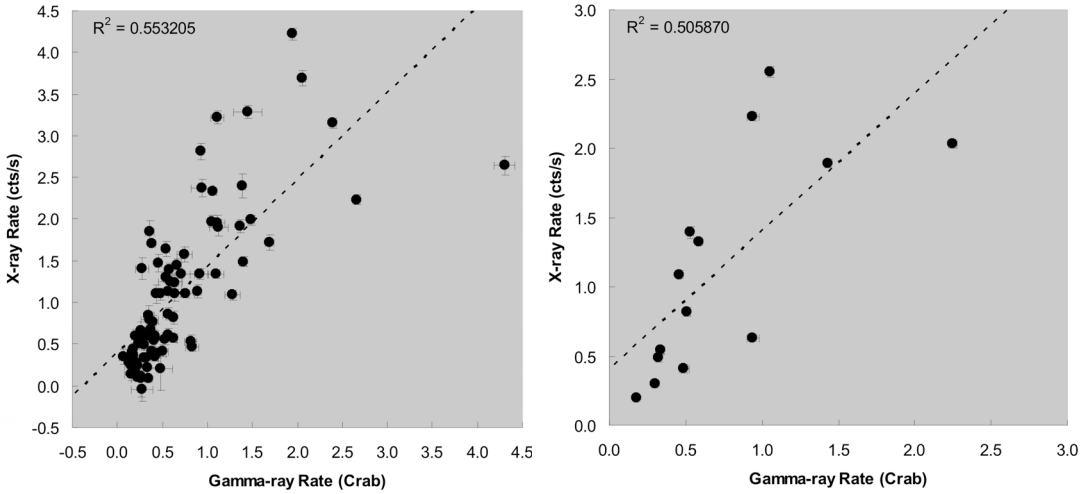

Figure 6.10 Flux-flux correlation for the Whipple 10m and *RXTE* ASM Mrk 421 data on different timescales. The dashed line shows the best-fit straight line. *Left*: monthly-binned γ-ray and *RXTE* ASM data (slope 1.04); *Right*: annual-binned γ-ray and *RXTE* ASM data (slope 0.99).

Due to the small variability amplitude for the radio waveband on the monthly-binned light curves only annual light-curve data are taken in consideration for the flux-flux plots. Metsähovi (2002 – 2008) and UMRAO (2005 – 2008) data are shown in Figure 6.11. The high *R*-squared values for 14.5 GHz and 4.8 GHz cannot be taken as indicating strong correlation but are due rather to the almost constant radio fluxes and the small number of data points available.

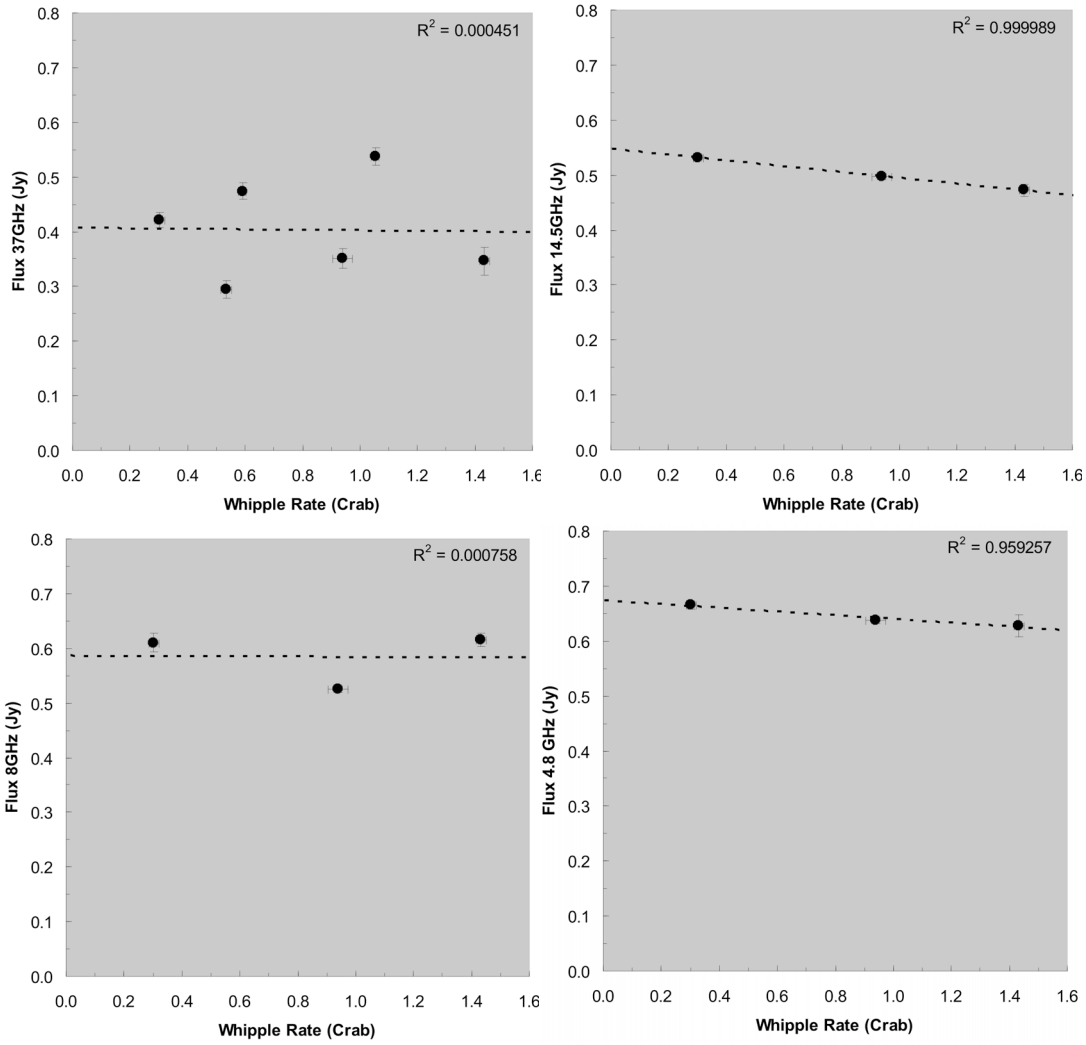

Figure 6.11 Flux-flux correlations for annual-binned Mrk 421 data. *Top left*: Whipple 10m and Metsähovi 37 GHz data; *Top right*: Whipple 10m and UMRAO 14.5 GHz data; *Bottom left*: Whipple 10m and UMRAO 8.0 GHz data; *Bottom right*: Whipple 10m and UMRAO 4.8 GHz data.

6.4 Discrete Correlation Function

To investigate in more detail the relationship between the radio, X-ray, Milagro and γ-ray light curves during the 1995 – 2009 period the *discrete correlation function* (DCF) was calculated. This method, described by Edelson & Krolik (1988), is analogous to the classical correlation function except that it can work with sparse, unevenly sampled data.

For each pair of points $[a(t_i), b(t_j)]$, taken from two datasets a and b, the time difference $\Delta t_{ij} = t_i - t_j$ is calculated, and the *unbinned discrete correlation function* (UDCF) is obtained using the equation shown below

$$UDCF_{ij} = \frac{\left[a(t_i) - \langle a \rangle\right]\left[b(t_j) - \langle b \rangle\right]}{\sqrt{\left(\sigma_a^2 - e_a^2\right)\left(\sigma_b^2 - e_b^2\right)}} \tag{6.6}$$

For dataset a, $\langle a \rangle$ is the mean, σ_a is the standard deviation and e_a is the mean measurement error, and similarly for dataset b. For any specified time delay T_{lag} between the two datasets, the $UDCF_{ij}$ values are then sorted into bins of width τ containing the N pairs (t_i, t_j) for which $T_{lag} - \tau/2 < \Delta t_{ij} < T_{lag} + \tau/2$. The more directly useful quantity DCF (T_{lag}) is then obtained by averaging over the N pairs:

$$DCF\left(T_{lag}\right) = \frac{1}{N}\sum UDCF_{ij} \tag{6.7}$$

Note that for $T_{lag} = 0$ the DCF should give a value similar to the standard correlation coefficient. The difference arises from the fact that the DCF takes into account the measurement error on each data point.

An estimate of the error in the DCF can be obtained from

$$\sigma_{DCF(T\,lag)} = \frac{1}{N-1}\sqrt{\sum\left[UDCF_{ij} - DCF\left(T_{lag}\right)\right]^2} \tag{6.8}$$

6.5 Discrete Correlation Functions for Multiwavelength Data

Figure 6.12 shows the DCF between the Whipple 10m and Milagro light curves for different values of the time lag, T_{lag} using bins of width τ = 30 days (the minimum bin width available for Milagro data). A maximum DCF value is observed for synchronous variability of both samples, i.e., a time lag shorter than 30 days, but the value is not statistically significant. The rather high value of the DCF at a time lag of about +2600 days can be traced to specific flaring features in the Whipple 10m data, and does not indicate a significant correlation between the two datasets.

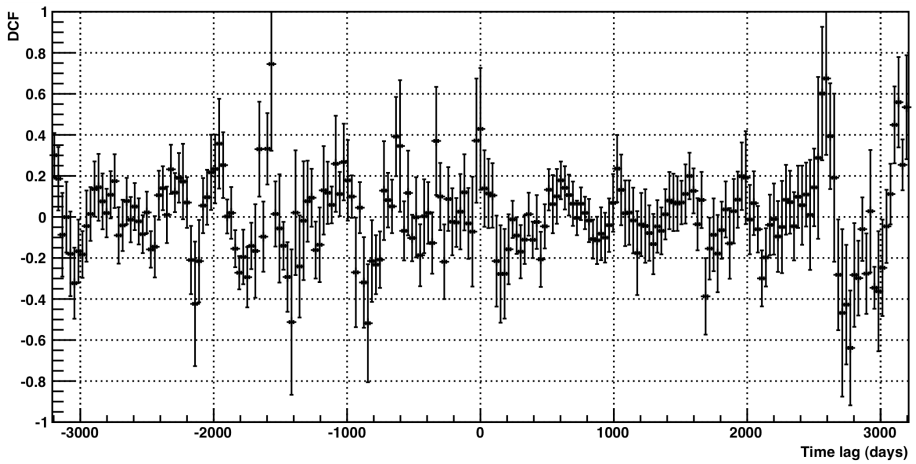

Figure 6.12 Discrete correlation function (DCF) for the complete Milagro and Whipple 10m Mrk 421 datasets, 30-day bins.

The DCF of the Whipple 10m and *Fermi*-LAT daily-binned data is shown in Figure 6.13. This comparison shows no evidence of correlation at any time lag, which is not surprising, as stated earlier, since there is very little variation in the *Fermi*-LAT flux.

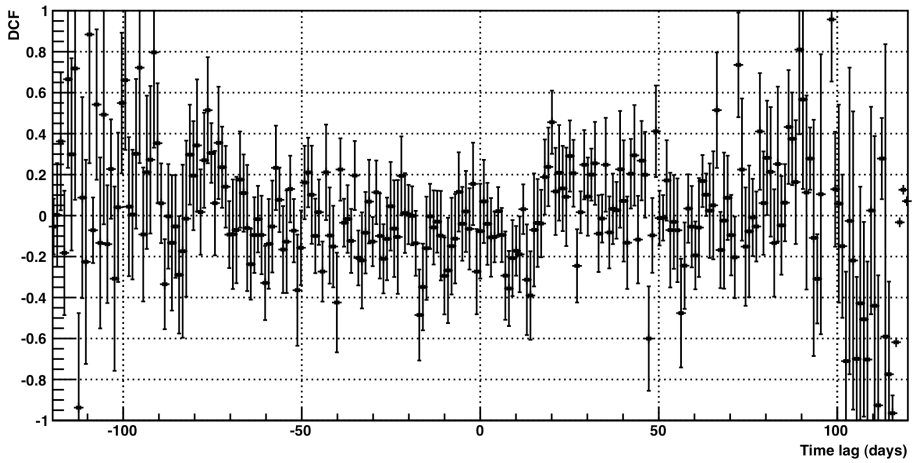

Figure 6.13 The DCF for the *Fermi*-LAT and Whipple 10m Mrk 421 datasets, 1-day bins.

The DCF between γ-ray and X-ray monthly averaged fluxes for time lags between -4800 and +4800 days is shown in Figure 6.14. The TeV and X-ray fluxes are seen to be significantly correlated (with a DCF value ~0.75) for a time shift shorter than 30 days; the maximum of the DCF is centred at a lag of (0 ± 15) days. The peak at -2000 days is an artefact, which occurs only because of the coincidence of maximum γ-ray rate at MJD 51595 and maximum X-ray rate at MJD 53597 (see Figure 5.23).

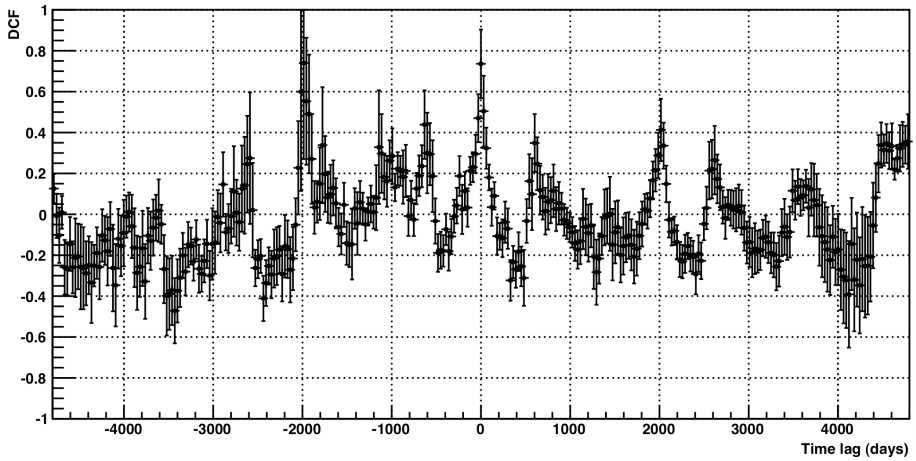

Figure 6.14 The DCF between Mrk 421 X-ray and γ-ray light curves. The apparent peak at -2000 days is spurious: it results from a coincidence between a maximum γ-ray rate and a maximum X-ray rate.

The *discrete autocorrelation function* (DACF) allows one to study the level of autocorrelation in unevenly sampled datasets (Edelson & Krolik 1988, Hufnagel & Bregman 1992) without any interpolation or addition of artificial data points. The DACF is essentially the DCF of a dataset with itself, i.e., in Equation 6.6, the dataset *b* is identical to *a*. The DACF can be used to look for evidence of periodicity in a sampled dataset.

The DACF for the Whipple 10m γ-ray dataset for Mrk 421 is plotted in Figure 6.15, and shows no evidence for periodicity at any period between 2 months and 7 years.

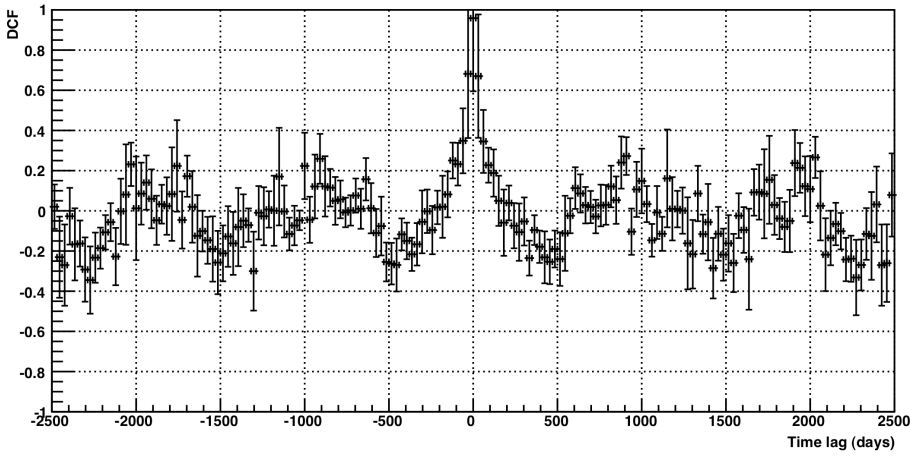

Figure 6.15 DACF for monthly-binned Mrk 421 γ-ray light curve (Whipple 10m telescope).

The corresponding plot for the *RXTE* ASM X-ray data is shown in Figure 6.16; again, there is no evidence for periodicity at any period between 2 months and 7 years.

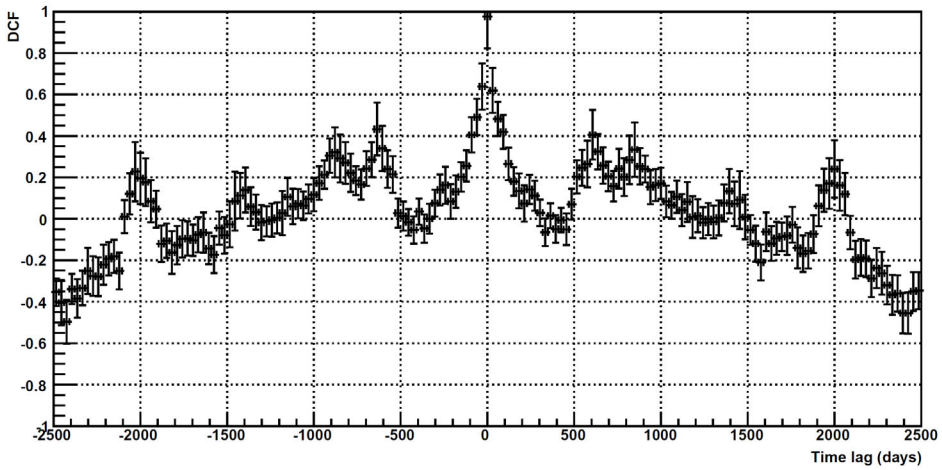

Figure 6.16 DACF for monthly-binned Mrk 421 X-ray light curve (*RXTE* ASM).

6.6 The Gamma-ray–Radio Connection

It is generally accepted that VHE γ-ray radiation in blazars comes from the base of the jet close to the black hole itself. It is possible that the disturbance responsible for this radiation could propagate out along the jet at close to the speed of light, and might gives rise to changes in the radio emission at larger distances. This effect is likely to be most evident in the morphology of the radio maps and can be illustrated by a simple geometrical model. Figure 6.17a shows a radio image of Mrk 421 looking down the jet, with the red superimposed sinusoid representing a disturbance which originates at the core and propagates at the speed of light; the angular distance relative to the core (i.e., *c4*) is ~2.2 mas. This corresponds to 1.4 pc at the distance 127.2 Mpc (Crook et al. 2007) derived for Mrk 421 from its redshift, z = 0.031, and Hubble's Law with an assumed slope of H_0 = 73 km s^{-1} Mpc^{-1} (Spergel et al. 2007). Therefore, if the disturbance propagates at the speed of light orthogonal to the line of sight it will take 4.6 years to travel the distance *c4*. Since the jet is approximately aligned with the line of sight, the geometry involved in this process is the one shown

in Figure 6.17b, where $\theta < 10°$ (as expected for blazars). The γ-ray signal emitted from the disturbance at the base of the jet will reach Earth after travelling the distance $a+b$ (which is 127.2 Mpc), while the disturbance itself follows the jet and gives rise after a distance A to synchrotron radiation which travels a distance B to Earth. The radio signal will then be delayed by $\Delta t = [(A+B)-(a+b)]/c$ relative to the γ-ray signal.

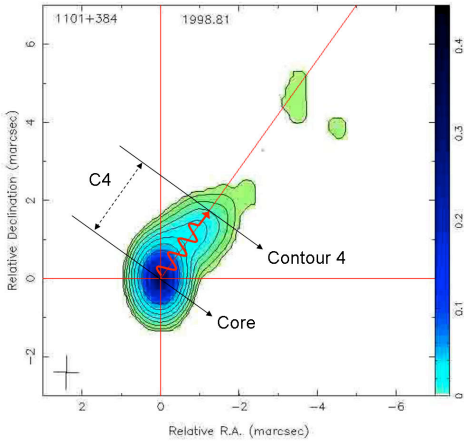

(*a*)

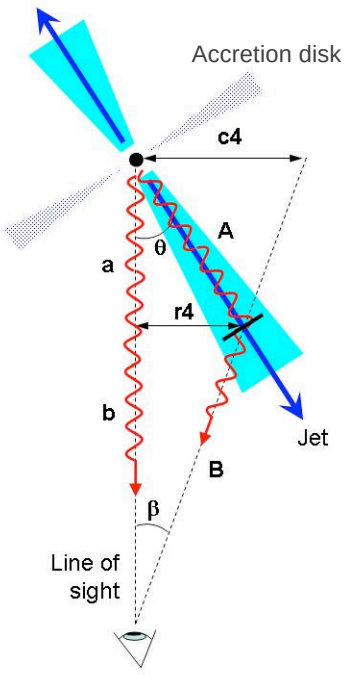

(*b*)

Figure 6.17 (*a*) Radio image of Mrk 421 showing the propagation of a disturbance orthogonal to the line of sight. (*b*) Disturbance propagating along the jet (β = 2.2 mas).

The orthogonal component of the real distance travelled by the disturbance is *r4* rather than *c4*, as shown in Figure 6.17b. The distance *r4* can be calculated using the following equation:

$$r4 = \frac{\tan\theta \cdot \tan\beta(a+b)}{\tan\theta + \tan\beta} \tag{6.9}$$

where β = 2.2 mas. The distance *r4* is always smaller than *c4*. For a small angle of the jet respect to the line of sight, for example, θ = 10°, the distance *r4* is equal to 1.37 pc. In this case, $c\Delta t$ is equal to 0.12 pc (0.36 light-years), which corresponds to a delay of ~5 months for a signal travelling the distance *A*+*B* at the speed of light. Of course if the actual jet angle is less than 10° the expected delay will be shorter.

The DCF approach can be used to search for evidence of such an effect.

6.6.1 Gamma-ray Flux versus Radio Contour Distance

The DCF between the radio core-contour distance *c4* (see Figure 5.21) and the γ-ray light curve for the period 1995 – 2001 is shown in Figure 6.18; a *positive* time lag means that changes in the γ-ray flux *precede* the radio variation.

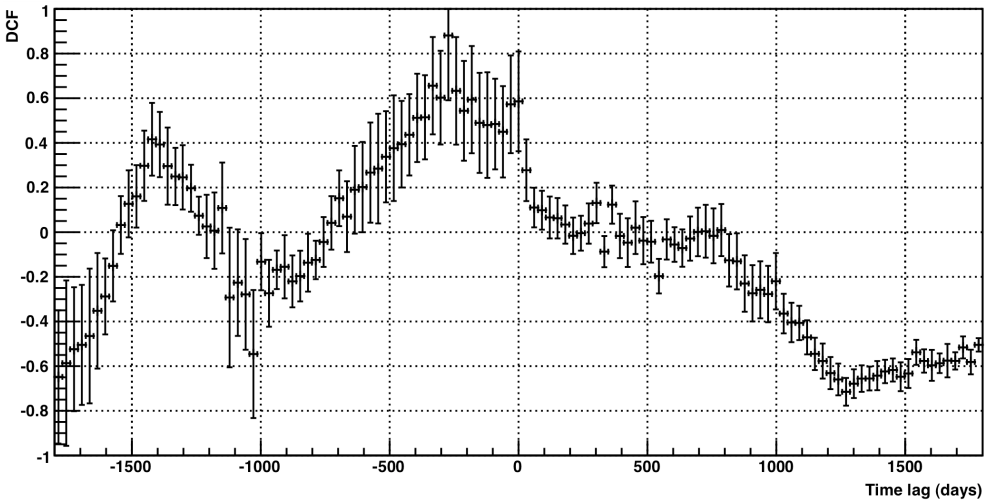

Figure 6.18 The DCF between γ-ray flux and *c4* distance.

The values of the DCF are very small for lags between 0 and +1000 days, indicating that the effect hypothesised earlier in this section is not present. Interestingly, there appears to be a peak in the DCF plot at a lag of about -300 days, which would correspond to changes in the radio morphology preceding changes in the γ-ray flux. Such behaviour is difficult to explain on the basis of any plausible physical model. Either the time lag is due to unrelated processes, or it is a real causal effect, in which case the magnitude of the delay implies that radio and γ-ray emission regions are separate. For example, one can consider material from the accretion disk falling onto the central black hole. Interaction of this material with the magnetic field would cause the emission of synchrotron radiation in radio frequencies first, affecting contours in the radio maps. The γ-ray emission would then arise when the effect of the infalling material propagates to the jet. Another explanation is that this time lag could be related to small movements of the jet due to the presence of a binary black hole system (Section 7.2). These movements would be detectable in the radio maps, forecasting an increase or decrease in γ-ray activity as the jet aligns more or less with the line-of-sight.

DCFs between the radio core-contour distances *c6* and *c8* and the γ-ray flux are shown in Figures 6.19 and 6.20. Again, a positive time lag means that the γ-ray flux precedes the radio variation. In the DCF plot for the *c6* contour, there again appears to be a feature at a time delay similar to that seen for *c4*.

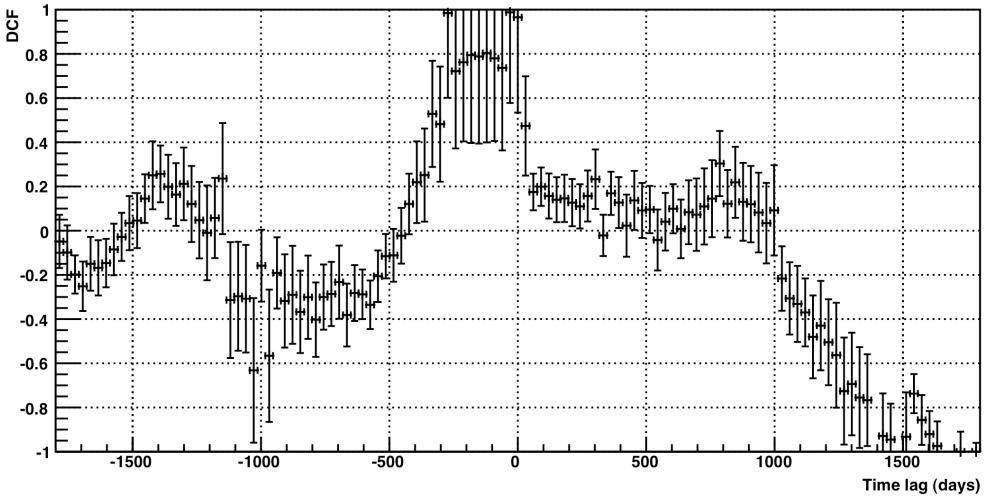

Figure 6.19 DCF between γ-ray flux and *c6* distance.

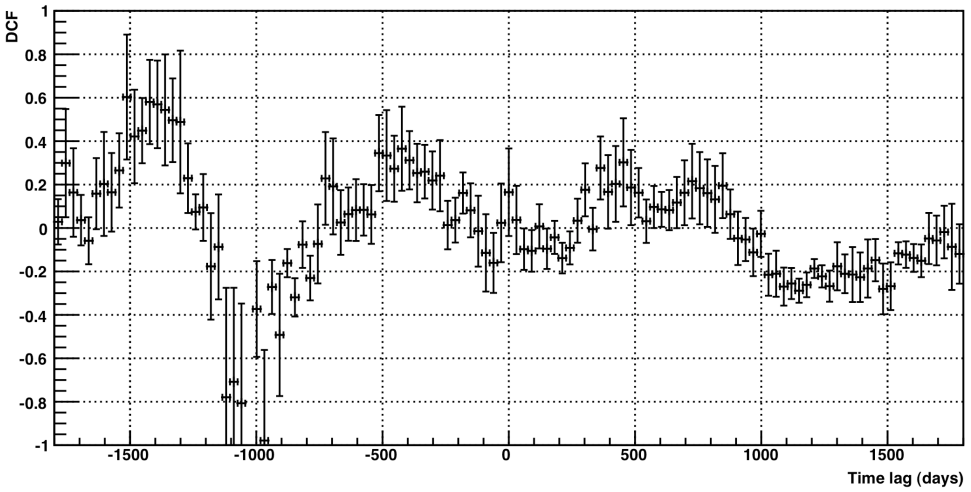

Figure 6.20 DCF between γ-ray flux and *c8* distance.

For Figure 6.18, for contour *c4* at a time lag of -270 days, the DCF value appears to be fairly high, although the error bar is large. To investigate this in more detail, γ-ray points that have a corresponding *c4* distance point 270 days earlier (within a bin of ±15 days) were selected in order to generate a plot of *c4* (at time *t*-270 days) against γ-ray flux (at time *t*), as shown in Figure 6.21. The R^2 value for this plot is rather low, and the plot is heavily influenced by a small number of high-flux points (from flaring episodes). Moreover, the bump at -270 days does not appear in the DCF plot for radio contour *c4* versus X-ray flux, shown in Figure 6.22; given that the γ-ray and X-ray fluxes appear to be well correlated, this result also suggests that the effect in Figure 6.18 may not be highly significant.

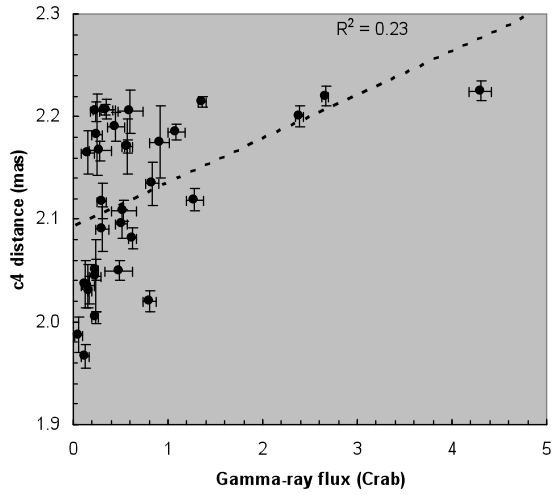

Figure 6.21 Correlation plot for *c4* distance at time *t* – 270(±15) days versus γ-ray flux at time *t*.

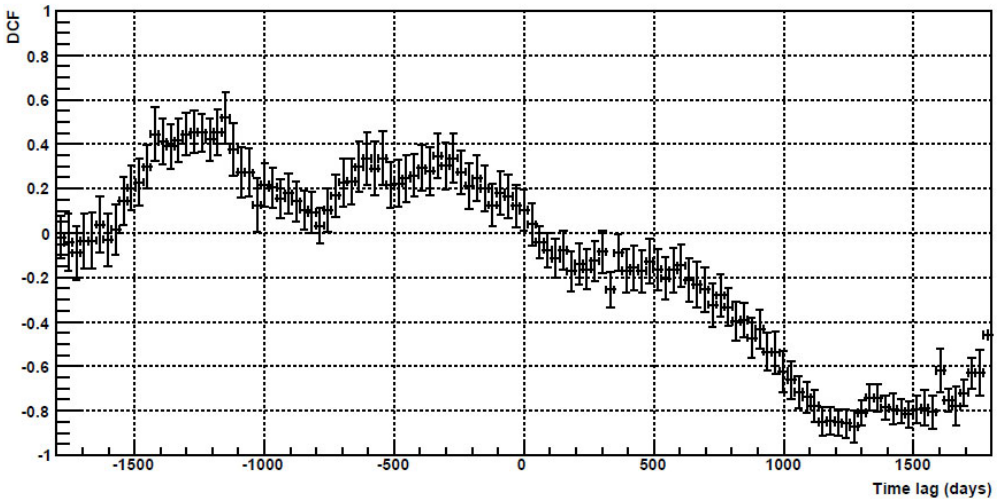

Figure 6.22 DCF between X-ray flux and *c4* distance: this plot shows no evidence for any effect in the region of -270 days.

Chapter 7

Interpretation and Discussion

The behaviour of broadband radio-to-γ-ray emissions from Mrk 421 revealed substantial differences in the level of variability, increasing with the energy. The multiwavelength data taken over the extended period 1995 – 2009 provides information on the monthly and annual flux variability of this source. No significant correlation between emission in the low-energy and high-energy regimes was found, although some interesting results were obtained when analysing radio contours from VLBA images of Mrk 421 and comparing them with the γ-ray light curves, as described in Section 6.3. Previous work has shown how the two energy peaks of the characteristic SED of blazars (Section 1.4) shift to higher energies when the source goes in high state activity. Section 7.1 attempts to give an explanation of how the flux variability observed for Mrk 421 in specific energy regimes can depend on the shape of its SED, and how this can help in interpreting the results obtained from the correlation studies.

Different mechanisms can cause variability in the brightness of the non-thermal emission from blazar jets. In Section 7.2, three different ideas of how the behaviour of the γ-ray light curve of Mrk 421 can be related to the radio jet development are presented.

Very-high-energy γ-ray photons can be observed from the ground by detecting the Cherenkov radiation from secondary particles in the atmospheric cascades initiated by the interaction of the γ-ray photons with the atmosphere. The current generation of instruments has demonstrated that TeV astronomy is a rich field of research. Section 7.3 summarises the present and possible future of ground-based γ-ray astronomy, which was born about 20 years ago with the detection of TeV γ-ray radiation from the Crab Nebula (Section 1.4.1) using the Whipple 10 m telescope.

7.1 Major Results from Long-term Observations of Mrk 421

Observations of Mrk 421 over a wide energy range and over an extended time period can lead to profound implications and limitations for proposed emission models. For the data taken from 1995 to 2009, the X-ray flux shows a definite correlation with the TeV flux, as expected in blazar leptonic models. For both monthly and annual timescales (see Figure 6.10) strong linear correlation coefficients were obtained, $R = 0.74$ and $R = 0.71$, respectively. These findings are consistent with results from previous multiwavelength campaigns (Buckley et al. 2008, Rebillot et al. 2006, Maraschi et al. 1999).

The fact that the *Fermi*-LAT flux does not show much variation did at first seem surprising. It could be attributed to the relatively low sensitivity on such a short timescale (one month), which would tend to obscure any variability unless very pronounced. On the other hand, the absence of any significant variability may be a very interesting result in the light of the X-ray and TeV variability. It could be a reflection of the shape of the SED, and the way that changes. Both the X-ray and TeV observations are on negative-slope regions of the SED, whereas the *Fermi* range is on a positive slope. It is possible that when the electron density increases (in a flare, for example), the level of the SED rises but at the same time the two peaks shift to higher energy: it is then easy to imagine a situation where the X-ray and TeV fluxes rise as the SED rises, but because *Fermi* is on an upward-slope region, the effect of the rising SED is offset by the shift to higher energy. This could explain the behaviour seen in Figure 6.9.

Applying the Pearson's product moment-correlation method on flux-flux diagrams, no evidence was found for a correlation between the observed (4.8, 8.0, 14.5 and 37 GHz) radio and γ-ray fluxes (see Figure 6.11). The same result is obtained using the discrete correlation function (DCF) value for a time lag of 0. There is some evidence of a delay between the core-contour distances and the γ-ray month-scale variability. On the DCF diagrams, there is a tendency for the contour distances *c*4 and *c*6 to lead the γ-ray fluxes, but the statistical significance is not high.

The pattern of variability in different wavelength regions can have important implications for the modelling of the radiation processes. If the variability in two

bands shows the same pattern as a function of time, with the variations occurring in phase, then one can conclude that the radiation in the two bands is very likely to be produced by the same mechanism and in the same spatial region. However if the variation in one band systematically lags behind that in the other, then *propagation* from one region to another may be involved. This could explain possible lags that might exist between the radio contour measurements and the γ-ray data.

In Figure 7.1, the Discrete Autocorrelation Function (DACF) for 14 years of γ-ray data is shown. This is essentially the same plot as that shown in Figure 6.15, but in this case the data have been grouped in bins of three months each, to make it easier to visualise the long-term behaviour. The discrete autocorrelation function is found by calculating the DCF for a time series with itself. Investigating how well a time series correlates with a copy of itself may expose periodicity (intrinsic or spurious) in the time series. The main idea behind this is that the DACF of a periodic function is itself periodic with the same period. So, if there is a period, *p*, in the light curve, then the DACF can reveal the periodical component. It is clear from the Figure 7.1 that no periodic behaviour exists on time scales up to ~7 years (the maximum period that can be investigated with a 14-year observation span). On the other hand, with the one-month binning in Figure 6.15, periods greater than 2 months can be excluded. For periodic times less than 2 months, the number of events is generally too small to identify any periodic trends.

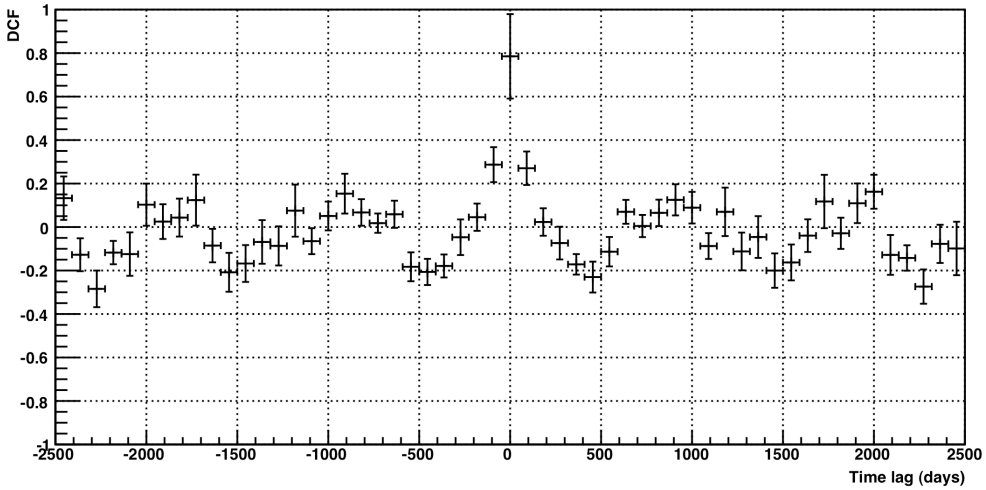

Figure 7.1 DACF of three-month binned γ-ray data on Mrk 421 taken with the Whipple telescope.

However, there have been various reports of a periodic or quasi-periodic component to the γ-ray and X-ray emission from Mrk 501 on week and month timescales (Nishikawa et al. 1999; Kranich et al. 2001; Rödig et al. 2009). For Mrk 421, Liu et al. (1997), using optical data reaching back to 1900, suggest evidence for two possible periods: one of about 23 years and another (less significant) of about 15 years. In this work, the search for similar periodicities in the Mrk 421 Whipple and *RXTE* data using the DACF shows no evidence for any periodic component with period between 2 months and 7 years, but further study of the long-term characteristic variability of Mrk 421 using the Lomb-Scargle periodogram (Lomb 1976; Scargle 1982) or the Jurkevich method (Jurkevich 1971) may be warranted.

7.2 Jet Components and Emission Models

In May 1996, Markarian 421 underwent an unprecedented outburst at TeV energies (Gaidos et al. 1996), motivating observations with the VLBA to investigate whether changes in the milliarcsecond structure are associated with such VHE flares, but no significant connection was found (Edwards et al. 1998).

The complicated light curves of blazars can be explained reasonably well by a physical scenario in which a twisted relativistic jet containing a hydromagnetically turbulent plasma undergoes fluctuations in its energy input. This causes shock waves to develop and propagate. The evolution of the emission from such shocks can account for both the long-term and short-term behaviour of the observed light curves. In this thesis, an interpretation of the long-term behaviour of Mrk421 light curves, through a possible link between high-energy fluxes and radio-jet morphology has been attempted. Three different scenarios have been considered which would suggest that changes in the radio morphology should lag changes in the high-energy flux (positive lag). However, it should be noted that the behaviour exhibited in the DCF plots would imply the opposite behaviour (negative lag), a situation which is more difficult to account for on the basis of plausible physical models.

- **Synchrotron cooling**

The behaviour of the DCF plots in Figures 6.18 and 6.19 suggests a negative lag between radio morphology and γ-ray flux (i.e., radio map changes *lead* the γ-ray flux changes), but this is opposite to what would be expected for a reasonable physical model. If the electron density is altered, asymmetric changes in the fluxes of the synchrotron and self-Compton components occur, with the Compton component more affected by these changes (Bloom & Marscher, 1996). Variations in the amplitude of the spectrum of injected electrons results in flaring at X-ray and TeV energies (Mastichiadis & Kirk 1997). Flares at low energies lag prompt flares at high energies. It is suggested that this is because the higher-energy electrons have a shorter synchrotron cooling time so that the newly-injected high-amplitude electron population cools with emission of high frequencies first and lower frequencies later, giving rise to the lag, so that changes in the radio morphology would be expected to occur some time after the changes in γ-ray flux.

- **Plasma Propagation.**

Models that attempt to describe the radiation processes must take into account the pattern of variability in different bands of the spectrum. In this case, for the available radio data of Mrk 421, between 1995 and 2001, the variation seems to lag behind the γ-ray band.

As mentioned in the introduction of Chapter 6, if the source is bigger than the limit imposed by Equation 6.1, different parts of the source cannot vary in phase with one other. Mrk 421 showed extremely strong flares in 1996, 2001 and 2008, as described in detail in Section 5.1.2. The rise and fall of the Mrk 421 flares have sometimes as short as a few minutes, implying a very compact emission region. In the TeV range, if the observed variability time scale is ~200 seconds it implies a minimum bulk Lorentz factor greater than 50 (Begelman, Fabian & Rees 2008) assuming an homogeneous one-zone model. However, such high values of the bulk Lorentz factor are in contradiction with constraints derived from other observational evidence (Urry & Padovani 1995; Henri & Saugé 2006). Furthermore, one-zone models are unable to fit the entire spectrum, with the low-energy radio points being generally attributed to more distant emitting regions. Boutelier et al. (2008) presented

a new approach, unifying small and large scales emission regions. They consider that the radio jet is actually filled by the same particles originating from the high energy emitting region at the bottom of the jet that have propagated along the jet. They thus describe the emitting plasma by a continuous (although variable) particle injection, subjected to continuous reacceleration and radiative cooling.

Figure 6.17 illustrates a propagation phenomenon geometrically. Essentially the question is: if something happens in the core of the radio map, how long will it take, travelling at speed of light, to get to a specific distance (in this case contours C8, C6 and C4) from the core? The precision of the delay calculations depend on the accuracy of the measurement of the distance of Mrk421 from Earth and the resolution of the radio images.

- **Binary black holes**

The high variability of the flux observed in AGN may be periodic, which in turn could be the signature of a binary black hole (BBH). Systems of black holes are strong emitters of gravitational waves whose amplitude depends on the binary orbital parameters such as the component mass, orbital semi-major axis and eccentricity (Rödig et al. 2009). The existence of BBHs seems plausible since the host galaxies of most AGN are ellipticals, which originate from galaxy mergers. BBHs have already been detected (Sillanpää 1998; Sudou et al. 2003; Hudson et al. 2006), but most sources are far too distant for to be resolved in radio or X-rays. A simultaneous periodicity in different wavelengths would provide evidence for bound BBHs in the core of AGN. The Chandra satellite was able to show X-rays coming from two nuclei in the central region of the starburst galaxy NGC 6240 (Komossa et al. 2003), as shown in Figure 7.2.

As suggested in Section 5.2, the VHE activity of Mrk 421 at any given time may depend on the orientation of the jet at that time, i.e., it is possible that the observed γ-ray variability of Mrk 421 has a geometrical origin. This hypothesis relies on the assumption that the variation of the γ-ray flux can be caused by a slight change of the inclination angle with respect to the line of sight, which is caused by the orbital motion of the jet-emitting (secondary) black hole. A periodically changing viewing angle (due to a precession of the jet or to small periodic perturbations) may

thus naturally lead to a periodicity, or flux modulation, in the observed light curves. The core-contour distance variations studied in this thesis could also be the effect of slight movements of the jet.

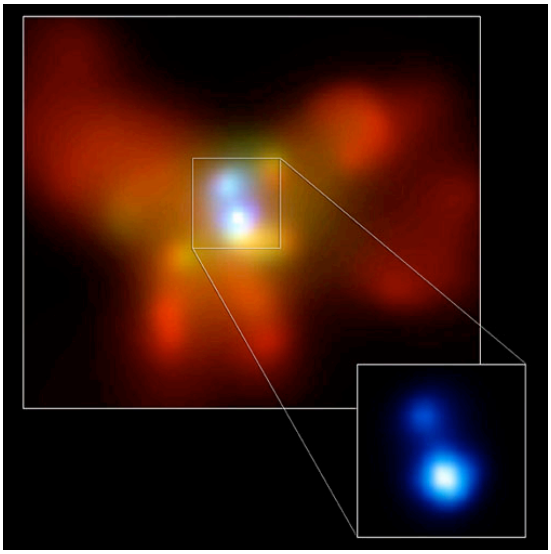

Figure 7.2 NGC 6240 is a galaxy that is the product of the collision of two smaller galaxies. This Chandra image revealed that the central region of NG C6240 contains two active giant black holes. Credit: NASA/CXC/MPE/S.Komossa et al.

The results related to the core-contour distances and γ-ray fluxes do not lead to definitive conclusions, however. No correlation between radio contours (*c*4, *c*6, *c*8), and γ-ray fluxes of Mrk 421 was found in this work, but further investigation and richer long-term observations of this source could reveal interesting features. Radio and VHE observations of the radio galaxy Messier 87 revealed a period of extremely strong VHE γ-ray flares accompanied by a strong increase of the radio flux from its nucleus. These results imply that particles are accelerated to very high energies in the immediate vicinity of the black hole (Acciari et al. 2009b), and shows also a connection between the low-energy and high-energy regimes. It is likely that similar behaviour can be found in the blazar population also.

Time lags with longer wavelengths leading shorter ones have been interpreted as fluctuations in the accretion disc, propagating from the outer emitting regions toward the innermost γ-ray emitting region. Several multiwavelength monitoring campaigns have searched for correlations and time lags between the two energy bands, in a number of AGN (Maraschi et al. 1994; Rebillot et al. 2006; Buckley et al.

2008; Horan et al. 2009). However, the sign of the time lag can be different from case to case, and even the existence of correlations is not always confirmed. The global picture is still quite confusing and the problem seems not definitively settled; at least not yet!

7.3 The Future of Ground-based γ-ray Astronomy

TeV γ-ray astronomy saw its first major success in the year 1989 with the firm detection of a cosmic source of TeV γ-ray emission, the Crab Nebula, with the Whipple 10m telescope (Weekes et al. 1989). Advances in instrumentation and analysis techniques have since established TeV γ-ray astronomy as one of the most exciting new windows on the Universe. The VERITAS, H.E.S.S. and MAGIC experiments have shown a glimpse of the discovery potential of this new type of astrophysics. The present generation of atmospheric Cherenkov telescopes (ACTs) such as VERITAS can detect point sources with a flux sensitivity of 1% of the Crab Nebula (corresponding to a νF_ν-flux of $\sim 5\times10^{-13}$ ergs cm^{-2} s^{-1} at 1 TeV) in as little as 25 hours. The improvement of sensitivity by two orders of magnitude during the last two decades has been made possible due to critical advances in ACT technology. Large extensive air shower (EAS) arrays provide complementary technology for observations of very high-energy γ-ray radiation. While the instantaneous sensitivity is currently a factor ~150 lower than that of ACTs, their large field of view and nearly 100% duty cycle make these observatories particularly suited to conduct all-sky surveys and detect emission from extended astrophysical sources. Milagro was the first ground-based γ-ray observatory which utilized EAS technology (Section 3.4). Due to the increased sensitivity of all these instruments, the number of known TeV γ-ray sources has increased from ~10 to ~100 in the past few years.

The present generation of ground-based instruments was joined in mid-2008 by the Fermi Gamma-ray Space Telescope (*Fermi*). One of the instruments on board, the Large Area Telescope (see Section 3.3.2 for details), covers the γ-ray energy band from 30 MeV to 300 GeV and therefore has some spectral overlap with ACTs. The present generation of ACTs match the νF_ν-sensitivity of *Fermi*.

Ground-based TeV γ-ray observatories have made spectacular discoveries including imaging spectroscopy observations of galactic sources of different classes, and the discovery of rapid γ-ray flares from radio galaxies and AGN containing supermassive black holes. These discoveries, and the fact that γ-ray astronomy has the potential to map the radiation from dark-matter annihilation in our Galaxy and in extragalactic systems, have attracted the attention of the wider scientific community.

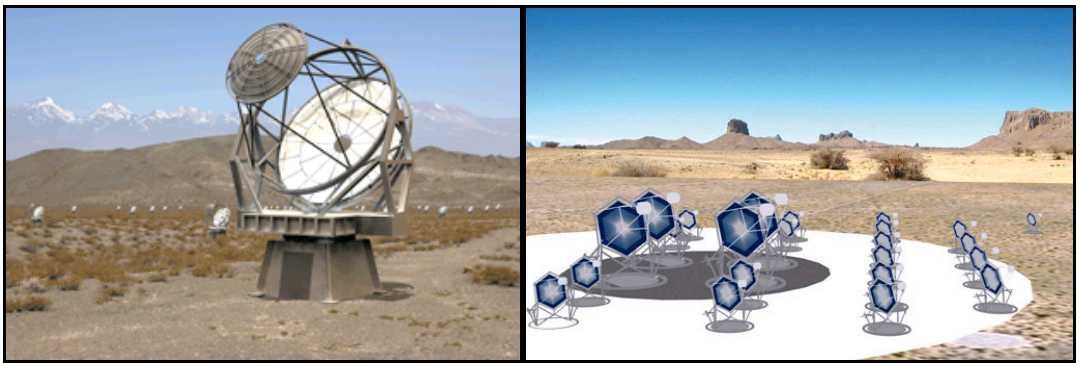

Figure 7.3 The next generation of atmospheric Cherenkov telescopes. *Left*: Proposed AGIS telescopes. *Right*: A possible design of CTA, using different sized telescopes throughout the array. Large mirrors in the centre collect enough light to catch dim showers from low-energy gamma rays. To collect large statistics at high energies, where particles are rare but the associated showers are bright, smaller mirrors cover an area of a few square kilometres (CTA Consortium 2010).

The way forward has been spearheaded by two proposals for the next ground-based gamma-ray observatory: the Advanced Gamma-ray Imaging System (AGIS) in the U.S. (AGIS Collaboration 2008; Buckley et al. (2008)) and the European Cherenkov Telescope Array (CTA). A number of possible designs were put forward for both projects (an artist's concept of AGIS and CTA is shown in Figure 7.3). Since early 2010, the U.S. and European efforts have combined in the worldwide CTA Collaboration, with the aim of constructing a γ-ray observatory capable of addressing the needs of the astronomical community for the next several decades. The CTA observatory is likely to consist of two arrays: a southern hemisphere array (of about 100 ACTs) covering the full energy range from about 10 GeV to about 100 TeV to allow for a deep investigation of galactic sources, and a

complementary northern hemisphere array (of about 50 ACTs) with a smaller energy range (from ~10 GeV to ~1 TeV) dedicated mainly to northern extragalactic objects (CTA Consortium 2010). A factor of 5–10 improvement in sensitivity compared with current arrays is foreseen (in the energy range ~100 GeV to ~20 TeV), together with a lower energy threshold (<40 GeV) and a higher energy resolution (large effective area). Construction of the experiment could begin within the next few years.

The Whipple 10m telescope, which has been described in detail in this thesis, set the standard for ground-based γ-ray astronomy and was the most powerful instrument in this field for many years. The enormous amount of data taken with this telescope has made possible the long-term study of Mrk 421 discussed in this thesis. Even though its sensitivity is much smaller than the newer ACT arrays, it remains a valuable scientific instrument. It has the ability to detect blazars when they are flaring at or near the flux level of the Crab Nebula. It continues to operate as an AGN monitoring instrument, with alerts sent to VERITAS. It can also be used in the future to test new pieces of optics and electronics, such as implementing a new type of PMT camera, for example. Finally, it is a magnificent didactic tool for new observers. For all of these reasons and more, the Whipple 10m telescope can surely continue to make important contributions to the future of ground-based γ-ray astronomy.

Bibliography

Abdo, A. A., et al. 2007a, *Discovery of TeV Gamma-ray Emission from the Cygnus Region of the Galaxy*, The Astrophysical Journal Letters 658, 33.

Abdo, A. A., et al. 2007b, *Milagro Constraints on Very High Energy Emission from Short-Duration Gamma-Ray Bursts*, The Astrophysical Journal 666, 361.

Abdo, A. A., et al. 2011, *Gamma-Ray Flares from the Crab Nebula*, Science, DOI: 10.1126/science.1199705.

Acciari, V. A., et al. 2008, *Observations of Gamma-ray Emission from the Galaxy M87 above 250 GeV with VERITAS*, The Astrophysical Journal 679, 397.

Acciari, V. A., et al. 2009a, *A connection between star formation activity and cosmic rays in the starburst galaxy M82*, Nature 462, 770.

Acciari, V. A., et al. 2009b, *Radio Imaging of the Very-High-Energy γ-Ray Emission Region in the Central Engine of a Radio Galaxy*, Science 325, 444.

Acciari, V. A., et al. 2009c, *Simultaneous Multiwavelength Observations of Markarian 421 During Outburst*, The Astrophysical Journal 703, 169.

Acciari, V. A., et al. 2010a, *VERITAS Search for VHE Gamma-ray Emission from Dwarf Spheroidal Galaxies*, The Astrophysical Journal 720, 1174.

Acciari, V. A., et al. 2010b, *Observations of the Shell-type Supernova Remnant Cassiopeia A at TeV Energies with VERITAS*, The Astrophysical Journal 714, 163.

Acero, F., et al. 2009, *Detection of Gamma Rays from a Starburst Galaxy*, Science, 326, 1080.

AGIS Collaboration 2008, http://www.agis-observatory.org.

Aharonian, F., et al. 2003, *Is the giant radio galaxy M 87 a TeV gamma-ray emitter?*, Astronomy and Astrophysics 403, 1.

Aharonian, F., et al. 2005a, *H.E.S.S. observations of PKS 2155-304*, Astronomy and Astrophysics 430, 865.

Aharonian, F., et al. 2005b, *Observations of Mkn 421 in 2004 with HESS at large zenith angles*, Astronomy and Astrophysics 437, 95.

Aharonian, F., et al. 2007, *An Exceptional Very High Energy Gamma-Ray Flare of PKS 2155-304*, The Astrophysical Journal 664, 71.

Aharonian, F., et al. 2009, *Discovery of Very High Energy γ-Ray Emission from Centaurus A with H.E.S.S.*, The Astrophysical Journal Letters 695, 40.

Aliu, E., et al. 2008, *Observation of Pulsed Gamma-rays Above 25 GeV from the Crab Pulsar with MAGIC*, Science 322, 1221.

Aller, H. D., Aller, M. F., Latimer, G. E. and Hodge, P. E. 1985, *Spectra and linear polarizations of extragalactic variable sources at centimeter wavelengths*, The Astrophysical Journal Supplement 59, 513.

Atkins, R., et al. 2005, *Constraints on Very High Energy Gamma-Ray Emission from Gamma-Ray Bursts*, The Astrophysical Journal 630, 996.

Begelman, M. C., Fabian, A. C. and Rees, M. J. 2008, *Implications of very rapid TeV variability in blazars*, Monthly Notices Royal Astronomical Society Letters 384, 19.

Beilicke, M., et al. 2007, *Discovery of fast variability of the TeV γ-ray flux from the giant radio galaxy M87 with H.E.S.S.*, AIP Conference Proceedings 921, 147.

Benbow, W., et al. 2001, *A Search for TeV Gamma-Ray Emission from Selected AGN Using Milagro*, Proceedings of 27th International Cosmic Ray Conference (Hamburg) 7, 2649.

Biretta, J. A., Sparks, W. B. and Macchetto, F. 1999, *Hubble Space Telescope Observations of Superluminal Motion in the M87 Jet*, The Astrophysical Journal 520, 621.

Błażejowski, M., et al. 2005, *A multiwavelength view of the TeV blazar Markarian 421: correlated variability, flaring, and spectral evolution*, The Astrophysical Journal 630, 130.

Bloom, S. D. and Marscher, A. P. 1996, *An Analysis of the Synchrotron Self-Compton Model for the Multi-wave Band Spectra of Blazars*, Astrophysical Journal 461, 657.

Boutelier, T., Henri, G. and Petrucci, P.-O. 2008, *An inhomogeneous jet model for the rapid variability of TeV blazars*, Monthly Notices Royal Astronomical Society Letters 390, 73.

Bradt, H. V., Rothschild, R. E. and Swank, J. H. 1993, *X-ray timing explorer mission*, Astronomy and Astrophysics Supplement 97, 335.

Brighton, A., et al. 2001, http://archive.eso.org/cms/tools-documentation/skycat.

Buckley, J. 2000, *Gamma ray astronomy*, Proceedings of 26th International Cosmic Ray Conference (Salt Lake City) 516, 195.

Buckley, J., et al. 2008, *The Status and future of ground-based TeV gamma-ray astronomy. A White Paper prepared for the Division of Astrophysics of the American Physical Society*, eprint arXiv:0810.0444.

Carroll, B. W. and Ostlie, D. A. 1996, *An Introduction to Modern Astrophysics*, Addison-Wesley Publishing Company.

Catanese, M., et al. 1998, *Discovery of Gamma-Ray Emission above 350 GeV from the BL Lacertae Object 1ES 2344+514*, The Astrophysical Journal 501, 616.

Cawley, M. F., et al. 1990, *A high resolution imaging detector for TeV gamma-ray astronomy*, Experimental Astronomy 1, 173.

Chadwick, P. M., et al. 1999, *Very High Energy Gamma Rays from PKS 2155-304*, The Astrophysical Journal 513, 161.

Clark, D. H. and Stephenson, F. R. 1977, *Do all galactic supernovae produce long-lived remnants?*, Monthly Notices Royal Astronomical Society 179, 87.

Clark, D. H. and Stephenson, F. R. 1977, *The historical supernovae*, Pergamon Press.

Cocconi, G. 1960, *An air shower telescope and the detection of 1012 eV photon sources*, Proceedings of 6th International Cosmic Ray Conference (Moscow) 2, 309.

Condon, J. J., et al. 1998, *The NRAO VLA Sky Survey*, The Astrophysical Journal 115, 1693.

Costamante, L. 2004, *A brief (blazar oriented) overview on topics for multiwavelength observations with TeV photons*, New Astronomy Review 48, 497.

Cranshaw, T. E. 1963, *Cosmic Rays*, Clarendon Press.

Crook, A. C., et al. 2007, *Groups of Galaxies in the Two Micron All Sky Redshift Survey*, The Astrophysical Journal 655, 790.

CTA Consortium 2010, *Design Concepts for the Cherenkov Telescope Array*, arXiv:1008.3703v2.

Cui, W. 2004, *X-Ray Flaring Activity of Markarian 421*, The Astrophysical Journal 605, 662.

Dar, A. and Laor, A. 1997, *Hadronic Production of TeV Gamma-Ray Flares from Blazars*, The Astrophysical Journal Letters 478, 5.

Davies J. M. and Cotton E. S. 1957, *Design of the Quartermaster solar furnace*, Journal of Solar Energy 1, 16.

Dermer, C. D., Schlickeiser, R. and Mastichiadis, A. 1992, *High-energy gamma radiation from extragalactic radio sources*, Astronomy and Astrophysics 256, 27.

Dunlea, S. 2001, *TeV Astrophysical Gamma-ray selection using a multivariate Kernel selection algorithm*, PhD Thesis, University College Dublin.

Edelson, R. A. and Krolik, J. H. 1988, *The Discrete Correlation Function: A New Method for Analyzing Unevenly Sampled Variability Data*, The Astrophysical Journal 333, 646.

Edwards, P. G., Moellenbrock, G. A., Unwin, S. C., Wehrle, A. E. and Weekes, T. C. 1998, *Markarian 421: TeV Gamma-ray Flares and VLBI Structure*, Astronomical Society of the Pacific Conference Series 144, 45.

Fanaroff, B. L. and Riley, J. M. 1974, *The morphology of extragalactic radio sources of high and low luminosity*, Monthly Notices Royal Astronomical Society 167, 31.

Fegan, S. 2006, private communication.

Fermi-LAT Collaboration 2008, http://www.nasa.gov/mission_pages/GLAST/spacecraft/index.html.

Finley, J. P., et al. 2001, *The Granite III Upgrade Program of the Whipple Observatory*, Proceedings of 27th International Cosmic Ray Conference (Hamburg) 7, 2827.

Fossati, G., et al. 1998, *A unifying view of the spectral energy distributions of blazars*, Monthly Notices Royal Astronomical Society 299, 433.

Fossati, G., et al. 2008, *Multiwavelength Observations of Markarian 421 in 2001 March: An Unprecedented View on the X-Ray/TeV Correlated Variability*, The Astrophysical Journal 677, 906.

Freedman, W. L., et al. 2001, *Final results from the Hubble Space Telescope key project to measure the Hubble constant*, The Astrophysical Journal 553, 47.

Gaidos, J. A., et al. 1996, *Extremely rapid bursts of TeV photons from the active galaxy Markarian 421*, Nature 383, 319.

Galbraith, W. and Jelley, J. V. 1953, *Light Pulses from the Night Sky associated with Cosmic Rays*, Nature 171, 349.

Ghisellini, G. and Madau, P. 1996, *On the origin of the gamma-ray emission in blazars*, Monthly Notices Royal Astronomical Society 280, 67.

Gil, J., Lyubarsky, Y. and Melikidze, G. I., 2004, *Curvature Radiation in Pulsar Magnetospheric Plasma*, The Astrophysical Journal 600, 872.

Grube, J. 2007, *X-ray and Gamma-ray Study of TeV Blazars with RXTE, XMM-Newton, and the Whipple 10 m Telescope*, PhD Thesis, University of Leeds.

Harwit, M. 1988, *Astrophysical Concepts*, Springer-Verlag.

Hays, E. A. 2004, *A Search for TeV Emission from Active Galaxies using the Milagro Observatory*, PhD Thesis, University of Maryland.

Henri, G. and Saugé, L. 2006, *The Bulk Lorentz Factor Crisis of TeV Blazars: Evidence for an Inhomogeneous Pileup Energy Distribution?*, The Astrophysical Journal 640, 185.

Hillas, A. M. 1982, *The sensitivity of Cerenkov radiation pulses to the longitudinal development of cosmic-ray showers*, Journal of Physics G: Nuclear and Particle Physics 8, 1475.

Hillas, A. M. 1985, *Cerenkov light images of EAS produced by primary gamma*, Proceedings of 19th International Cosmic Ray Conference (La Jolla) 3, 445.

Hillas, A. M. 1996, *Differences between Gamma-Ray and Hadronic Showers*, Space Science Reviews 75, 17.

Hillas, A. M. 1998, *High-energy astrophysics: Cosmic rays without end*, Nature 395, 15.

Hillas, A. M., et al. 1998, *The Spectrum of TeV Gamma Rays from the Crab Nebula*, The Astrophysical Journal 503, 744.

Hofmann, W., et al. 2005, *H.E.S.S Status*, Proceedings of Conference Towards a Network of Atmospheric Cherenkov Detectors VII (Palaiseau), 43.

Holder, J., et al. 2003, *Detection of TeV Gamma Rays from the BL Lacertae Object 1ES 1959+650 with the Whipple 10 Meter Telescope*, The Astrophysical Journal Letters 583, 9.

Holt, S. S., et al. 1980, *X-Ray Spectral Constrains on the Broad-line Cloud Geometry of NGC 4151*, The Astrophysical Journal 241, 13.

Horan, D. 2001, *The Discovery of TeV γ-rays from the BL Lacertae object, 1H1426+428*, PhD Thesis, University College Dublin.

Horan, D. 2007, *VERITAS: Status, Performance and Latest Results*, Bulletin of the American Astronomical Society, 39, 784.

Horan, D., et al. 2002, *Detection of the BL Lacertae Object H1426+428 at TeV Gamma-ray Energies*, The Astrophysical Journal 571, 753.

Horan, D., et al. 2009, *Multiwavelength Observations of Markarian 421 in 2005-2006*, The Astrophysical Journal 695, 596.

Hudson, D. S., Reiprich, T. H., Clarke, T. E. and Sarazin, C. L. 2006, *X-ray Detection of the Proto Supermassive Binary Black Hole at the Centre of Abell 400*, Astronomy and Astrophysics 453, 433.

Hufnagel, B. R. and Bregman, J. N. 1992, *Optical and radio variability in blazars*, The Astrophysical Journal 386, 473.

Jahoda, K., et al. 1996, *Recent Progress in Calibration of the Rossi X-ray Timing Explorer Proportional Counter Array*, American Astronomical Society 28, 1285.

Jahoda, K., et al. 2006, *Calibration of the Rossi X-Ray Timing Explorer Proportional Counter Array*, The Astrophysical Journal Supplement 163, 401.

Jenner, L. 2008, http://www.nasa.gov/mission_pages/GLAST/spacecraft/index.html.

Jurkevich, I. 1971, *A Method of Computing Periods of Cyclic Phenomena*, Astrophysics and Space Science 13, 154.

Kellermann, K. I., et al. 2004, *Sub-Milliarcsecond Imaging of Quasars and Active Galactic Nuclei. III. Kinematics of Parsec-scale Radio Jets*, The Astrophysical Journal 609, 539.

Kembhavi, A. K. and Narlikar J. V. 1999, *Quasars and Active Galactic Nuclei - An Introduction*, Cambridge University Press.

Kildea, J. 2002, *Studies of the Crab Nebula and Pulsar at TeV Energies*, PhD Thesis, University College Dublin.

Kildea, J. 2008, private communication.

Kildea, J., et al. 2007, *The Whipple Observatory 10m Gamma-ray Telescope, 1997-2006*, Astroparticle Physics 28,128.

Kiuchi R., et al. 2009, *CANGAROO-III Search for TeV Gamma-rays from two Clusters of Galaxies*, The Astrophysical Journal 704, 240.

Komossa, S., et al. 2003, *Discovery of a Binary Active Galactic Nucleus in the Ultraluminous Infrared Galaxy NGC 6240 Using Chandra*, The Astrophysical Journal 582, 15.

Kovalev, Y. Y., et al. 2005, *Sub-Milliarcsecond Imaging of Quasars and Active Galactic Nuclei. IV. Fine-Scale Structure*, The Astronomical Journal 130, 2473.

Kranich, D., et al. 2001, *QPO analysis of the TeV and X-ray lightcurve of Mkn 501 in 1997 final results*, Proceedings of 27th International Cosmic Ray Conference (Hamburg) 7, 2630.

Kraus, J. 1966, *Radio Astronomy*, McGraw-Hill.

Krawczynski, H., et al. 2001, *Simultaneous X-Ray and TeV Gamma-Ray Observation of the TeV Blazar Markarian 421 during 2000 February and May*, The Astrophysical Journal 559, 187.

Krawczynski, H., et al. 2004, *Multiwavelength observations of strong flares from TeV Blazar 1ES 1959+650*, The Astrophysical Journal 601, 151.

Krennrich, F., et al. 1999, *Measurement of the Multi-TeV Gamma-Ray Flare Spectra of Markarian 421 and Markarian 501*, The Astrophysical Journal 511, 149.

Krennrich, F., et al. 2002, *Discovery of Spectral Variability of Markarian 421 at TeV Energies*, The Astrophysical Journal 575, 9.

Le Bohec, S., et al. 2004, *Observation of M87 at 400 GeV with the Whipple 10 Meter Telescope*, The Astrophysical Journal 610, 156.

Le Bohec, S. and Holder, J. 2003, *The cosmic ray background as a tool for relative calibration of atmospheric Cherenkov telescopes*, Astroparticle Physics 19, 221.

Lee, K. 2008, *Gamma-ray and Optical Variability of the TeV Blazars*, PhD Thesis, Washington University, Saint Louis.

Levine, A. M., et al. 1996, *First Results from the All-Sky Monitor on the Rossi X-Ray Timing Explorer*, The Astrophysical Journal Letters 469, 33.

Lister, M. L. and Homan, D. C. 2005, *MOJAVE: Monitoring of Jets in Active Galactic Nuclei with VLBA Experiments. I. First-epoch 15 GHz Linear Polarization Images*, The Astronomical Journal 130, 1389.

Liu, F. K., Liu, B. F. and Xie, G. Z. 1997, *The long-term optical behavior of Mkn 421*, Astronomy and Astrophysics Supplement 123, 569.

Lomb, N. R. 1976, *Least-squares frequency analysis of unequally spaced data*, Astrophysics and Space Science 39, 447.

Lyutikov, M. 2003, *Role of reconnection in AGN jets*, New Astronomy Reviews 47, 513.

Mannheim, K. 1993, *The proton blazar*, Astronomy and Astrophysics 269, 67.

Mannheim, K. and Biermann, P. L. 1992, *Gamma-ray flaring of 3C 279 - A proton-initiated cascade in the jet?*, Astronomy and Astrophysics 253, L21.

Maoz, D., Markowitz, A., Edelson, R. and Nandra, K. 2002, *X-ray versus Optical Variation in the Seyfert 1 Nucleus NGC 3516: A Puzzling Disconnectedness*, The Astrophysical Journal 124, 1988.

Maraschi, L., et al. 1994, *The 1993 multiwavelength campaign on 3C 279: The radio to gamma-ray energy distribution inlow state*, The Astrophysical Journal Letters 435, 91.

Maraschi, L., et al. 1999, *Simultaneous X-Ray and TEV Observations of a Rapid Flare from Markarian 421*, The Astrophysical Journal 526, 81.

Marshall, K., Ryle, W. T. and Miller, H. R. 2008, *Correlated X-Ray and Optical Variability in Markarian 509*, The Astrophysical Journal 677, 880.

Marscher, A. P., et al. 2008, *The inner jet of an active galactic nucleus as revealed by a radio-to-γ-ray outburst*, Nature 452, 966.

Mastichiadis, A. 1996, *The Hadronic Model of Active Galactic Nuclei*, Space Science Reviews 75, 317.

Mastichiadis, A. and Kirk, J. G. 1997, *Variability in the synchrotron self-Compton model of blazar emission*, Astronomy and Astrophysics 320, 19.

McCann, A., Hanna, D. and McCutcheon, M. 2009, *An Alignment System for Imaging Atmospheric Cherenkov Telescopes*, Proc. 31st International Cosmic Ray Conference (Lodz), http://icrc2009.uni.lodz.pl/proc/pdf/icrc0650.pdf.

McEnery, J. E. 1997, *TeV Gamma-Ray Variability of the BL Lacertae Object Markarian 421*, PhD Thesis, University College Dublin.

McEnery, J. E., et al. 1997, *TeV Observations of the Variability and Spectrum of Markarian 421*, Proceedings of 25th International Cosmic Ray Conference (Durban) 3, 252.

MOJAVE Collaboration 2009, http://www.physics.purdue.edu/astro/MOJAVE.

Moriarty, P., et al. 1997, *Strategies for selection of small γ-ray showers using the Imaging Atmospheric Cherenkov Technique*, Astroparticle Physics 7, 315.

Morrison, P. 1958, *On gamma-ray astronomy*, Nuovo Cimento 7, 858.

Murphy P. 2009, http://www.cv.nrao.edu/course/astr534/Radiometers.html.

NASA/CXC/M. Weiss 2008, http://chandra.harvard.edu/resources/illustrations/quasar.html.

Nieppola, E., et al. 2007, *37 GHz observations of a large sample of BL Lacertae objects*, The Astronomical Journal 133, 1947.

Nishikawa, D., et al. 1999, *Periodicity in the TeV gamma rays and X rays from Markarian 501*, Proceedings of 26th International Cosmic Ray Conference (Salt Lake City) 3, 354.

Piner, B. G. and Edwards, P. G. 2004, *The Parsec-Scale Structure and Jet Motions of the TeV Blazars 1ES 1959+650, PKS 2155-304, and 1ES 2344+514*, The Astrophysical Journal 600, 115.

Piner, B. G. and Edwards, P. G. 2005, *VLBA Polarization Observations of Markarian 421 after a Gamma-Ray High State*, The Astrophysical Journal 622, 168.

Porkess, R. 2004, *Statistics*, Harper Collins Publishers.

Press, W. H., et al. 2007, *Numerical Recipes*, Cambridge University Press.

Punch, M., et al. 1992, *Detection of TeV photons from the active galaxy Markarian 421*, Nature 358, 477.

Quinn, M. 2005, *Extreme Galaxies: TeV Gamma-ray Emission from the Blazar 1ES2344+514*, MSc Thesis, Galway-Mayo Institute of Technology.

Rebillot, P. F., et al. 2006, *Multiwavelength Observations of the Blazar Markarian 421 in 2002 December and 2003 January*, The Astrophysical Journal 641, 740.

Rees, D. G. 1995, *Essential Statistics (3rd Edition)*, Chapman & Hall.

Roache, E., et al. 2007, *Mirror Facets for the VERITAS Telescopes*, Proceedings of 30th International Cosmic Ray Conference (Merida) 3, 1397.

Rödig, C., Burkart, T., Elbracht, O. and Spanier, F. 2009, *Mutiwavelength periodicity study of Markarian 501*, Astronomy and Astrophysics 501, 925.

Rodriguez-Pascual, P. M., et al. 1997, *Steps toward determination of the size and structure of the broad-line region in active galactic nuclei. IX. Ultraviolet observations of Fairall 9*, The Astrophysical Journal Supplement 110, 9.

Rohlfs, K. and Wilson, T. L. 2000, *Tools of Radio Astronomy (3rd Edition)*, Springer-Verlag.

Rolnick, W. B. 1994, *The Fundamental Particles and Their Interactions*, Addison-Wesley Publishing Company.

Rothschild, R. E., et al. 1998, *In-Flight Performance of the High-Energy X-Ray Timing Experiment on the Rossi X-Ray Timing Explorer*, The Astrophysical Journal 496, 538.

Scargle, J. D. 1982, *Studies in astronomical time series analysis. II - Statistical aspects of spectral analysis of unevenly spaced data*, The Astrophysical Journal 263, 835.

Schmidt, M. 1963, *3C 273: A Star-Like Object with Large Red-Shift*, Nature 197, 1040.

Schroedter, M. 2004, *The Very High Energy Gamma-ray Spectra of AGN*, PhD Thesis, The University of Arizona.

Seyfert, C. K. 1943, *Nuclear Emission in Spiral Nebulae*, The Astrophysical Journal 97, 28.

Sikora, M. and Madejski, G. 2001, *On pair content of quasar jets*, AIP Conference Proceedings 599, 935.

Sikora, M., Begelman, M. and Rees, M. 1994, *Comptonization of diffuse ambient radiation by a relativistic jet: The source of gamma rays from blazars?*, The Astrophysical Journal, 421, 153.

Sikora, M. and Madejski, G. 2001, *Blazars*, AIP Conference Proceedings 558, 275.

Sillanpää, A. K. 1998, *New Evidences for the OJ 287 Binary Black Hole Model*, Abstracts of 19th Texas Symposium on Relativistic Astrophysics and Cosmology (Paris) 435S.

Silva, W. P. 2008, http://zeus.df.ufcg.edu.br/labfit/index_xyExtract.htm.

Sinigaglia, G. 1977, *Elementi di Tecnica Radioastronomica*, C&C Edizioni Radioelettroniche.

Sinnis, C., et al. 2001, *First Use of Background Rejection in an EAS Array to Detect TeV Gamma Rays from an Astronomical Source*, Proceedings of 27th International Cosmic Ray Conference (Hamburg) 6, 2579.

Smith A. J., et al. 2001, *A search for burst of TeV gamma rays with Milagro*, Proceedings of 27th International Cosmic Ray Conference (Hamburg) 7, 2731.

Smith A. J., et al. 2007, *Long Duration Variability and Spectrum of Mrk421*, Proceedings of 30th International Cosmic Ray Conference (Merida) 3, 973.

Spada, M., Ghisellini, G., Lazzati, D. and Celotti, A. 2001, *Internal shocks in the jets of radio-loud quasars*, Monthly Notices Royal Astronomical Society 325, 1559.

Spergel, D. N., et al. 2007, *Wilkinson Microwave Anisotropy Probe (WMAP) Three Year Results: Implications for Cosmology*, The Astrophysical Journal Supplement 170, 377.

Sudou, H., Iguchi, S., Murata, Y. and Taniguchi, Y. 2003, *Orbital Motion in the Radio Galaxy 3C 66B: Evidence for a Supermassive Black Hole Binary*, Science 300, 1263.

Tavani, M., et al. 2011, *Discovery of Powerful Gamma-Ray Flares from the Crab Nebula*, Science, DOI: 10.1126/science.1200083.

Tavecchio, F. and Ghisellini, G. 2008, *Structured jets and VHE emission of blazars and radiogalaxies*, AIP Conference Proceedings 1085, 431.

Teräsranta, H., et al. 1998, *Fifteen years monitoring of extragalactic radio sources at 22, 37 and 87 GHz*, Astronomy and Astrophysics Supplement 132, 305.

Toner, J. 2008, *Multiwavelength Observations of TeV Blazars in 2006-07*, PhD Thesis, National University of Ireland, Galway.

Toner, J., et al. 2007, *Bias Alignment of the VERITAS Telescopes*, Proceedings of 30th International Cosmic Ray Conference (Merida) 3, 1401.

Tornikoski, M., Mujunen, A. and Hurta, S. 2006, *Metsähovi Radio Observatory Annual Report 2005*.

UCD High-Energy Astrophysics Group 1999, *UCD Data Analysis Manual*.

Urry, C. M. and Padovani, P. 1995, *Unified Schemes for Radio-Loud Active Galactic Nuclei*, Publications of Astronomical Society Pacific 107, 803.

Véron-Cetty, M.-P. & Véron, P. 2010, *A catalogue of quasars and active nuclei (13th Edition)*, Astronomy and Astrophysics, 518, 10.

Weekes, T. C. 2003, *Very High Energy Gamma-ray Astronomy*, Institute of Physics Publishing.

Weekes, T. C. 2008, private communication.

Weekes, T. C., et al. 1989, *Observation of TeV gamma rays from the Crab nebula using the atmospheric Cerenkov imaging technique*, The Astrophysical Journal 342, 379.

Whipple Collaboration 2004, *Whipple Gamma-ray Telescope Manual*.

Zhang, Y. H., et al. 2005, *XMM-Newton View of PKS 2155-304: Characterizing the X-ray Variability Properties with EPIC pn*, The Astrophysical Journal 629, 686.